Doctoral Dissertation

Studies on MIMO Spatial Multiplexing for High-Speed Wireless Communications

Graduate School of Information Science and Technology
Hokkaido University

Hiroshi Nishimoto

2007

Contents

List of Tables

List of Figures

List of Abbreviations

2D-MUSIC	2-dimensional multiple signal classification
3GPP	third generation partnership project
AEC	anechoic chamber
ARQ	automatic repeat request
AS	antenna spacing
BCC	binary convolutional code
BER	bit error rate
B-SDM	beam-space division multiplexing
BLAST	Bell Laboratories layered space-time
BLER	block error rate
bps	bits per second
BPSK	binary phase shift keying
CDF	cumulative distribution function
CDMA	code division multiple access
COS	coding over substreams
CP	cyclic prefix
CPS	coding per substream
CRC	cyclic redundancy check
CSI	channel state information
DC	direct current
DFT	discrete Fourier transform
DOA	direction-of-arrival
DS-CDMA	direct sequence (direct spread) code division multiple access

E_s/N_0	received-signal-energy-per-symbol-to-noise-power-spectral-density ratio
E-SDM	eigenbeam-space division multiplexing
EVD	eigenvalue decomposition
FDCE	frequency-domain channel estimation
FDD	frequency division duplex
FDE	frequency domain equalization
FEC	forward error correction
FER	frame error rate
FFT	fast Fourier transform
GI	guard interval
GS	Gram-Schmidt
HARQ	hybrid automatic repeat request
HSDPA	high speed downlink packet access
IDFT	inverse discrete Fourier transform
IEEE	The Institute of Electrical and Electronics Engineers
IFFT	inverse fast Fourier transform
i.i.d.	independent and identically distributed
IMT-2000	International Mobile Telecommunications 2000
LDPC	low-density parity-check
LLR	log-likelihood ratio
LOS	line-of-sight
LTE	long term evolution
MC-CDMA	multi-carrier code division multiple access
MCS	modulation and coding schemes
MIMO	multiple-input multiple-output
MLD	maximum likelihood detection
MMSE	minimum mean square error
MSE	mean square error
MSSP	modified spatial smoothing preprocessing

MUSIC	multiple signal classification
NLOS	non-line-of-sight
OFDM	orthogonal frequency division multiplexing
OSD	ordered successive detection
PC	phase compensation
PDC	personal digital cellular
PE-SDM	pseudo eigenbeam-space division multiplexing
PEV	pseudo eigenvector
PHS	personal handy-phone system
PIC	parallel interference canceller
QAM	quadrature amplitude modulation
QoS	quality of service
QPSK	quadrature phase shift keying
RMS	root mean square
RX	receive
SC	single-carrier
SIC	serial interference canceller
SISO	single-input single-output
SINR	signal-to-interference-and-noise power ratio
SIR	signal-to-interference power ratio
SNR	signal-to-noise power ratio
SSP	spatial smoothing preprocessing
SVD	singular value decomposition
TDD	time division duplex
TDMA	time division multiple access
TEV	true eigenvector
TOA	time-of-arrival
TX	transmit
ULA	uniform linear array
UMTS	universal mobile telephone system

VA	Viterbi algorithm
V-BLAST	vertical Bell Laboratories layered space-time
VNA	vector network analyzer
WF	water-filling
WiMAX	worldwide interoperability for microwave access
WLAN	wireless local area network
WMAN	wireless metropolitan area network
ZF	zero-forcing

List of Notation

$\boldsymbol{a}$	column vector $\boldsymbol{a}$ (bold-faced small letter)
$\boldsymbol{A}$	matrix $\boldsymbol{A}$ (bold-faced capital letter)
a^*	complex conjugate of a scalar a
$\boldsymbol{a}^T$	transpose of $\boldsymbol{a}$ (row vector)
$\boldsymbol{A}^T$	transpose of $\boldsymbol{A}$
$\boldsymbol{a}^H$	Hermitian transpose of $\boldsymbol{a}$ $(\boldsymbol{a}^H = (\boldsymbol{a}^*)^T)$
$\boldsymbol{A}^H$	Hermitian transpose of $\boldsymbol{A}$
$\boldsymbol{A}^{-1}$	inverse of a square matrix $\boldsymbol{A}$
$\boldsymbol{A}^+$	Moore-Penrose pseudo inverse of $\boldsymbol{A}$
$\mathcal{GS}[\boldsymbol{A}]$	Gram-Schmidt orthonormalization of $\boldsymbol{A}$
$\boldsymbol{I}_N$	N-dimensional unit matrix
$\mathrm{diag}(a_1, \ldots, a_N)$	N-dimensional diagonal matrix of which diagonal elements are $a_1, \ldots, a_N$
$\lvert a \rvert$	absolute value of a scalar a
$\lVert \boldsymbol{a} \rVert$	vector norm of $\boldsymbol{a}$
$E[\cdot]$	expectation
$\min(a_1, \ldots, a_N)$	the minimum (smaller) value among the given entries $a_1, \ldots, a_N$ (also represented as $\min_{i;\, 1 \le i \le N} a_i$)
$\max(a_1, \ldots, a_N)$	the maximum (larger) value among the given entries $a_1, \ldots, a_N$ (also represented as $\max_{i;\, 1 \le i \le N} a_i$)
$\mathcal{F}[\cdot]$	Fourier transform
$\mathcal{F}^{-1}[\cdot]$	inverse Fourier transform

Chapter 1

Introduction

1.1 Background

Today the demand for ever higher data-rate communications has been still growing. In wired communications, the penetration of broadband lines enabled us to transmit and receive large volumes of data easily and freely via the Internet. The appearance of various multimedia devices and services over broadband networks, e.g., digital camera, portable music player, DVD, video streaming, etc., has accelerated the demand. In wireless communications, the dramatic spread of mobile phones changed our lives thoroughly. In Japan, the number of contracts of mobile phones including personal handy-phone system, or PHS, in 2007 already exceeds one hundred million [1]. The diffusion allowed us to talk with anyone and to receive any information irrespective of the time and location. Moreover, due to highly-functionalized mobile phones and camera phones, the frequent use of large data transmission has appeared even in mobile phone systems. Not only in mobile phones, there has been the need for higher data rates also in other wireless network fields. The concept of wireless local area network (WLAN), which does not require any cables to connect to networks or other devices, has developed gradually along with the growth of Internet markets. Then today we see not only private and business use but also commercial use of WLAN; public Internet wireless access services using WLAN, so-called *hot spot* or *free spot*, are expanding, and last-one-mile services using WLAN (in this case also referred to as wireless metropolitan area network, or WMAN) are being established especially in country or suburban areas which have difficulties in having wired networks. Thus, it is indispensable to meet the growing demand in wireless fields.

The origin of radio communications dates back to the close of the 19th century. In 1898, Guglielmo Marconi succeeded to transmit his signal across the English Channel, 52 km wide, between Wimereux and Dover. It was the dawn of the radio era. Over the past 100 years, steady progress in radio fields has been brought by support of various

technologies.

In particular, for the last two or three decades, wireless fields have been dramatically developed by the emergence of mobile phones. Originally, the Bell Laboratories proposed the cellular concept for a large number of mobile users, which is to divide the service area into cells with smaller size without expanding bandwidth [2]. During the 1970s–1980s, companies such as AT&T and Motorola engaged in fierce competition in the cellular field. In Japan, Nippon Telephone and Telegraph (NTT) began to serve a commercial cellular automobile phone system with 800 MHz in Tokyo in 1979. Today such systems are referred to as systems of the first generation (1G) [3, 4]. Since then, mobile cellular systems have evolved rapidly. Due to the rapid growth of the cellular market and the demand for digital communications, in the beginning of the 1990s, the deployment of the global system for mobile communications, or GSM, was started first in Europe. On the other hand, in the U.S.A. the most popular standards were the TDMA/136 using time division multiple access and IS-95 using code division multiple access (CDMA). In Japan, the personal digital cellular (PDC) system served by NTT DoCoMo in 1993, which employs frequency division duplex (FDD) and TDMA, became widely accepted. These cellular systems in the 1990s are called the second generation (2G) systems.

However, combined with explosive diffusion of the Internet in the 1990s, the demand for higher data rates and spectral efficiency has led to the development of the new wireless technologies, i.e., the third generation (3G) phone systems. 3G standards have evolved under the names of International Mobile Telecommunications 2000 (IMT-2000) and CDMA2000. IMT-2000 is also called wideband CDMA (W-CDMA) or universal mobile telephone system (UMTS), and employs wideband direct sequence (or direct spread) CDMA (DS-CDMA). CDMA2000 is based on multi-carrier CDMA (MC-CDMA). Compared with 2G systems, 3G systems are capable of supporting much higher data rates, user mobility, and quality of service (QoS). In Japan, NTT DoCoMo started the W-CDMA service named FOMA in 2001, and au by KDDI launched the cdma2000 1x service based on CDMA2000 in 2002. Then, in 2006 NTT DoCoMo also started the higher data-rate packet telecommunication service named high speed downlink packet access (HSDPA), which can deliver the maximum data rate of 14.4 Mbps in downlink by employing advanced technologies: hybrid automatic repeat request (HARQ), fast packet scheduling, adaptive modulation and coding, and so on. Ongoing 3G standardization is being initiated by the third generation partnership project, or 3GPP, toward long term evolution, or LTE, which targets the future wireless era including Super3G (also referred to as Beyond 3G or 3.9G) and fourth generation (4G). It is expected that bit rates in Super3G systems reach up to 100 Mbps, and that those in 4G systems are a maximum of about 1 Gbps.

Such growing demands for higher data rates and QoS are not only in cellular systems as mentioned before. While cellular systems have evolved from voice services, wireless networking systems such as WLAN have developed independently for the purpose of data transmission for portable personal computers. The Institute of Electrical and Electronics Engineers (IEEE) launched the IEEE802.11 working group for WLAN [5, 6], and in 1999 it established IEEE802.11a as an indoor WLAN standard which theoretically delivers bit

rates up to 54 Mbps. Recently, researchers in the group have discussed a new standard named IEEE802.11n, which targets bit rates over 100 Mbps (planned up to about 600 Mbps in the future), and they already have laid down its draft version. Also, another working group IEEE802.16 established a WMAN standard, so-called worldwide interoperability for microwave access, or WiMAX, which covers indoor and outdoor, intermediate and long distance broadband communications.

Meeting these demands in wireless fields is the mission for us that should be accomplished, and it will contribute to the future public welfare where anyone benefits from the information technology (IT) "anytime, anywhere," i.e., the ubiquitous society.

1.2 Objectives of the Dissertation

A multiple-input multiple-output (MIMO) system in which multiple antennas are placed at both the transmitter and receiver has been expected as one of the promising breakthroughs to meet the growing demands for high-data-rate services in wireless communications [7–13], and is already one of the core technologies in some wireless standards [5,6,14,15]. The initial theoretical work on the MIMO system based on the Shannon capacity limit [16] was developed by Telatar in 1995 [17] and Foschini in 1996 [18]. They showed the potential of the MIMO system that it can increase channel capacity as the number of antenna elements increases. Both of them were with Bell Laboratories, where many pioneers on the MIMO system have been produced. A group of them including Foschini developed a vertical Bell Laboratories layered space-time (V-BLAST) architecture and demonstrated the world's first implementation of MIMO and the architecture in the laboratory [19–21].

Exploiting a MIMO system offers array gain, diversity gain yielded by space-time coding such as space-time block code (STBC) [22–24], and spatial multiplexing. In particular, spatial multiplexing enables us to transmit multiple spatial substreams without expanding frequency bandwidth so that data rates can increase in proportion to the number of substreams. Here the author classifies it into two schemes for the following discussion: space division multiplexing (SDM) [19, 25, 26] and eigenbeam-space division multiplexing (E-SDM) [27–31]. The former technique, SDM, in which each transmit antenna sends an independent signal substream with equal resource (bits and power) allocation, is a simple and promising way to increase data transfer speeds when the MIMO channel state information (CSI) is not available at the transmitter. When the MIMO CSI is available at both the transmitter and receiver, on the other hand, E-SDM can be applied. This transmission technique enables us to transmit spatially orthogonal substreams when eigenvectors obtained by singular value decomposition (SVD) of the MIMO channel matrix are used as transmit weight vectors. Therefore, this architecture is also called SVD-MIMO [32] (or closed-loop MIMO [33] since the CSI feedback is generally required). The maximum throughput of the MIMO channel can be achieved by E-SDM with resource (data rate and transmit power) adaptation. Accordingly, this scheme can potentially provide enormous capacities and excellent communication quality in MIMO systems.

1.2.1 Measurement-Based Performance Evaluation of MIMO Spatial Multiplexing

Coding and signal processing are key elements to successful implementation of a MIMO system. However, issues related to antennas and electromagnetic propagation also play a significant role in determining MIMO system performance [34]. A low correlation between channels is desirable because SDM needs to demultiplex the received signals in order to detect the transmitted substreams at the receiver end. Availability of spatial multiplexing has been assessed for independent and identically distributed (i.i.d.) Rayleigh fading channels caused by many scattered signals from surrounding objects. Fades between pairs of transmit–receive antenna elements (channels) are, however, correlated in real propagation environments due to insufficient antenna spacing [35]. Moreover, since mutual coupling effects [36–41] exist in a multiple antenna system, characteristics of the antennas vary from those of a single isolated antenna case. Therefore, in actual MIMO communication systems, there is no guarantee that channels are i.i.d. and even that MIMO channel elements obey identically distributed fading.

Uncorrelated channels generally may exist in NLOS environments where there is no direct wave from the transmitter to the receiver. However, there are also many situations in which communications are done in LOS environments. In such cases, while the LOS component can increase the received power level, the channels lose independence and are correlated. Highly correlated channels may make it difficult to detect the transmitted streams. Many radio propagation measurement campaigns have already been conducted on MIMO systems [21, 42–50]. So far, most of researchers have evaluated the performance of the MIMO systems as a function of average signal-to-noise power ratio (SNR). Because of the evaluation, some reports have presented that NLOS environments give higher channel capacities than LOS ones [42, 46]. However, the author must raise the following issue regarding these conclusions. In NLOS environments, the transmit power must be higher than in LOS environments in order to obtain the same SNR. In [42], while channel capacities under the same SNR condition are evaluated for both LOS and NLOS environments, it is also briefly discussed that the comparison is not necessarily fair. Moreover, it has been reported in [47, 48] that the actual SNR enlarged by the LOS component provides higher channel capacities. The author agrees with their viewpoint and considers that the performance evaluation of the MIMO system should be done under the same transmit power condition.

In measurement-based studies, MIMO systems have ordinarily been evaluated using channel capacities [42–48, 50]. Channel capacity is, however, the limit of digital communications given by the information theory. It would be achieved only if we employed an ideal transmission method that includes coding and modulation. From the implementational viewpoint, the author considers that not only channel capacity but also bit error rate (BER) can be used to evaluate digital wireless communications.

Also, some measurement-based MIMO research has been done with respect to virtual channels, especially Kronecker reconstructed channels [45, 49, 50]. When the number of measured channel samples is insufficient for a statistical analysis, such a channel produc-

tion scheme is effective because it can infinitely generate MIMO channels based on the measured data. Statistical characteristics of generated channels, however, may differ from those in the actual measurement environment [51]. Furthermore, the Kronecker reconstruction is generally used to produce virtual NLOS channels so that LOS channels, which are evaluated in my study, are out of the consideration. The author thinks that the MIMO characteristics in a target environment should be investigated using the measured channels themselves as much as possible.

On the basis of these ideas, the author conducted a MIMO channel measurement campaign in an indoor propagation environment where there are many scattered waves. While keeping a constant distance between the transmitter and the receiver, the author measured both 2×2 and 4×4 MIMO channels with mutual coupling between antennas in both LOS and NLOS conditions. The author has obtained enough actual channel samples for statistical analyses by collecting data in both the spatial and frequency domains [50]. This measurement scheme enables the MIMO characteristics in real environments to be analyzed more accurately. The performance of SDM and E-SDM in both the environments was examined under the same transmit power condition. In this dissertation, the author used channel capacity for the evaluation of ideal performance, and used BER under a constant bit rate requirement for more realistic and practical performance evaluation.

To investigate the effects of mutual coupling on the measured channel responses, the author paid attention to the array element patterns. Compared with the single antenna case, the antenna gain with mutual coupling depends on the direction and the array configuration. In particular, in LOS environments, the variation of antenna gain changes the impact of the LOS component in the measured channel. The author explored, therefore, the influence of array element patterns on the statistical properties of the measured channels and the relationship between the influence and the performance of MIMO systems. Moreover, as mentioned above, the author examined the BER performance based on the propagation measurement campaign. This means that, spatial multiplexing is comprehensively evaluated in the range from antennas and propagation to signal processing in this dissertation.

1.2.2 Pseudo Eigenbeam Transmission for Frequency-Selective MIMO Channels

In a frequency-selective MIMO channel, the use of orthogonal frequency division multiplexing (OFDM) transmission is effective because it is robust to delay paths [14, 15, 52, 53]. The optimum processing at the transmitter in a MIMO-OFDM system is beamforming based on eigenvectors at each subcarrier to orthogonalize the MIMO channel [54, 55]. Also in MIMO single-carrier (SC) transmission, we can apply eigenbeams to space-frequency domain equalization where the eigenbeam is calculated at each orthogonal frequency point [56]. However, since the computational complexity of SVD or eigenvalue decomposition (EVD) is very high, the total calculation load of SVD or EVD increases in proportion to the number of active frequency points. Hence, it is necessary to reduce the load.

In addition, conventional SVD or EVD has another problem. This procedure includes phase ambiguity itself and is individually executed at each frequency point. Even if it would be possible to remove such phase ambiguity, the order of eigenvalues/eigenvectors may change at some frequency points in a frequency selective channel, and it is still difficult to find such order switching over discrete frequency points. Thus, frequency correlation (hereinafter referred to as frequency continuity) of the transmit weight is difficult to be maintained. These emphasize frequency selectivity of the effective channel, which is observed at the receiver through both the effects of transmit weight and the MIMO channel. As a result, the impulse response has very large delay spread.

In the case without beamforming, it has been reported that the receiver can accurately estimate frequency-selective MIMO channels by using time windowing in both time- and frequency-domain estimation [57–62]. These schemes are commonly based on the concept of improving SNR by limiting the impulse response duration and suppressing the noise power outside the window. Unfortunately, it is difficult to employ these schemes to estimate the effective channel because of its large delay spread, as will be shown later. Maintaining frequency continuity of the effective channel is, therefore, one of the important issues in a beamforming system.

Choi and Heath proposed an interpolation-based beamforming scheme with considering phases of weight vectors in a MIMO-OFDM system with limited weight feedback [63]. In the method, the phases of eigenvectors are adjusted to provide good interpolation property at the transmitter side. However, the method does not guarantee maintaining frequency continuity so that utilizing the method as a solution for frequency continuity is currently inapplicable in that form.

To solve the issues raised above, the author proposes the pseudo eigenvector (PEV) technique which can reduce the calculation load and maintain frequency continuity of the effective channel. It will be shown that the pseudo E-SDM (PE-SDM) technique can provide almost the same or better MIMO-OFDM performance compared with the E-SDM when the receiver refines the effective channel estimate with time windowing. Such frequency-domain beamforming can also be applied to SC systems with frequency domain equalization (FDE) at the receiver [62]. Thus, in addition to MIMO-OFDM, the author evaluates the throughput performance of PE-SDM in MIMO-SC systems with minimum mean square error based FDE (MMSE-FDE) comparing with the E-SDM where a similar concept proposed in [63] is applied to improve frequency continuity. Also, focusing on the calculating process of PEVs, a spatial windowing scheme is proposed for improving the accuracy of effective channel estimates. Furthermore, the author also proposes an estimator of effective channels incorporating both the time and spatial windowing schemes, i.e., space-time windowing.

1.3 Contents of the Dissertation

The outline of the dissertation is illustrated in Fig. 1.1. Chapter 2 introduces a handled MIMO channel model and a brief overview of spatial multiplexing along with an original

study on i.i.d. MIMO channels based on the Jakes model. Chapter 3 explains a conducted measurement campaign and describes characteristics of the measurement environment including TOA/DOA estimation using two-dimensional multiple signal classification (2D-MUSIC) algorithm and estimation of Nakagami-Rice K-factor which specifies dominance of the direct wave in the LOS environment.

In Chapter 4, first the author shows azimuthal patterns of antennas used in the measurement, fading correlations, channel distributions, and eigenvalue distributions of measured channels in order to discuss the performance of spatial multiplexing thereafter. Then, by using channel capacity and BER under a total transmit power constraint, the availability of SDM in actual environments is discussed, and E-SDM performance compared with SDM is reported. In addition, the behavior of coded MIMO-OFDM SDM in the same environments is examined as a practical case of spatial multiplexing.

The latter part of the dissertation discusses the proposed PE-SDM transmission for broadband MIMO wireless systems. Chapter 5 first clarifies the model of broadband MIMO systems and the issues of the conventional frequency-domain beamforming using eigenvectors. Next, a PEV scheme proposed for mitigating the issues is explained, and its advantages of frequency continuity and low computational complexity are demonstrated. Then the author proposes a channel estimation scheme named time windowing exploiting the frequency continuity, and proves its effect on PE-SDM transmission through MIMO-OFDM computer simulations. On the other hand, PE-SDM can also be applied to broadband SC systems, so the author examines its throughput performance and benefits of spatial and space-time windowing schemes proposed in addition to the time windowing.

Chapter 6 presents the PE-SDM performance in actual propagation environments, i.e., composition of the measurement-based study on spatial multiplexing in Chapter 4 and PE-SDM proposed in Chapter 5. Assuming an indoor use such as WLAN [5, 6], the author explores the advantages and availability of the proposed PE-SDM and channel estimation schemes in practical environments. Finally, the author summarizes all the studies in the dissertation and draws conclusions in Chapter 7. In addition, future work that should be considered and tackled for prospective wireless fields is briefly discussed.

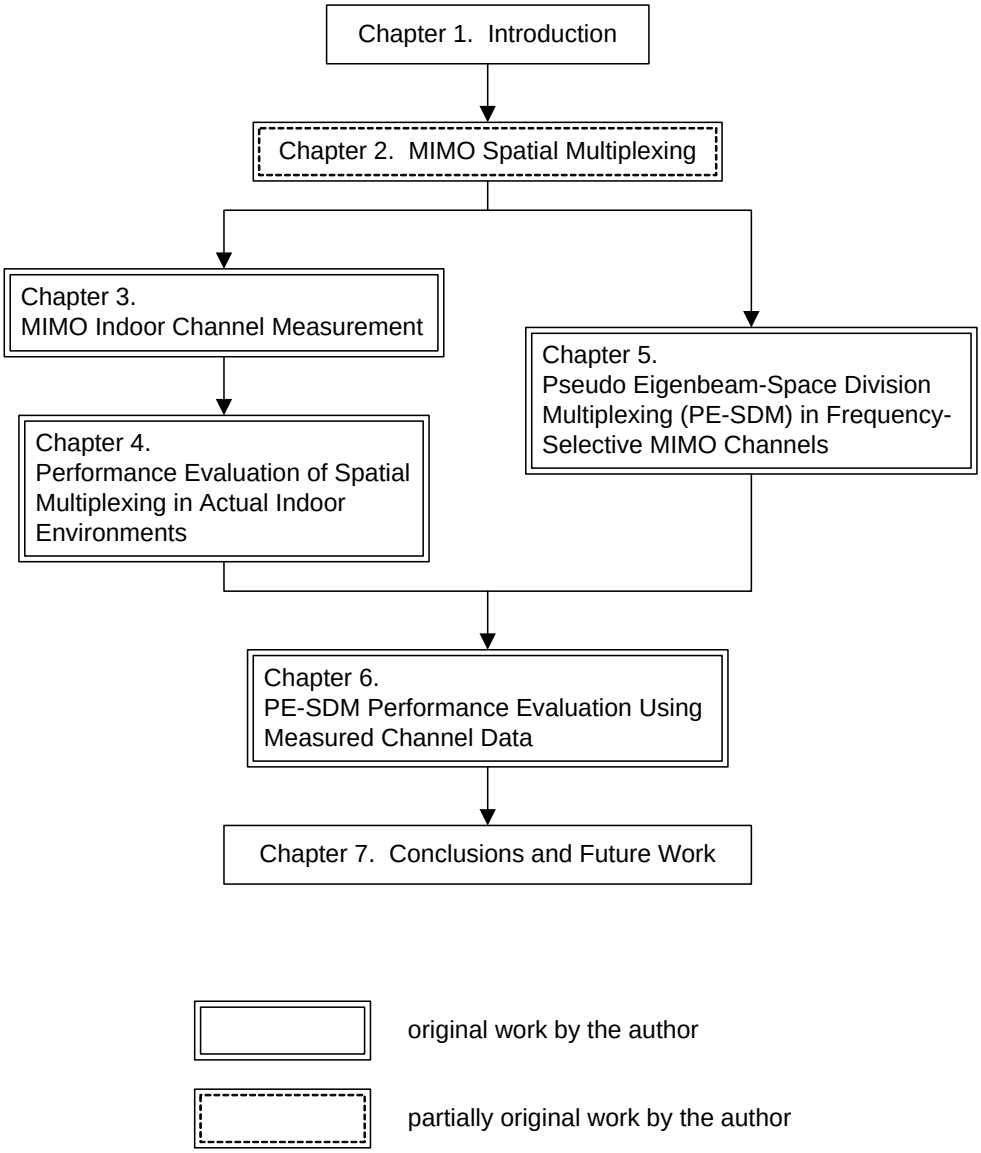

Figure 1.1: Outline of the dissertation.

Chapter 2

MIMO Spatial Multiplexing

2.1 MIMO Flat-Fading Channel Model

Figure 2.1 illustrates an image of a MIMO system. Here, it is assumed that the transmission frequency bandwidth is so narrow that the fading is frequency-flat. This assumption is applicable also in a broadband system because at each frequency point a channel can be regarded as a flat-fading one. When the MIMO system is assumed to have N_{tx} transmit (TX) antennas and N_{rx} receive (RX) antennas, an $N_{\mathrm{rx}} \times N_{\mathrm{tx}}$ MIMO channel matrix $\boldsymbol{H}$

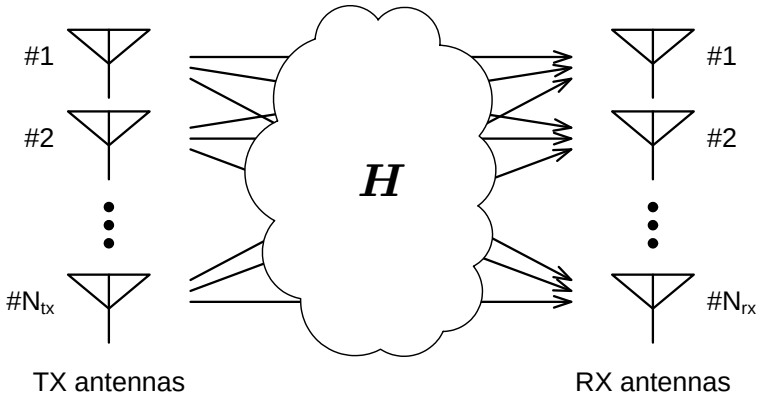

Figure 2.1: Concept of a MIMO channel.

between the TX and RX ends is expressed as

$$\boldsymbol{H} = \begin{bmatrix} h_{11} & h_{12} & \cdots & h_{1N_{\mathrm{tx}}} \\ h_{21} & h_{22} & \cdots & h_{2N_{\mathrm{tx}}} \\ \vdots & \vdots & h_{ij} & \vdots \\ h_{N_{\mathrm{rx}}1} & h_{N_{\mathrm{rx}}2} & \cdots & h_{N_{\mathrm{rx}}N_{\mathrm{tx}}} \end{bmatrix}, \tag{2.1}$$

where h_{ij}, which is an element of the ith row and the jth column in the matrix $\boldsymbol{H}$, denotes a channel from the jth TX antenna to the ith RX antenna.

As will be stated in the next chapter, the MIMO channels that the author measured in actual indoor environments have mutual coupling effects. When mutual coupling matrices in the TX and RX arrays are defined as $\boldsymbol{C}_{\mathrm{tx}}$ and $\boldsymbol{C}_{\mathrm{rx}}$, respectively, the measured channel matrix $\boldsymbol{H}$ is expressed as

$$\boldsymbol{H} = \boldsymbol{C}_{\mathrm{rx}} \bar{\boldsymbol{H}} \boldsymbol{C}_{\mathrm{tx}}^{T}, \tag{2.2}$$

where $\bar{\boldsymbol{H}}$ is an $N_{\mathrm{rx}} \times N_{\mathrm{tx}}$ actual channel matrix which does not include mutual coupling effects. When all of N antennas in an N-element array are assumed to have the same load impedance Z_L, an $N \times N$ mutual coupling matrix $\boldsymbol{C}$ is defined as

$$\boldsymbol{C}^{-1} = \frac{1}{Z_L} \begin{bmatrix} Z_L + Z_{11} & Z_{12} & \cdots & Z_{1N} \\ Z_{21} & Z_L + Z_{22} & \cdots & Z_{2N} \\ \vdots & \vdots & \ddots & \vdots \\ Z_{N1} & Z_{N2} & \cdots & Z_L + Z_{NN} \end{bmatrix}, \tag{2.3}$$

where Z_{ij} is self/mutual impedance between the ith and jth antennas [36, 37]. Note that $\boldsymbol{C}_{\mathrm{tx}}$ and $\boldsymbol{C}_{\mathrm{rx}}$ can actually have different definitions. In this dissertation, however, the author does not discuss them because it is beyond the scope of this dissertation. For the experimental study, MIMO transfer matrices including mutual coupling effects were obtained from channel data measured in actual indoor propagation environments (see next chapter). Using the measured channels, the characteristics and the performance of spatial multiplexing were evaluated as will be presented in Chapter 4.

2.2 Generation of i.i.d. MIMO Channels Using Jakes Model

In general, characteristics of MIMO channels are dependent on the fading environment so that actual channels should have various properties such as the number of paths, path loss, angular spreads of arriving waves, spatial correlation, and so on.

Therefore, as a beginning of a study on MIMO, many researchers, especially who study signal processing on MIMO, have started with i.i.d. Rayleigh fading in order to simplify the discussion. In computer simulations, we can obtain such channels by two approaches

of Gaussian random number generation and the Jakes model. The former is generally used for simulating quasi-static i.i.d. fading. On the other hand, the latter can be used for both quasi-static and time-varying i.i.d. fading conditions. Recently a MIMO system has been investigated as one of the promising ways to meet the growing demand for high data-rate service with high mobility. Thus, there are many opportunities to use a time-varying i.i.d. MIMO channel model in performance evaluations of MIMO systems.

Jakes model has been extensively used for simulating time-varying Rayleigh fading with U-shaped Doppler power spectrum [2,64]. The model can be simply applied to MIMO channels. When each element of a MIMO channel matrix independently obeys the model, i.e., by using multiple scattering rings, we can obtain i.i.d. time-varying MIMO channels, theoretically. Statistical validity of the MIMO channels is achieved with a sufficiently large number of scatterers in the rings. Since it is not desirable for prompt numerical analyses to locate many scattering points, relatively small numbers of scatterers are often used in fact. However, decreasing the scattering points without consideration on their arrangement may lead to statistical fluctuation depending on the initial phase at each point, as will be shown later. In this section, the author establishes simple and effective conditions on the arrangement of scattering points when using the MIMO Jakes model for sufficient stability of statistics.

2.2.1 Simplified Jakes Model

We consider a narrow-band MIMO system equipped with N_{tx} TX antennas and N_{rx} RX antennas. It is assumed that the kth RX antenna, which is surrounded by a scattering ring R_{kl} with M scattering points for paths from the lth TX antenna, moves with a velocity v as illustrated in Fig. 2.2. Thus, a time-varying channel $h_{kl}(t)$ from the lth TX antenna to the kth RX antenna, which is an element of the kth row and lth column in the MIMO channel matrix, can be generated using the Jakes model with the corresponding scattering ring R_{kl}.

We define x- and y-axes as the direction of motion and its orthogonal one, respectively. In a complex baseband system, the channel $h_{kl}(t)$ is represented as

$$h_{kl}(t) = \sum_{m=1}^{M} a_{kl,m}\, e^{j\left\{2\pi f_D\left(\cos\theta_{kl,m}\right)t+\phi_{kl,m}\right\}} \tag{2.4}$$

$$= \sum_{m=1}^{M} h_{kl,m}(t), \tag{2.5}$$

where $a_{kl,m}$, $\theta_{kl,m}$, and $\phi_{kl,m}$ are a received amplitude, an angle of arrival, and an initial phase of the mth scattered wave component $h_{kl,m}(t)$, respectively, and f_D is the maximum Doppler frequency. The Doppler shift caused by the mth scatterer is $f_D \cos\theta_{kl,m}$. Both $\theta_{kl,m}$ and $-\theta_{kl,m}$ contribute to the same Doppler shift because of $\cos\theta_{kl,m} = \cos\left(-\theta_{kl,m}\right)$. Thus, in Jakes model, it is known that scattering points should not be arranged symmetrically to the x-axis.

Here, it is defined that all M points are distributed only in the range of $0 \le \theta_{kl,m} \le \pi$ with equal interval π/M to facilitate the following discussion, as illustrated in Fig. 2.3.

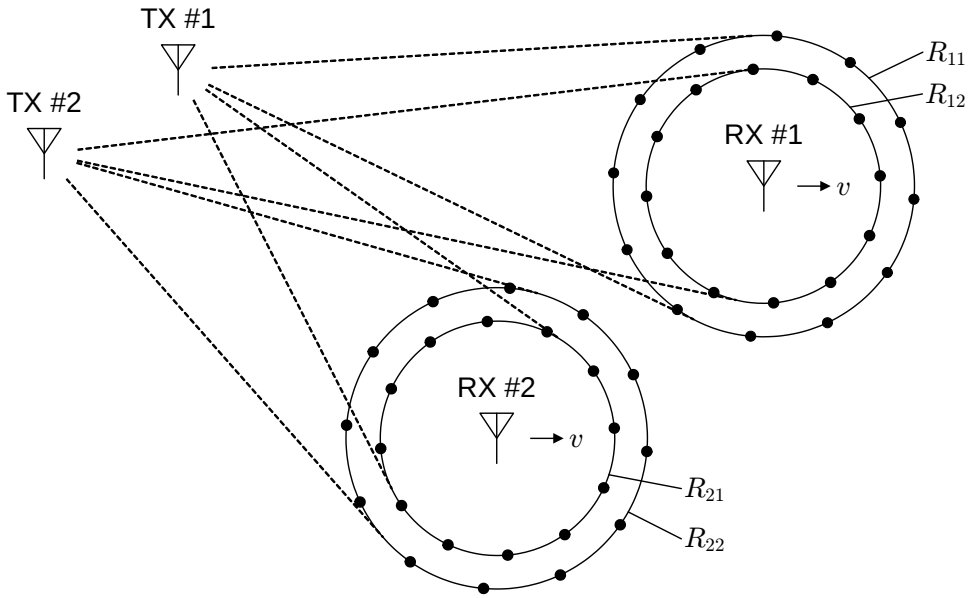

Figure 2.2: Concept of an i.i.d. time-varying MIMO channel model using multiple Jakes rings ($N_{\mathrm{tx}} = N_{\mathrm{rx}} = 2$).

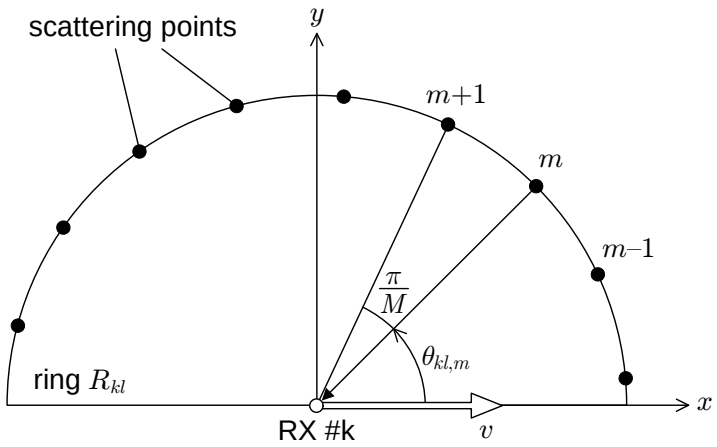

Figure 2.3: Simplified Jakes model.

Although, strictly speaking, each ring becomes a semicircle under the above angular condition, the author still refers to it as a ring hereinafter. In addition, we assume $a_{kl,m} = a = 1/\sqrt{M}$ for all k, l, and m for the sake of simplicity. Under the assumption, we obtain an ergodic channel power $E\left[|h_{kl}(t)|^2\right] = 1$.

2.2.2 Intra-Ring Condition

First, we consider the scattering ring R_{kl} only. When an arbitrary pair of scattering points m and m' locates in y-axis symmetry, i.e., $\theta_{kl,m} = \pi - \theta_{kl,m'}$, their absolute values of Doppler shift components are the same, i.e., $\left|f_D \cos\theta_{kl,m}\right| = \left|f_D \cos\left(\pi - \theta_{kl,m'}\right)\right|$. In this case, the channel may have exceptional characteristics depending on the initial phase. For example, consider the case of $\phi_{kl,m} = \phi_{kl,m'} = 0$. A superposed wave composed of these two scattered waves is expressed as $a\, e^{j2\pi f_D(\cos\theta_{kl,m})t} + a\, e^{-j2\pi f_D(\cos\theta_{kl,m})t} = 2a\cos\{2\pi f_D(\cos\theta_{kl,m})t\}$. This means that this component does not have its imaginary part, and that the amplitude becomes double. For another example, in the case of $\phi_{kl,m} = 0$ and $\phi_{kl,m'} = \pi$, it does not have its real part because it is expressed as $j2a\sin\{2\pi f_D\,(\cos\theta_{kl,m})\,t\}$. Thus, the y-axis symmetric arrangement of scattering points may cause instability on statistical fading properties. To avoid such phenomena, the following condition on arrangement of scattering points should be satisfied

$$\theta_{kl,m} \neq \pi - \theta_{kl,m'} \qquad \text{for } 1 \leq m, m' \leq M. \tag{2.6}$$

That is, scattering points should not be arranged symmetrically to the y-axis. The author defines the above condition as the intra-ring condition.

2.2.3 Inter-Ring Condition

When using multiple scattering rings, arrangement of scattering points across the rings should be considered. At first, we assume a time-varying $N_{\mathrm{rx}} \times N_{\mathrm{tx}}$ MIMO channel $\boldsymbol{H}(t)$ based on $N_{\mathrm{tx}}N_{\mathrm{rx}}$ scattering rings, where all the rings have the same scattering-point structure. The channel $\boldsymbol{H}(t)$ can be decomposed into M channel components $\boldsymbol{H}_1(t), \ldots, \boldsymbol{H}_M(t)$, where the mth component $\boldsymbol{H}_m(t)$ is composed of the mth scattered waves in all the $N_{\mathrm{tx}}N_{\mathrm{rx}}$ rings, i.e., $h_{kl,m}(t)$ for $k = 1, \ldots, N_{\mathrm{rx}}$ and $l = 1, \ldots, N_{\mathrm{tx}}$. In $\boldsymbol{H}_m(t)$, all the angles of arrival of wave components are the same, i.e., $\theta_{kl,m} = \theta_m$ regardless of antenna indices k and l, due to the same arrangement. Hence, $\boldsymbol{H}_m(t)$ can be expressed as

$$\boldsymbol{H}_m(t) = a\, e^{j2\pi f_D(\cos\theta_m)t}\boldsymbol{\Phi}_m, \tag{2.7}$$

where $\boldsymbol{\Phi}_m$ represents an $N_{\mathrm{rx}} \times N_{\mathrm{tx}}$ initial phase matrix in which an element of the kth row and lth column is $\phi_{kl,m}$.

The above equation implies that regularity of the matrix $\boldsymbol{H}_m(t)$ depends on the given initial phase set $\boldsymbol{\Phi}_m$. In the case of $\phi_{11,m} = \phi_{12,m} = \cdots = \phi_{N_{\mathrm{rx}}N_{\mathrm{tx}},m}$, it is obvious that the matrix is singular, i.e., $\mathrm{rank}\,[\boldsymbol{H}_m(t)] = 1$, regardless of time. Of course this is an over-simplified example, and the actual channel matrix $\boldsymbol{H}(t)$ is superposed by M channel components so that its regularity will be maintained. It is supposed, however, that such singular matrix components may cause an unstable property of $\boldsymbol{H}(t)$. The simplest way to avoid this is to satisfy the following condition on arrangement of scattering points across

rings defined as the inter-ring condition

$$\theta_{kl,m} \neq \theta_{k'l',m'} \qquad \text{for} \begin{cases} 1 \leq k, k' \leq N_{\mathrm{rx}} \\ 1 \leq l, l' \leq N_{\mathrm{tx}} \\ 1 \leq m, m' \leq M \end{cases}, \tag{2.8}$$

except $m = m'$ in the case of $k = k'$ and $l = l'$.

2.2.4 Numerical Analysis

The author simulated time-varying channels based on Jakes model for single-input single-output (SISO) and 2 $\times$ 2 MIMO cases to evaluate the intra- and inter-ring conditions. The author set $M = 12$ for each scattering ring and prepared 10,000 initial phase sets randomly given[1]. For each initial phase set, time-varying channels were generated based on (2.4), and 1,000,000 snapshots were captured in order to obtain its cumulative distribution function (CDF) of amplitudes and eigenvalues for SISO and MIMO cases, respectively.

Figure 2.4 demonstrates three examples for SISO channels yielded by different initial phase sets, where all the three Jakes rings had the same scattering-point structure without the intra-ring condition, i.e., y-axis symmetric structure. Figure 2.4(a) shows CDFs of amplitudes for the three cases. For comparison, the performance obtained by a complex Gaussian random process is also shown. It can be seen in Fig. 2.4(a) that the three CDFs do not agree with that of the Gaussian random process case and depend on given initial phases while they all show the Rayleigh distribution characteristic, i.e., the increase of one order of magnitude with an amplitude increment of 10 dB in their linear regions. Its impact on BER performance is shown in Fig. 2.4(b), where QPSK modulation was used. In the BER performance, difference similar to that in CDFs can be seen. This implies that the variation in CDFs of channels directly appears in transmission performance. To evaluate the fluctuation, the author observed an additional CDF of 10% values (hereinafter referred to as 10%-value CDF) for each scattering-point arrangement. Also, the author measured a value spread Δ defined as the difference between 1% and 99% values in the 10%-value CDF. The value spread Δ corresponds to possible fluctuation range of transmission performance over time-varying channels generated by Jakes model with different initial phase sets.

The author first evaluated the intra-ring condition for SISO channels by using 10%-value CDFs of the amplitudes and their value spreads shown in Fig. 2.5. Here, "conventional" denotes a case of y-axis symmetric arrangement of scattering points. As a reference, a 10% value for a Gaussian random process case is also shown. It is clear that the conventional arrangement yields various fading states depending on the initial phase setting. On the other hand, the arrangement under the intra-ring condition provides more stable fading properties compared to the conventional arrangement. The value spread is effectively reduced to 0.81 dB from 2.93 dB with the intra-ring condition. It was confirmed that $M > 30$

[1] In [2], Jakes showed that Rayleigh fading can be simulated with $M = 8$.

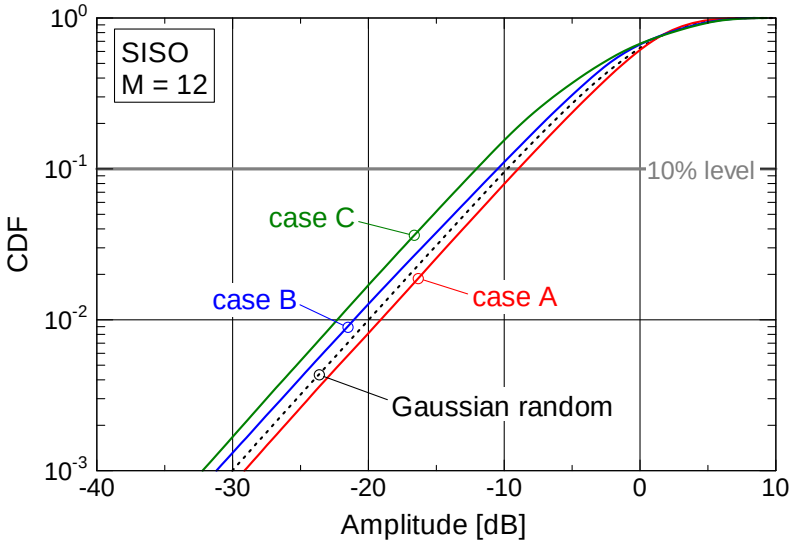

(a) CDF of amplitudes

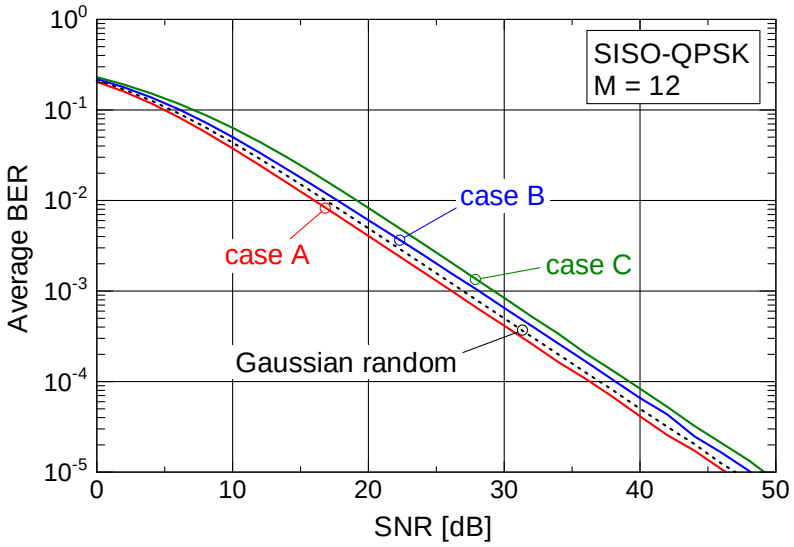

(b) BER performance

Figure 2.4: Examples of SISO channels based on Jakes model.

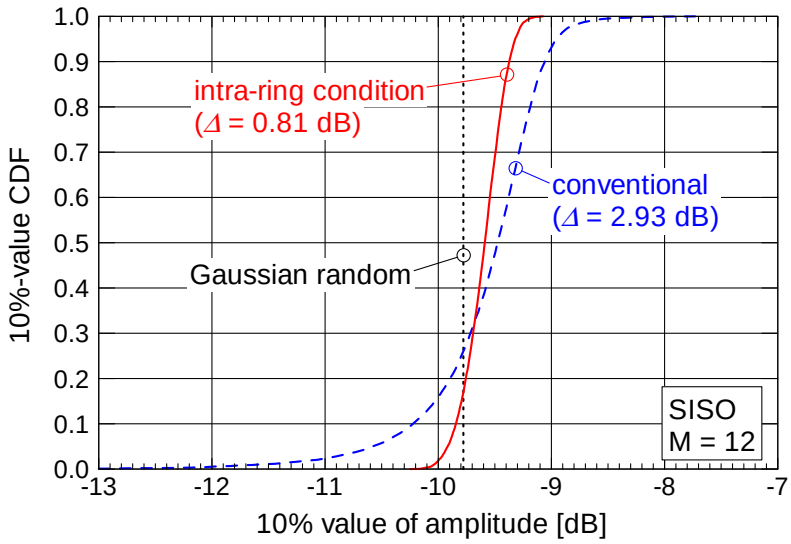

Figure 2.5: 10%-value CDFs of amplitudes for SISO cases.

is necessary for the conventional arrangement to achieve the same stability as the arrangement under the intra-ring condition with $M = 12$, i.e., to reduce the value spread Δ to 0.81 dB.

Next, the inter-ring condition is evaluated. Figure 2.6 shows 10%-value CDFs of the first (maximum) and second (minimum) eigenvalues for 2×2 MIMO channels, where both arrangement types, "inter-ring condition" and "conventional," are constrained by the intra-ring condition. We can see from the CDFs for the conventional arrangement that a common arrangement over all the scattering rings causes properties dependent upon the initial phase setting even though under the intra-ring condition. Furthermore, the difference is larger for the second eigenvalues. In contrast, the arrangement under the inter-ring condition gives much more stable eigenvalue properties. With the condition, the value spread for the first eigenvalues is reduced to 0.25 dB from 0.77 dB, and that for the second eigenvalues is reduced to 0.73 dB from 1.69 dB.

It is seen in Figs. 2.5 and 2.6 that 10%-value CDFs of Jakes rings are mostly located in higher amplitude/eigenvalue regions than those of Gaussian random process cases. We can achieve a random process similar to the Gaussian random case if we have a sufficiently large number of scattering points, i.e., $M \to \infty$. However, using Jakes model implies angular sampling of a uniformly distributed angular spectrum by finite scattering points, which may result in an insufficient random nature. This is therefore a specific issue of Jakes model with a finite number of scatterers. It is expected that the issue may be mitigated by increasing the number of scattering points M. Figure 2.7 demonstrates 10%-value CDFs of SISO channels under the intra-ring condition in the cases of $M = 12$, 24, and 36. Although locating many scatterers is not desirable for us as mentioned before, it is proved from Fig. 2.7 that CDFs of Jakes model approach the Gaussian random case as M

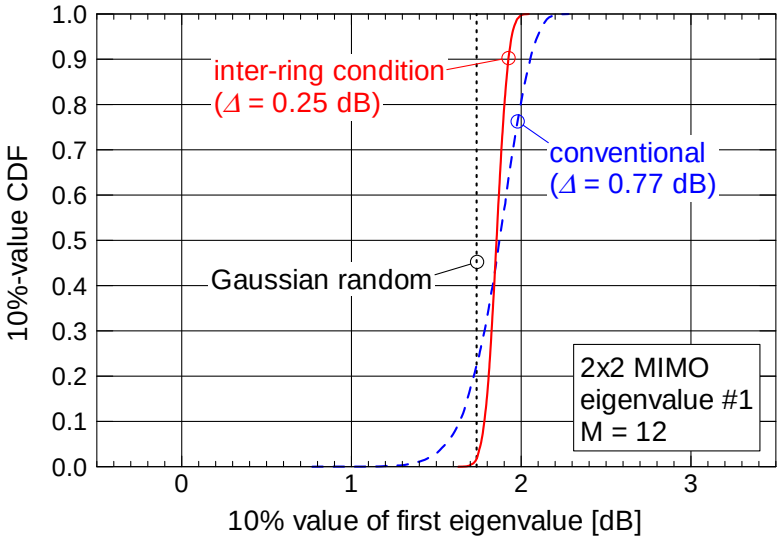

(a) First eigenvalue

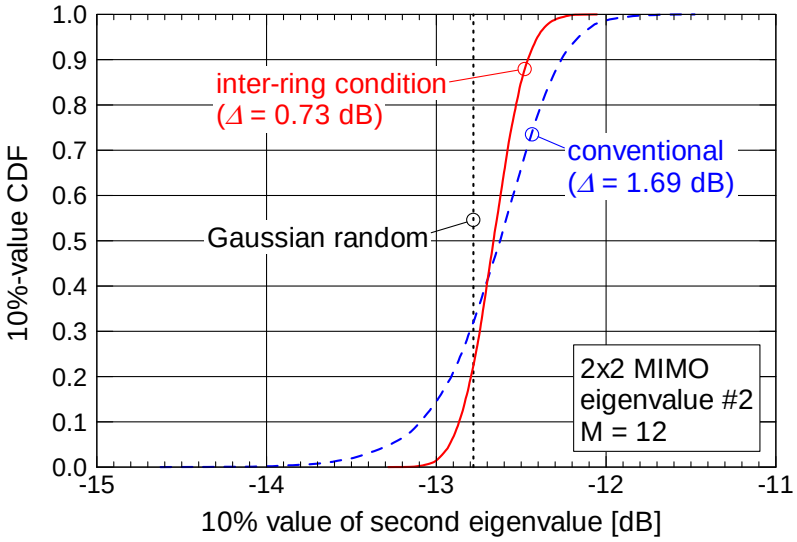

(b) Second eigenvalue

Figure 2.6: 10%-value CDFs of eigenvalues for 2×2 MIMO cases.

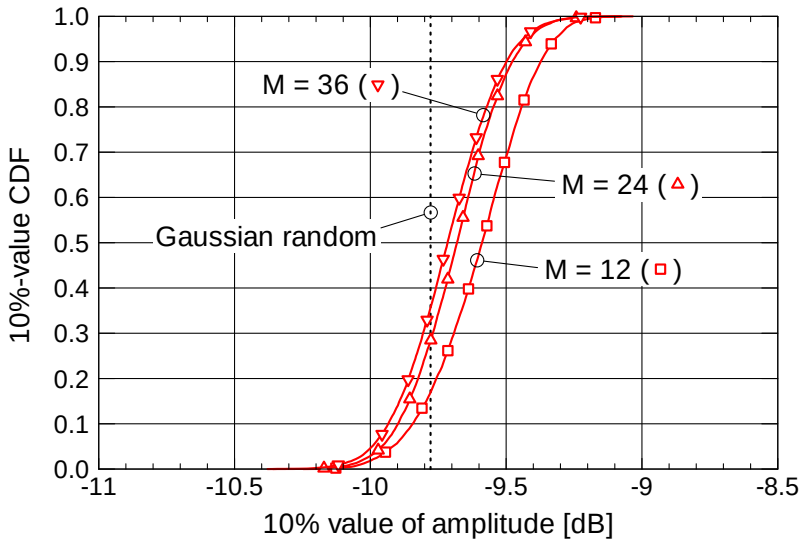

Figure 2.7: 10%-value CDFs of SISO channels under the intra-ring condition in the cases of $M = 12$, 24, and 36.

increases. Consequently, the phenomenon mentioned above is not clearly seen in the case of $M = 36$.

2.2.5 Conclusions

The author has established simple and effective conditions on scattering-point arrangement in Jakes model for stable fading simulations. It is confirmed that, for a single scattering ring, the intra-ring condition is effective for obtaining stable fading property in the aspect of statistics regardless of the initial phase setting. Moreover, it was shown that arrangement under the inter-ring condition provides fading properties robust to the given initial phases in a multiple-ring case such as 2×2 MIMO channels. It should be noted that the proposed inter-ring condition can be effective not only for MIMO flat fading channels but also for other fading channels, e.g., SISO channels.

2.3 Spatial Multiplexing

Spatial multiplexing can be classified into SDM and B-SDM. SDM, in which each TX antenna sends an independent signal substream as illustrated in Fig. 2.8(a), is a promising way to increase channel capacity or data transfer speed when MIMO CSI is available only at the receiver. Note that, although it is possible to adaptively allocate the TX resource (bits and power) over substreams in SDM, this dissertation deals with only the case with equal resource allocation because effective allocation requires CSI at the transmitter. On the other

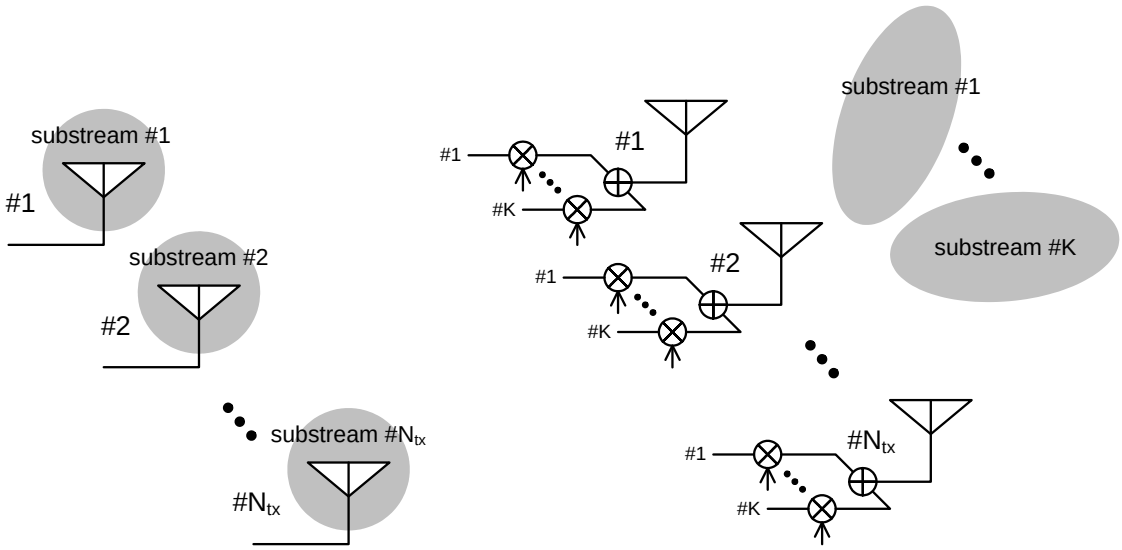

(a) SDM (b) B-SDM

Figure 2.8: Concepts of SDM and B-SDM.

hand, B-SDM, in which substreams are transmitted by TX beamforming as illustrated in Fig. 2.8(b), has a potential for further high-speed wireless communications. Note that the above SDM is a specific case of B-SDM. If CSI is available also at the transmitter, we can form TX beams improving SNR and system performance based on the CSI.

The optimum TX beams in B-SDM are eigenbeams obtained by SVD of $\boldsymbol{H}$ or EVD of $\boldsymbol{H}^H\boldsymbol{H}$, and such a case is specifically called E-SDM. This transmission technique enables us to transmit spatially orthogonal substreams and maximizes the throughput of the MIMO channel by allocating the TX resource to each substream optimally. These advantages of E-SDM will make MIMO systems effective for increasing data transfer speeds in future wireless communications. Hereafter, general B-SDM techniques are not discussed, and only E-SDM is dealt with as the optimum and typical case of B-SDM.

In the following sections, SDM and E-SDM techniques are concisely explained.

2.3.1 SDM

When the transmitter does not know the MIMO CSI, high-speed communications can be obtained by using SDM, in which independent signal substreams are transmitted from the TX antennas with equal power as shown in Fig. 2.8(a). In SDM transmission, an N_{rx}-dimensional RX signal vector $\boldsymbol{r}_{\mathrm{SDM}}(t)$ can be represented by

$$\boldsymbol{r}_{\mathrm{SDM}}(t) = \boldsymbol{H}\boldsymbol{s}(t) + \boldsymbol{n}(t), \tag{2.9}$$

where $\boldsymbol{s}(t)$ is an N_{tx}-dimensional TX signal vector consisting of signals from TX antennas and $\boldsymbol{n}(t)$ is an N_{rx}-dimensional additive white Gaussian noise vector. While SDM

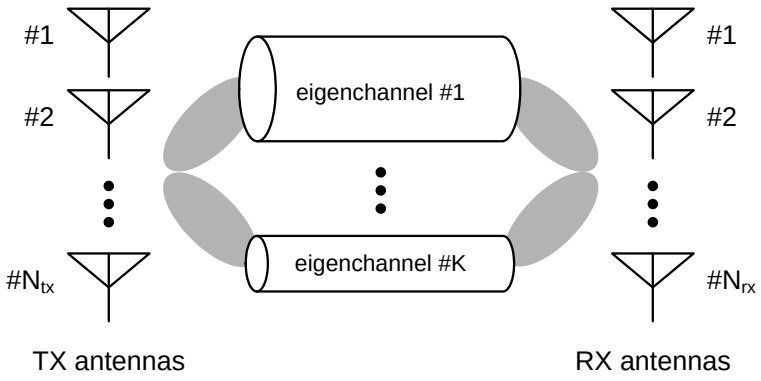

Figure 2.9: Concept of E-SDM transmission.

can increase data rates in proportion to the number of TX antennas, the receiver needs to demultiplex the inter-substream interfered signal.

2.3.2 E-SDM

If the MIMO CSI is available at the transmitter, the channel space between the TX and RX antennas can be orthogonalized by using eigenbeams. The eigenvalue decomposition of an $N_{\mathrm{tx}} \times N_{\mathrm{tx}}$ non-negative Hermitian matrix $\boldsymbol{H}^H \boldsymbol{H}$ can be expressed as

$$\boldsymbol{H}^H \boldsymbol{H} = \boldsymbol{U} \boldsymbol{\Lambda} \boldsymbol{U}^H, \tag{2.10}$$

where

$$\boldsymbol{U} = [\boldsymbol{e}_1 \, \boldsymbol{e}_2 \, \cdots \, \boldsymbol{e}_K], \tag{2.11}$$

$$\boldsymbol{\Lambda} = \mathrm{diag}\,(\lambda_1, \lambda_2, \ldots, \lambda_K) \quad (\lambda_1 \geq \cdots \geq \lambda_K). \tag{2.12}$$

Here, K ($K \leq \min(N_{\mathrm{tx}}, N_{\mathrm{rx}})$) indicates the rank of $\boldsymbol{H}$, $\mathrm{diag}\,(\cdot)$ denotes a diagonal matrix, and $\boldsymbol{\Lambda}$ is defined as an $K \times K$ diagonal matrix composed of positive eigenvalues $\lambda_1, \ldots, \lambda_K$ of $\boldsymbol{H}^H \boldsymbol{H}$. When eigenvectors $\boldsymbol{e}_1, \ldots, \boldsymbol{e}_K$ respectively corresponding to eigenvalues $\lambda_1, \ldots, \lambda_K$ are multiplied as TX weights, we can form an orthogonal multi-beam space between the TX and RX antennas as shown in Fig. 2.9. This is the E-SDM technique, and when it is used the received signal vector is given by

$$\boldsymbol{r}_{\text{E-SDM}}(t) = \boldsymbol{H}\boldsymbol{U}\boldsymbol{s}(t) + \boldsymbol{n}(t). \tag{2.13}$$

Unlike $\boldsymbol{s}(t)$ in (2.9), $\boldsymbol{s}(t)$ in this equation is a K-dimensional transmitted signal vector composed of signals sent through eigenchannels. In the ideal E-SDM in which the TX weight vectors completely match an instantaneous MIMO channel response, spatially orthogonal substreams cause no inter-substream interference at the RX end, which is an issue in the conventional SDM. Under such a condition, it is easy to demultiplex received signals by

using maximal ratio combining (MRC) processing, which maximizes the SNR at the RX end by multiplying the received signal vector $\boldsymbol{r}_{\text{E-SDM}}(t)$ by $(\boldsymbol{HU})^H$ [65]. Moreover, we can maximize the throughput of the MIMO system by optimizing bit (modulation) and power allocation to each substream.

2.4 Demultiplexing Schemes in Spatial Multiplexing

In this section the author introduces some demultiplexing schemes in MIMO spatial multiplexing. Hereinafter, SDM systems are taken for instance, i.e., the handled channel is $\boldsymbol{H}$, and the number of transmitted substreams is N_{tx}. The following processes can be discussed also in beamforming systems such as E-SDM by replacing $\boldsymbol{H}$ by the effective channel $\boldsymbol{HU}$. Note that TX power allocated to substreams is assumed to be included in the transmitted signal vector $\boldsymbol{s}(t)$.

2.4.1 Zero-forcing

Since a spatial multiplexing system over a flat-fading MIMO channel can be linearly expressed as in (2.9) or (2.13), a simple way to detect the transmitted signal at the receiver is to linearly demultiplex the received signal by multiplying $\boldsymbol{r}(t)$ by an $N_{\text{tx}} \times N_{\text{rx}}$ weight matrix $\boldsymbol{W}$ based on the channel matrix. That is, we obtain a transmitted signal estimate by

$$\hat{\boldsymbol{s}}(t) = \boldsymbol{W}\boldsymbol{r}(t). \tag{2.14}$$

Such a detection scheme is also called spatial filtering. Note that linear demultiplexing requires the condition of $N_{\text{rx}} \geq N_{\text{tx}}$. Zero-forcing (ZF) is the simplest spatial filter of which process is described next.

An N_{rx}-dimensional ZF weight vector $\boldsymbol{w}_{\text{zf},k}$ for the kth transmitted substream is calculated by

$$\boldsymbol{w}_{\text{zf},k}^T = \boldsymbol{g}_k^T \boldsymbol{H}^+, \tag{2.15}$$

where the superscript $^+$ denotes the Moore-Penrose (MP) pseudo inverse, and $\boldsymbol{g}_k$ is an N_{tx}-dimensional vector whose elements are zero except the kth element corresponding to 1. Multiplying $\boldsymbol{H}^+$ by $\boldsymbol{g}_k^T$ is to pick out the kth row vector in $\boldsymbol{H}^+$. Since ZF, which is one of the linear demultiplexing schemes, requires the condition of $N_{\text{rx}} \geq N_{\text{tx}}$ as stated above, an MP pseudo inverse matrix of $\boldsymbol{H}$ is computed as

$$\boldsymbol{H}^+ = \left(\boldsymbol{H}^H \boldsymbol{H}\right)^{-1} \boldsymbol{H}. \tag{2.16}$$

To detect all transmitted substreams, therefore, the weight matrix is given by the MP pseudo inverse matrix $\boldsymbol{H}^+$

$$\boldsymbol{W}_{\text{zf}} = \begin{bmatrix} \boldsymbol{w}_{\text{zf},1}^T \\ \vdots \\ \boldsymbol{w}_{\text{zf},N_{\text{tx}}}^T \end{bmatrix} = \boldsymbol{H}^+. \tag{2.17}$$

In general, substream detection can be achieved not only by MP pseudo inverse but also by other inverse schemes. The reason why ZF employs MP pseudo inverse is because MP pseudo inverse can output norm-minimized and least-squares-type weight vectors. When multiplying $\boldsymbol{r}(t)$ by $\boldsymbol{W}_{\text{zf}}$, the N_{tx}-dimensional output signal vector is expressed as

$$\begin{aligned}
\hat{\boldsymbol{s}}(t) &= \boldsymbol{W}_{\text{zf}}\,\boldsymbol{r}(t) && (2.18)\\
&= \boldsymbol{W}_{\text{zf}}\,\{\boldsymbol{H}\boldsymbol{s}(t) + \boldsymbol{n}(t)\} && (2.19)\\
&= \boldsymbol{s}(t) + \boldsymbol{W}_{\text{zf}}\,\boldsymbol{n}(t) && (2.20)\\
&= \boldsymbol{s}(t) + \begin{bmatrix} \boldsymbol{w}_{\text{zf},1}^{T}\boldsymbol{n}(t) \\ \vdots \\ \boldsymbol{w}_{\text{zf},N_{\text{tx}}}^{T}\boldsymbol{n}(t) \end{bmatrix}. && (2.21)
\end{aligned}$$

It is clear from the above equation that thermal noise components included in the output signal can be reduced by using MP pseudo inverse.

The ZF algorithm acts to force substreams interfering the desired substream to be zero in the output as its name suggests. As a result, it maximizes the signal-to-interference power ratio (SIR) of the filter output. However, received power of the desired signal may be sacrificed for the SIR maximization so that the ZF algorithm provides lower SNR compared with the other schemes.

2.4.2 Minimum Mean Square Error

Another spatial filtering algorithm is minimum mean square error (MMSE), which minimizes an error between an output signal $\hat{s}(t)$ and a reference signal $d(t)$. Mean square error $J(\boldsymbol{w})$ is defined as

$$\begin{aligned}
J(\boldsymbol{w}) &= E\left[|d(t) - \hat{s}(t)|^2\right] && (2.22)\\
&= E\left[|d(t) - \boldsymbol{w}^T\boldsymbol{r}(t)|^2\right] && (2.23)\\
&= E\left[|d(t)|^2\right] - \boldsymbol{w}^H\boldsymbol{v}_{rd} - \boldsymbol{w}^T\boldsymbol{v}_{rd}^{*} + \boldsymbol{w}^H\boldsymbol{R}_{rr}\boldsymbol{w}, && (2.24)
\end{aligned}$$

where $E[\cdot]$ means ensemble average (expectation). Also, $\boldsymbol{v}_{rd}$ and $\boldsymbol{R}_{rr}$ are a correlation vector and a correlation matrix, respectively, defined as follows:

$$\begin{aligned}
\boldsymbol{v}_{rd} &= E\left[\boldsymbol{r}^{*}(t)d(t)\right] && (2.25)\\
\boldsymbol{R}_{rr} &= E\left[\boldsymbol{r}^{*}(t)\boldsymbol{r}^{T}(t)\right]. && (2.26)
\end{aligned}$$

When $J(\boldsymbol{w})$ is minimized, the following relation is satisfied

$$\frac{\partial J(\boldsymbol{w})}{\partial \boldsymbol{w}} = 0. \tag{2.27}$$

We also have the following relations when differentiating terms in (2.24) with respect to $\boldsymbol{w}$:

$$\frac{\partial}{\partial \boldsymbol{w}}(\boldsymbol{w}^H \boldsymbol{v}_{rd}) = 2\boldsymbol{v}_{rd} \tag{2.28}$$

$$\frac{\partial}{\partial \boldsymbol{w}}(\boldsymbol{w}^T \boldsymbol{v}_{rd}^*) = 0 \tag{2.29}$$

$$\frac{\partial}{\partial \boldsymbol{w}}(\boldsymbol{w}^H \boldsymbol{R}_{rr} \boldsymbol{w}) = 2\boldsymbol{R}_{rr}\boldsymbol{w}. \tag{2.30}$$

Hence, substituting (2.24) and (2.28)–(2.30) into (2.27) yields

$$\frac{\partial J(\boldsymbol{w})}{\partial \boldsymbol{w}} = -2\boldsymbol{v}_{rd} + 2\boldsymbol{R}_{rr}\boldsymbol{w} = 0, \tag{2.31}$$

then we have the following equation

$$\boldsymbol{w}_{\text{mmse}} = \boldsymbol{R}_{rr}^{-1}\boldsymbol{v}_{rd}. \tag{2.32}$$

An MMSE weight vector detecting the desired signal is obtained this way. Since there are multiple substreams in spatial multiplexing, we need to calculate weight vectors for all substreams. Expanding the above procedure, an $N_{\text{tx}} \times N_{\text{rx}}$ MMSE weight matrix $\boldsymbol{W}_{\text{mmse}}$ is given by

$$\boldsymbol{W}_{\text{mmse}}^T = [\boldsymbol{w}_1 \ \cdots \ \boldsymbol{w}_{N_{\text{tx}}}] = \boldsymbol{R}_{rr}^{-1}\boldsymbol{V}_{rd}, \tag{2.33}$$

where $\boldsymbol{V}_{rd}$ is a correlation matrix calculated by the received signal vector $\boldsymbol{r}(t)$ and an N_{tx}-dimensional reference signal vector $\boldsymbol{d}(t)$:

$$\boldsymbol{V}_{rd} = E\left[\boldsymbol{r}^*(t)\boldsymbol{d}^T(t)\right]. \tag{2.34}$$

When we have a sufficiently large number of ensembles or perfect estimates of a channel and noise power, by defining P_t as the mean TX signal power per TX antenna[2], the correlation vector in (2.25) and the correlation matrix in (2.26) are ideally represented as

$$\boldsymbol{v}_{rd} = \boldsymbol{H}^* E\left[\boldsymbol{s}^*(t)d_k(t)\right] = P_t\boldsymbol{H}^*\boldsymbol{g}_k = P_t\boldsymbol{h}_k^* \tag{2.35}$$

$$\boldsymbol{R}_{rd} = \boldsymbol{H}^* E\left[\boldsymbol{s}^*(t)\boldsymbol{s}^T(t)\right]\boldsymbol{H}^T + \sigma^2\boldsymbol{I}_{N_{\text{rx}}} = P_t\left(\boldsymbol{H}^*\boldsymbol{H}^T + \frac{\sigma^2}{P_t}\boldsymbol{I}_{N_{\text{rx}}}\right), \tag{2.36}$$

where σ^2 and $\boldsymbol{I}_{N_{\text{rx}}}$ denote thermal noise power and an N_{rx}-dimensional unit matrix, respectively. Also, $\boldsymbol{h}_k$ is the channel vector corresponding to the kth TX antenna, i.e., the

[2]Here SDM with equal power allocation is assumed. Note that in transmission with adaptive power allocation we have $E\left[\boldsymbol{s}^*(t)\boldsymbol{s}^T(t)\right] = \text{diag}\left(p_1, \ldots, p_{N_{\text{tx}}}\right)$ and $E\left[\boldsymbol{s}^*(t)d_k(t)\right] = p_k\boldsymbol{g}_k$ when $E\left[|d_k(t)|^2\right] = p_k$.

kth column vector in $\boldsymbol{H}$. An optimum weight vector $\boldsymbol{w}_{\text{mmse},k}$ is calculated by

$$\boldsymbol{w}_{\text{mmse},k} = \boldsymbol{R}_{rr}^{-1}\boldsymbol{v}_{rd} \tag{2.37}$$

$$= \frac{1}{P_t}\left(\boldsymbol{H}^*\boldsymbol{H}^T + \frac{\sigma^2}{P_t}\boldsymbol{I}_{N_{\text{rx}}}\right)^{-1} P_t\boldsymbol{h}_k^* \tag{2.38}$$

$$= \left(\boldsymbol{H}^*\boldsymbol{H}^T + \frac{\sigma^2}{P_t}\boldsymbol{I}_{N_{\text{rx}}}\right)^{-1}\boldsymbol{h}_k^*. \tag{2.39}$$

Furthermore, expanding on the spatial multiplexing case, an $N_{\text{tx}} \times N_{\text{rx}}$ optimum MMSE weight matrix is obtained by

$$\boldsymbol{W}_{\text{mmse}} = \left(\boldsymbol{R}_{rr}^{-1}\boldsymbol{V}_{rd}\right)^T \tag{2.40}$$

$$= \boldsymbol{H}^H\left(\boldsymbol{H}\boldsymbol{H}^H + \frac{\sigma^2}{P_t}\boldsymbol{I}_{N_{\text{rx}}}\right)^{-1}. \tag{2.41}$$

Unlike the ZF algorithm, the MMSE algorithm involves thermal noise power in the calculation process so that it acts to enlarge the desired signal component in the filter outputs, i.e., to maximize the SINR of outputs.

2.4.3 Maximum Likelihood Detection

So far, linear demultiplexing schemes based on inversion have been introduced. In such cases, however, we need the condition of $N_{\text{rx}} \geq N_{\text{tx}}$ due to linearity. On the other hand, there are detection schemes independent of weight multiplication. One of the schemes is maximum likelihood detection (MLD), which is also called joint detection. MLD is the optimum scheme to estimate the transmitted signal from a viewpoint of probability statistics and does not have the constraint of $N_{\text{rx}} \geq N_{\text{tx}}$ because it is not a linear process. Based on (2.9), a transmitted symbol candidate $\tilde{\boldsymbol{s}}(t)$ which minimizes the following vector norm is the maximum likelihood candidate

$$\tilde{\boldsymbol{s}}(t) = \arg\min_{\tilde{\boldsymbol{s}}(t)} \left\|\boldsymbol{r}(t) - \boldsymbol{H}\tilde{\boldsymbol{s}}(t)\right\|. \tag{2.42}$$

Since we have finite symbol candidates in digital modulation, in the MLD procedure we calculate the above vector norm for all candidates possible and seek the maximum likelihood $\tilde{\boldsymbol{s}}(t)$ giving the minimum norm. Because of the benefit, MLD provides excellent performance. On the other hand, the calculation load exponentially increases depending on the number of TX antennas N_{tx} and level of modulation. For example, when two TX antennas transmit QPSK-modulated symbols ($N_{\text{tx}} = 2$ and 2 bits/symbol/antenna), the receiver requires norm calculation and seeking the optimum estimate from $(2^2)^2 = 16$ candidates per symbol interval. However, when four TX antennas transmit 64QAM-modulated symbols ($N_{\text{tx}} = 4$ and 6 bits/symbol/antenna), we have $(2^6)^4 = 16{,}777{,}216$ candidates resulting

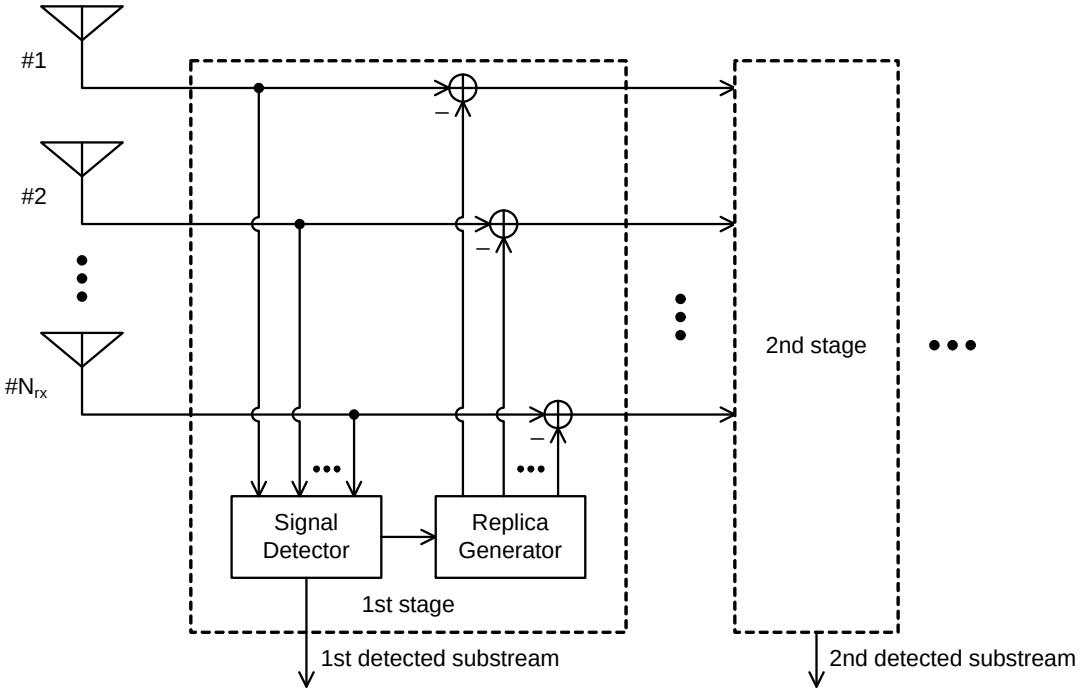

Figure 2.10: Concept of SIC.

in serious computational complexity. Therefore, many researchers have studied mitigation of calculation load by reducing the number of symbol candidates, e.g., sphere decoding [66–68], hierarchized MLD based on QR decomposition and M-algorithm (QRM-MLD) [69, 70][3], etc.

2.4.4 Serial Interference Canceller

Spatially different multiple substreams pass through different channels. Substream quality is, therefore, dependent on the channel. When successively detecting signals, it is a necessity to consider that a signal having better channel property should be detected first in order to avoid error propagation. This is ordered successive detection (OSD), of which the pioneer was the BLAST architecture [18–20, 25, 26]. The scheme is also known as a serial interference canceller (SIC). Figure 2.10 illustrates a concept of SIC.

SIC-ZF

It is general to combine an SIC with a spatial filter in order to separate the multiplexed signal. Consider to employ the ZF algorithm as a spatial filter. The mean ZF output signal

[3] A hierarchical approach using QR decomposition is regarded as one of the SIC detection schemes.

power of the kth substream is represented as

$$E\left[|\hat{s}_k(t)|^2\right] = E\left[\boldsymbol{w}_{\text{zf},k}^H \boldsymbol{r}^*(t)\boldsymbol{r}^T(t)\boldsymbol{w}_{\text{zf},k}\right] \tag{2.43}$$

$$= P_t \boldsymbol{w}_{\text{zf},k}^H \boldsymbol{H}^* \boldsymbol{H}^T \boldsymbol{w}_{\text{zf},k} + \sigma^2 \left\|\boldsymbol{w}_{\text{zf},k}\right\|^2. \tag{2.44}$$

Substituting (2.15) and (2.16) into (2.44) yields

$$E\left[|\hat{s}_k(t)|^2\right] = P_t + \sigma^2 \left\|\boldsymbol{w}_{\text{zf},k}\right\|^2. \tag{2.45}$$

Hence, the SNR of the ZF output is given by

$$\gamma_{\text{zf},k} = \frac{P_t}{\sigma^2 \left\|\boldsymbol{w}_{\text{zf},k}\right\|^2}. \tag{2.46}$$

We notice that higher output SNR is obtained by using a smaller-norm weight vector resulting in reducing thermal noise components included in the output. In the ZF case we seek the minimum-norm weight vector and detect the corresponding signal in each stage.

The following is a brief explanation of an SIC followed by the ZF algorithm (SIC-ZF), which corresponds to V-BLAST architecture initially reported in 1999 [19]. Hereinafter, symbols with a superscript $^{(i)}$ denote those in the ith stage. Note that symbols in the first stage, or those with $^{(1)}$, are given as follows:

$$\boldsymbol{w}_{\text{zf},k}^{(1)} = \boldsymbol{w}_{\text{zf},k} \tag{2.47}$$

$$\boldsymbol{r}^{(1)}(t) = \boldsymbol{r}(t) \tag{2.48}$$

$$\boldsymbol{H}^{(1)} = \boldsymbol{H}. \tag{2.49}$$

Let us assume that $\boldsymbol{w}_{\text{zf},k}^{(1)}$ has the smallest vector norm in (2.17). First we estimate the symbol replica $\tilde{s}_k^{(1)}(t)$ of the kth substream according to the ZF spatial filter output $\hat{s}_k^{(1)}(t)$. Next, using the corresponding channel vector $\boldsymbol{h}_k$, the kth substream component is cancelled from the received signal vector $\boldsymbol{r}^{(1)}(t)$

$$\boldsymbol{r}^{(2)}(t) = \boldsymbol{r}^{(1)}(t) - \tilde{s}_k^{(1)}(t)\boldsymbol{h}_k. \tag{2.50}$$

Simultaneously the corresponding channel vector is removed from the channel matrix

$$\boldsymbol{H}^{(1)} = \underbrace{[\boldsymbol{h}_1 \ \cdots \ \boldsymbol{h}_{k-1} \ \boldsymbol{h}_k \ \boldsymbol{h}_{k+1} \ \cdots \boldsymbol{h}_{N_{\text{tx}}}]}_{N_{\text{tx}} \text{ column vectors}} \tag{2.51}$$

$$\boldsymbol{H}^{(2)} = \underbrace{[\boldsymbol{h}_1 \ \cdots \ \boldsymbol{h}_{k-1} \ \boldsymbol{h}_{k+1} \ \cdots \boldsymbol{h}_{N_{\text{tx}}}]}_{N_{\text{tx}}-1 \text{ column vectors}}. \tag{2.52}$$

The channel matrix in the second stage, thereby, becomes the size of $N_{\text{rx}} \times (N_{\text{tx}} - 1)$ by processing above. This is the first stage.

In the second stage, we calculate a weight matrix from $\boldsymbol{H}^{(2)}$, or MP pseudo inverse of $\boldsymbol{H}^{(2)}$, and seek the minimum-norm weight vector $\boldsymbol{w}_{\text{zf},l}^{(2)}$ to estimate the symbol replica of

the lth substream. The corresponding components $\tilde{s}_l^{(2)}(t)$ and $\boldsymbol{h}_l$ are cancelled from both $\boldsymbol{r}^{(2)}(t)$ and $\boldsymbol{H}^{(2)}$

$$\boldsymbol{r}^{(3)}(t) = \boldsymbol{r}^{(2)}(t) - \tilde{s}_l^{(2)}(t)\boldsymbol{h}_l \tag{2.53}$$

$$\boldsymbol{H}^{(2)} = \underbrace{[\boldsymbol{h}_1 \ \cdots \ \boldsymbol{h}_{l-1} \ \boldsymbol{h}_l \ \boldsymbol{h}_{l+1} \ \cdots \boldsymbol{h}_{N_{\mathrm{tx}}-1}]}_{N_{\mathrm{tx}}-1 \text{ column vectors}} \tag{2.54}$$

$$\boldsymbol{H}^{(3)} = \underbrace{[\boldsymbol{h}_1 \ \cdots \ \boldsymbol{h}_{l-1} \ \boldsymbol{h}_{l+1} \ \cdots \boldsymbol{h}_{N_{\mathrm{tx}}-1}]}_{N_{\mathrm{tx}}-2 \text{ column vectors}}. \tag{2.55}$$

The above procedure continues up to the N_{tx}th stage to obtain all symbol estimates. We can obtain the spatial diversity effect more as the procedure progresses in stages so that SIC-ZF outperforms the conventional ZF algorithm.

SIC-MMSE

When applying the MMSE algorithm onto SIC, we can obtain better performance than SIC-ZF because the algorithm maximizes output signal gain, or output SINR. An SIC incorporating the MMSE algorithm for substream separation is referred to as SIC-MMSE. Its procedure is the same as the SIC-ZF case mentioned above except an evaluation of substream quality, where we select the weight vector minimizing the evaluation function $J(\boldsymbol{w})$ given by (2.24) in each stage. Assuming $E\left[|d(t)|^2\right] = E\left[|s(t)|^2\right] = P_t$, substituting (2.24) into (2.32) yields the following modification of $J(\boldsymbol{w})$

$$J(\boldsymbol{w}) = P_t - \boldsymbol{w}^H\boldsymbol{v}_{rd} - \boldsymbol{w}^T\boldsymbol{v}_{rd}^* + \boldsymbol{w}^H\boldsymbol{R}_{rr}\boldsymbol{R}_{rr}^{-1}\boldsymbol{v}_{rd} \tag{2.56}$$

$$= P_t - \boldsymbol{w}^H\boldsymbol{v}_{rd} - \boldsymbol{w}^T\boldsymbol{v}_{rd}^* + \boldsymbol{w}^H\boldsymbol{v}_{rd} \tag{2.57}$$

$$= P_t - \boldsymbol{w}^T\boldsymbol{v}_{rd}^*. \tag{2.58}$$

Also, $J(\boldsymbol{w})$ can be represented as follows when the optimum weight calculation in (2.39) is available

$$J(\boldsymbol{w}) = P_t - P_t\boldsymbol{w}^T\boldsymbol{h} \tag{2.59}$$

$$= P_t\left(1 - \boldsymbol{w}^T\boldsymbol{h}\right). \tag{2.60}$$

The function $J(\boldsymbol{w})$ can be regarded as error power between reference and output signals. It can also be considered as power of both residual inter-substream interference and thermal noise because it is given by subtracting the desired signal power $P_t\boldsymbol{w}^T\boldsymbol{h}$ from the reference (ideal) signal power P_t. That is, SINR of MMSE output is approximately expressed by

$$\gamma_{\mathrm{mmse}} = \frac{P_t\boldsymbol{w}^T\boldsymbol{h}}{P_t\left(1 - \boldsymbol{w}^T\boldsymbol{h}\right)} \tag{2.61}$$

$$= \frac{\boldsymbol{w}^T\boldsymbol{h}}{1 - \boldsymbol{w}^T\boldsymbol{h}}. \tag{2.62}$$

Using the MMSE weight minimizing the function $J(\boldsymbol{w})$ (or maximizing γ_{mmse}) in each stage yields more diversity effect than SIC-ZF as the number of antennas increases.

SIC-QRD

By applying QR decomposition to the channel matrix, we obtain two matrices, an N_{rx}-dimensional unitary matrix $\boldsymbol{Q}$ and an $N_{\mathrm{rx}} \times N_{\mathrm{tx}}$ upper triangular matrix $\boldsymbol{R}$. That is,

$$\boldsymbol{H} = \boldsymbol{Q}\boldsymbol{R}, \tag{2.63}$$

where $\boldsymbol{R}$ can be expressed as

$$\boldsymbol{R} = \begin{bmatrix} a_{11} & a_{12} & \cdots & a_{1N_{\mathrm{tx}}} \\ 0 & a_{22} & \cdots & a_{2N_{\mathrm{tx}}} \\ \vdots & \ddots & \ddots & \vdots \\ 0 & 0 & \cdots & a_{N_{\mathrm{tx}}N_{\mathrm{tx}}} \\ \vdots & \vdots & \vdots & \vdots \\ 0 & 0 & \cdots & 0 \end{bmatrix} \quad (N_{\mathrm{rx}} \geq N_{\mathrm{tx}}). \tag{2.64}$$

When multiplying the received signal vector by $\boldsymbol{Q}^H$ on the left, the system can be equivalently represented by

$$\begin{aligned} \boldsymbol{y}(t) &= \boldsymbol{Q}^H \boldsymbol{r}(t) && (2.65)\\ &= \boldsymbol{Q}^H \{\boldsymbol{H}\boldsymbol{s}(t) + \boldsymbol{n}(t)\} && (2.66)\\ &= \boldsymbol{Q}^H \{\boldsymbol{Q}\boldsymbol{R}\boldsymbol{s}(t) + \boldsymbol{n}(t)\} && (2.67)\\ &= \boldsymbol{R}\boldsymbol{s}(t) + \boldsymbol{Q}^H \boldsymbol{n}(t). && (2.68) \end{aligned}$$

Note that the above multiplication of $\boldsymbol{Q}^H$ for the noise vector does not cause noise enhancement because $\boldsymbol{Q}^H$ is an unitary matrix. Focusing on the signal components in the above equation, the output vector $\boldsymbol{y}(t) = [y_1(t), \ldots, y_{N_{\mathrm{rx}}}(t)]^T$ can be expressed as

$$\begin{bmatrix} y_1(t) \\ \vdots \\ y_{N_{\mathrm{tx}}-1}(t) \\ y_{N_{\mathrm{tx}}}(t) \\ \vdots \\ y_{N_{\mathrm{rx}}}(t) \end{bmatrix} = \begin{bmatrix} a_{11}s_1(t) + \cdots + a_{1N_{\mathrm{tx}}}s_{N_{\mathrm{tx}}}(t) \\ \vdots \\ a_{(N_{\mathrm{tx}}-1)(N_{\mathrm{tx}}-1)}s_{N_{\mathrm{tx}}-1}(t) + a_{(N_{\mathrm{tx}}-1)N_{\mathrm{tx}}}s_{N_{\mathrm{tx}}}(t) \\ a_{N_{\mathrm{tx}}N_{\mathrm{tx}}}s_{N_{\mathrm{tx}}}(t) \\ \vdots \\ 0 \end{bmatrix} + \boldsymbol{Q}^H \boldsymbol{n}(t). \tag{2.69}$$

In the above equation, it is obvious that the N_{tx}th element in $\boldsymbol{y}(t)$ includes only the N_{tx}th substream signal component $a_{N_{\mathrm{tx}}N_{\mathrm{tx}}}(t)s_{N_{\mathrm{tx}}}(t)$ except thermal noise components, i.e., it does not have inter-substream interference. Note that diagonal channel elements in $\boldsymbol{R}$ correspond to desired substreams and the other off-diagonal channel elements are inter-substream interference components

$$\begin{aligned} y_k(t) &= \sum_{i=k}^{N_{\mathrm{tx}}} a_{ki}s_i(t) + n_k(t) && (2.70)\\ &= a_{kk}s_k(t) + \sum_{i=k+1}^{N_{\mathrm{tx}}} a_{ki}s_i(t) + n_k(t) \quad (k \leq N_{\mathrm{tx}}), && (2.71) \end{aligned}$$

where $n_k(t)$ denotes the kth element in the equivalent noise vector $\boldsymbol{Q}^H\boldsymbol{n}(t)$. Therefore, first we can estimate the symbol replica $\tilde{s}_{N_{\rm tx}}(t)$ from an output signal $\hat{s}_{N_{\rm tx}}(t)$ obtained as follows

$$\hat{s}_{N_{\rm tx}}(t) = \frac{y_{N_{\rm tx}}(t)}{a_{N_{\rm tx}N_{\rm tx}}}. \tag{2.72}$$

Then we cancel an inter-substream interference component and obtain the $(N_{\rm tx}-1)$th symbol estimate by using $\tilde{s}_{N_{\rm tx}}(t)$ and the corresponding channel components as

$$\hat{s}_{N_{\rm tx}-1}(t) = \frac{y_{N_{\rm tx}-1}(t) - a_{(N_{\rm tx}-1)N_{\rm tx}}\tilde{s}_{N_{\rm tx}}(t)}{a_{(N_{\rm tx}-1)(N_{\rm tx}-1)}}. \tag{2.73}$$

All symbol estimates can be obtained successively by applying the above processing to the subsequent signals, i.e.,

$$\hat{s}_k(t) = \frac{y_k(t) - \sum_{i=k+1}^{N_{\rm tx}} a_{ki}\tilde{s}_i(t)}{a_{kk}}. \tag{2.74}$$

This hierarchical detection scheme is referred to as SIC-QRD and does not require inverse calculation unlike SIC-ZF and SIC-MMSE. We can see that, however, it does not exploit the output signals $y_{N_{\rm tx}+1}(t), \ldots, y_{N_{\rm rx}}(t)$ so that remaining RX branches may be futile when $N_{\rm rx} > N_{\rm tx}$. Also, while the absolute values of diagonal channel elements $|a_{11}|, \ldots, |a_{N_{\rm tx}N_{\rm tx}}|$ reflect quality of the corresponding substreams, they may depend on the QR algorithm. Detection order should be taken into account as well as the substream quality, where the order is also related to the QR algorithm. In computer simulations in the next section, the author employed a QR algorithm suitable for SIC-QRD described in Appendix B.

2.4.5 Parallel Interference Canceller

SIC systems are effective to obtain diversity gain. However, in the systems we cannot detect the second substream unless we estimate the first substream. This constraint may cause system delay. Also, SIC systems are not applicable when spatially interleaving the coded sequence at the transmitter, as will be explained later.

A parallel interference canceller (PIC) does not have such problems. It has $N_{\rm tx}$ stages for simultaneously cancelling inter-substream interference and detecting substreams in parallel as shown in Fig. 2.11. First we predetect all substreams by a detection algorithm such as ZF (PIC-ZF) or MMSE (PIC-MMSE) and obtain symbol replicas $\tilde{s}_1(t), \ldots, \tilde{s}_{N_{\rm tx}}(t)$. In the kth stage, inter-substream interference components are cancelled from the received signal vector using replicas, and we obtain the modified signal vector $\boldsymbol{r}^{(k)}(t)$ as

$$\boldsymbol{r}^{(k)}(t) = \boldsymbol{r}(t) - \sum_{i=1, i\neq k}^{N_{\rm tx}} \boldsymbol{h}_i\tilde{s}_i(t). \tag{2.75}$$

If we had perfect symbol replicas[4], i.e., $\tilde{s}_i(t) = s_i(t)$ $(i = 1, \ldots, N_{\rm tx}; i \neq k)$, the system

[4]We also need to have perfect CSI in order to achieve the SIMO system in fact.

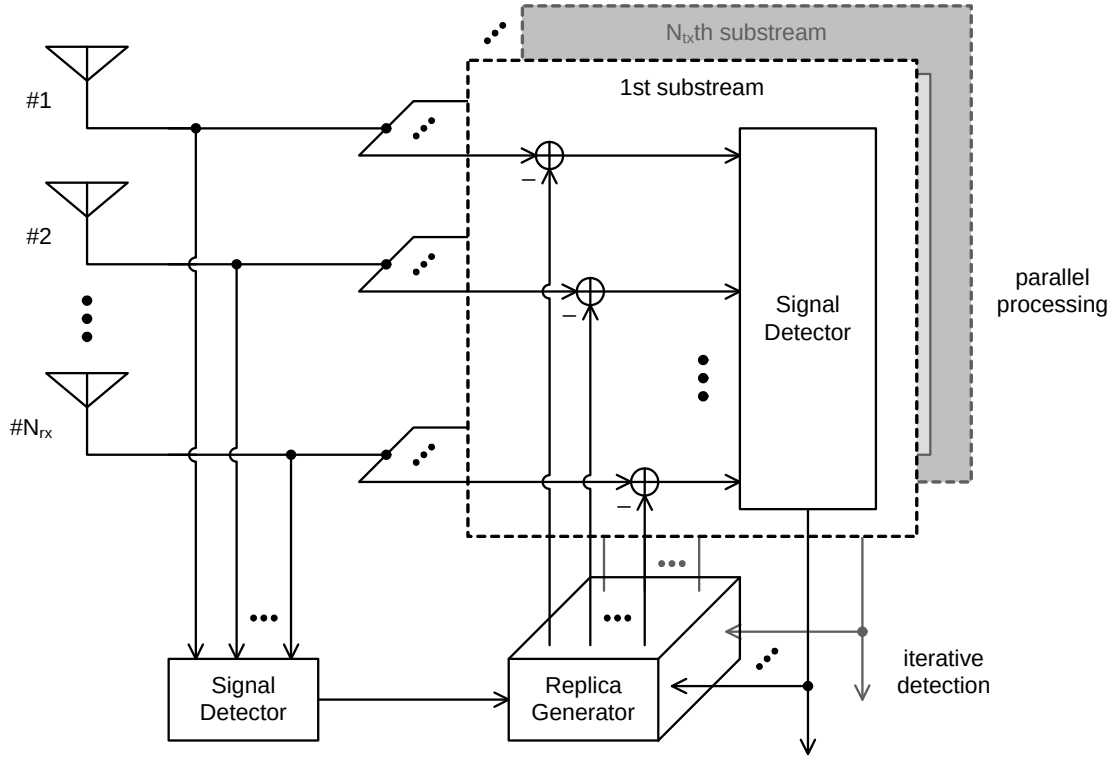

Figure 2.11: Concept of PIC.

would become equivalently a SIMO system for the kth substream, i.e.,

$$\boldsymbol{r}^{(k)}(t) = \boldsymbol{h}_k s_k(t) + \boldsymbol{n}(t). \tag{2.76}$$

Assuming this, the kth output signal can be simply obtained by MRC as

$$\hat{s}_k(t) = \frac{\boldsymbol{h}_k^H}{\|\boldsymbol{h}_k\|^2}\boldsymbol{r}^{(k)}(t) \tag{2.77}$$

$$= s_k(t) + \frac{\boldsymbol{h}_k^H}{\|\boldsymbol{h}_k\|^2}\boldsymbol{n}(t). \tag{2.78}$$

With a series of processing for all N_{tx} stages, we obtain a PIC output sequence. For more accurate estimates, we can then iterate the above procedure by applying the output sequence to replica generation.

Note that the above MRC detection is based on ideal cancellation. On the other hand, in actual $\boldsymbol{r}'_k(t)$ may have residual inter-substream interference components due to estimation errors in predetected signals. Another detecting approach is the introduction of filtering factors in spatial filtering. The channel matrix in the kth stage is multiplied by filtering

factors except the desired channel vector $\boldsymbol{h}_k$ as

$$\boldsymbol{H}^{(k)} = \left[\alpha_{f,1}^{(k)}\boldsymbol{h}_1 \ \cdots \ \alpha_{f,k-1}^{(k)}\boldsymbol{h}_{k-1} \ \boldsymbol{h}_k \ \alpha_{f,k+1}^{(k)}\boldsymbol{h}_{k+1} \ \cdots \alpha_{f,N_{\mathrm{tx}}}^{(k)}\boldsymbol{h}_{N_{\mathrm{tx}}}\right] \tag{2.79}$$

$$= \boldsymbol{H}\,\mathrm{diag}\left(\alpha_{f,1}^{(k)}, \ldots, \alpha_{f,k-1}^{(k)}, 1, \alpha_{f,k+1}^{(k)}, \ldots, \alpha_{f,N_{\mathrm{tx}}}^{(k)}\right), \tag{2.80}$$

where the filtering factor $\alpha_{f,i}^{(k)}$ ($i = 1, \ldots, N_{\mathrm{tx}}; i \neq k$) is set in the range of $0 \leq \alpha_{f,i}^{(k)} \leq 1$. By multiplying $\boldsymbol{r}^{(k)}(t)$ by a weight vector calculated based on $\boldsymbol{H}^{(k)}$, e.g., via the ZF or MMSE algorithm, we can expect that residual inter-substream interference components are suppressed in the filter output.

We can introduce cancelling factors in anticipation of iterative processing in a PIC. With cancelling factors, the modified signal vector can be given by

$$\boldsymbol{r}^{(k)}(t) = \boldsymbol{r}(t) - \sum_{i=1, i\neq k}^{N_{\mathrm{tx}}} \alpha_{c,i}^{(k)}\boldsymbol{h}_i\tilde{s}_i(t), \tag{2.81}$$

where the cancelling factor $\alpha_{c,i}^{(k)}$ ($i = 1, \ldots, N_{\mathrm{tx}}; i \neq k$) is set in the range of $0 \leq \alpha_{c,i}^{(k)} \leq 1$ as well as filtering factors. This scheme can be regarded as one of the soft cancellation schemes, which originally uses soft output of a decoder. With introduction of cancelling factors, we can expect to approach the actual signals step-by-step by iteratively cancelling interference components. Although $\boldsymbol{r}^{(k)}(t)$ may have larger residual inter-substream interference components than the case without cancelling factors, each cancellation stage does not affect the other stages, i.e., does not cause error propagation in PIC processing. So, introduction of cancelling factors to SIC systems seems incompatible due to propagation of residual inter-substream interference. Note that both filtering and cancelling factors can be set again in each iterative stage.

2.5 MIMO SDM Performance Using Various Demultiplexing Schemes

Some demultiplexing schemes have been introduced in the previous section. In this section the author shows the MIMO SDM performance over i.i.d. Rayleigh fading when using those demultiplexing schemes at the receiver.

2.5.1 System Structure

We can roughly consider two coding cases in a MIMO SDM system. One is coding per substream (CPS) as illustrated in Fig. 2.12. An input sequence is multiplexed over N_{tx} substreams and then encoded and interleaved at each substream. We can say that this coding case has an affinity for an ARQ system because the transmitter can resend a sequence with small length. Moreover, in an interference cancellation scheme, especially in an SIC

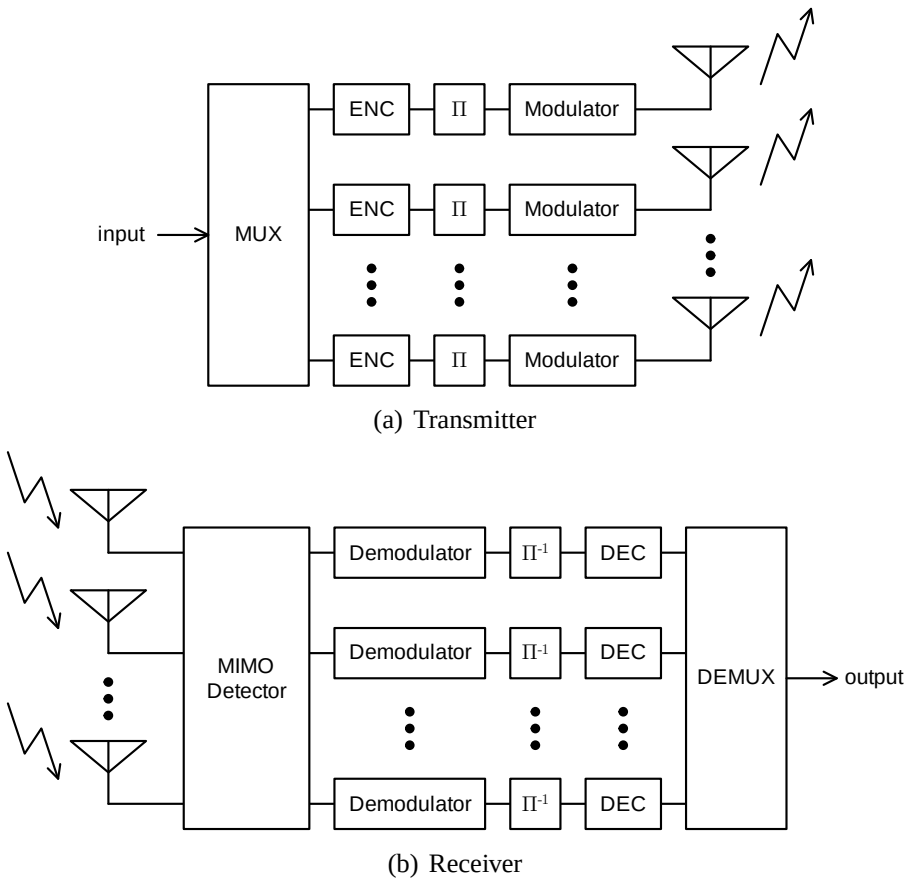

Figure 2.12: System structure in a case of CPS.

system, the receiver can use re-encoded sequences to generate symbol replicas so that we can expect more spatial diversity effect than the case without re-encoding.

The other coding scheme is to encode and interleave the input sequence before multiplexing, i.e., coding over substreams (COS) as illustrated in Fig. 2.13. In the system, while the entire coded sequence is longer than that in the CPS system, we can expect spatial diversity even with a simple demultiplexing scheme such as a spatial filter.

In this section, performance in both the coding cases will be presented.

2.5.2 Computer Simulations

Table 2.1 lists MIMO SDM computer simulation parameters. Simulations in both coding and no coding cases were computed. In the coding cases, input data sequences were coded by a simple convolutional encoder with constraint length of three and coding rate of 1/2 [71]. Then, random bit-interleaving was employed before modulation. At the receiver, soft-decision Viterbi decoding was applied [71]. A soft-input decoder requires the

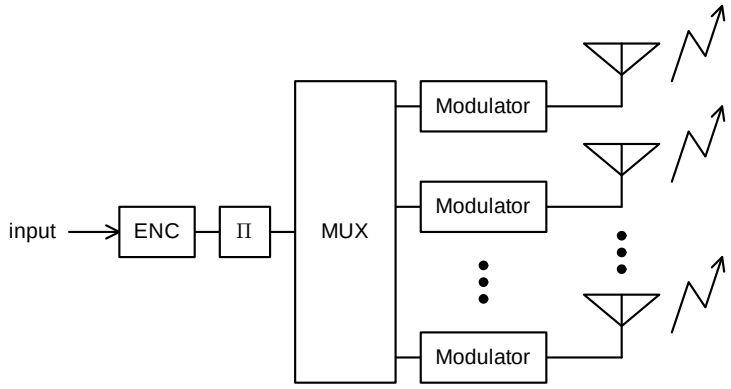

(a) Transmitter

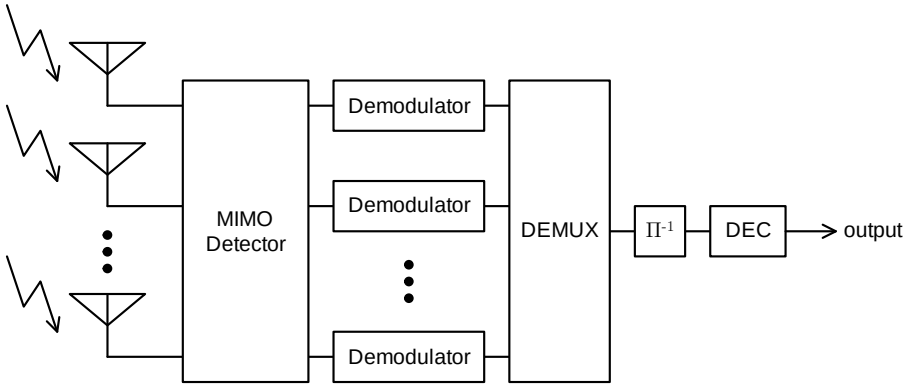

(b) Receiver

Figure 2.13: System structure in a case of COS.

likelihood of each bit. For the sake of simplicity, in each case of corresponding bit 1 or 0, the decoder used the squared Euclidean distance between the output symbol and the closest replica symbol candidate as its log-likelihood [72]. Except MLD, in order to reflect channel quality depending on the substream, the obtained log-likelihood ratio (LLR) was multiplied by the corresponding SNR/SINR at the filter output given by (2.46) and (2.62) in ZF and MMSE cases, respectively. In SIC-QRD, the output SNR of the kth substream is given by the corresponding diagonal element in $\boldsymbol{R}$ and thermal noise power, i.e., $P_t|a_{kk}|^2/\sigma^2$. Using decoder outputs, hard replicas were generated in interference cancellation systems for the sake of simplicity. Also, in PIC cases, MRC detection in (2.77) was employed, and filtering and cancelling factors were not introduced. In the MRC detection, output SNR of the kth substream is given by $P_t\|\boldsymbol{h}_k\|^2/\sigma^2$. Note that the performance of SIC-ZF, SIC-MMSE, and SIC-QRD in the COS case was not examined because in the system we cannot use re-encoded sequences in symbol replica generation. Also, it should be noted that an amplitude correction scheme was introduced when using an MMSE spatial filter, even in SIC-MMSE and PIC-MMSE (see Appendix C).

Table 2.1: Computer simulation parameters.

No. of antennas ($N_{\mathrm{tx}} \times N_{\mathrm{rx}}$)	4 × 4 MIMO
Modulation scheme	QPSK
Thermal noise	Additive white Gaussian noise
Fading	Quasi-static i.i.d. Rayleigh fading
CSI	Perfect at the receiver
Frame length	256 SDM symbols
FEC (coding case)	BCC with constraint length of 3 and rate 1/2
Decoding	Viterbi algorithm
No. of iterations in PIC	5
No. of trial frames	1,000,000

Figures 2.14, 2.15, and 2.16 present the MIMO SDM BER performances with the various detection schemes in the no coding, CPS, and COS cases, respectively. Figures 2.15 and 2.16 also include frame error rate (FER) performances. The abscissa denotes the total TX power normalized to the TX power yielding average E_s/N_0 of 0 dB in a case of single-antenna transmission in the corresponding fading scenario. Note that in the coding cases the performances of SIC-MMSE and PIC-MMSE excel MLD, which ought to be the optimum scheme. This is due to the used encoder, which is the simplest convolutional encoder. Therefore, excellent MLD performance should be obtained when using a more powerful error-correcting code such as a turbo code or a low-density parity-check (LDPC) code [73–75].

The author would like to rely on the readers to consider the performance in detail because properties of the demultiplexing schemes and coding systems have already been introduced. You can see some discussions on the performance in [65].

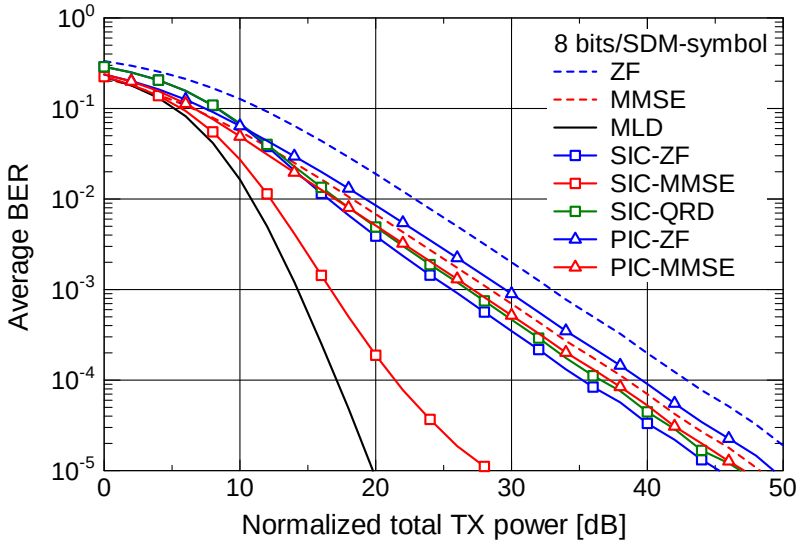

Figure 2.14: BER performance in the no coding case.

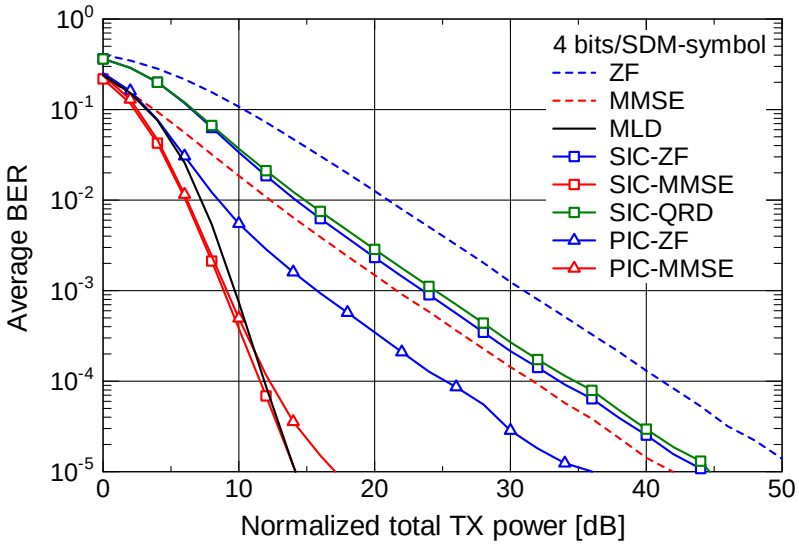

(a) BER

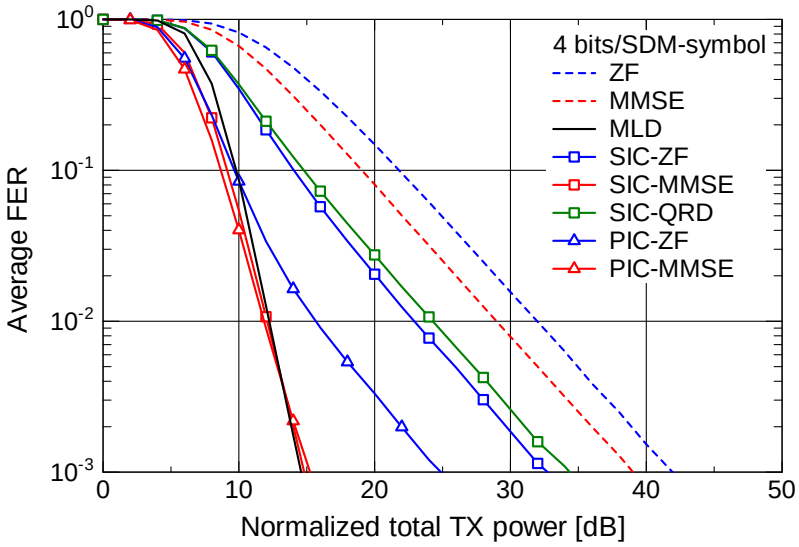

(b) FER

Figure 2.15: BER and FER performances in the CPS case.

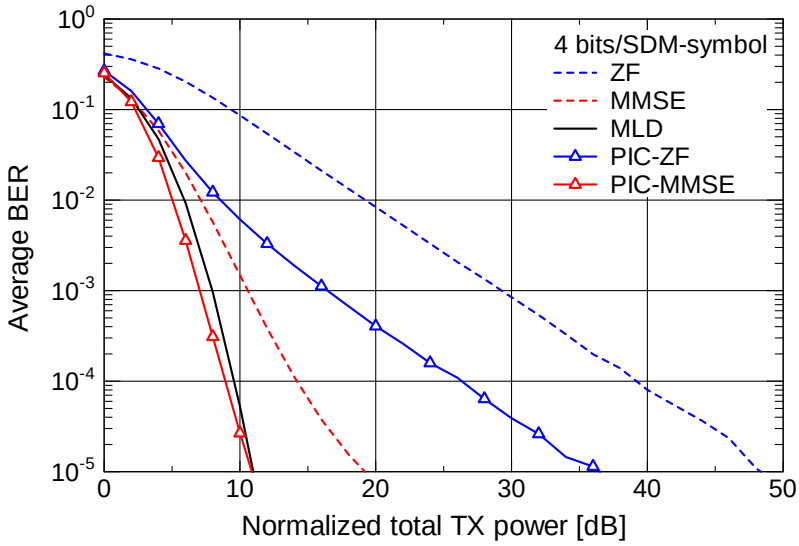

(a) BER

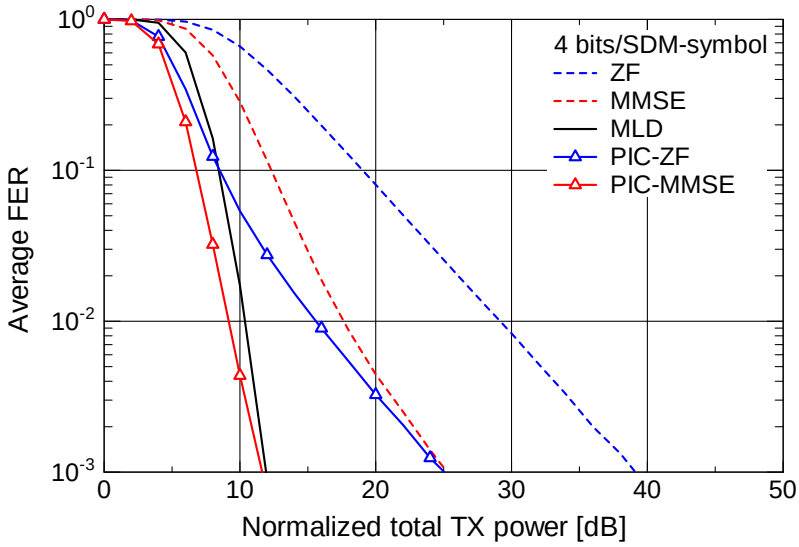

(b) FER

Figure 2.16: BER and FER performances in the COS case.

Chapter 3

MIMO Indoor Channel Measurement

This chapter outlines the conducted 5.2 GHz-band MIMO indoor channel measurement campaign and analyzes characteristics of measured propagation environments with example measurements, TOA/DOA estimation, and Nakagami-Rice K-factor estimation.

3.1 Measurement Setup

The measurement campaign was carried out in a conference room in a building of the Graduate School of Information Science and Technology at Hokkaido University (Figs. 3.1 and 3.2). The room had many scatterers. The walls consisted of plasterboard around reinforced concrete pillars and metal doors. In this room, the author set up TX and RX tables and a VNA to measure the channel responses. Table 3.1 lists measurement parameters. The measurement band was from 5.15 GHz to 5.4 GHz (250 MHz bandwidth), and it was swept with a 156.25 kHz interval (1,601 frequency sample points). Each channel was averaged over 10 snapshots in order to reduce thermal noise included in raw measurements. The TX and RX tables were separated by 4 m, as shown in the dashed circles in Fig. 3.1. The LOS scenario was taken as the absence of an obstructing object between the TX and RX tables (Fig. 3.2(a)). The NLOS scenario was created by placing a metal partition between the TX and RX (Fig. 3.2(b)). The partition was large enough to avoid deterministic waves, which were diffracted at edges of the partition, arriving at the receiver. There was a metal screen (whiteboard) on the wall behind the TX table. The height of its bottom was 1 m, and antenna height was 0.9 m. Channel data were obtained while noone was in the room, to ensure statistical stationarity of propagation.

The x- and y-axes were defined as in Fig. 3.1. The MIMO measurement campaign was carried out for 2×2 and 4×4 MIMO systems and used ULAs for antenna arrays. TX and RX antennas aligned along the x-axis are denoted as the TX-*x*/RX-*x* orientation (Fig. 3.3(a)), and antennas aligned along the y-axis are denoted as the TX-*y*/RX-*y* orienta-

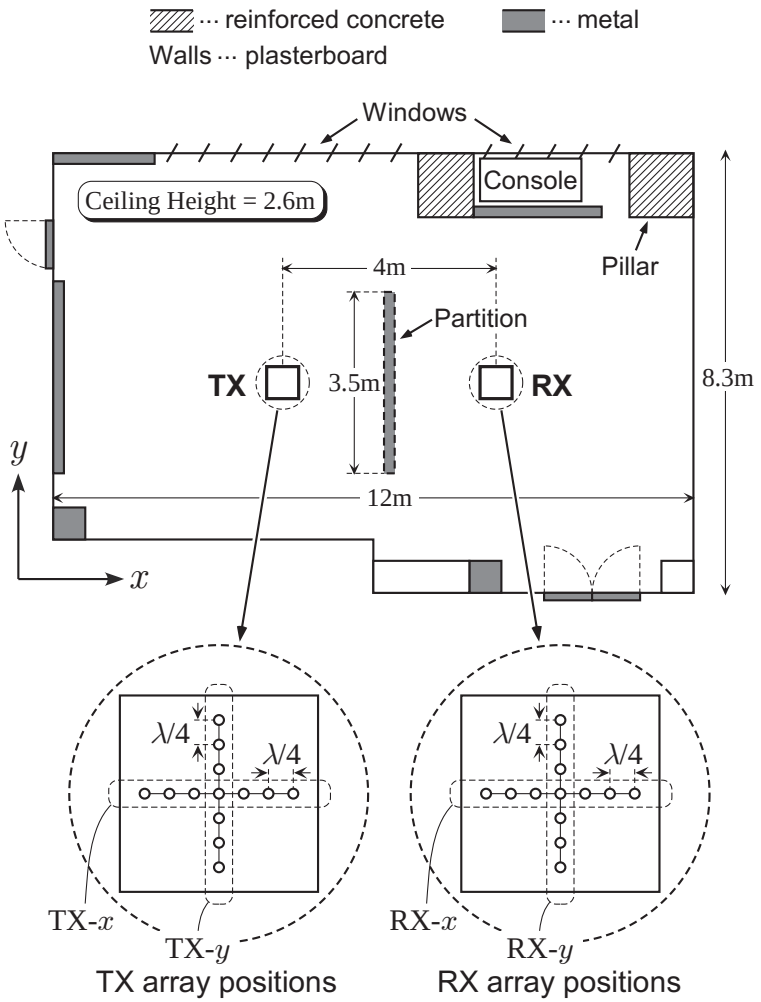

Figure 3.1: Top view of measurement site.

Table 3.1: MIMO channel measurement parameters.

Measurement band	5.15 – 5.4 GHz (250 MHz)
No. of frequency points	1,601
No. of array positions	$7 \times 7 = 49$
No. of total channel data	$1{,}601 \times 49 = 78{,}449$
No. of antennas ($N_{\mathrm{tx}} \times N_{\mathrm{rx}}$)	$2 \times 2,\ 4 \times 4$
Array type	ULA
Antenna spacing (AS)	0.25λ, 0.50λ, 0.75λ, 1.00λ
Array orientations	TX-*x*/RX-*x*, TX-*y*/RX-*y*

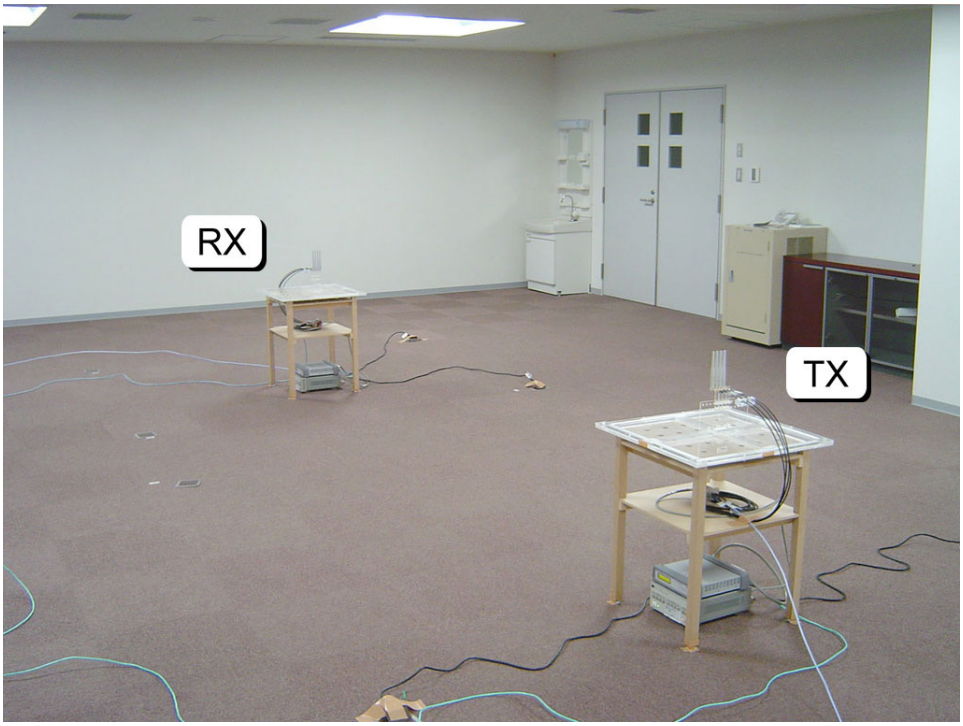

(a) LOS

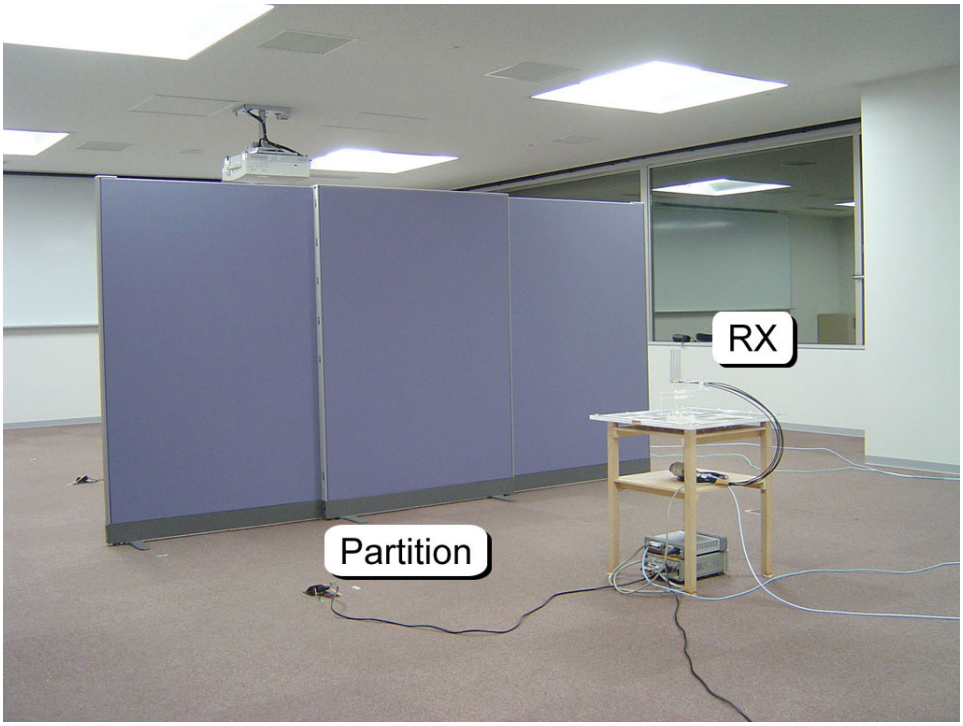

(b) NLOS

Figure 3.2: Pictures of measurement site.

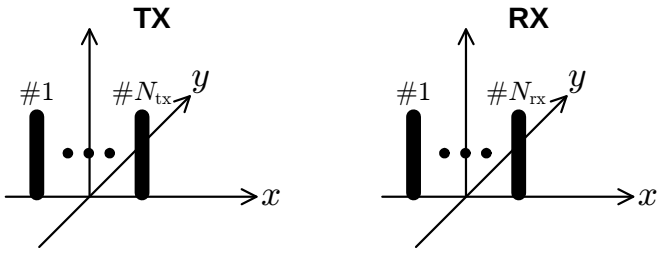

(a) TX-*x*/RX-*x*

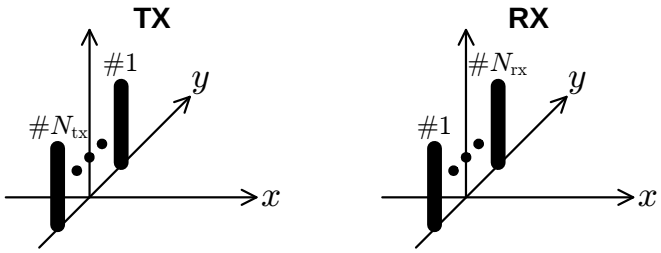

(b) TX-*y*/RX-*y*

Figure 3.3: Antenna array orientations.

tion (Fig. 3.3(b)). To obtain spatially different fading channels, there were seven positions on the TX and RX tables for the antenna array mount along the x- and y-axes separated with an interval of $\lambda/4$ (1.5 cm), as shown in the dashed circles in Fig. 3.1, where λ denotes the wavelength at 5 GHz (6 cm). The antenna array orientation corresponds to the array position direction also as shown in the dashed circles in Fig. 3.1. For example, the positions of the TX and the RX arrays for the TX-*x*/RX-*x*orientation were changed in the x direction. The array's AS had four values: 0.25λ, 0.50λ, 0.75λ, and 1.00λ. By changing the TX and RX array positions, $7 \times 7 = 49$ spatially different data were obtained. Because we had 1,601 frequency-domain data, a total of $49 \times 1{,}601 = 78{,}449$ different MIMO channel matrices were obtained for each array orientation, antenna spacing, and LOS/NLOS scenario. That is, strictly speaking, the author measured $\hat{\boldsymbol{H}}(m, f)$ for the space-domain index $m = 1, \ldots, 49$ and the frequency-domain index $f = 1, \ldots, 1{,}601$. In the study the author treated the 78,449 channel matrices independently as flat fading channels based on (2.1). All of the characteristics presented in the next section were derived from statistical processing of all the 78,449 MIMO channel data.

The author employed collinear antennas AT-CL010 (TSS JAPAN Co., Ltd.) designed for omni-directional characteristics on the horizontal (x-y) plane. Figure 3.4 shows an azimuth antenna pattern of one of the used antennas. The measurement frequency was 5.2 GHz. It is seen in Fig. 3.4 that antenna gain is almost uniform at around 3 dBi, and that the characteristic is omni-directional. All of the antennas had return loss less than -10 dB

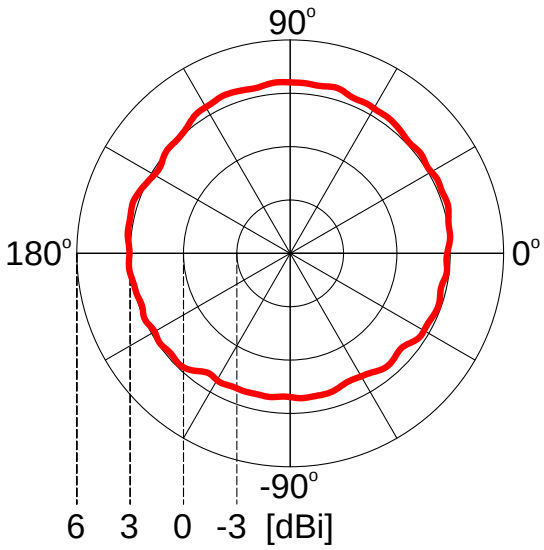

Figure 3.4: Isolated azimuthal antenna pattern of a measurement antenna at 5.2 GHz.

from 5.15 GHz to 5.4 GHz. When a SISO channel was measured in an AEC by using the antennas as the TX and RX ones, the maximum amplitude variation of the observed direct wave was 0.7 dB in this measurement band.

Figure 3.5 shows an example of a 2×2 MIMO measurement system, for which the basic idea is the same for the 4×4 MIMO system. RF switches at the TX and RX sides were used to select the TX antenna and the RX antenna. According to this selection, each element in the MIMO channel matrix was chosen. The measured channel responses were normalized to calibration data that had been obtained when the cables to the antenna ports from the RF switches were directly connected. Therefore, the calibrated data did not have the frequency characteristics of the cables and switches. The unselected antennas were automatically connected to 50 Ω dummy loads. Figure 3.6 shows a picture of the RX table which is a part of the system.

3.2 Example Measurements

Figure 3.7 shows example measurements. These data were obtained at the central positions on the TX and RX tables as shown in the dashed circles in Fig. 3.1 when TX and RX ends each used a single antenna (SISO case). Thus, the antennas did not have mutual coupling. Figure 3.7(a) shows measured frequency-domain data. It is clear that the received power for the LOS scenario was generally larger than the power for the NLOS one due to the direct wave. Time-domain data shown in Fig. 3.7(b) are the results of performing the IDFT on the frequency-domain data shown in Fig. 3.7(a). Note that, before the IDFT, the frequency-domain data were multiplied by the following Gaussian window function to

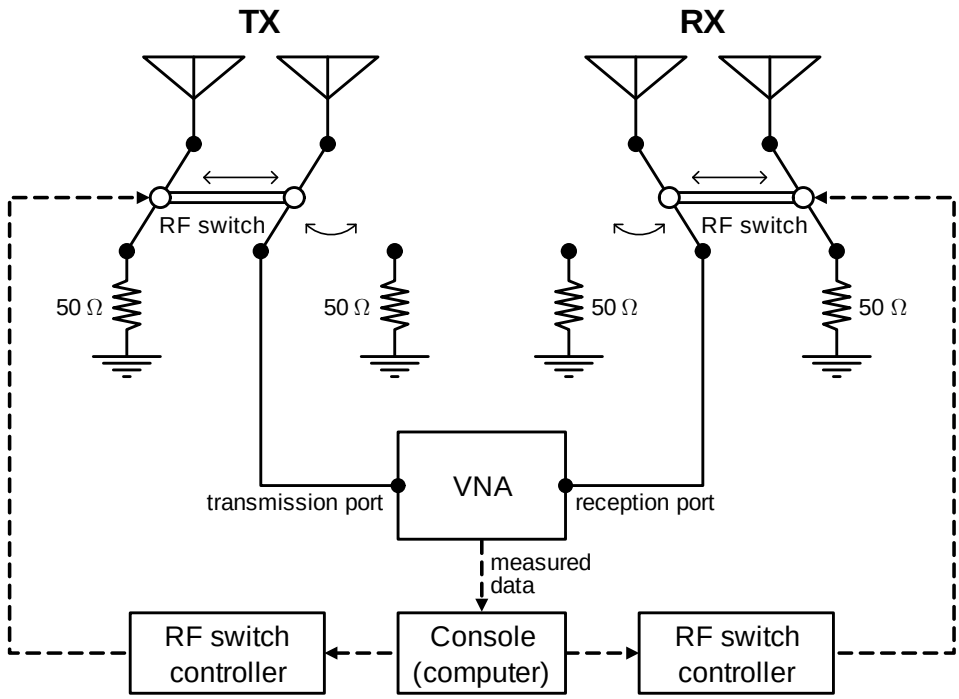

Figure 3.5: Channel measurement system.

reduce side-lobe level

$$w(f_i) = \sqrt{\frac{10.58}{\pi}} \exp\left\{-\frac{10.58}{B^2}(f_i - f_c)^2\right\}, \tag{3.1}$$

where f_c and B denote the center frequency in the measured band and the measured bandwidth, respectively ($f_c = 5.275$ GHz and $B = 250$ MHz). f_i $(i = 0, 1, \cdots, 1{,}600)$ indicates the index of the measured frequency point (5.15 GHz $\leq f_i \leq$ 5.4 GHz). The many peaks for the LOS and NLOS scenarios indicate that the measurement environments had many scattered waves. The maximum peak was around 14 ns for the LOS scenario. This is considered to be from the direct wave because the distance of 4 m between the TX and RX ends gives a propagation time of $4/(3.0 \times 10^8) = 13.3$ ns and the peak disappeared for the NLOS scenario. Furthermore, unlike NLOS, LOS gave larger amplitudes for the waves with short propagation delays within 60 ns.

Figure 3.8 shows examples of eigenvalues for the 2×2 MIMO case with AS $= 0.50\lambda$ and the TX-*y*/RX-*y* orientation. These data were obtained at the same position that those in the aforementioned SISO case were obtained. In contrast to the antennas in the SISO case, the antennas in this case had the effect of mutual coupling. Figure 3.8(a) shows eigenvalues in the NLOS scenario, and Fig. 3.8(b) shows those in the LOS one. There are two eigenvalues λ_1 and λ_2 because of a 2×2 MIMO system. Under both of the scenarios the change of λ_1 is smaller than that of λ_2. It can be expected that spatial diversity appears

Figure 3.6: Measurement table including antennas (top), RF switch (middle), and RF switch controller (bottom).

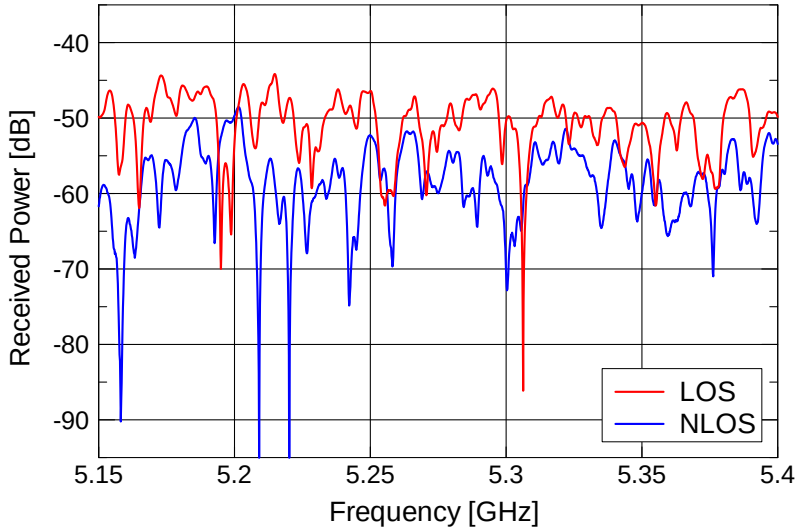

(a) Frequency domain

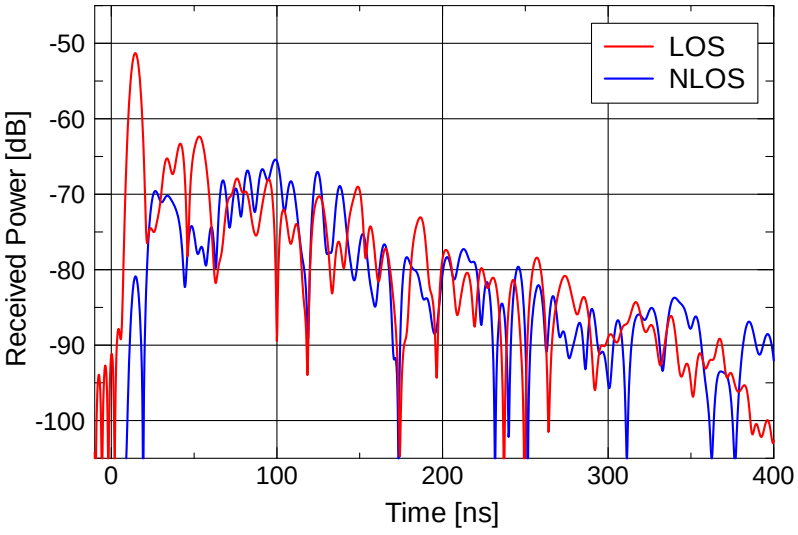

(b) Time domain

Figure 3.7: Example measurements (SISO case).

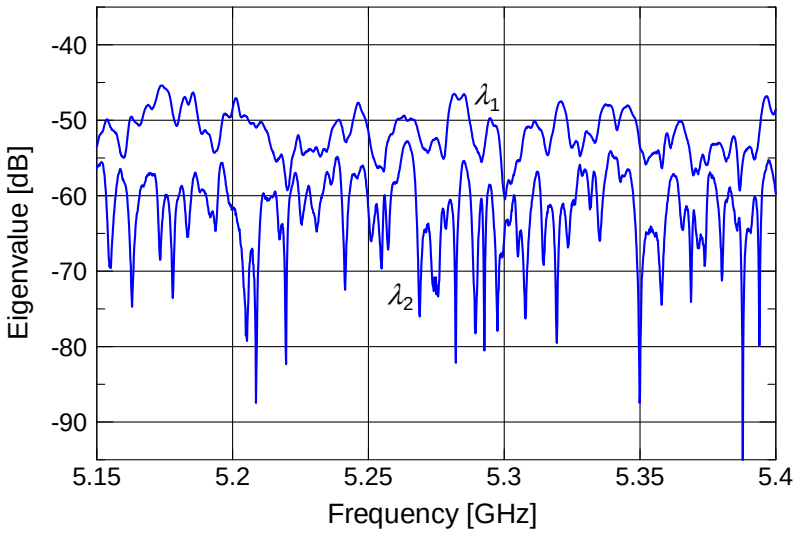

(a) NLOS

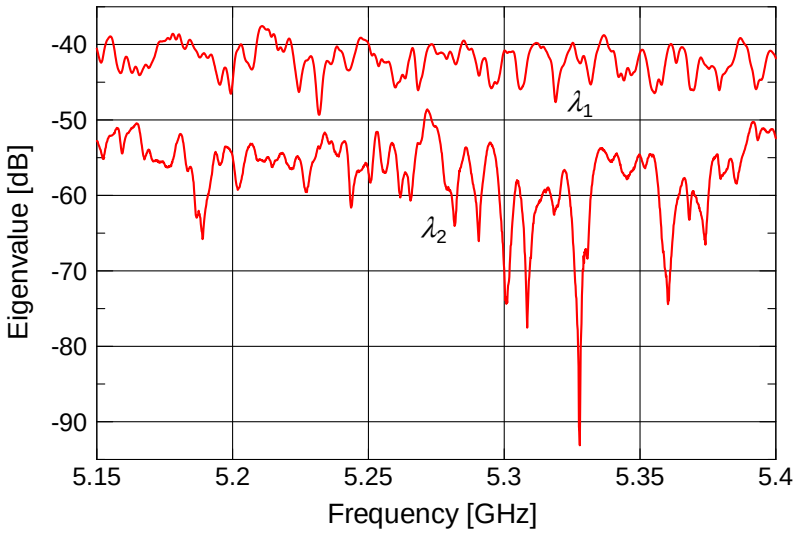

(b) LOS

Figure 3.8: Examples of eigenvalues for the 2×2 MIMO case (AS $= 0.50\lambda$, TX-y/RX-y orientation).

significantly for the eigenchannel corresponding to the maximum eigenvalue. It can be also seen that the LOS scenario gives a larger λ_1 than the NLOS one does. As in the SISO case, the direct wave in the LOS case seems to have increased the magnitude of λ_1.

3.3 TOA/DOA Estimation Using 2D-MUSIC Algorithm

This section presents TOA/DOA simultaneous estimation of the direct and scattered waves for the measurement site using 2D-MUSIC algorithm [76]. In the following, 2D-MUSIC algorithm is first explained, and then results of TOA/DOA estimation are demonstrated.

3.3.1 2D-MUSIC Algorithm

The 2D-MUSIC algorithm can achieve high-resolution TOA/DOA estimation for a propagation environment by applying the MUSIC algorithm to received data both in the frequency and spatial domains, i.e., two-dimensional received data. The following is a simple explanation of 2D-MUSIC algorithm. See [76] for the details of the algorithm. Note that a ULA is assumed as the RX array in the following.

It is assumed that there are D multipath waves arriving at the RX antennas in a propagation environment. We consider a received data $r(f_i, x_j)$ at the frequency point f_i and the spatial position x_j obtained by a VNA:

$$r(f_i, x_j) = \sum_{d=1}^{D} s_d \exp\left\{-j2\pi f_i\left(t_d + \frac{x_j}{c}\sin\theta_d\right)\right\} + n(f_i, x_j), \tag{3.2}$$

where c represents the velocity of light, and $n(f_i, x_j)$ denotes a thermal noise component at f_i and x_j. s_d, t_d, and θ_d indicate an amplitude, TOA, and DOA to the broadside direction of the dth wave, respectively.

Next, by selecting M ($M > D$) data with equal intervals from f_m to f_{m+M-1} in the frequency domain, an M-dimensional frequency data vector $\hat{\boldsymbol{r}}_m(x_j)$ received at the spatial position x_j is defined as follows

$$\hat{\boldsymbol{r}}_m(x_j) = \left[r(f_m, x_j)\ r(f_{m+1}, x_j)\ \cdots\ r(f_{m+M-1}, x_j)\right]^T. \tag{3.3}$$

Moreover, by selecting M spatial samples with equal intervals from x_m to x_{m+M-1} in the spatial domain, an M^2-dimensional subarray vector $\boldsymbol{r}_m$ is formed using spatially different sets $\hat{\boldsymbol{r}}_m(x_m), \ldots, \hat{\boldsymbol{r}}_m(x_{m+M-1})$ as follows

$$\boldsymbol{r}_m = \left[\hat{\boldsymbol{r}}_m^T(x_m)\ \hat{\boldsymbol{r}}_m^T(x_{m+1})\ \cdots\ \hat{\boldsymbol{r}}_m^T(x_{m+M-1})\right]^T. \tag{3.4}$$

On the other hand, an M^2-dimensional mode vector $\boldsymbol{a}(t_d, \theta_d)$ for the dth wave is defined as

$$\boldsymbol{a}(t_d, \theta_d) = \left[\hat{\boldsymbol{a}}_m^T(t_d, \theta_d, x_m)\ \hat{\boldsymbol{a}}_m^T(t_d, \theta_d, x_{m+1})\ \cdots\ \hat{\boldsymbol{a}}_m^T(t_d, \theta_d, x_{m+M-1})\right]^T, \tag{3.5}$$

where

$$\hat{\boldsymbol{a}}_m(t_d, \theta_d, x_j) = \begin{bmatrix} \exp\left\{-j2\pi f_m \left(t_d + \dfrac{x_j}{c}\sin\theta_d\right)\right\} \\ \exp\left\{-j2\pi f_{m+1} \left(t_d + \dfrac{x_j}{c}\sin\theta_d\right)\right\} \\ \vdots \\ \exp\left\{-j2\pi f_{m+M-1} \left(t_d + \dfrac{x_j}{c}\sin\theta_d\right)\right\} \end{bmatrix}. \tag{3.6}$$

Using the mode vector $\boldsymbol{a}(t_d, \theta_d)$, the subarray $\boldsymbol{r}_m$ can be expressed as

$$\boldsymbol{r}_m = \sum_{d=1}^{D} s_d \, \psi_d^{m-1} \boldsymbol{a}(t_d, \theta_d) + \boldsymbol{n}_m, \tag{3.7}$$

where $\boldsymbol{n}_m$ denotes an M^2-dimensional vector composed of additive thermal noise elements, and ψ_d is represented by the following equation

$$\psi_d = \exp\left\{-j2\pi \left(\Delta f t_d + \frac{\Delta x}{c}\sin\theta_d\right)\right\}. \tag{3.8}$$

Here, Δf and Δx denote the frequency interval ($f_{i+1} - f_i$) and the spatial interval ($x_{j+1} - x_j$), respectively.

Furthermore, with an $M^2 \times D$ matrix $\boldsymbol{A}$ composed of mode vectors and a D-dimensional diagonal matrix $\boldsymbol{\Psi}$, (3.7) can be reformulated as

$$\boldsymbol{r}_m = \boldsymbol{A}\,\boldsymbol{\Psi}^{m-1}\boldsymbol{s} + \boldsymbol{n}_m, \tag{3.9}$$

where

$$\boldsymbol{A} = [\boldsymbol{a}(t_1, \theta_1)\ \boldsymbol{a}(t_2, \theta_2)\ \cdots\ \boldsymbol{a}(t_D, \theta_D)] \tag{3.10}$$

$$\boldsymbol{\Psi} = \mathrm{diag}\,(\psi_1, \psi_2, \ldots, \psi_D) \tag{3.11}$$

$$\boldsymbol{s} = [s_1, s_2, \ldots, s_D]^T. \tag{3.12}$$

With $\boldsymbol{r}_m$, an $M^2 \times M^2$ correlation matrix $\boldsymbol{R}_m$ is defined by

$$\boldsymbol{R}_m = \boldsymbol{r}_m^* \boldsymbol{r}_m^T. \tag{3.13}$$

Since multipath waves are coherent, it is required to decorrelate them. Here, we preprocess the data by using spatial smoothing preprocessing (SSP) before applying 2D-MUSIC as follows

$$\boldsymbol{R}_{\mathrm{SSP}} = \frac{1}{N} \sum_{m=n}^{n+N-1} \boldsymbol{R}_m. \tag{3.14}$$

With the above preprocessing, N coherent waves can be decorrelated. Note that $N \geq D$ is necessary to estimate all the arriving waves in the SSP case.

On the other hand, we can decorrelate up to $2N$ coherent waves only with N correlation matrices by using the following modified SSP (MSSP) technique

$$\boldsymbol{R}_{\mathrm{MSSP}} = \frac{1}{2N} \sum_{m=n}^{n+N-1} \left(\boldsymbol{R}_m + \boldsymbol{J} \boldsymbol{R}_m^* \boldsymbol{J} \right), \tag{3.15}$$

where $\boldsymbol{J}$ is an M^2-dimensional square matrix expressed as

$$\boldsymbol{J} = \begin{bmatrix} 0 & 0 & \cdots & 0 & 1 \\ 0 & 0 & \cdots & 1 & 0 \\ \vdots & \vdots & & & \vdots \\ 0 & 1 & \cdots & 0 & 0 \\ 1 & 0 & \cdots & 0 & 0 \end{bmatrix}. \tag{3.16}$$

In the MSSP case, we can decorrelate all the arriving waves with $N \geq D/2$ subarrays.

It is presumed that correlations among all the D waves are suppressed with SSP or MSSP. Then, the correlation matrix $\boldsymbol{R}$ can be expressed by using an M^2-dimensional unitary matrix $\boldsymbol{U}$ and an M^2-dimensional diagonal matrix $\boldsymbol{\Lambda}$ composed of eigenvalues of $\boldsymbol{R}$:

$$\boldsymbol{R} = \boldsymbol{U} \boldsymbol{\Lambda} \boldsymbol{U}^H, \tag{3.17}$$

where

$$\boldsymbol{U} = [\boldsymbol{e}_1 \, \boldsymbol{e}_2 \, \cdots \, \boldsymbol{e}_{M^2}] \tag{3.18}$$

$$\boldsymbol{\Lambda} = \mathrm{diag}\left(\lambda_1, \lambda_2, \ldots, \lambda_{M^2}\right). \tag{3.19}$$

Note that M^2 eigenvalues $\lambda_1, \ldots, \lambda_{M^2}$ in the above equation are in descending order as follows

$$\lambda_1 \geq \lambda_2 \geq \cdots \geq \lambda_D \geq \lambda_{D+1} = \cdots = \lambda_{M^2} = \sigma^2. \tag{3.20}$$

Here, σ^2 denotes thermal noise power. The above equation implies that an M^2-dimensional vector space can be classified into a D-dimensional signal subspace and an $(M^2 - D)$-dimensional noise subspace. These subspaces are orthogonal each other, and a D-dimensional mode vector space formed by $\boldsymbol{a}(t_1, \theta_1), \ldots, \boldsymbol{a}(t_D, \theta_D)$, i.e., $\boldsymbol{A}$, corresponds to the D-dimensional signal subspace included in the correlation matrix $\boldsymbol{R}$. That is, the following relation holds:

$$\boldsymbol{a}^H(t_i, \theta_i)\boldsymbol{e}_j = 0 \qquad (i = 1, \ldots, D, \; j = D+1, \ldots, M^2). \tag{3.21}$$

Exploiting the above property, an evaluation function of propagation estimation is defined as

$$P_{\mathrm{music}}(t, \theta) = \frac{\boldsymbol{a}^H(t, \theta)\boldsymbol{a}(t, \theta)}{\sum_{i=D+1}^{M^2} |\boldsymbol{a}^H(t, \theta)\boldsymbol{e}_i|}. \tag{3.22}$$

As seen from the relation in (3.21), the denominator of the right hand side of the above equation should be 0 in the case of $(t = t_i, \theta = \theta_i)$ $(i = 1, \ldots, D)$, so that the left hand side, i.e., $P_{\mathrm{music}}(t, \theta)$, can obtain maxima by being swept with time t and angle θ. Consequently, simultaneous TOA/DOA estimation of multipath waves can be achieved.

Table 3.2: 2D-MUSIC estimation parameters.

No. of elements in a subarray	$M = 16$
Antenna spacing	$\Delta x = \lambda/4$ (1.5 cm)
No. of subarrays	$N = 6$
Preprocessing	MSSP (12 coherent waves can be decorrelated when $N = 6$.)
Used frequency band	5.3 – 5.4 GHz
Frequency interval	$\Delta f = 5$ MHz
RX array orientation	RX-*x*, RX-*y*
No. of estimated waves	$D = 8$

3.3.2 Results of Propagation Estimation

Propagation estimation for the measurement site was conducted by using 2D-MUSIC algorithm. Table 3.2 lists the estimation parameters. The used data were obtained for this estimation with a single omni-directional antenna, unlike the data described in §3.1. While the TX antenna was fixed to the central position on the TX table, the RX antenna was linearly moved with $\lambda/4$ intervals to measure at a total of 21 spatial positions. In the estimation, the measurements were classified into six 16-element subarrays. Note that expansion of spatial data using interpolation [76] was not applied in the estimation. Frequency data were measured at 5 MHz intervals from 5.3 to 5.4 GHz. MSSP was applied for suppressing correlations so that $6 \times 2 = 12$ coherent waves would be decorrelated. RX array orientations were RX-*x* and RX-*y* (see Fig. 3.1). The number of arriving waves was set to $D = 8$.

Figures 3.9–3.12 show the results of TOA/DOA estimation for the measurement site. Like Fig. 3.7(b), in the LOS scenario the highest peak, considered as the direct wave, is observed at around 14 ns (90° direction for RX-*x* and 0° direction for RX-*y*). Also, a peak is seen at around 40 ns from the 90° direction in the case of LOS and RX-*x*. Taking into account the DOA, the peak seems to be a reflected wave from the wall on the receiver side. However, a clear peak corresponding to it cannot be observed in the case of RX-*y*. In the NLOS scenario, we can see multiple peaks at various TOA and DOA. That is, the measurement site is considered as a multipath-rich environment.

3.4 Estimation of Nakagami-Rice K-factor

In general, amplitudes of faded channels in NLOS multipath environments statistically obey a Rayleigh distribution. Such channel variation is therefore called Rayleigh fading. On the other hand, in LOS environments, addition of a direct wave to Rayleigh channels yields Nakagami-Rice fading [2, 31, 71]. In this section, a K-factor, which is a measure for propagation property of Nakagami-Rice fading environments, is estimated for the LOS

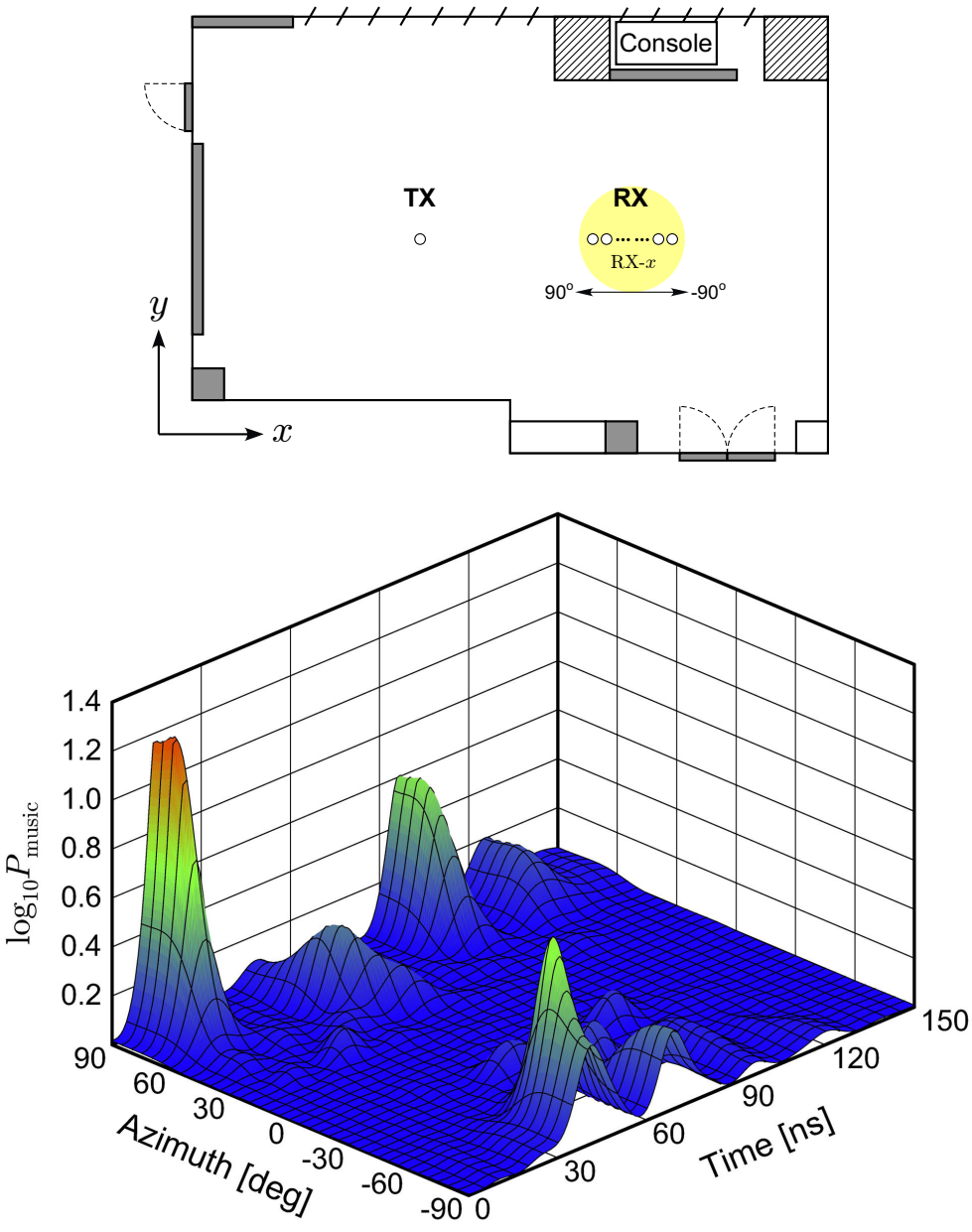

Figure 3.9: TOA/DOA estimation result (LOS, RX-*x*).

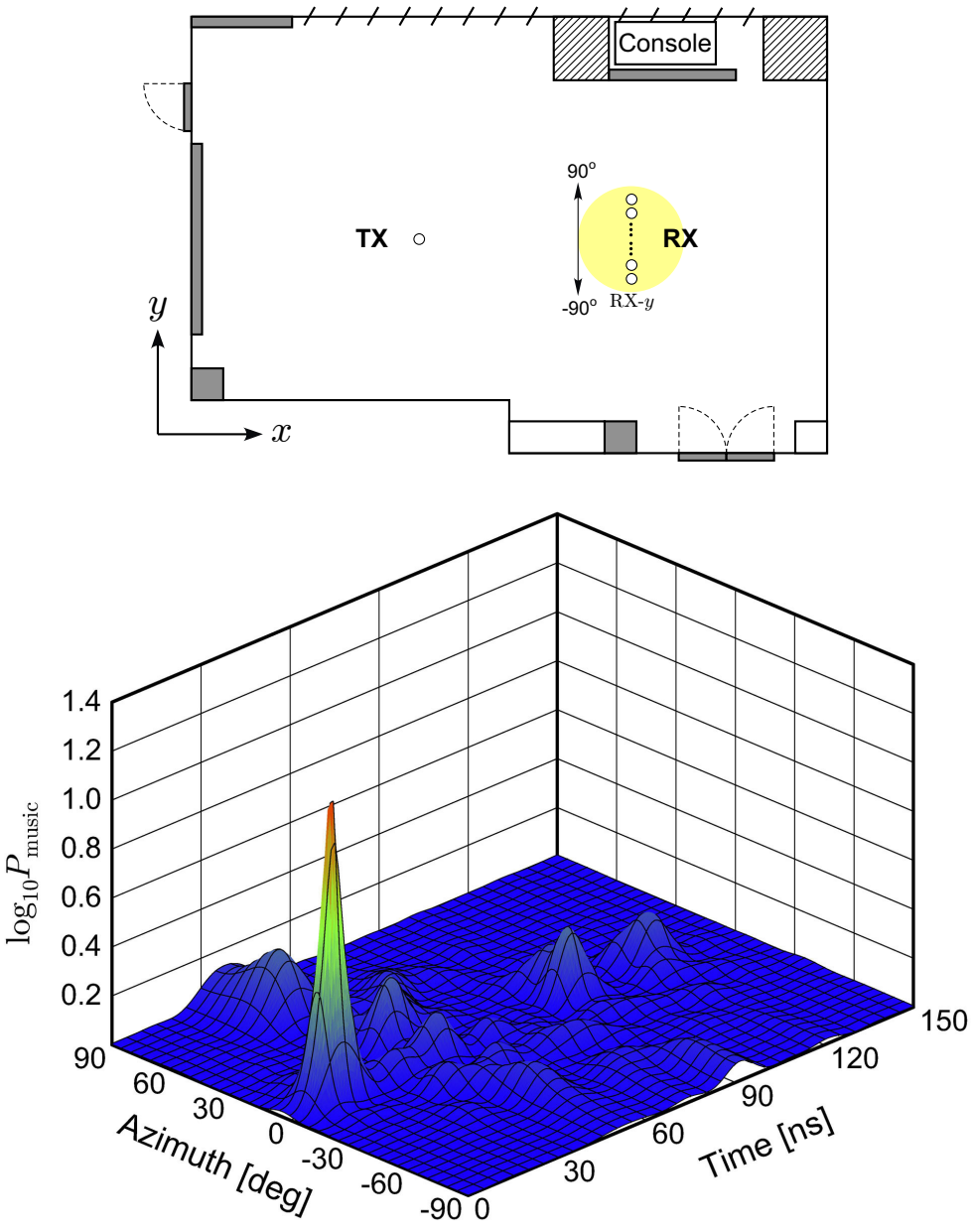

Figure 3.10: TOA/DOA estimation result (LOS, RX-*y*).

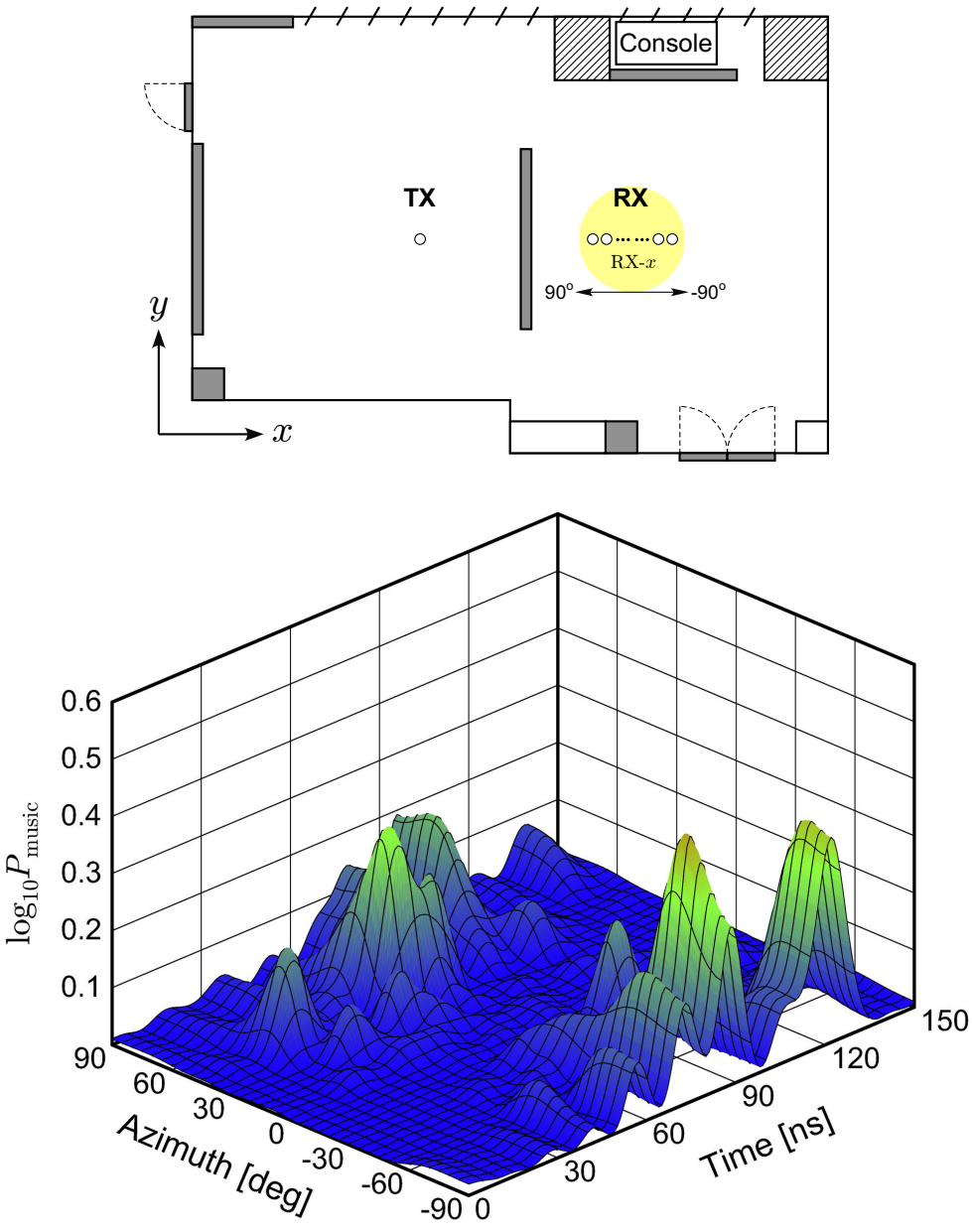

Figure 3.11: TOA/DOA estimation result (NLOS, RX-*x*).

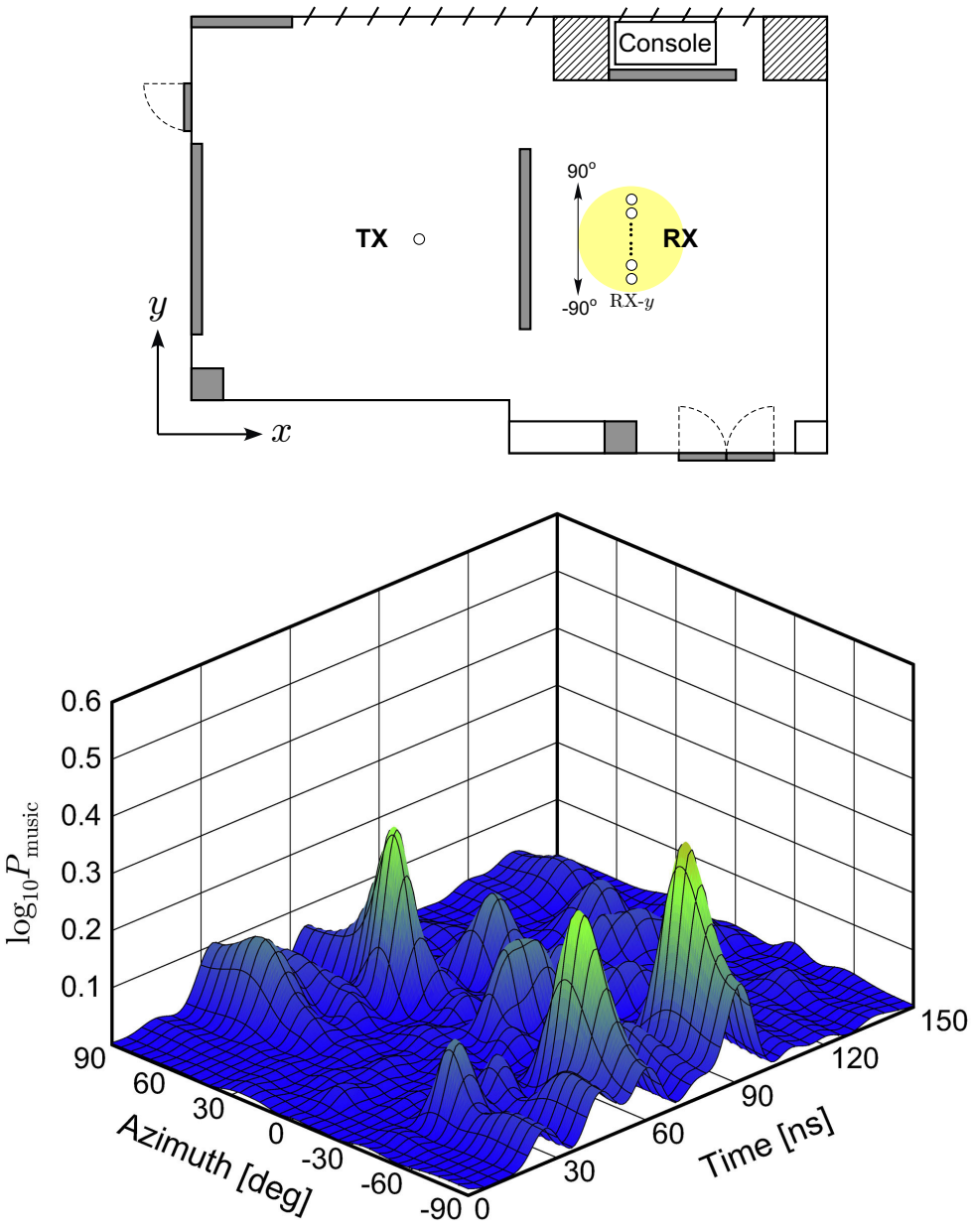

Figure 3.12: TOA/DOA estimation result (NLOS, RX-*y*).

scenario in the measurement site.

It is assumed that an LOS channel response $h(m, f)$, which is measured with a single omni-directional antenna at the spatial position m and frequency point f, consists of a direct-wave component $h_D(m, f)$ and a scattered-wave component $h_U(m, f)$:

$$h(m, f) = h_D(m, f) + h_U(m, f). \tag{3.23}$$

Ergodic power of the direct-wave component and that of the scattered-wave component are defined as A^2 and σ_U^2, respectively:

$$A^2 = E\left[|h_D(m, f)|^2\right] \tag{3.24}$$

$$\sigma_U^2 = E\left[|h_U(m, f)|^2\right], \tag{3.25}$$

where $E[\cdot]$ represents average over the spatial and frequency domains. Then, the K-factor can be defined as follows

$$K = \frac{A^2}{\sigma_U^2}. \tag{3.26}$$

That is, the K-factor is a power ratio of the direct wave to the scattered waves. The larger K-factor means that the direct wave is more dominant compared with the scattered waves in the propagation environment.

3.4.1 K-factor Calculation Using Average Channel Power

When assuming that $h_D(m, f)$ and $h_U(m, f)$ are statistically uncorrelated, the ergodic power of the measured channel $h(m, f)$ can be written as

$$P_{\text{ch}} = E\left[|h(m, f)|^2\right] = A^2 + \sigma_U^2. \tag{3.27}$$

Hence, in the case where the average power of the direct wave, A^2, is already known, the K-factor can be calculated by

$$K = \frac{A^2}{P_{\text{ch}} - A^2}. \tag{3.28}$$

In total 82 spatially different SISO channels were measured in the frequency band from 5.15 GHz to 5.40 GHz in both the LOS and NLOS scenarios while keeping the distance of 4 m between the TX and RX tables. The measured SISO channels provided the CDFs of the wave amplitudes as shown in Fig. 3.13. The received amplitudes for the LOS scenario were about 7.6 dB higher at the 50% level compared with those for the NLOS scenario. The mean received power averaged over space and frequency samples in the SISO-LOS measurement was $G_{\text{LOS}} = -49.26$ dB (1.186×10^{-5}), and that in the SISO-NLOS one was $G_{\text{NLOS}} = -56.05$ dB. Comparing the mean received powers, G_{LOS} was about 6.8 dB higher than G_{NLOS}. Also, the mean received power G_{AEC} was obtained under the SISO

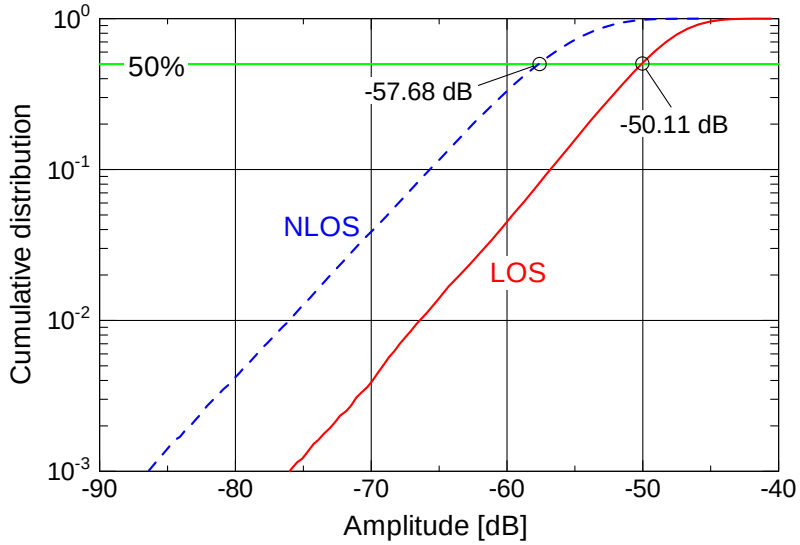

Figure 3.13: CDFs of amplitudes (SISO case).

and LOS scenario in the AEC in which the TX and RX tables were set 4 m apart. The data were averaged over the space and frequency samples. G_{AEC} which is the estimated direct wave power was -51.52 dB (7.047×10^{-6}). Since G_{LOS} is composed of the direct and scattered wave power, the Nakagami-Rice K-factor in the LOS environment can be easily estimated by the following calculation

$$K = \frac{A^2}{P_{\mathrm{ch}} - A^2} \tag{3.29}$$

$$= \frac{G_{\mathrm{AEC}}}{G_{\mathrm{LOS}} - G_{\mathrm{AEC}}} \tag{3.30}$$

$$= \frac{7.047 \times 10^{-6}}{1.186 \times 10^{-5} - 7.047 \times 10^{-6}} \tag{3.31}$$

$$= 1.66 \text{ dB}. \tag{3.32}$$

The scattered wave power was, therefore, comparable to the direct wave power. Moreover, the scattered wave power in the LOS scenario ($G_{\mathrm{LOS}} - G_{\mathrm{AEC}} = -53.18$ dB) was 2.87 dB higher than G_{NLOS}. It is natural that an LOS component causes higher received power. However, the above result indicates that, under the LOS scenario of this room, the direct wave also increased scattered signal power.

3.4.2 K-factor Estimation Using CDF of Amplitudes

When a probability variable R is defined as $R = |h(m, f)|$, i.e., envelope of the LOS channel $h(m, f)$, its probability distribution function $P(R)$ obeys the Nakagami-Rice dis-

tribution [71] and is given by

$$P(R) = \frac{1}{\sigma^2} \int_{-\infty}^{R} t \exp\left(-\frac{A^2 + t^2}{2\sigma_U^2}\right) I_0\left(\frac{At}{\sigma_U^2}\right) \, dt, \tag{3.33}$$

where $I_0(x)$ represents the zeroth-order modified Bessel function of the first kind, which is defined as

$$I_0(x) = \frac{1}{2\pi} \int_0^{2\pi} \exp\left(x \cos\phi\right) \, d\phi. \tag{3.34}$$

Note that, in (3.33), $P(R)$ becomes the Rayleigh distribution when $A = 0$.

Next, we normalize R to its 50% value $R_{50\%}$, which yields $P(R) = 0.5$. The normalized probability variable is defined as $\hat{R}$. Also, A and σ_U are normalized to $R_{50\%}$ as well, and then $\hat{A}$ and $\hat{\sigma}_U$ are obtained, respectively:

$$\hat{R} = \frac{R}{R_{50\%}} \tag{3.35}$$

$$\hat{A} = \frac{A}{R_{50\%}} \tag{3.36}$$

$$\hat{\sigma}_U = \frac{\sigma_U}{R_{50\%}}. \tag{3.37}$$

With $\hat{A}$ and $\hat{\sigma}_U$, a new probability distribution function $P_{\text{cal}}(\hat{R})$ is defined as

$$P_{\text{cal}}(\hat{R}) = \frac{1}{\hat{\sigma}_U^2} \int_{-\infty}^{\hat{R}} t \exp\left(-\frac{\hat{A}^2 + t^2}{2\hat{\sigma}_U^2}\right) I_0\left(\frac{\hat{A}t}{\hat{\sigma}_U^2}\right) \, dt. \tag{3.38}$$

By fitting the above function and a CDF of amplitudes of measured data, we can estimate the K-factor of the measurement site.

Figure 3.14 demonstrates Nakagami-Rice probability distribution functions with various K-factors. Figures 3.14(a) and (b) show $P(R)$ and $P_{\text{cal}}(\hat{R})$, respectively. $P(R)$ was obtained under the condition of $\sigma_U^2 = 1$. Note that abscissas of both graphs are in dB scale. All the functions of $P_{\text{cal}}(\hat{R})$ intersect at the point of 0 dB and $P_{\text{cal}}(\hat{R}) = 0.5$ due to the normalization in (3.35)–(3.37). The larger K-factor is, the steeper its gradient is in the region of $\hat{R} < 0$ dB. Hence, by normalizing a CDF of measured data to its 50% value and verifying it with various probability distribution functions, it is possible to estimate the Nakagami-Rice K-factor of the LOS environment.

Figure 3.15 shows CDFs of amplitudes of measured channels for both the LOS and NLOS scenarios. The RX-*x* and RX-*y* data samples used in the previous section were combined for this estimation. Therefore, a total of $21 \times 2 \times 1{,}601 = 67{,}242$ channel samples were used. As mentioned above, both CDF curves are normalized to their 50% values. We can see that the CDF for the LOS scenario almost corresponds to $P_{\text{cal}}(\hat{R})$ of the $K = 1.6$ case ($K = 2.0$ dB). Also, it is verified that the CDF for the NLOS scenario fits in with $P_{\text{cal}}(\hat{R})$ of the $K = 0.0$ case, i.e., Rayleigh distribution.

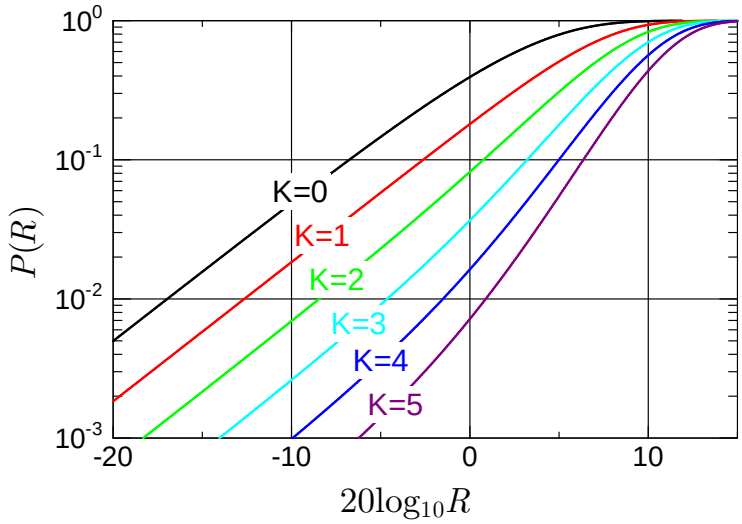

(a) $P(R)$ ($\sigma_U^2 = 1$)

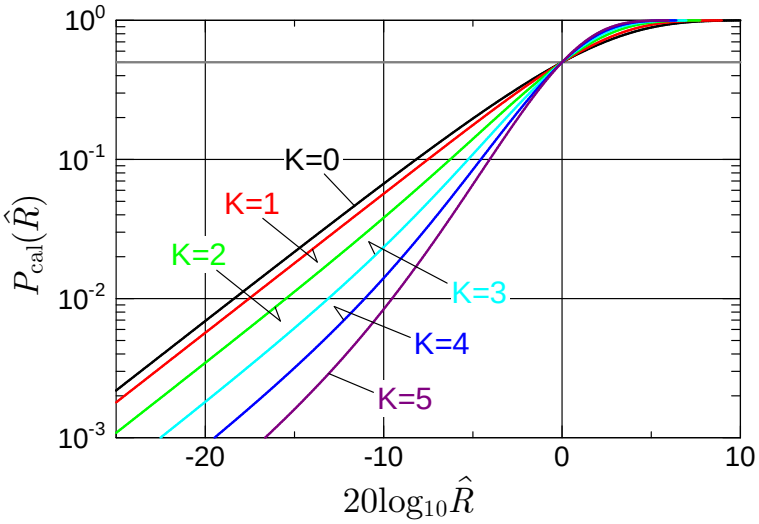

(b) $P_{\mathrm{cal}}(\hat{R})$

Figure 3.14: Nakagami-Rice probability distribution functions.

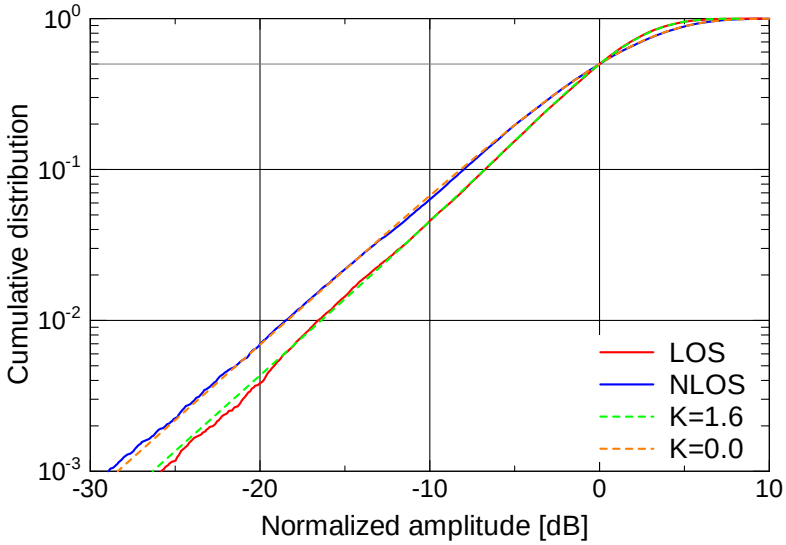

Figure 3.15: CDFs of amplitudes of measured channels normalized to 50% values.

Summarizing §3.2–3.4, it can be said that the measurement site was a multipath-rich environment, and that the K-factor in the LOS scenario was relatively small because it appears in the range of 1.6 dB $\leq K \leq$ 2.0 dB. On the other hand, it is considered that the NLOS scenario provided Rayleigh fading.

Note that the measured channel response h and MIMO channel matrix $\boldsymbol{H}$ used hereafter are given by the following normalizations of the measured $\hat{h}$ and $\hat{\boldsymbol{H}}$.

$$h = \frac{\hat{h}}{\sqrt{G_{\mathrm{AEC}}}} \tag{3.39}$$

$$\boldsymbol{H} = \frac{\hat{\boldsymbol{H}}}{\sqrt{G_{\mathrm{AEC}}}} \tag{3.40}$$

It can be said that the channel response is normalized to the direct wave amplitude.

Chapter 4

Performance Evaluation of Spatial Multiplexing in Actual Indoor Environments

4.1 Properties of Measured MIMO Channels

4.1.1 Antenna Patterns

When multiple antennas are closely arranged, they have mutual coupling and their antenna patterns change. A MIMO system has antenna arrays at both ends, so we cannot ignore the effect of the changing pattern on the MIMO performance. Thus, before presenting the measured characteristics of the MIMO channels, this subsection examines the antenna patterns for each antenna array. See Appendix A for more characteristics of the measured antenna arrays.

The solid curves in Figs. 4.1 and 4.2 show the patterns at the frequency of 5.2 GHz for each two-element array and four-element ULA, respectively. The number under each pattern corresponds to the one in Fig. 3.3. These azimuth patterns for multiple antennas were obtained when all the antennas except the measured one were connected to 50 Ω dummy loads. Therefore they include the mutual coupling effect. In each of these figures, the pattern of a single isolated antenna is shown for comparison by a dashed curve. We see that the single antenna has an almost omni-directional pattern when it does not have the mutual coupling effect. The patterns in the multiple-antenna case, however, are significantly different from those in the omni-directional case. (The patterns for AS $= 0.50\lambda$ and 1.00λ in the two-element arrays are in good agreement with the simulation results in [41].) The patterns tend to become similar to the omni-directional one as the AS becomes larger. We can also see that patterns of four-element ULAs tend to change more than those of two-

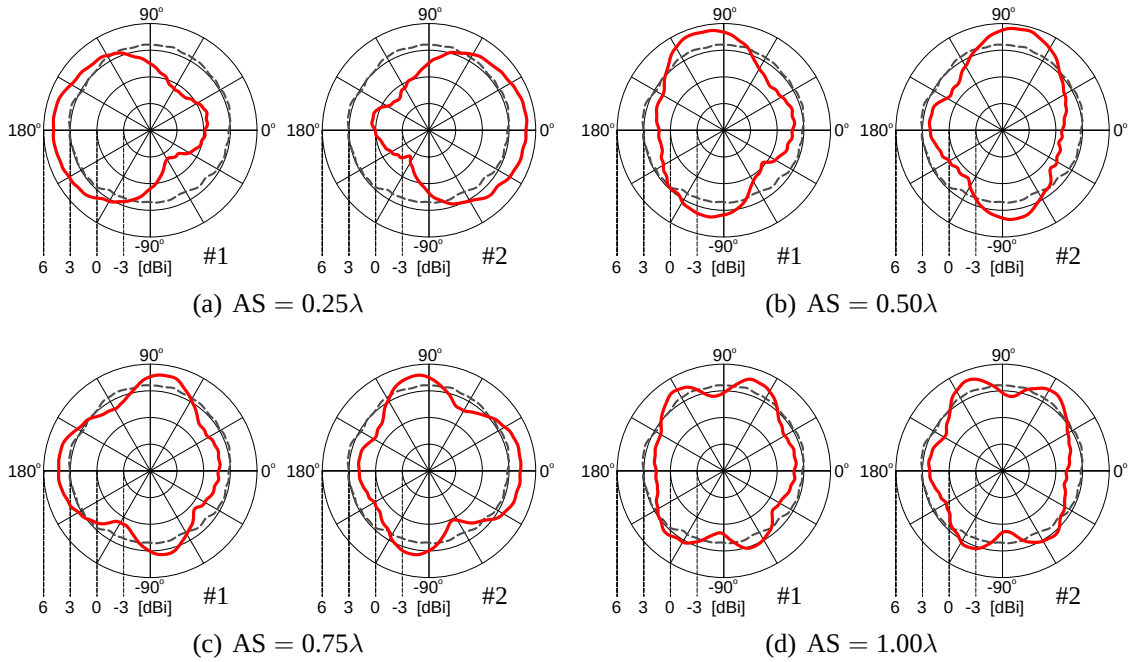

(a) AS $= 0.25\lambda$ (b) AS $= 0.50\lambda$

(c) AS $= 0.75\lambda$ (d) AS $= 1.00\lambda$

Figure 4.1: Antenna patterns for each two-element array with mutual coupling (solid curve), and single antenna pattern (dashed curve).

element arrays. This seems to be due to the effect of mutual coupling between antennas increasing with the number of antennas.

In the TX-*x*/RX-*x* orientation, the RX end is located in the 0° direction with respect to the TX end, and the TX end is located in the 180° direction with respect to the RX end. Thus, in the LOS scenario, the direct wave departs from the TX end in the 0° direction and arrives at the RX end in the 180° direction. In the TX-*y*/RX-*y* orientation, on the other hand, the RX end is located in the 90° direction with respect to the TX end, and the TX end is also located in the 90° direction with respect to the RX end. Thus the direct wave departs from the TX end and arrives at the RX end in the 90° direction. The gain in the 0° and 180° directions tends to be small. On the other hand, the gain in the 90° direction is higher than it is in the single-antenna case, especially when AS $= 0.50\lambda$ and 0.75λ.

As will be shown later, especially in the LOS scenario, eigenvalue distributions and MIMO system performance depend on the array configuration. The antenna gain directionality mentioned above seems to affect the LOS component included in a MIMO channel. Because the relation between the LOS component and antenna gain directionality is necessary to explain the following behavior of MIMO performance, it is referred to as "LOS gain variation" to simplify the following discussions.

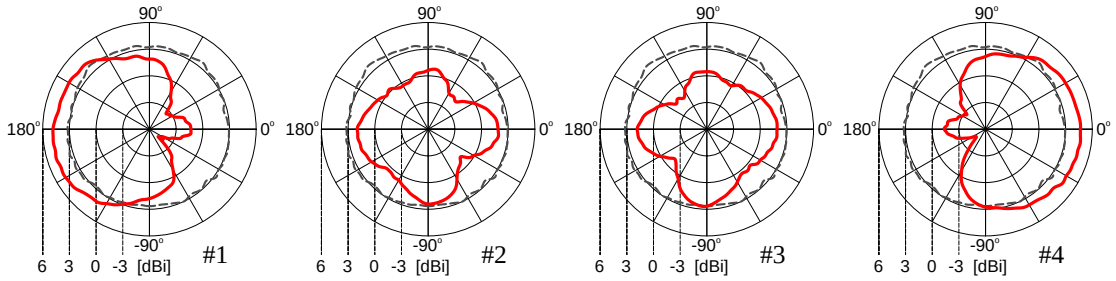

(a) AS = 0.25λ

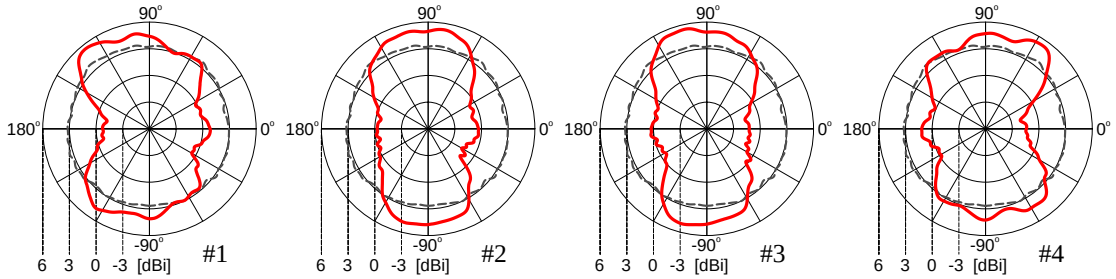

(b) AS = 0.50λ

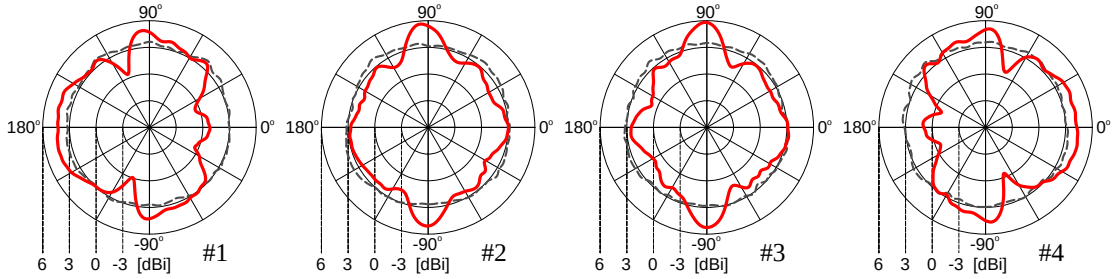

(c) AS = 0.75λ

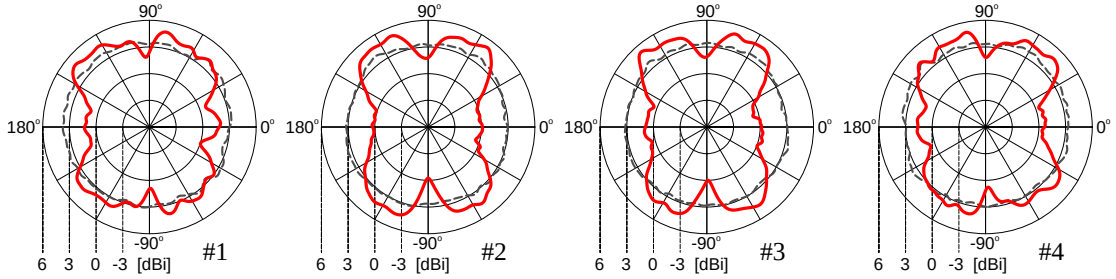

(d) AS = 1.00λ

Figure 4.2: Antenna patterns for each four-element ULA with mutual coupling (solid curve), and single antenna pattern (dashed curve).

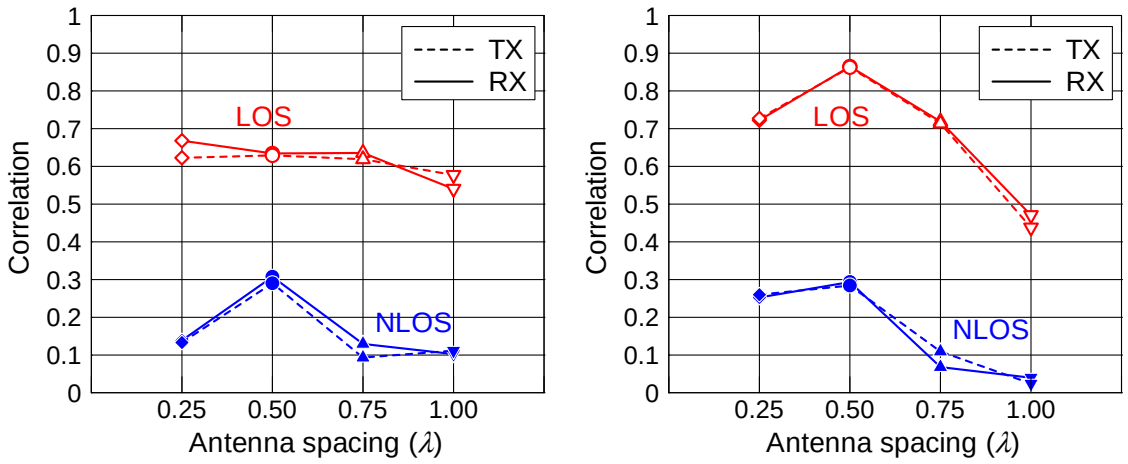

(a) TX-*x*/RX-*x* (b) TX-*y*/RX-*y*

Figure 4.3: Fading correlations $|\rho_{\mathrm{tx},ij}|$ and $|\rho_{\mathrm{rx},ij}|$ for the measured 2×2 MIMO channels.

4.1.2 Fading Correlations

To investigate the characteristics of the MIMO channels measured in the propagation environment, we examined fading correlations [50]. The TX fading correlation $\rho_{\mathrm{tx},ij}$ between the ith and jth TX antennas and the RX fading correlation $\rho_{\mathrm{rx},ij}$ between the ith and jth RX antennas are given by the following equations

$$\rho_{\mathrm{tx},ij} = \frac{\sum_{m=1}^{M}\sum_{f=1}^{N}\sum_{l=1}^{N_{\mathrm{rx}}} h_{li}^{*}(m,f)h_{lj}(m,f)}{\sqrt{\sum_{m=1}^{M}\sum_{f=1}^{N}\sum_{l=1}^{N_{\mathrm{rx}}} |h_{li}(m,f)|^2}\sqrt{\sum_{m=1}^{M}\sum_{f=1}^{N}\sum_{l=1}^{N_{\mathrm{rx}}} |h_{lj}(m,f)|^2}} \tag{4.1}$$

$$\rho_{\mathrm{rx},ij} = \frac{\sum_{m=1}^{M}\sum_{f=1}^{N}\sum_{k=1}^{N_{\mathrm{tx}}} h_{ik}^{*}(m,f)h_{jk}(m,f)}{\sqrt{\sum_{m=1}^{M}\sum_{f=1}^{N}\sum_{k=1}^{N_{\mathrm{tx}}} |h_{ik}(m,f)|^2}\sqrt{\sum_{m=1}^{M}\sum_{f=1}^{N}\sum_{k=1}^{N_{\mathrm{tx}}} |h_{jk}(m,f)|^2}}. \tag{4.2}$$

Here, l and k indicate the RX and TX antenna indices, respectively. m represents the index of measured spatial positions, and M is the total number of spatial positions ($M = 49$). Also, f represents the frequency point index, and N is the total number of frequency points ($N = 1{,}601$). The absolute values of the fading correlations are in the range from 0 to 1. In addition, the correlations $|\rho_{\mathrm{tx},ij}|$ and $|\rho_{\mathrm{rx},ij}|$ ($i \neq j$) have ${}_{N_{\mathrm{tx}}}\mathrm{C}_2$ and ${}_{N_{\mathrm{rx}}}\mathrm{C}_2$ different values, respectively, where an operator ${}_p\mathrm{C}_q$ denotes the total number of combinations of q-subsets possible out of a set of p distinct items. That is, ${}_p\mathrm{C}_q = p!/\{q!(p-q)!\}$ holds.

Using (4.2) and (4.1), the TX and RX fading correlations for the measured MIMO channels were obtained. Figures 4.3, 4.4, and 4.5 shows TX and RX fading correlations

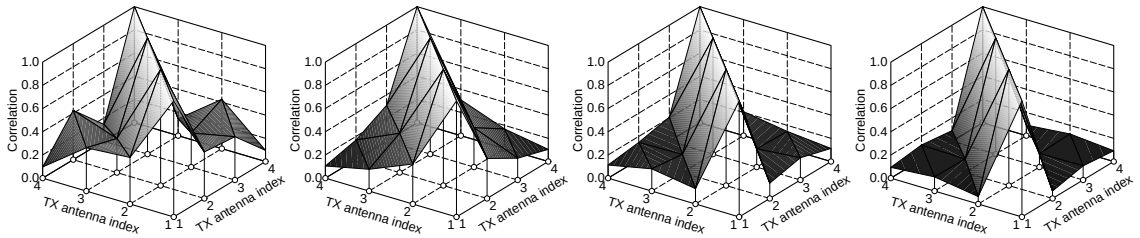

$\mathrm{AS} = 0.25\lambda$ $\mathrm{AS} = 0.50\lambda$ $\mathrm{AS} = 0.75\lambda$ $\mathrm{AS} = 1.00\lambda$

(a) TX-*x*/RX-*x*, $|\rho_{\mathrm{tx},ij}|$

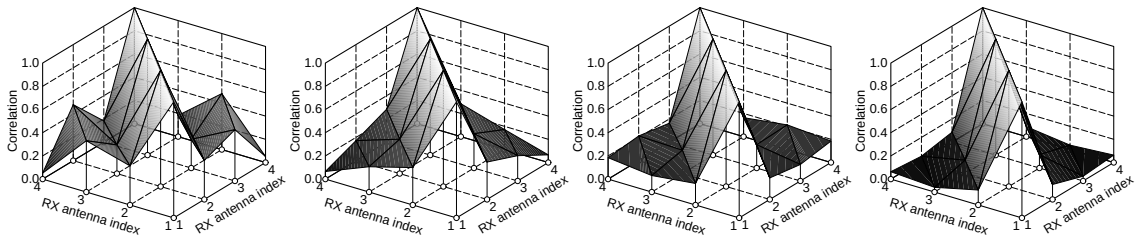

$\mathrm{AS} = 0.25\lambda$ $\mathrm{AS} = 0.50\lambda$ $\mathrm{AS} = 0.75\lambda$ $\mathrm{AS} = 1.00\lambda$

(b) TX-*x*/RX-*x*, $|\rho_{\mathrm{rx},ij}|$

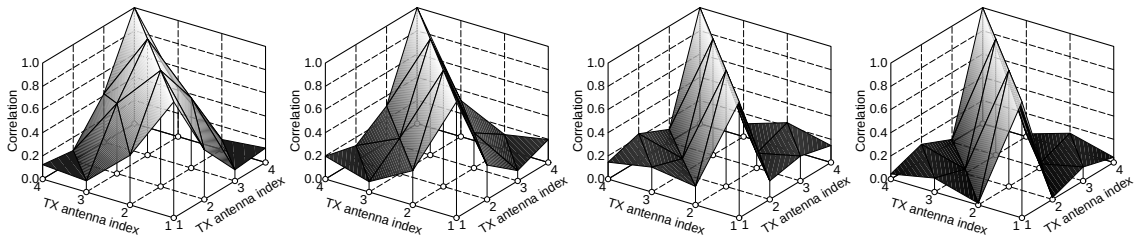

$\mathrm{AS} = 0.25\lambda$ $\mathrm{AS} = 0.50\lambda$ $\mathrm{AS} = 0.75\lambda$ $\mathrm{AS} = 1.00\lambda$

(c) TX-*y*/RX-*y*, $|\rho_{\mathrm{tx},ij}|$

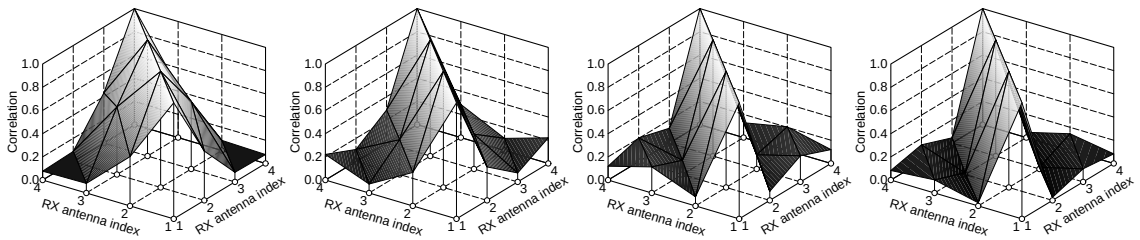

$\mathrm{AS} = 0.25\lambda$ $\mathrm{AS} = 0.50\lambda$ $\mathrm{AS} = 0.75\lambda$ $\mathrm{AS} = 1.00\lambda$

(d) TX-*y*/RX-*y*, $|\rho_{\mathrm{rx},ij}|$

Figure 4.4: Fading correlations $|\rho_{\mathrm{tx},ij}|$ and $|\rho_{\mathrm{rx},ij}|$ for the measured 4×4 MIMO NLOS channels.

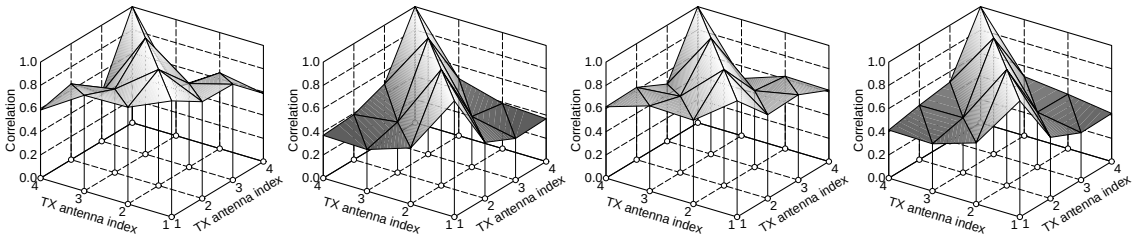

$\mathrm{AS} = 0.25\lambda$ $\mathrm{AS} = 0.50\lambda$ $\mathrm{AS} = 0.75\lambda$ $\mathrm{AS} = 1.00\lambda$

(a) TX-*x*/RX-*x*, $|\rho_{\mathrm{tx},ij}|$

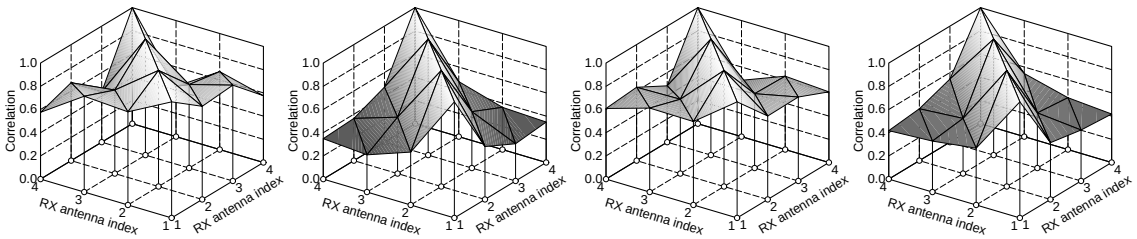

$\mathrm{AS} = 0.25\lambda$ $\mathrm{AS} = 0.50\lambda$ $\mathrm{AS} = 0.75\lambda$ $\mathrm{AS} = 1.00\lambda$

(b) TX-*x*/RX-*x*, $|\rho_{\mathrm{rx},ij}|$

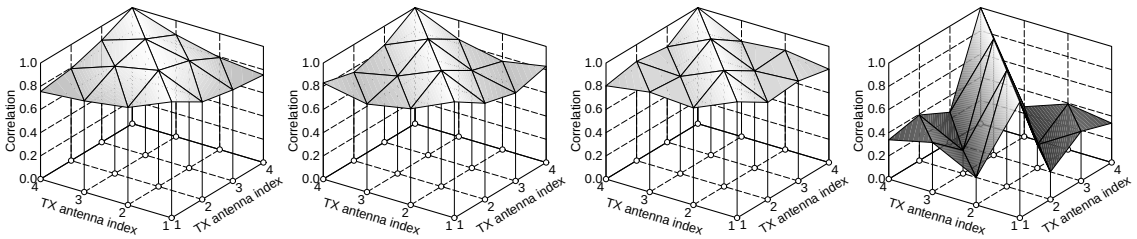

$\mathrm{AS} = 0.25\lambda$ $\mathrm{AS} = 0.50\lambda$ $\mathrm{AS} = 0.75\lambda$ $\mathrm{AS} = 1.00\lambda$

(c) TX-*y*/RX-*y*, $|\rho_{\mathrm{tx},ij}|$

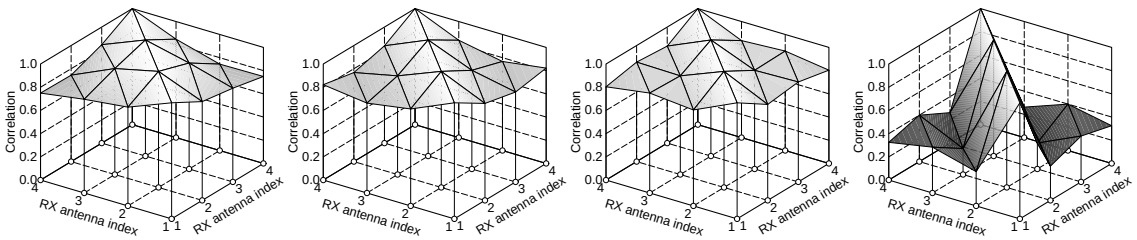

$\mathrm{AS} = 0.25\lambda$ $\mathrm{AS} = 0.50\lambda$ $\mathrm{AS} = 0.75\lambda$ $\mathrm{AS} = 1.00\lambda$

(d) TX-*y*/RX-*y*, $|\rho_{\mathrm{rx},ij}|$

Figure 4.5: Fading correlations $|\rho_{\mathrm{tx},ij}|$ and $|\rho_{\mathrm{rx},ij}|$ for the measured 4×4 MIMO LOS channels.

for the measured 2×2 MIMO, 4×4 MIMO NLOS, and 4×4 MIMO LOS channels, respectively. The correlations for 4×4 MIMO cases are drawn in the three-dimensional style as shown in Figs. 4.4 and 4.5 because the combination of four antennas gives ${}_4\mathrm{C}_2 = 6$ values. This plot is in the same style as in [50]. In addition, for both Figs. 4.4 and 4.5, figures (a) and (b) are for the TX-*x*/RX-*x* orientation, and (c) and (d) are for the TX-*y*/RX-*y* one. We can see that all of the MIMO cases have almost the same correlation values between the TX and RX ones. In the NLOS scenario, the fading correlations generally have low values, and they become lower as AS increases. Higher correlations in the LOS scenario are due to the LOS component that is a deterministic signal.

Focusing on the correlations in the LOS scenario, we find that the TX-*y*/RX-*y* orientation tends to provide higher correlations than the TX-*x*/RX-*x* one. We can consider two reasons for this. The direct wave and reflected waves from the walls behind the TX and behind the RX were conjectured to be dominant. These reflected rays along the x-axis lowered the correlation for the TX-*x*/RX-*x* orientation, but did not cause the decorrelation for the TX-*y*/RX-*y* case. We can analyze the other reason by considering the antenna patterns shown in Fig. 4.2. Narrow spacing seems to give high correlations for both of the orientations in the case of AS $= 0.25\lambda$. However, as mentioned in §4.1.1, the cases of AS $= 0.50\lambda$ and 0.75λ give higher gain in the 90° direction, which corresponds to the direct path. Consequently, the effect of the direct wave becomes stronger, so that we have higher correlations for the TX-*y*/RX-*y* orientation. The patterns for AS $= 1.00\lambda$ incidentally show a little dip in the antenna pattern in the 90° direction. This decreases the effect of the direct wave and causes lower correlation values in the TX-*y*/RX-*y* orientation.

4.1.3 CDFs of Channel Elements in MIMO Matrices

Many MIMO channel models assume that each element in a channel matrix obeys i.i.d. fading. However, actual MIMO systems can be strongly affected by propagation environments and mutual coupling between antennas. Actual channel elements, thereby, may have different statistical characteristics. As stated in the previous subsection, some LOS channels have very high correlations, and are never independent. Here, the author attempts to determine whether the indoor MIMO channels are identical or not. Using the measured 78,449 MIMO channels, CDFs of amplitudes of each channel element were examined as shown in Figs. 4.6–4.9. Data for the 2×2 MIMO cases are shown in Figs. 4.6 and 4.7, and those for the 4×4 MIMO cases are shown in Figs. 4.8 and 4.9. Also, those for the TX-*x*/RX-*x* orientation are shown in Figs. 4.6 and 4.8, and those for the TX-*y*/RX-*y* orientation are shown in Figs. 4.7 and 4.9. In addition, figures (a), (b), (c), and (d) show the CDFs for the cases of AS $= 0.25\lambda$, 0.50λ, 0.75λ, and 1.00λ, respectively. Each of the LOS/NLOS scenario in the graph has $2 \times 2 = 4$ CDF curves ($|h_{11}|$, $|h_{12}|$, $|h_{21}|$, and $|h_{22}|$) and $4 \times 4 = 16$ curves ($|h_{11}|$, $|h_{12}|$, ..., and $|h_{44}|$) for the 2×2 and 4×4 MIMO cases, respectively. The abscissa value is different from that in Fig. 3.13 owing to the normalization by (3.40). Also, for each case in the LOS scenario, the average Ricean factor K_{avg} estimated from all the $N_{\mathrm{tx}}N_{\mathrm{rx}}$ CDFs of channel elements is put on each graph. For the sake of simplicity, the following discussion is mainly for the 4×4 MIMO cases because that

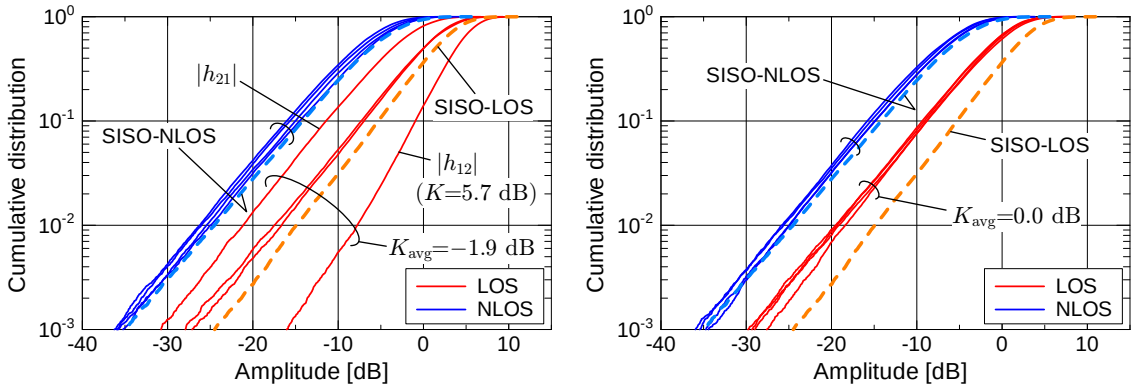

(a) AS = 0.25λ (b) AS = 0.50λ

(c) AS = 0.75λ (d) AS = 1.00λ

Figure 4.6: CDFs of amplitudes of the measured 2 × 2 MIMO channels (TX-*x*/RX-*x* orientation).

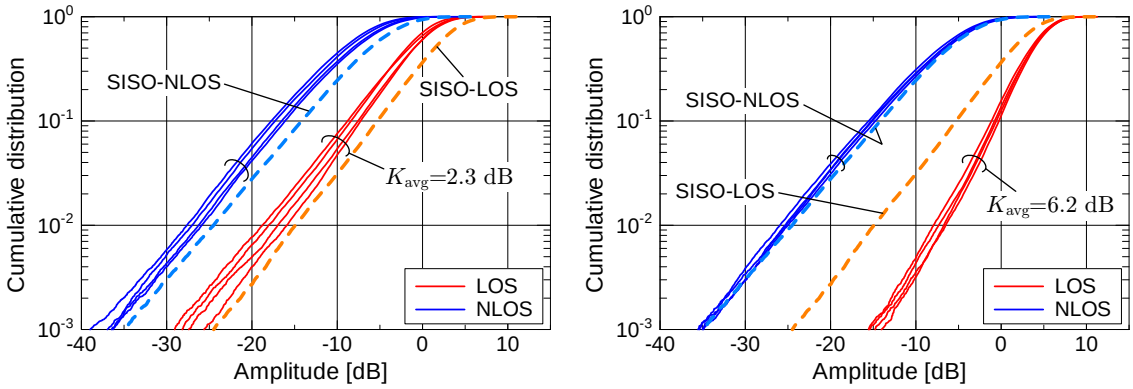

(a) AS $= 0.25\lambda$

(b) AS $= 0.50\lambda$

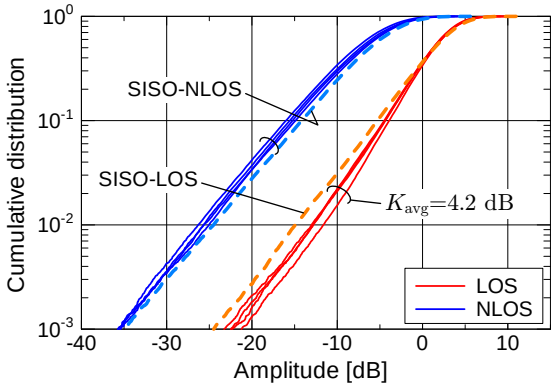

(c) AS $= 0.75\lambda$

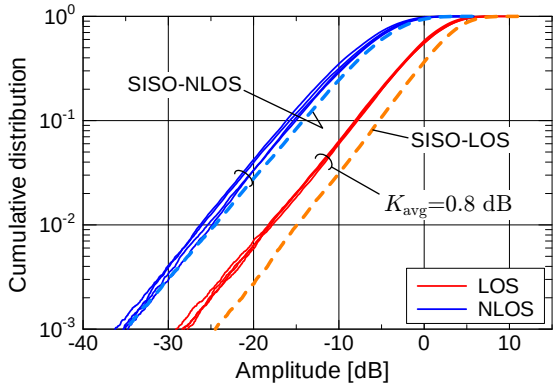

(d) AS $= 1.00\lambda$

Figure 4.7: CDFs of amplitudes of the measured 2×2 MIMO channels (TX-*y*/RX-*y* orientation).

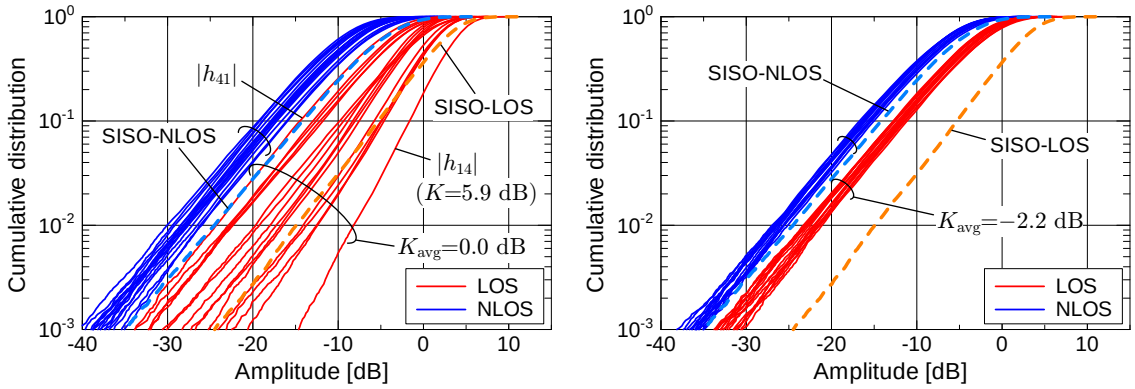

(a) AS $= 0.25\lambda$ (b) AS $= 0.50\lambda$

(c) AS $= 0.75\lambda$ (d) AS $= 1.00\lambda$

Figure 4.8: CDFs of amplitudes of the measured 4×4 MIMO channels (TX-*x*/RX-*x* orientation).

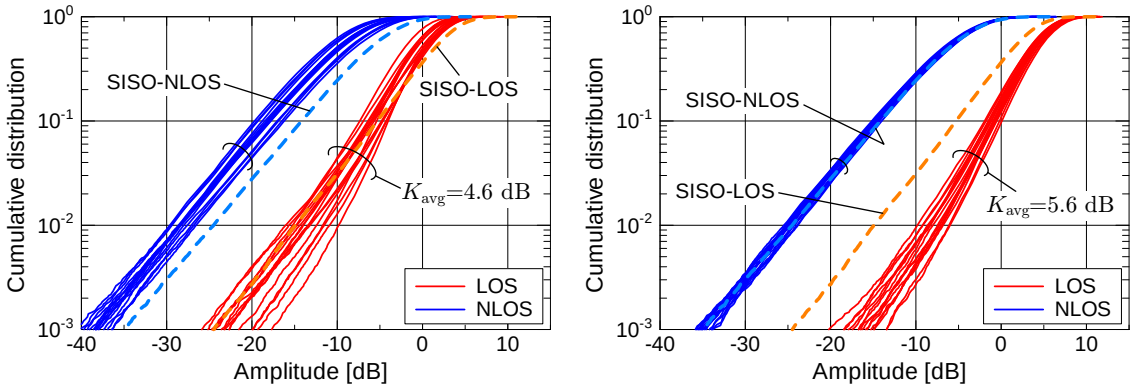

(a) AS $= 0.25\lambda$

(b) AS $= 0.50\lambda$

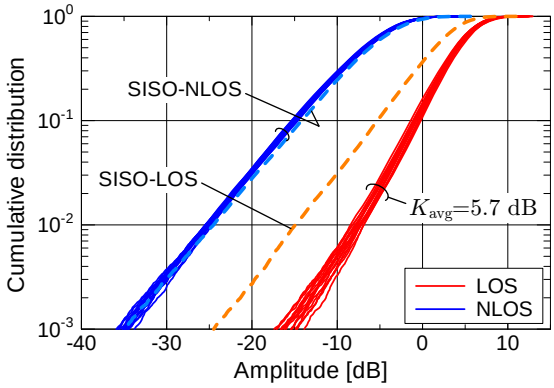

(c) AS $= 0.75\lambda$

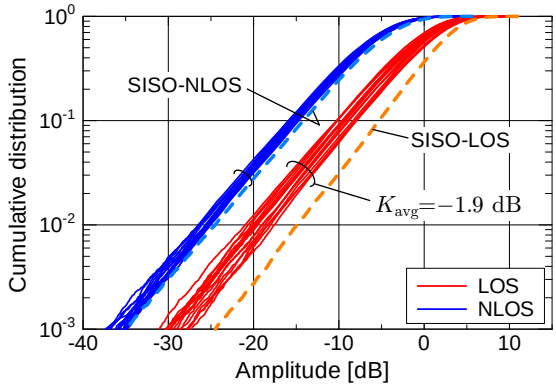

(d) AS $= 1.00\lambda$

Figure 4.9: CDFs of amplitudes of the measured 4×4 MIMO channels (TX-*y*/RX-*y* orientation).

for the 2×2 MIMO cases is similar.

First, as in Fig. 3.13, the MIMO channel elements in the LOS scenario generally have higher amplitudes than those in the NLOS one. Second, except for the narrowest spacing cases of AS $= 0.25\lambda$, distributions under the NLOS scenario are independent of the antenna spacing and array orientation, and differ less than about 2 dB. Looking at the region where the cumulative frequencies are less than the 10% level and the curves are almost straight lines, we can see that all the CDFs increase by almost an order of magnitude with an amplitude increment of 10 dB. Thus, the NLOS channels are Rayleigh fading channels. In the previous subsection, It was verified that almost all of the cases under the NLOS scenario give low fading correlations (Figs. 4.3, 4.4, and 4.5). Hence, It can be said that MIMO channels under the NLOS scenario with AS equal to or greater than 0.50λ obey almost i.i.d. Rayleigh fading. As for the cases of AS $= 0.25\lambda$, the difference at the 10% level is a maximum of approximately 3 dB. It may be caused by different antenna gain among antenna elements, especially significant gain loss in inner two elements #2 and #3, due to mutual coupling effects as shown in Fig. 4.2(a).

However, channels under the LOS scenario do not behave in this way. The amplitudes and gradients of the CDFs differ depending on the AS and array orientation. Since the LOS scenario has the direct wave, the antenna gain has a great influence on the channel distributions. This behavior can be explained by using the antenna patterns shown in Figs. 4.1 and 4.2. When the gain in the direct wave's direction is high, CDFs become located in a higher amplitude region and their gradients become steeper. That is, the fading is Ricean with a large K-factor. On the other hand, when the gain toward the direct wave is low, the amplitudes are distributed in a lower region. Consider the cases of AS $= 0.25\lambda$ and 0.75λ in the TX-*x*/RX-*x* orientation. From figures (a) and (c) in Figs. 4.6 and 4.8, we see that the channel distributions are significantly different. In these graphs, the CDF of $|h_{1N_{\rm tx}}|$ is in the highest amplitude region and has the steepest gradient (largest K-factor) among the MIMO channel elements. For example, in the case of 4×4 MIMO with AS $= 0.25\lambda$, while $K_{\rm avg}$ is 0.0 dB, the K-factor of $|h_{14}|$ is 5.9 dB. In the case of 4×4 MIMO with AS $= 0.75\lambda$, $K_{\rm avg}$ is 0.7 dB whereas the K-factor of $|h_{14}|$ is 3.8 dB. On the other hand, the CDF of $|h_{41}|$ is in the lowest region under the LOS scenario. Note that each antenna index corresponds to the one shown in Figs. 3.3 and 4.2. Here, let us consider these 4×4 MIMO cases with antenna patterns shown in Fig. 4.2. As for channel h_{14} in the TX-*x*/RX-*x* orientation, the direct wave departs from TX antenna #4 in the 0° direction and arrives at RX antenna #1 in the 180° direction. As seen from Fig. 4.2(a) and (c), antennas #1 and #4 have higher gain in the directions of 180° and 0°, respectively. Thus, the direct wave is strongly received through channel h_{14}. This is why the CDF of $|h_{14}|$ is in the highest region and has the steepest gradient for AS $= 0.25\lambda$ and 0.75λ. As for channel h_{41} in the TX-*x*/RX-*x* orientation, the direct wave departs from TX antenna #1 in the 0° direction and arrives at RX antenna #4 in the 180° direction. Antennas #1 and #4 have lower gain in the directions of 0° and 180°, respectively. The direct wave is weakly received through channel h_{41}. Thus, the CDF of $|h_{41}|$ is in the lowest region for AS $= 0.25\lambda$ and 0.75λ. The relationship between the LOS component and antenna gain indicates that these two

particular cases caused very different distributions among channel elements. That is, LOS gain variation among channel elements yields this phenomenon. Consequently, while it is well known that in LOS environments fading channels do not have independence due to the LOS component, the MIMO channel elements under the LOS scenario do not have the same statistical characteristics.

4.1.4 Eigenvalue Distribution

The number of positive eigenvalues of an $N_{\rm tx} \times N_{\rm tx}$ Hermitian matrix $\boldsymbol{H}^H\boldsymbol{H}$ corresponds to the number of available eigenchannels between the TX and RX ends, and the magnitude of the eigenvalue is proportional to the SNR of the corresponding channel. This means that data transfer rates can be increased with the number of large eigenvalues. The number and magnitude of positive eigenvalues therefore determine the transmission performance in E-SDM. On the other hand, the channel capacity in SDM is also given by eigenvalues as will be described in §4.2.1. It has also been reported that the average BER performance of SDM tends to be determined by the minimum eigenvalue $\lambda_{N_{\rm tx}}$ when demultiplexing the received signal by spatial filtering [77]. Eigenvalues are considered to have large influence on not only the performance of E-SDM but also that of SDM. This subsection therefore examines the CDFs of eigenvalues $\lambda_1, \ldots, \lambda_{N_{\rm tx}}$ in each MIMO cases.

The CDFs of the eigenvalues for the measured 2×2 and 4×4 MIMO channels are shown in Figs. 4.10 & 4.11 and Figs. 4.12 & 4.13, respectively. Figures (a) and (b) are for the TX-*x*/RX-*x* and TX-*y*/RX-*y* orientations, respectively. We can see from these figures that the eigenvalues in the LOS scenario are generally larger than those in the NLOS one. In particular, the maximum eigenvalues λ_1 in the LOS scenario become significantly large. Since the direct wave in the LOS scenario increases the channel power, its effect largely appears in λ_1.

Comparing the CDFs in each scenario, we can see that although the NLOS scenario gives similar distributions in all the cases, the CDFs in the LOS scenario, particularly those of the maximum eigenvalues λ_1, change depending on the array configuration. This can be explained by the relation between the direct wave and antenna patterns shown in Figs. 4.1 and 4.2, i.e., the LOS gain variation. The effect of LOS gain variation is especially evident in the magnitude of the maximum eigenvalue λ_1, as mentioned before. That is, when the antennas have higher gain in the LOS direction, λ_1 tends to be larger. In contrast, when the antennas have lower gain in the LOS direction, λ_1 tends to be lower. For example, looking at the case of the TX-*y*/RX-*y* array orientation in the LOS scenario, we can see that the arrays of AS $= 0.50\lambda$ and 0.75λ have large λ_1 for both of the 2×2 and 4×4 MIMO systems. In the cases of AS $= 0.25\lambda$ and 1.00λ, on the other hand, the CDFs of λ_1 are lower than those in the above two cases. As will be presented later, such variations of λ_1 in the LOS scenario appear to yield various MIMO performances, particularly E-SDM performances.

We can notice that the CDF of the minimum eigenvalue $\lambda_{N_{\rm tx}}$ is in a clearly lower magnitude region and is far apart from those of the other eigenvalues. Also, the gradients of the minimum eigenvalue CDFs show almost an order of magnitude increase with an eigenvalue

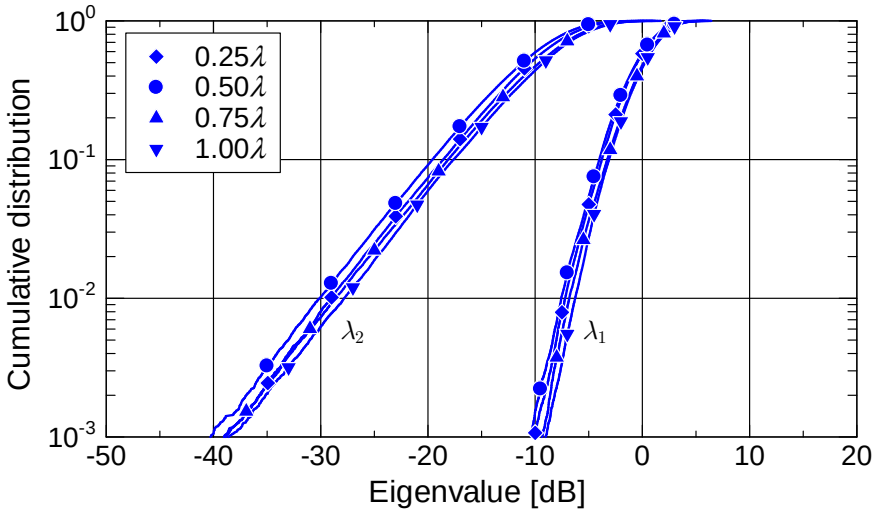

(a) TX-*x*/RX-*x*

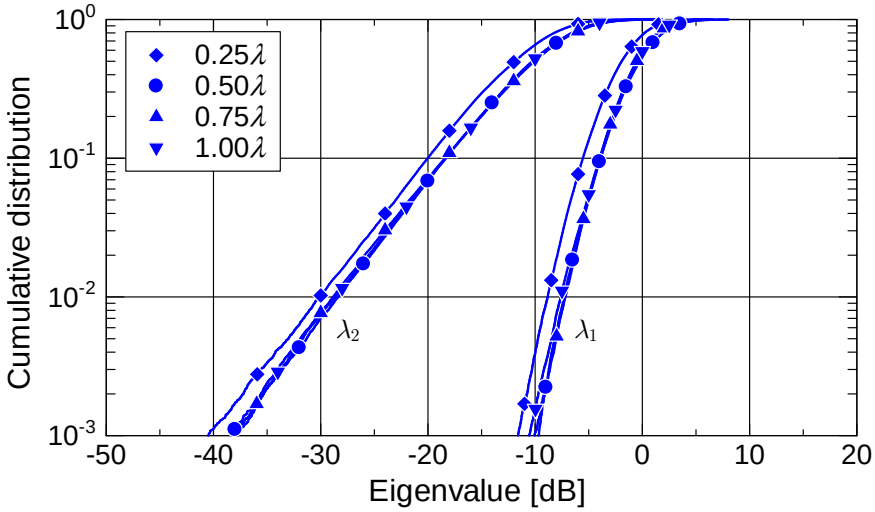

(b) TX-*y*/RX-*y*

Figure 4.10: CDFs of eigenvalues of $\boldsymbol{H}^H\boldsymbol{H}$ for the measured 2×2 MIMO NLOS channels.

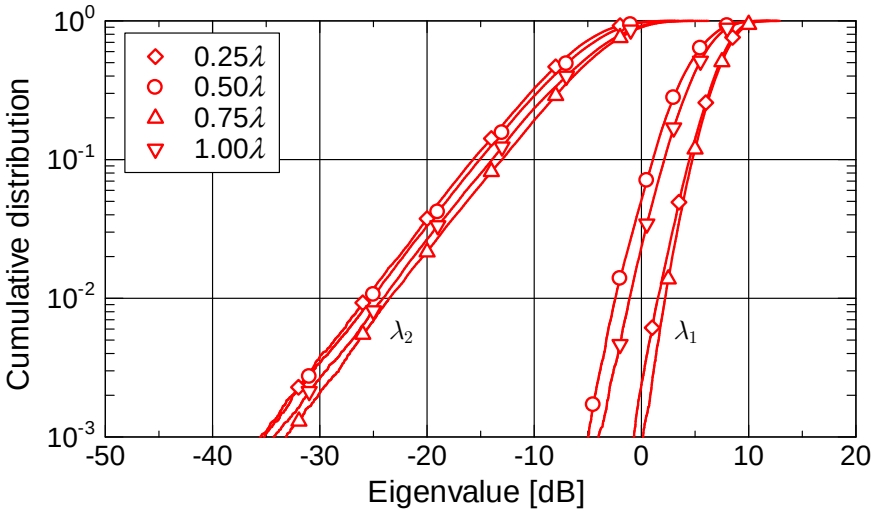

(a) TX-*x*/RX-*x*

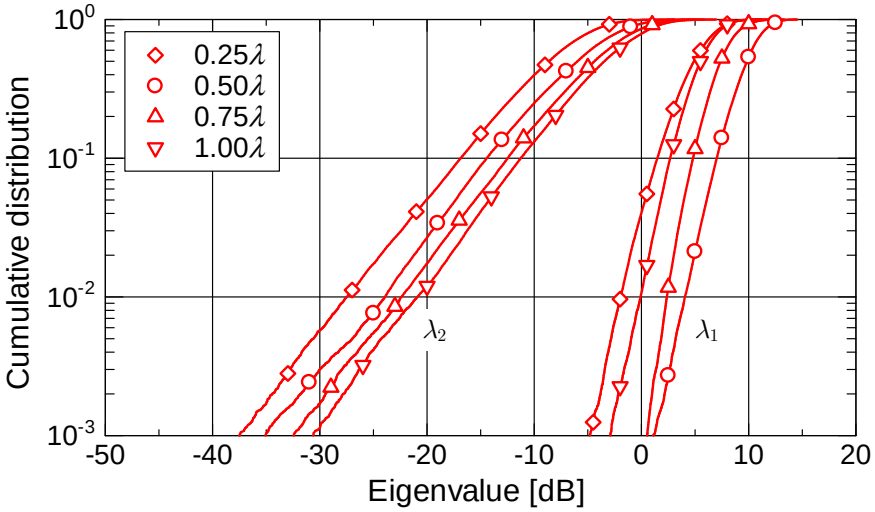

(b) TX-*y*/RX-*y*

Figure 4.11: CDFs of eigenvalues of $\boldsymbol{H}^H\boldsymbol{H}$ for the measured 2×2 MIMO LOS channels.

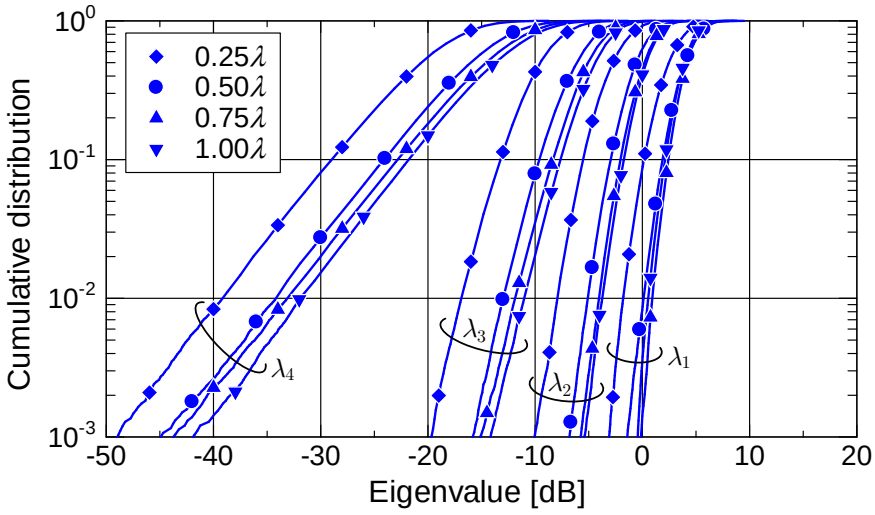

(a) TX-*x*/RX-*x*

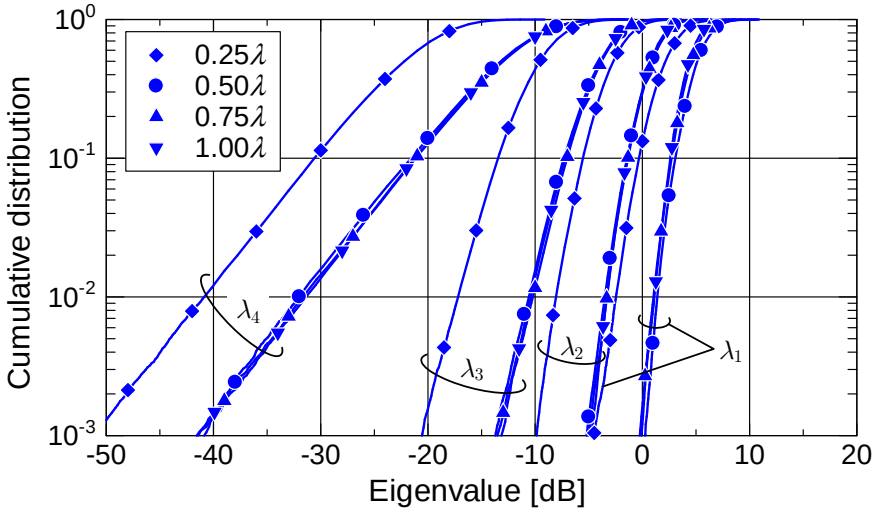

(b) TX-*y*/RX-*y*

Figure 4.12: CDFs of eigenvalues of $\boldsymbol{H}^H\boldsymbol{H}$ for the measured 4×4 MIMO NLOS channels.

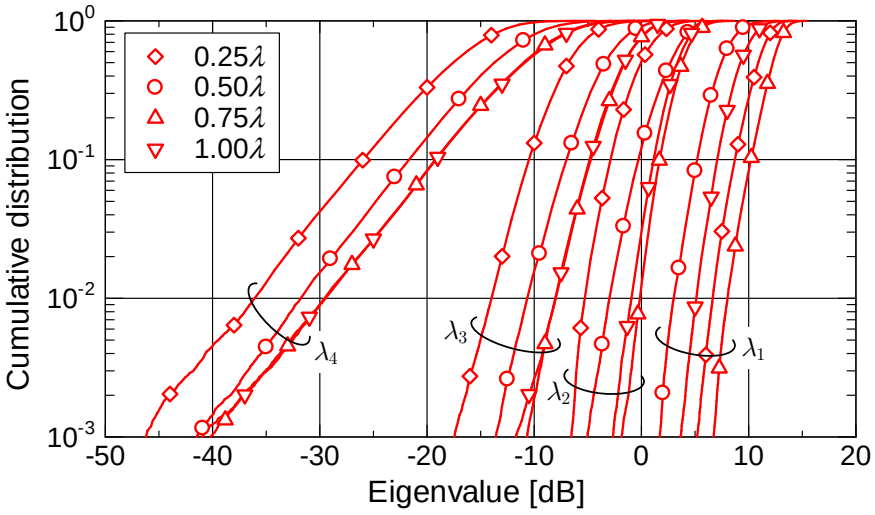

(a) TX-*x*/RX-*x*

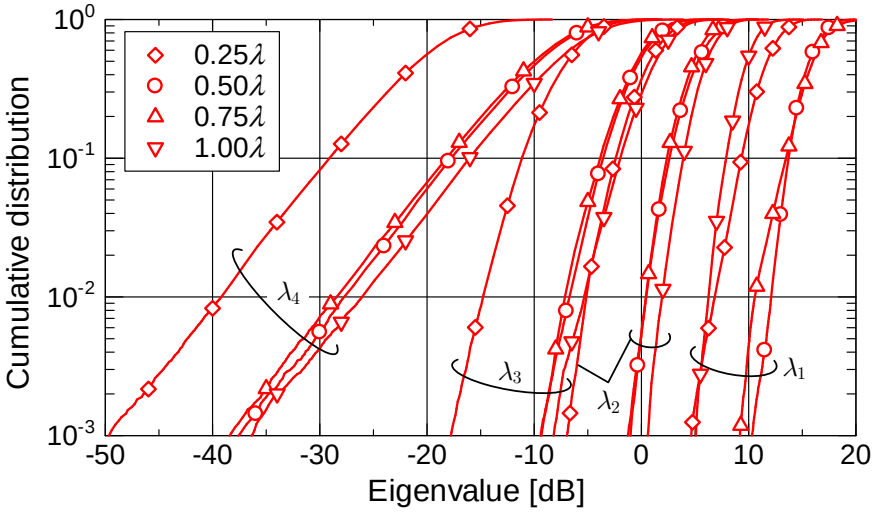

(b) TX-*y*/RX-*y*

Figure 4.13: CDFs of eigenvalues of $\boldsymbol{H}^H\boldsymbol{H}$ for the measured 4×4 MIMO LOS channels.

increment of 10 dB. In other words, an eigenchannel with the minimum eigenvalue does not have spatial diversity effect whereas the other eigenchannels have. It was confirmed that the same phenomena are observed for the i.i.d. Gaussian MIMO channels generated in computer simulations. This appears to cause a difference in substream utilization in E-SDM between channel capacity and BER as will be discussed in §4.3.2.

In addition, the CDFs of the eigenvalues for the AS $= 0.25\lambda$ case tend to be in lower regions compared with the other cases. In particular, the minimum eigenvalues stay in the lower regions independently of the environmental scenarios. As will be shown later, this phenomenon causes degradation of MIMO performance.

4.2 Performance of Narrowband SDM

4.2.1 SDM Channel Capacity

The channel capacity has been extensively used for evaluating the MIMO channel [25, 26, 34, 35, 39–48, 50, 78]. This is the limit of digital communications that could only be achieved if we employed an ideal communication method (coding and modulation). As for the measured MIMO channel, the following equation gives the channel capacity of SDM when channel state information is available only at the RX side.

$$C_{\mathrm{SDM}} = \log_2 \left\{ \det \left(\boldsymbol{I} + \frac{1}{N_{\mathrm{tx}}} \frac{P_{\mathrm{total}}}{P_{\mathrm{AEC}}} \boldsymbol{H}^H \boldsymbol{H} \right) \right\} \tag{4.3}$$

$$= \sum_{i=1}^{N_{\mathrm{tx}}} \log_2 \left(1 + \frac{1}{N_{\mathrm{tx}}} \frac{P_{\mathrm{total}}}{P_{\mathrm{AEC}}} \lambda_i \right) \tag{4.4}$$

Here, $\det(\cdot)$ denotes a determinant and P_{total} indicates total TX power. $\lambda_1, \ldots, \lambda_{N_{\mathrm{tx}}}$ are eigenvalues obtained by eigenvalue decomposition of $\boldsymbol{H}^H \boldsymbol{H}$. P_{AEC} is TX power when the previously mentioned SISO measurement in the AEC gives an average received E_s/N_0 of 0 dB. Note that $P_{\mathrm{total}}/P_{\mathrm{AEC}}$ in the above equation represents the normalized total TX power, which is used to evaluate the channel capacities and BERs through §4.2 and §4.3. Therefore, we can compare performances under the same total TX power condition. Using the above equation, this subsection examines CDFs of the 2×2 and 4×4 MIMO channel capacities for a normalized total TX power of 20 dB.

The results shown in Figs. 4.14 and 4.15 are SDM capacities for the 2×2 and 4×4 MIMO systems, respectively. Also, graphs (a) and (b) in both figures are those for TX-*x*/RX-*x* and TX-*y*/RX-*y* orientations, respectively. All of the capacities in the LOS scenario are higher than those in the NLOS scenario for both array orientations. The LOS component in the LOS scenario enlarges the received power. Under a constant total TX power condition, the higher received power due to the LOS component improves the capacity. It is clear from (4.4) that the channel capacity is given by the eigenvalues of the MIMO channel. We can also say that the LOS component enlarges the maximum eigenvalue which significantly increases the channel capacity. Moreover, we can say that the LOS component enlarges the maximum eigenvalue and this larger eigenvalue causes such a high capacity as

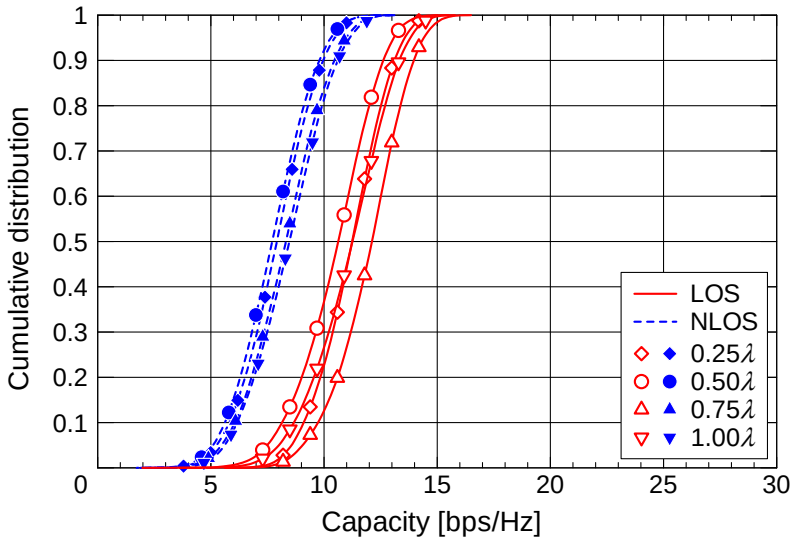

(a) TX-*x*/RX-*x*

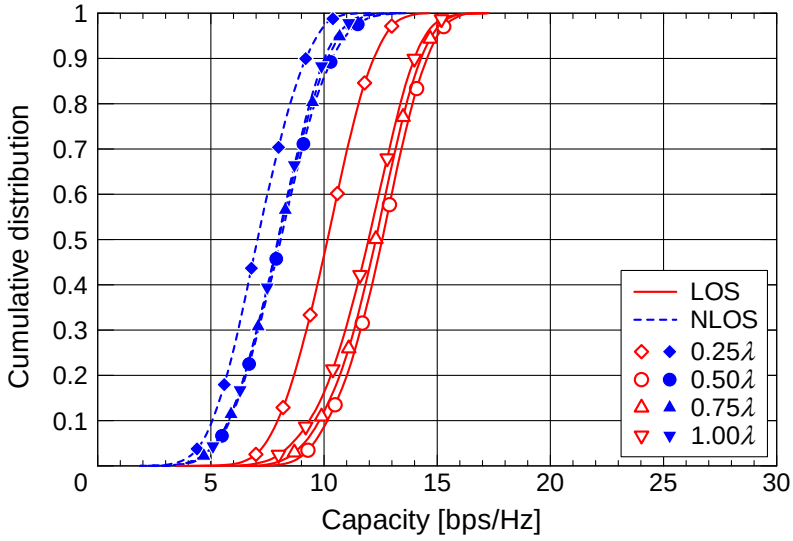

(b) TX-*y*/RX-*y*

Figure 4.14: CDFs of the measured 2 × 2 MIMO channel capacities for normalized total TX power of 20 dB.

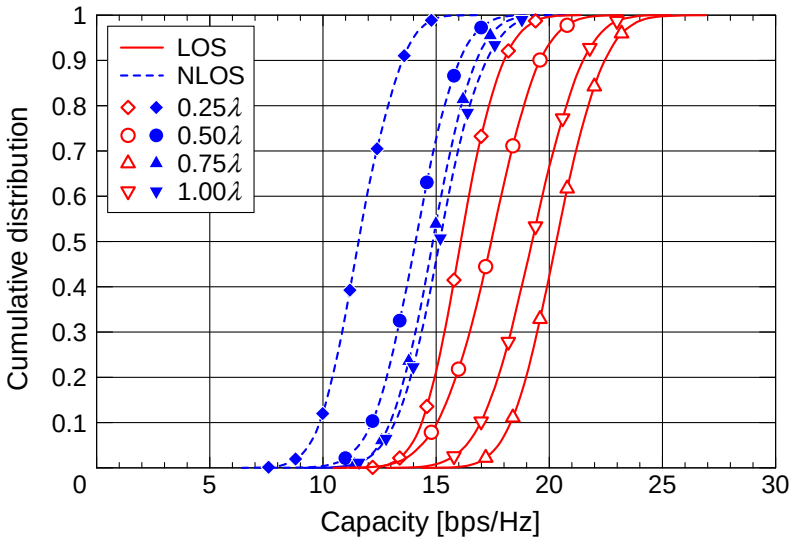

(a) TX-*x*/RX-*x*

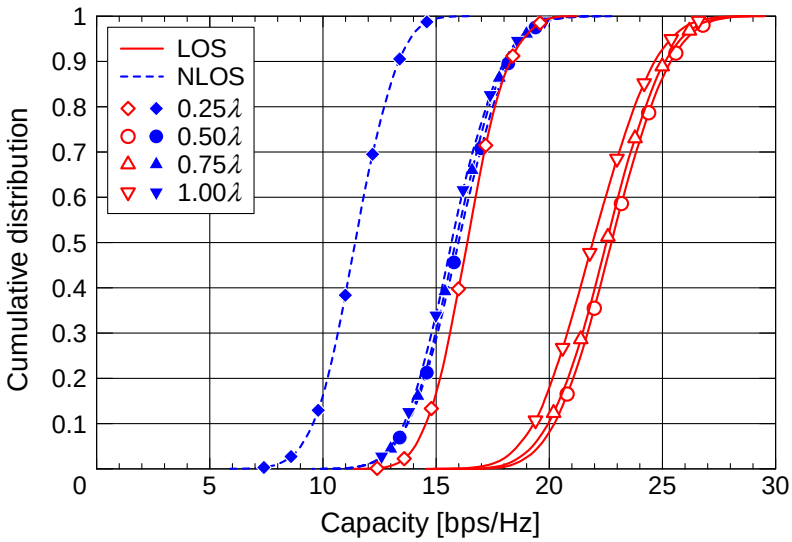

(b) TX-*y*/RX-*y*

Figure 4.15: CDFs of the measured 4 × 4 MIMO channel capacities for normalized total TX power of 20 dB.

seen in Figs. 4.10–4.13. On the other hand, the performance of AS $= 0.25\lambda$ deteriorates in both LOS and NLOS scenarios. This phenomenon can be analyzed by using the antenna patterns shown in Fig. 4.2. As described in §4.1.1, the patterns in the case of AS $= 0.25\lambda$ show significant reduction in gain. We consider that this low antenna gain causes the decline in channel capacity. Except for the case of AS $= 0.25\lambda$, we see that in the LOS scenario the TX-*y*/RX-*y* array orientation tends to give larger capacities than the TX-*x*/RX-*x* one. We illustrate this reason by using the antenna patterns shown in Figs. 4.1 and 4.2. As mentioned in §4.1.1 and §4.1.3, the antennas have higher gain than the single antenna in the 90° direction especially in the cases of AS $= 0.50\lambda$ and 0.75λ. The direct signal is considered to be strongly received in the TX-*y*/RX-*y* orientation. This increases capacity. The reason that AS $= 1.00\lambda$ gives a large capacity is conjectured to be lower fading correlations (Figs. 4.3 and 4.5). Moreover, in the LOS scenario, the CDFs of the channel capacities strongly depend on the array configuration (antenna spacing and orientation).

There is an idea that an LOS channel can be modeled approximately as

$$\boldsymbol{H} = \boldsymbol{H}_{\text{i.i.d.}} + \boldsymbol{H}_{\text{LOS}}, \tag{4.5}$$

where $\boldsymbol{H}_{\text{i.i.d.}}$ is an $N_{\text{rx}} \times N_{\text{tx}}$ i.i.d. Rayleigh channel component matrix and $\boldsymbol{H}_{\text{LOS}}$ is an $N_{\text{rx}} \times N_{\text{tx}}$ LOS component matrix [10]. Note that amplitudes of channel components are included in elements in these matrices. $\boldsymbol{H}_{\text{i.i.d.}}$ is a scattered ray component matrix in a multipath-rich environment with large antenna spacing. In this case, addition of $\boldsymbol{H}_{\text{LOS}}$ to the scattered ray components leads to the large maximum eigenvalue and enhances the channel capacity. However, as stated in Chapter 3, the scattered wave power in the LOS scenario was 2.87 dB higher than that in the NLOS scenario due to the short-delay paths caused by the direct wave. The direct LOS ray and enhanced scattered ray components further increase the channel capacity in the LOS environment. Also, when the received signal is linearly demultiplexed by a spatial filter, e.g., zero-forcing, the BER performance becomes better as the minimum eigenvalue becomes larger (see the next subsection). It is not sure that the above model makes the minimum eigenvalue large, and it is difficult to arrive at the conclusion that SDM in an LOS environment gives better BER performance. Therefore, the author examined the behavior of SDM in the LOS environment based on not channel models but measurement campaigns.

If we employ the LOS channel model given by (4.5), it is necessary to introduce the spherical-wave model [78] into $\boldsymbol{H}_{\text{LOS}}$ in order to consider the variation of the LOS component phase because the distance between the TX and RX ends was relatively short. Here, let us consider a free space, i.e., $K = \infty$. In the case of AS $= 1.00\lambda$ in the TX-*y*/RX-*y* array orientation, the fading correlation $|\rho_{14}|$ between antenna elements #1 and #4, which have the widest spacing of 3λ, is 0.95. Under the SNR of 20 dB, the channel capacity in this case becomes 30% higher than that in the case of $\text{rank}\,(\boldsymbol{H}) = 1$ (TX-*x*/RX-*x* case in a free space). However, if an environment based on the channel model (4.5) has $K = 1.66$ dB, which is the estimated Ricean factor in the measurement site (see §3.4), the correlation $|\rho_{14}|$ in the case of AS $= 1.00\lambda$ for the TX-*y*/RX-*y* array orientation is 0.56. Even for the TX-*x*/RX-*x* array orientation, the correlations for any antenna pairs are 0.59. It was confirmed

Table 4.1: Simulation parameters of MIMO SDM.

Array orientation	TX-*x*/RX-*x*, TX-*y*/RX-*y*
Total channel data	$7 \times 7 \times 1{,}601 = 78{,}449$
Modulation	QPSK
Bit rate	$2N_{\mathrm{tx}}$ bits/SDM-symbol
Burst length	128 symbols (no coding)
Thermal noise	White Gaussian noise
RX processing	ZF spatial filtering

that any array configurations give almost the same channel capacity and BER performance in the environment of $K = 1.66$ dB. Consequently, we can say that the variation of the LOS component phase makes little impact on fading correlations and the performance of SDM in propagation environments where the scattered wave power is comparable to the direct wave power. As mentioned previously, the variation of the antenna gain due to mutual coupling changes the LOS component level, i.e., LOS gain variation, and this affects the performance in the LOS scenario.

4.2.2 BER Performance of SDM with ZF Spatial Filtering

In the previous subsection, we evaluated the performance of MIMO SDM using the channel capacity. As mentioned previously, the channel capacity obtained by (4.3) or (4.4) is the limit of the SDM transmission. From the implementational viewpoint, we consider that evaluating the BER performance will be more practical. Thus, the author conducted computer simulations of SDM by using measured channel data and examined average BER performance under a constant bit rate requirement.

Table 4.1 lists the simulation parameters. As stated before, 78,449 channel data had been obtained for each MIMO configuration, and all BERs for these channel data were averaged. It is assumed that an independent QPSK-modulated uncoded substream was transmitted from each TX antenna with equal power. Therefore, $2N_{\mathrm{tx}}$ bits/symbol were constantly transmitted. A spatial filter based on a ZF scheme was employed to detect the substreams at the RX side [19]. As stated in §2.4.1, this scheme suppresses inter-substream interference completely by using the weight matrix $\boldsymbol{W}_{\mathrm{zf}}$ given by (2.17). An N_{tx}-dimensional ZF output vector $\hat{\boldsymbol{s}}(t)$ is obtained when the RX signal vector $\boldsymbol{r}(t)$ is multiplied by $\boldsymbol{W}_{\mathrm{zf}}$ as follows

$$\begin{aligned} \hat{\boldsymbol{s}}(t) &= \boldsymbol{W}_{\mathrm{zf}}\, \boldsymbol{r}(t) && (4.6)\\ &= \boldsymbol{W}_{\mathrm{zf}}\, \boldsymbol{H}\boldsymbol{s}(t) + \boldsymbol{W}_{\mathrm{zf}}\, \boldsymbol{n}(t) && (4.7)\\ &= \boldsymbol{s}(t) + \boldsymbol{W}_{\mathrm{zf}}\, \boldsymbol{n}(t). && (4.8) \end{aligned}$$

An SIC such as BLAST [19,25] was not applied. Results obtained by this processing show

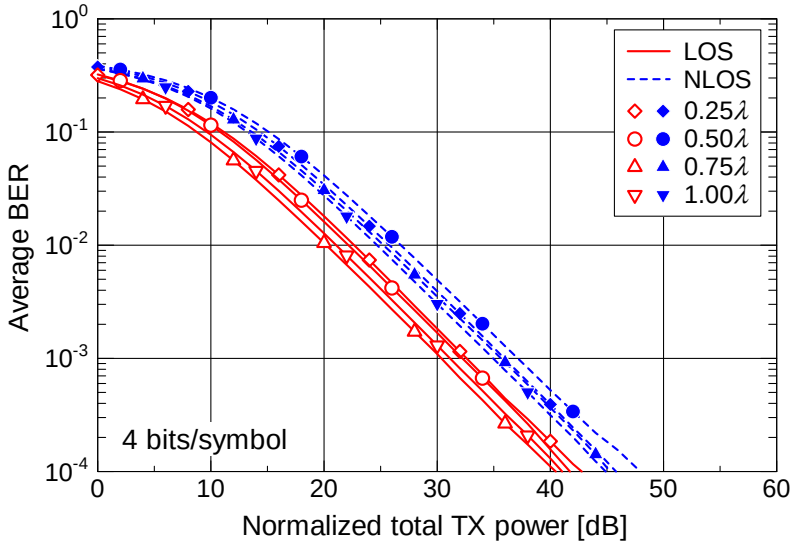

(a) TX-*x*/RX-*x*

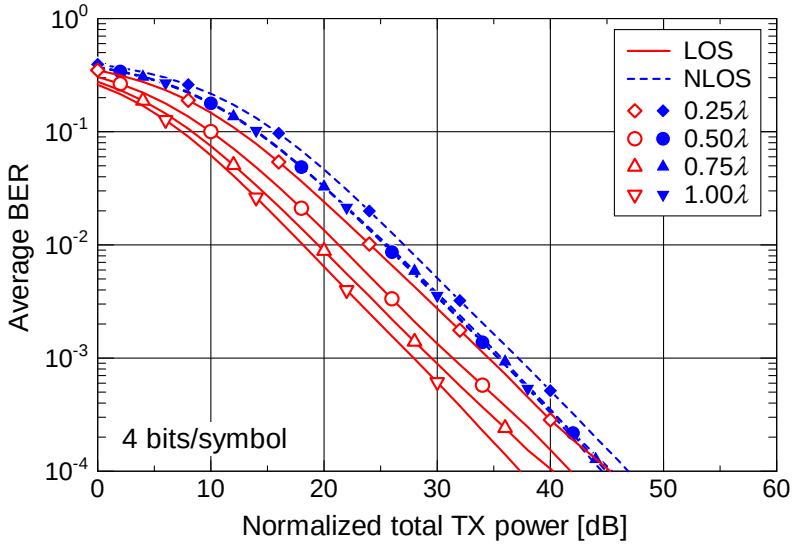

(b) TX-*y*/RX-*y*

Figure 4.16: Average BER performance of ZF processing for the measured 2×2 MIMO channels (uncoded 4 bits/SDM-symbol).

the performance of the simplest MIMO system without any error-correcting codes. This simulation also assumed that the receiver had perfect CSI.

Figures 4.16 and 4.17 show the average BER performances of 2×2 and 4×4 MIMO SDM, respectively. In these figures, graphs (a) and (b) are graphs for the TX-*x*/RX-*x* and TX-*y*/RX-*y* orientations, respectively. The bit rates are 4 bits/symbol and 8 bits/symbol for 2×2 and 4×4 MIMO cases, respectively. The abscissa is normalized total TX power. We

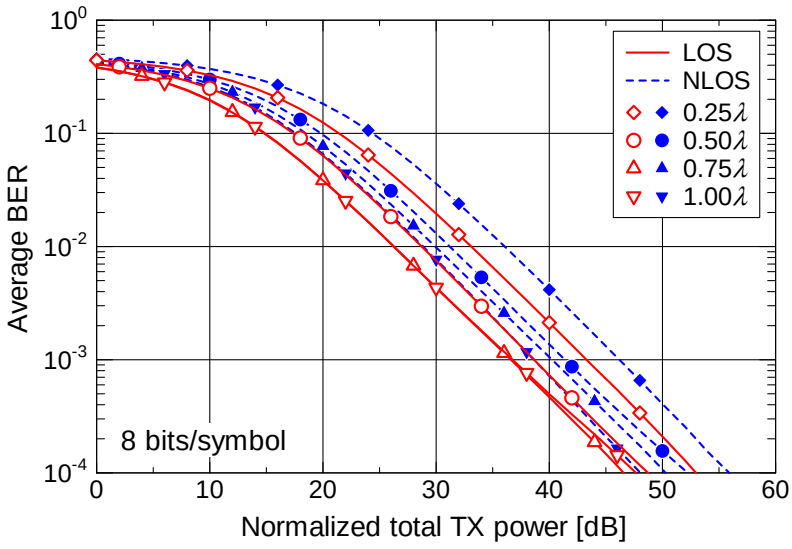

(a) TX-*x*/RX-*x*

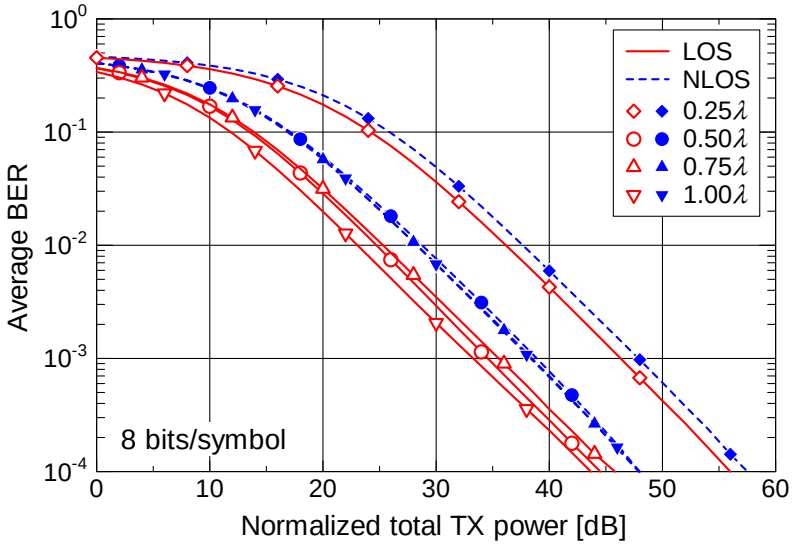

(b) TX-*y*/RX-*y*

Figure 4.17: Average BER performance of ZF processing for the measured 4×4 MIMO channels (uncoded 8 bits/SDM-symbol).

confirmed that the LOS scenario gave higher correlations than the NLOS one (Figs. 4.3–4.5). However, Figs. 4.16 and 4.17 clearly show that the BER performance for the LOS scenario is better than that for the NLOS one. As mentioned in §4.2.1, the higher received power level given by the LOS component improves the BER performance.

The channel capacities shown in Figs. 4.14 and 4.15 indicate that all the CDFs under the LOS scenario are better than those under the NLOS one regardless of the array orientation. In contrast, not all of the BERs under the LOS scenario show better performance than those under the NLOS one because the cases of AS $= 0.25\lambda$ seriously deteriorate in both scenarios. When considering the 4×4 MIMO case, as stated in §4.1.3, the gain decrease of the inner two antenna elements #2 and #3 is especially noticeable in the patterns of the AS $= 0.25\lambda$ case shown in Fig. 4.2(a). When we used this antenna array as the TX, more bit errors occurred on the substreams from TX antennas #2 and #3. Average BER was strongly affected by such deteriorated substreams.

The channel distributions shown in Figs. 4.6–4.9 indicate that the NLOS scenario generally gives the linear parts of CDFs an increase of one order of magnitude with an amplitude increment of 10 dB, and also that the LOS case has steeper curves owing to the direct wave. However, all the BER curves including those for the LOS scenario show almost Rayleigh fading with first-order diversity in the high power region. That is, the BER is reduced by an order of magnitude when the TX power increases by 10 dB. This behavior will be explained by using the minimum eigenvalue distributions shown in Figs. 4.10–4.13. That is, when employing a ZF spatial filtering at the receiver, its uncoded BER performance is dependent on the gradient of its minimum eigenvalue distribution, i.e., one order of magnitude with a TX power (or SNR) increment of 10 dB.

Although significant degradation occurs in the case of AS $= 0.25\lambda$ for both array orientations, under the LOS scenario the antenna spacing and array orientation affect performance more than in the NLOS case. This is almost the same as the CDFs of capacities stated in §4.2.1.

4.2.3 Conclusions

We have evaluated channel capacities and average BERs of 2×2 and 4×4 MIMO SDM by using measured MIMO channel data in an indoor multipath environment for the 5.2 GHz frequency band. The LOS and NLOS scenarios for various MIMO configurations were analyzed in terms of the antenna patterns, fading correlations, CDFs of channel elements, and CDFs of eigenvalues.

It is well known that an LOS environment does not produce independent fading because an LOS component causes high fading correlation. From the measurement results, we confirmed this fact and also found that the LOS scenario is not an identically distributed fading environment when each channel element is observed by antennas including mutual coupling effects. However, MIMO SDM in the LOS environment provides higher capacities and lower BERs than in the NLOS environment under the same TX power condition. Hence, the utility of MIMO SDM in an LOS environment has been proved. Meanwhile, the antenna gain in an array with narrow antenna spacing deteriorates because of mutual

coupling effects. The decrease in gain will cause performance degradations in MIMO systems with numerous antennas. Under the LOS scenario, the performance of MIMO SDM strongly depends on the MIMO configuration.

4.3 Performance of Narrowband E-SDM

Note that hereinafter the author does not present results in the case of AS $= 0.25\lambda$, which has specific characteristics such as a remarkable antenna gain loss as shown before, because the author would like to discuss E-SDM performances in practical conditions.

4.3.1 E-SDM Channel Capacity

The channel capacity has been used extensively for evaluating the MIMO channels and is the maximum amount of information that could be transferred if we used an ideal communication method (coding and modulation). When the MIMO CSI is known only at the RX side, the SDM channel capacity C_{SDM} of the measured MIMO channel is given by (4.3) or (4.4).

On the other hand, when the MIMO CSI is available at both the transmitter and receiver, we can employ E-SDM transmission that uses orthogonal eigenchannels. In this case, optimizing power allocation to each channel yields the maximum channel capacity in the MIMO channel. The ideal capacity is given by

$$C_{\text{E-SDM}} = \sum_{k=1}^{K} \log_2 \left(1 + \frac{P_{\text{total}}}{P_{\text{AEC}}} p_k \lambda_k\right). \tag{4.9}$$

Here the power coefficient p_k ($k = 1, \ldots, K$) allocated to the kth eigenchannel is optimally determined on the basis of the water-filling (WF) theorem [8, 71] represented as

$$p_k = \max\left(\eta - \frac{P_{\text{AEC}}}{P_{\text{total}}} \frac{1}{\lambda_k}, 0\right), \tag{4.10}$$

where η is a constant determined to satisfy the constraint of $\sum_{k=1}^{K} p_k = 1$. This equation means that more power is allocated to a channel that has a larger eigenvalue ($p_1 \geq \cdots \geq p_K \geq 0$). Equations (4.4) and (4.9) are used in this subsection to calculate the CDFs of the capacities C_{SDM} and $C_{\text{E-SDM}}$ of MIMO channels when the normalized total TX power is 20 dB.

The CDFs of the capacities of the measured 2×2 and 4×4 MIMO channels are shown in Figs. 4.18 and 4.19, respectively. In each figure, data for the orientations TX-*x*/RX-*x* and TX-*y*/RX-*y* are shown in parts (a) and (b). All the C_{SDM} and $C_{\text{E-SDM}}$ in the LOS scenario are higher than in the NLOS scenario. It is clear from (4.4) and (4.9) that channel capacities C_{SDM} and $C_{\text{E-SDM}}$ are given by the eigenvalues, and by comparing the capacity distributions shown in Figs. 4.18 and 4.19 with the eigenvalue distributions shown in Figs. 4.10–4.13 we

can see that the CDFs of capacities and eigenvalues display similar behavior. In short, it is clear that a MIMO case giving larger eigenvalues has a greater capacity than one giving smaller eigenvalues. Also, like the CDFs of eigenvalues, the CDFs of channel capacities in the LOS scenario appear to depend on the LOS gain variation.

Comparing $C_{\text{E-SDM}}$ with C_{SDM}, we can see that in both the LOS and NLOS scenarios the $C_{\text{E-SDM}}$ is a little higher in the low cumulative frequency region. These improvements in the channel capacities is thought to be due to the optimum power coefficients that the WF theorem allocates to eigenchannels. Moreover, the improvement in the 4×4 MIMO system is greater than that in the 2×2 MIMO system. Investigating the improvement of $C_{\text{E-SDM}}$ from C_{SDM} at the 1% level, however, we cannot say that the effects of the WF theorem are clear for any of the MIMO cases. The range of improvement is about 0.3–0.4 bps/Hz in the 2×2 MIMO system and about 0.5–0.7 bps/Hz in the 4×4 MIMO system, respectively. Therefore, the aforementioned dependence of channel capacities on the LOS gain variation is almost the same in C_{SDM} and $C_{\text{E-SDM}}$.

The percentages of used substreams (eigenchannels) in $C_{\text{E-SDM}}$ at the normalized total TX power of 20 dB are shown in Fig. 4.20 for the measured 4×4 MIMO channels. Each pie chart presents the proportion of substreams to which the WF theorem given by (4.10) allocates positive power coefficients ($p_m > 0$). That is, it shows the relative usages of various numbers of the available eigenchannels. We can see that none of the MIMO systems utilize a single substream or two substreams, and that the 4×4 MIMO systems utilize three- or four-substream parallel transmission. The proportion of four-substream transmission is the largest and is greater in the LOS scenario than in the NLOS scenario. As demonstrated by the eigenvalue CDFs shown in Figs. 4.12 and 4.13, not only the maximum eigenvalues λ_1 but also λ_2, λ_3, and λ_4 tend to be larger in the LOS scenario. Hence the probability that the WF theorem distributes the TX power even to the substream corresponding to the minimum eigenvalue λ_4 is higher in the LOS scenario. In other words, the control by the WF theorem works in such a way that it utilizes more substreams. The results shown in (4.4) and (4.9) indicate that C_{SDM} and $C_{\text{E-SDM}}$ are similar when all four of the substreams are utilized. The measured data confirms that four-substream transmission increases the E-SDM channel capacity by 0–0.5 bps/Hz and that three-substream transmission increases it by 0.4–1.3 bps/Hz compared to the SDM channel capacity. Since the four-substream transmission that uses all of the eigenvalues from λ_1 to λ_4 is mainly used in the LOS scenario, the performance of SDM and E-SDM tends to be similar. Although the pie charts for the 2×2 MIMO system are not shown, the proportions of used substreams in $C_{\text{E-SDM}}$ indicate that in that system the two-substream transmission accounts for over 95% in the LOS scenario and over 90% of all transmission in the NLOS scenario.

4.3.2 BER Performance of E-SDM

In the previous subsection, we evaluated the performance of E-SDM by using the channel capacity and compared it with the performance of the conventional SDM. The channel capacity given by (4.9) is a continuous quantity, and the number of used eigenchannels and their power allocation can be optimally determined by the WF theorem. The amount

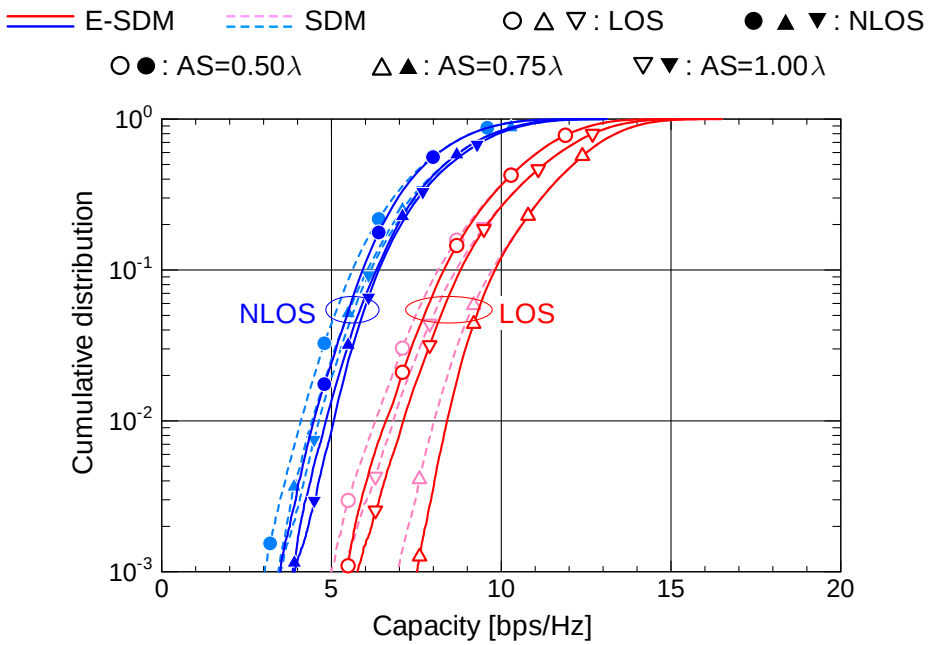

(a) TX-x/RX-x

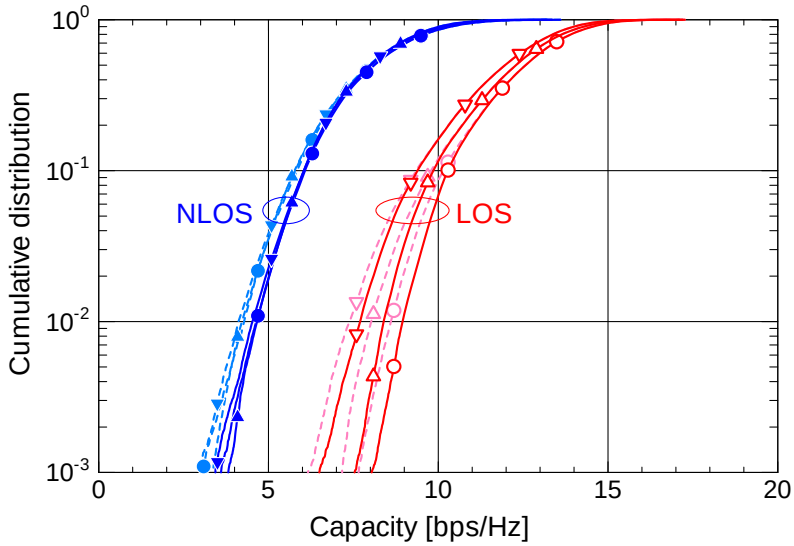

(b) TX-y/RX-y

Figure 4.18: Comparison of channel capacities C_{SDM} and $C_{\text{E-SDM}}$ with a normalized total TX power of 20 dB for the measured 2×2 MIMO channels.

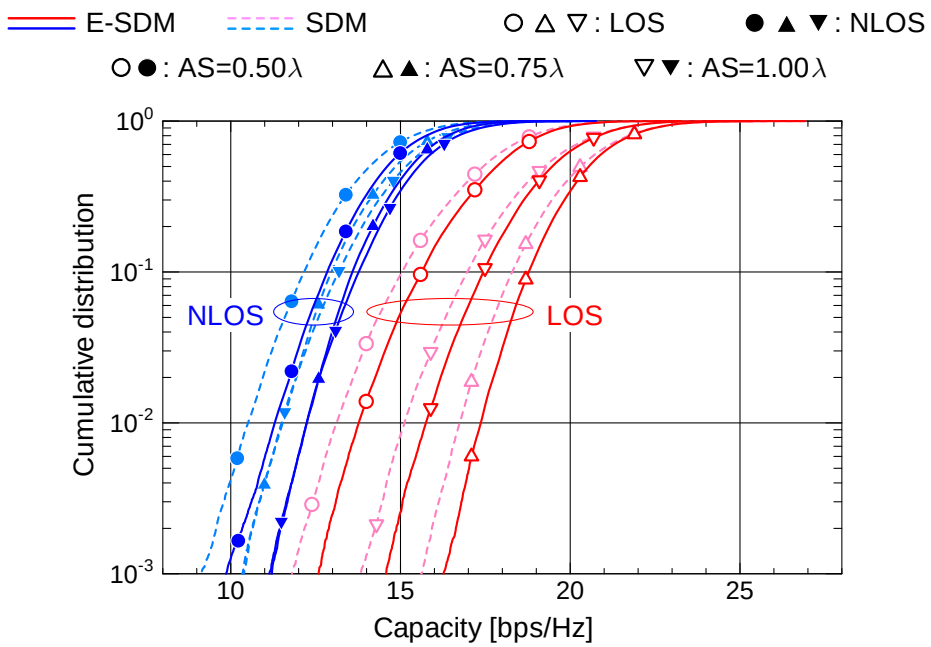

(a) TX-x/RX-x

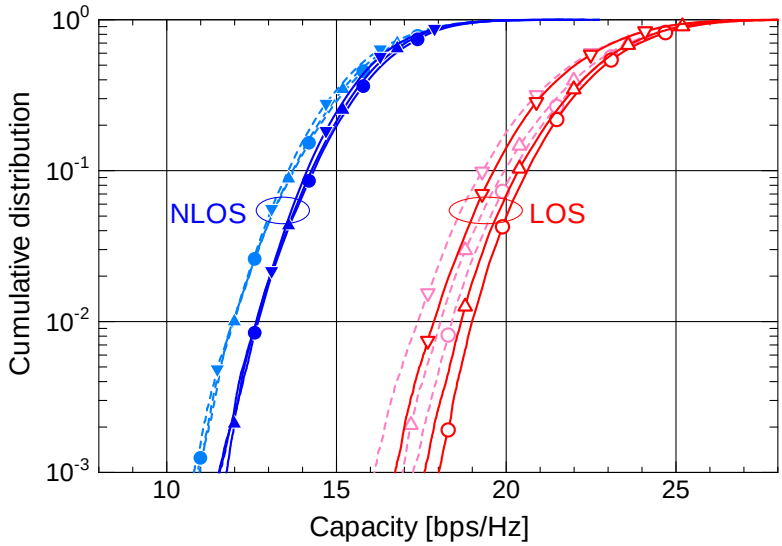

(b) TX-y/RX-y

Figure 4.19: Comparison of channel capacities C_{SDM} and $C_{\text{E-SDM}}$ with a normalized total TX power of 20 dB for the measured 4×4 MIMO channels.

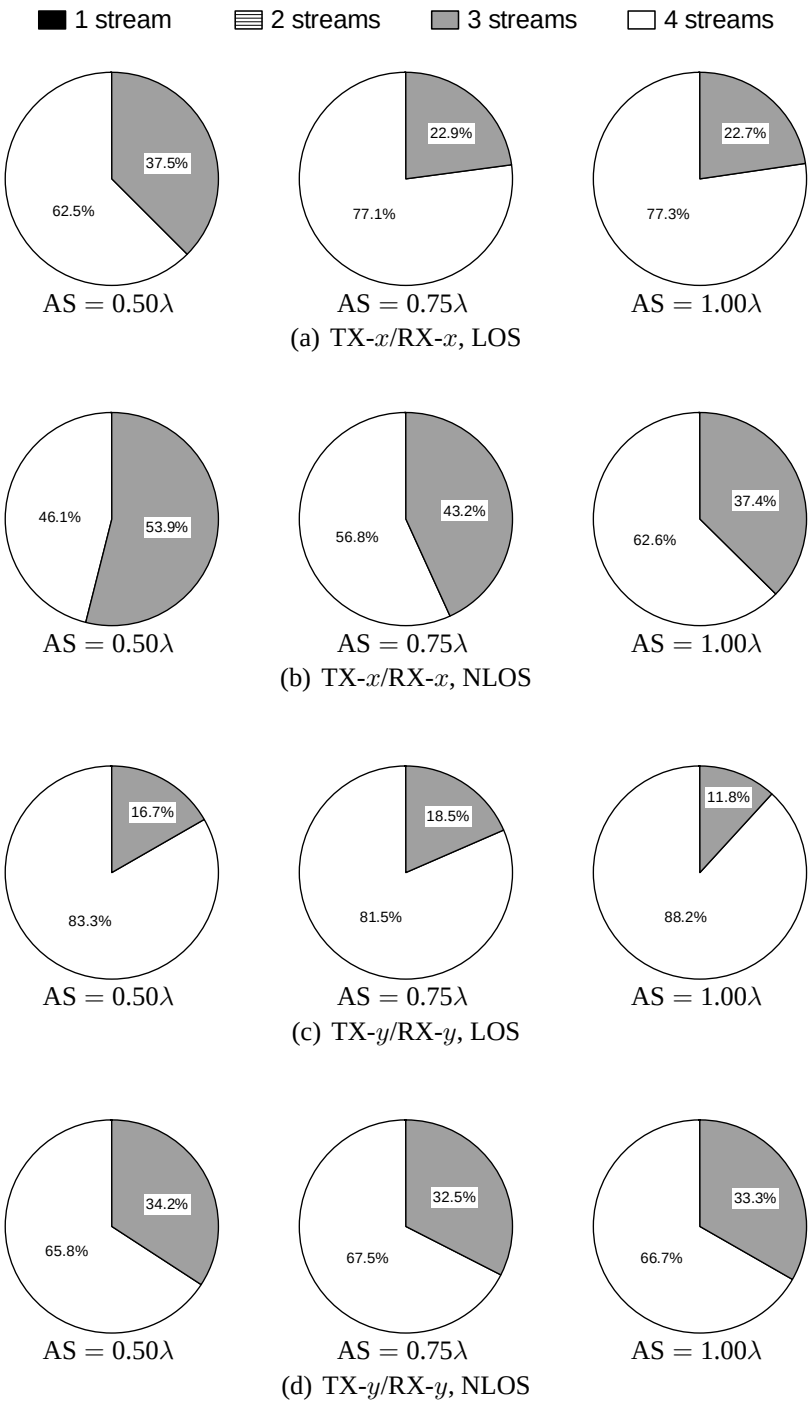

Figure 4.20: Percentages of substreams in E-SDM determined according to the WF theorem at the normalized total TX power of 20 dB for the measured 4×4 MIMO channels.

Table 4.2: MIMO E-SDM and SDM simulation parameters.

	E-SDM	SDM
Array orientation	TX-*x*/RX-*x*, TX-*y*/RX-*y*	
AS	0.50λ, 0.75λ, 1.00λ	
Modulation	QPSK, 16QAM, 64QAM, and 256QAM (QPSK and 16QAM in the 2×2 MIMO system)	QPSK
Resource control	Minimum BER criterion based on Chernoff upper-bound	—
RX signal processing	MRC	MLD
Data rates	$2N_{\mathrm{tx}}$ bits/SDM-symbol	
Burst length	128 symbols (no coding)	
Thermal noise	White Gaussian noise	

of information transmitted through each eigenchannel is a discrete quantity, however, and cannot actually be controlled on the basis of the WF theorem. From the implementational viewpoint, therefore, a concept of bit assignment and TX power allocation based on minimization of BER averaged over substreams has been proposed [30]. This subsection examines the average BER performance of E-SDM transmission based on that resource control method by using computer simulations.

The simulation parameters are listed in Table 4.2. As stated previously, 78,449 channel data had been obtained for each MIMO configuration and all the BERs were averaged. The author conducted simulations for E-SDM and also did for SDM for comparison. In SDM it was assumed that an independent QPSK-modulated uncoded substream was transmitted with equal power from each TX antenna, like the previous SDM simulation in §4.2.2. That is, a total of $2N_{\mathrm{tx}}$ bits/symbol were constantly transmitted (4 bits/symbol in the 2×2 MIMO and 8 bits/symbol in the 4×4 MIMO). In the simulations for E-SDM the transmitter was also assumed to send data with a fixed rate of $2N_{\mathrm{tx}}$ bits/symbol. Under this condition, in the 2×2 MIMO E-SDM the transmitter selected modulations from QPSK and 16QAM and in the 4×4 MIMO E-SDM it selected modulations from QPSK, 16QAM, 64QAM, and 256QAM. Thus 2×2 MIMO E-SDM had the following two selection patterns:

- 16QAM $\times\, 1\,(\lambda_1)$
- QPSK $\times\, 2\,(\lambda_1, \lambda_2)$

And 4×4 MIMO E-SDM had the following five selection patterns:

- 256QAM $\times\, 1\,(\lambda_1)$
- 64QAM $\times\, 1\,(\lambda_1) +$ QPSK $\times\, 1\,(\lambda_2)$
- 16QAM $\times\, 2\,(\lambda_1, \lambda_2)$

- 16QAM $\times$ 1 (λ_1) + QPSK $\times$ 2 (λ_2, λ_3)
- QPSK $\times$ 4 $(\lambda_1, \lambda_2, \lambda_3, \lambda_4)$

From these patterns the transmitter selected the combination expected to give the minimum BER averaged over utilized substreams by using the Chernoff upper-bound. Then Lagrange multipliers determined the optimum TX power coefficients for the substreams [30]. Maximum likelihood detection (MLD) was used for RX signal processing in the SDM simulations because it is the method that gives the best performance [65]. The E-SDM simulations also assumed that the TX and RX sides have perfect CSI, whereas the SDM simulations assumed that only the RX side has perfect CSI.

The average BER performances of 2 $\times$ 2 and 4 $\times$ 4 MIMO systems are shown in Figs. 4.21 and 4.22, respectively. Looking at the E-SDM BER performance, we see—as we saw when comparing channel capacities (Figs. 4.18 and 4.19)—that under the same TX power condition the LOS scenario gives better performance than the NLOS scenario does. The availability of conventional SDM in LOS environments has already been reported in the previous section and [43, 79, 80][1]. E-SDM transmission never suffers degradation due to a high channel correlation, which is one of the issues in SDM (see Figs. 4.3–4.5 for fading correlations). In LOS environments, eigenvalues become larger as the received power increases, and we have better performance in E-SDM. The better performance in the LOS scenario is thought to be due to the direct wave.

Figure 4.23 shows percentages of bit and substream assignments in 4 $\times$ 4 MIMO E-SDM at the normalized total TX power of 20 dB in order to explain some phenomena raised below. The determination of these assignments was based on the minimum BER criterion used in this simulation. Unlike the proportion of used substreams based on the WF theorem shown in Fig. 4.20, when the minimum BER criterion is used, most of the transmission is two- or three-substream transmission and there is no four-substream transmission. Furthermore, while the WF theorem selects mostly four-substream transmission in the LOS scenario, the minimum BER criterion selects fewer-substream transmission more frequently in the LOS scenario than in the NLOS one. This means that when discrete digital information is transmitted by forming eigenbeams, the BER performance obtained when sending much information through fewer eigenchannels with larger eigenvalues is better than that obtained when using many eigenchannels. This phenomenon is considered to be the difference between an ideal case given by the information theory and an actual case with limited finite modulations.

The differences in channel capacities between SDM and E-SDM are not large as described in the previous subsection. The BER performance obtained with E-SDM, in contrast, clearly excels in all of the MIMO configurations. This is considered to be due to fewer-substream transmission mentioned above. As stated in §4.1.4, overall minimum

[1] In [79, 80] and this dissertation, the author fairly compares the MIMO SDM performance in the LOS and NLOS scenarios under the same TX power constraint, and reports that LOS channels provide better performance due to higher received power. Note that, however, some NLOS performances outperform LOS ones under the same SNR condition, where fading correlations determine major performance of MIMO SDM.

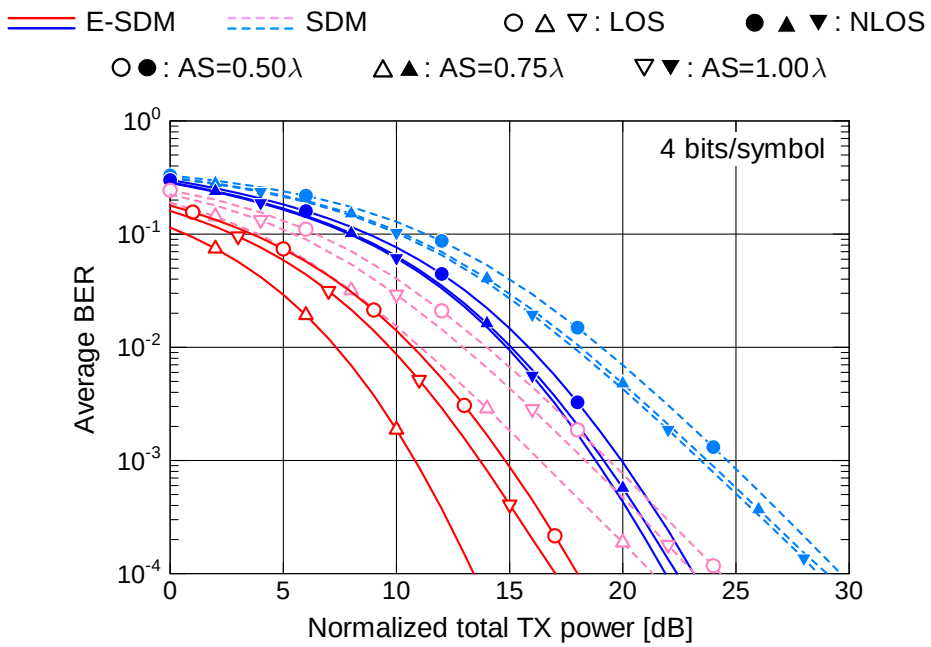

(a) TX-*x*/RX-*x*

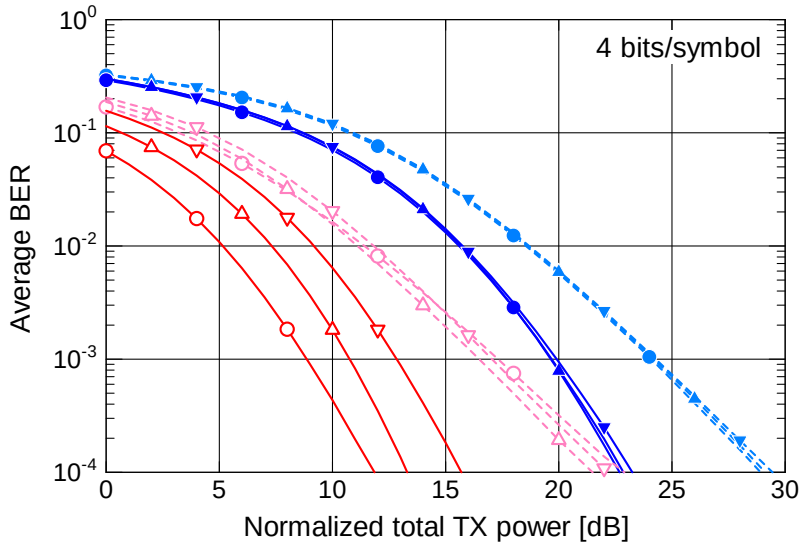

(b) TX-*y*/RX-*y*

Figure 4.21: Average BER performance of SDM and E-SDM for the measured 2×2 MIMO channels (uncoded 4 bits/SDM-symbol).

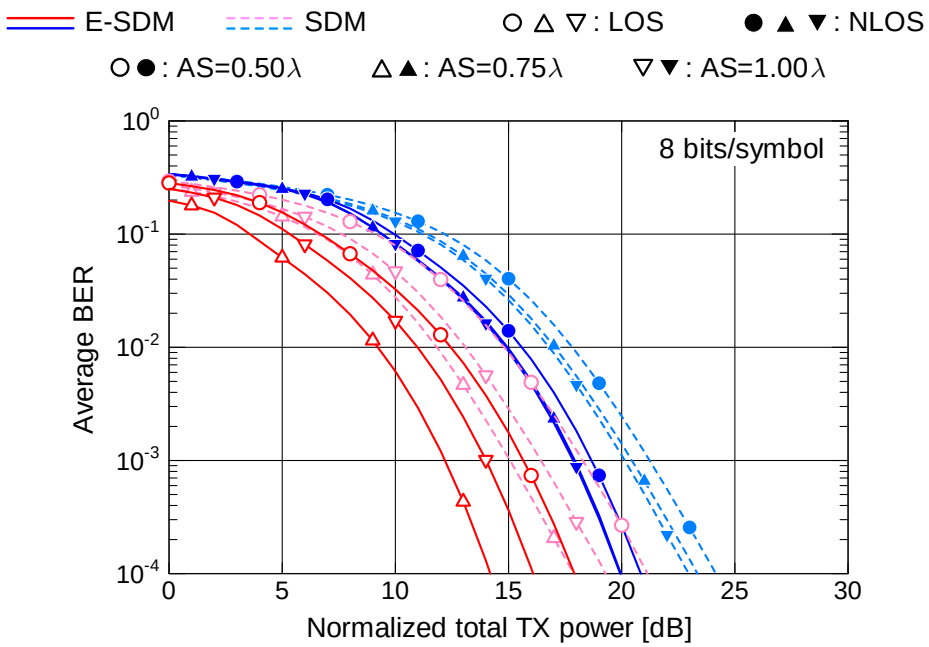

(a) TX-*x*/RX-*x*

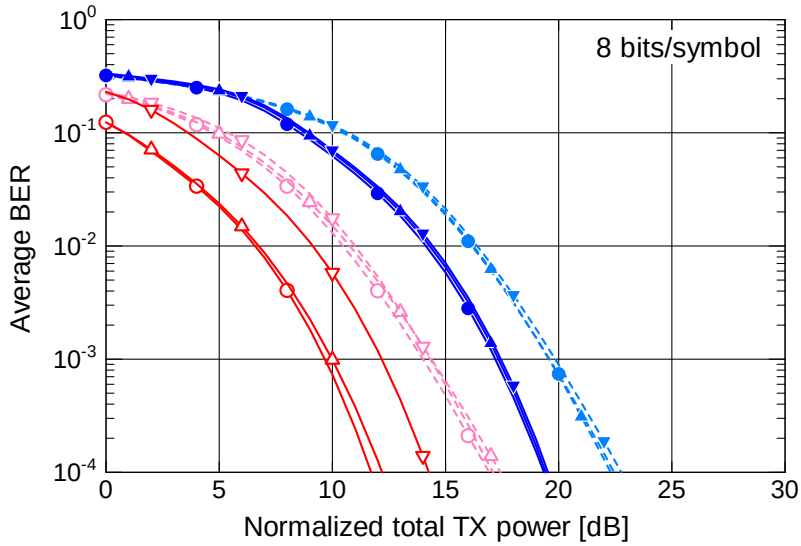

(b) TX-*y*/RX-*y*

Figure 4.22: Average BER performance of SDM and E-SDM for the measured 4×4 MIMO channels (uncoded 8 bits/SDM-symbol).

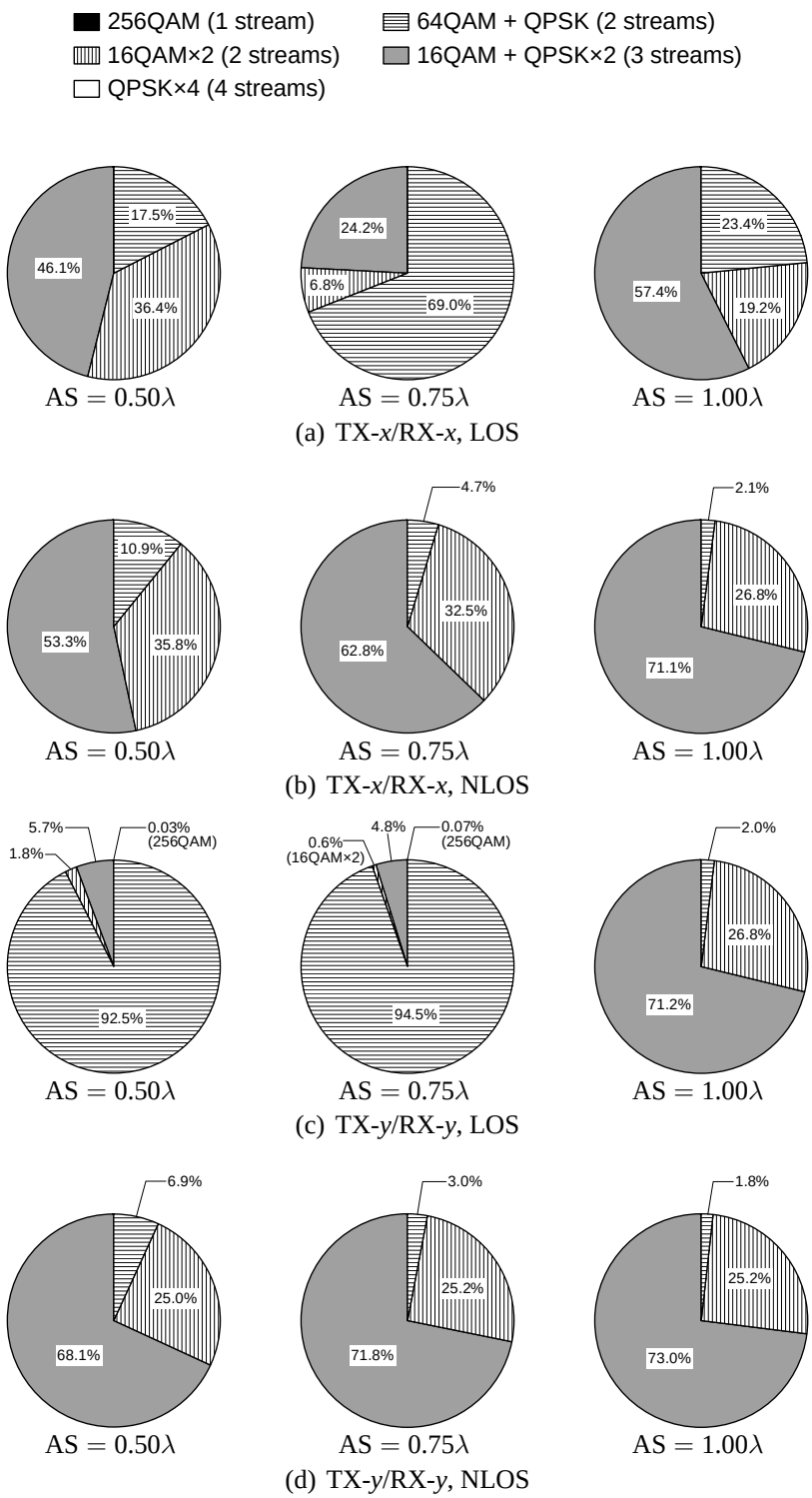

Figure 4.23: Percentages of substreams in E-SDM determined according to the minimum BER criterion at the normalized total TX power of 20 dB for the measured 4×4 MIMO channels.

eigenvalues have noticeably lower values than the others. Hence, unlike the WF theorem, the minimum BER criterion appears to judge minimum eigenvalues unavailable. In addition, Figs. 4.10–4.13 show that eigenchannels provide spatial diversity gain except the one with the minimum eigenvalue as described also in §4.1.4. Under a constant bit rate, advantages of more diversity gain obtained by choosing fewer-substream transmission seem to greatly outweigh the degradation caused by multilevel modulation schemes such as 16QAM and 64QAM.

The LOS gain variation appears to cause differences also in E-SDM BER performance and to result in a variety of trends in resource allocation, especially for 4×4 MIMO systems. For example, when AS $= 0.50\lambda$ or 0.75λ in the TX-*y*/RX-*y* orientation in the LOS scenario, predominant transmission is the two-substream transmission (in which 64QAM modulation is allocated to the first eigenchannel with the maximum eigenvalue λ_1 and QPSK modulation is allocated to the second eigenchannel with λ_2). Moreover, it is only in these cases that we find one-substream transmission in which 256QAM is allocated to the first eigenchannel. The first eigenchannel thus plays an important role in these cases. We can see in Fig. 4.13 that the eigenvalues λ_1 for these two cases are remarkably large. As stated in §4.1.1 and §4.1.4, the large values of λ_1 are due to higher gain in the 90° direction. Since the higher gain was caused by the mutual coupling in antennas, we can say that the BER performance of E-SDM tends to be affected by the mutual coupling effect. For this reason, the E-SDM performance in the TX-*y*/RX-*y* array orientation in the LOS scenario consequentially improves as the AS decreases.

Although as in the previous subsection the author does not present figures showing the percentages of substreams for the 2×2 MIMO system, it was confirmed that about 80% of the transmission in the NLOS scenario is one-substream transmission utilizing only 16QAM. The percentage of one-substream transmission in the LOS scenario also differs depending on the array configuration. In the TX-*x*/RX-*x* orientation it is 87.6% for AS $= 0.50\lambda$, 93.6% for AS $= 0.75\lambda$, and 85.8% for AS $= 1.00\lambda$, while in the TX-*y*/RX-*y* orientation it is 99.2% for AS $= 0.50\lambda$, 92.2% for AS $= 0.75\lambda$, and 74.2% for AS $= 1.00\lambda$. As in the 4×4 MIMO system, the results in the 2×2 MIMO system, that are obtained when the minimum BER criterion is used, differ from those obtained when the WF theorem is used.

4.3.3 Conclusions

We have evaluated the performance of MIMO E-SDM in the 5.2 GHz frequency band by using channel data measured in indoor LOS and NLOS environments. CDFs of channel capacities and average BERs were examined with array element patterns and CDFs of eigenvalues, and were compared with those of conventional SDM.

From the results, we found that the LOS scenario, in which there is the direct wave, gives better E-SDM performance. Also, although channel capacities did not indicate clear benefits of E-SDM, we obtained excellent BER performance by employing E-SDM compared with conventional SDM. We also found that the maximum channel capacity criterion (WF theorem) and the minimum BER criterion have different characteristics with

regard to TX resource allocation. Moreover, in the LOS scenario the BER performance especially in E-SDM strongly depends on the MIMO configuration.

4.4 Performance of Coded MIMO-OFDM SDM

So far, it has been clarified that the uncoded performance of SDM and E-SDM in LOS environments generally outperforms that in NLOS ones under the same TX power condition even though the existence of the direct wave increases fading correlations in LOS environments.

Applying the OFDM technique to the MIMO system (MIMO-OFDM) is a practical approach because OFDM is robust to multipath fading [5, 6, 14, 15]. In MIMO-OFDM SDM, a transmitted data sequence can obtain space-frequency diversity effect by being coded and interleaved over substreams and subcarriers. As mentioned above, the presence of the LOS component causes high fading correlations, which result in low spatial diversity gain. In addition, frequency selectivity in LOS environments tends to be lower due to such a high level component. Hence, we cannot expect high space-frequency diversity gain in LOS environments, therefore the performance may degrade unlike uncoded cases.

This section presents the practical performance of coded 2×2 and 4×4 MIMO-OFDM SDM based on the measured channels. Note that typical cases of AS $= 0.50\lambda$ and 1.00λ only are handled in order to simplify the discussion.

4.4.1 Simulation Conditions

Using measured channel data, the author examined the BER performance of spatially-multiplexed 2×2 and 4×4 MIMO-OFDM systems by computer simulations. Figure 4.24 illustrates the MIMO-OFDM SDM system structure, and Table 4.3 lists MIMO-OFDM SDM simulation parameters. Some of the simulation parameters were determined according to the contents of the IEEE802.11n standardization [5, 6]. The transmission bandwidth was assumed to be 20 MHz, which corresponds to 128 measurement frequency samples in the measurement (156.25 kHz $\times$ 128 $=$ 20 MHz). Therefore, the total number of OFDM channel data (i.e., the number of trial frames) became $(1{,}601 - 128) \times 49 = 72{,}177$. Figure 4.25 illustrates an image of sampling of measured channels to obtain broadband channel sets. Each set of 128-point channel data was decimated to 64 points (312.5 kHz interval), spectrally shaped (Fig. 4.26), and normalized to the direct wave amplitude. After applying the IFFT to the modified channel data, its first 16 samples (guard interval duration) were used as the corresponding channel impulse responses. 56 subcarriers out of 64 in total were used for data transmission, and a data frame was composed of eight OFDM symbols. QPSK modulation was employed. A data sequence was coded by a convolutional encoder (constraint length of seven and coding rate of 1/2) [6] and then randomly bit-interleaved over substreams and subcarriers to obtain sufficient space-frequency diversity gain. The receiver demultiplexed the received signal using an MMSE spatial filter at each subcarrier and then passed the data to a soft-decision Viterbi decoder. To sufficiently

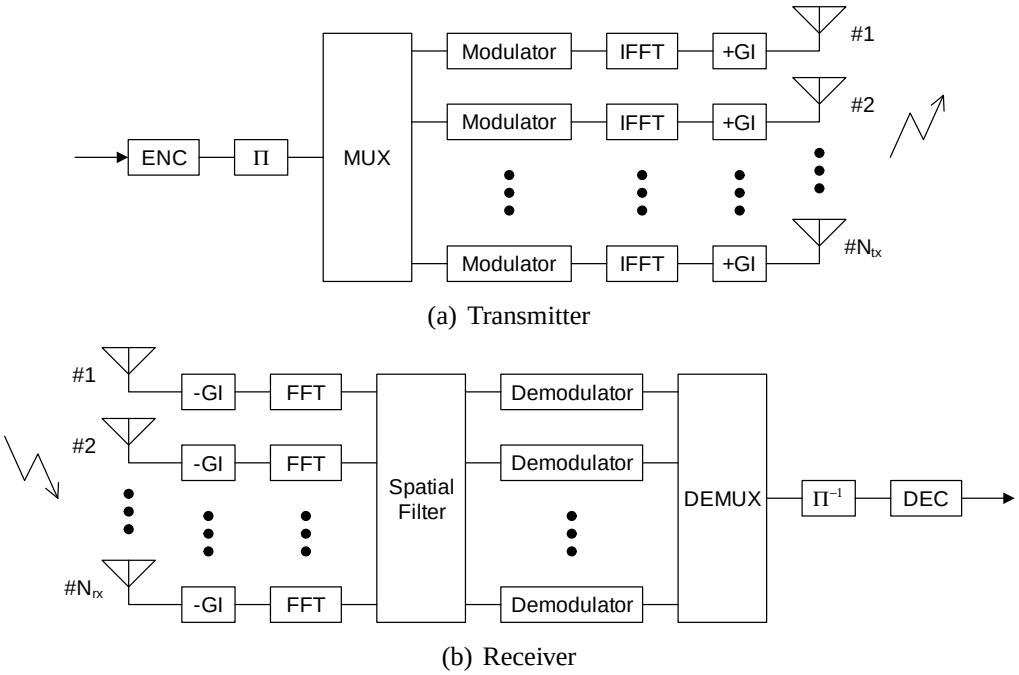

(a) Transmitter

(b) Receiver

Figure 4.24: Structure of a MIMO-OFDM SDM system.

Table 4.3: Simulation parameters of MIMO-OFDM SDM.

Array orientation	TX-*x*/RX-*x*, TX-*y*/RX-*y*
AS	0.50λ, 1.00λ
Total channel sets	$7 \times 7 \times 1{,}473 = 72{,}177$
Bandwidth	20 MHz
FFT size	64 points (312.5 kHz interval)
No. of active subcarriers	56
GI length	16 samples (800 ns)
Frame size	8 OFDM symbols
Modulation	QPSK
RX processing	MMSE spatial filtering
Thermal noise	White Gaussian noise
Encoding	BCC (constraint length 7 and rate 1/2) space-time-frequency random bit-interleaving
Decoding	Viterbi algorithm
Bit rate	Uncoded case: $2N_{\mathrm{tx}}$ bits/symbol/subcarrier Coded case: N_{tx} bits/symbol/subcarrier

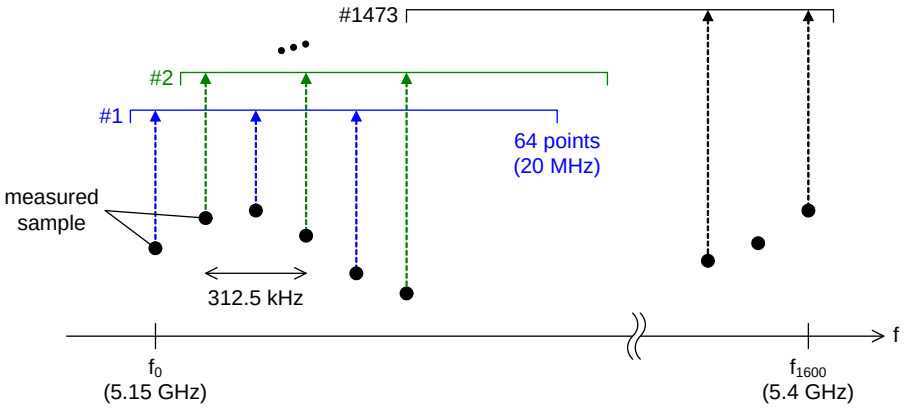

Figure 4.25: Image of the acquisition of broadband channel sets.

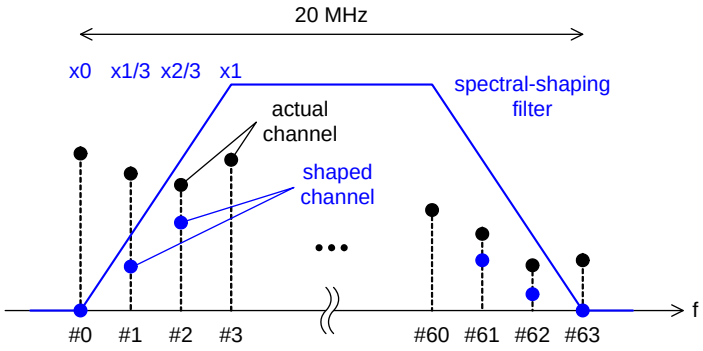

Figure 4.26: Spectral shaping (amplitudes of the outer three channels in each of lower and upper bands are multiplied by corresponding coefficients).

reflect the space-frequency diversity effect after demultiplexing, the obtained LLR was multiplied by the corresponding SINR at the MMSE spatial filter output, as in §2.5. It was assumed that a fading condition was static over a frame, and that the receiver had perfect CSI.

4.4.2 Simulation Results

BER performances for 2×2 and 4×4 MIMO-OFDM are shown in Figs. 4.27 and 4.28, respectively. The author also presents fading correlations for all the MIMO configurations in Table 4.4, where only RX correlations are listed because TX and RX correlations are similar as seen in Figs. 4.3–4.5. For 4×4 MIMO cases, each listed value is averaged over six correlations. Details on the correlations are discussed in §4.1.2. Here the normalized total TX power denotes the total TX power yielding average E_s/N_0 of 0 dB in the case of single-antenna OFDM transmission in an anechoic chamber with the same measurement setup. In addition to the coded case, the performance without coding is demonstrated for comparison. The uncoded case shows almost the same tendency as the narrowband case discussed in §4.2.2. From the results of the uncoded case, we can see that the LOS scenario provides better BER performance compared with the NLOS one. As reported in 4.2, this is because of higher received power given by the LOS component whereas it makes channels correlated as evidenced by Table 4.4. Also it should be noted that all the BER curves show first-order diversity regardless of the MIMO configuration.

The highest fading correlation in the case of AS $= 0.50\lambda$ in the TX-*y*/RX-*y* orientation is due to the LOS component equivalently-emphasized by the increased antenna gain as discussed in §4.1.2. Such a high correlation tends to affect the diversity gain as discussed in the following. We can evaluate the space-frequency diversity effect of a MIMO-OFDM system with the gradient of its BER curve. While the LOS scenario still gives better performance than the NLOS one even in the coded case, gradients of BER curves in LOS cases tend to be gentler than those in NLOS cases and to depend on the array configuration. Focusing on the case of TX-*y*/RX-*y* with AS $= 0.50\lambda$ in 2×2 MIMO, its gradient is clearly gentler compared with the other cases. This implies that relatively lower space-frequency diversity gain was obtained in the case because the equivalently enlarged LOS component caused higher fading correlations and lower frequency selectivity. However, its performance is still better than that of the NLOS cases at a BER of 10^{-5}. Although similar diversity gain loss can be observed in the case of TX-*y*/RX-*y* with AS $= 0.50\lambda$ in 4×4 MIMO, it does not appear evident compared with the case in 2×2 MIMO. It is supposed that a MIMO system equipped with more antennas can obtain higher spatial diversity effect even in a highly correlated case. From these results, we can say that a cyclic delay diversity technique [5, 81] is effective for solving the low-diversity issue in LOS environments, especially for a system equipped with fewer antennas such as 2×2 MIMO.

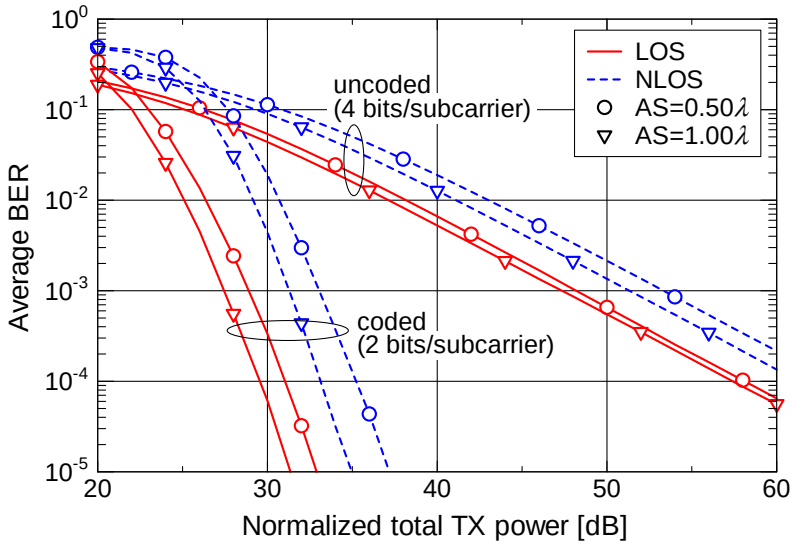

(a) TX-*x*/RX-*x*

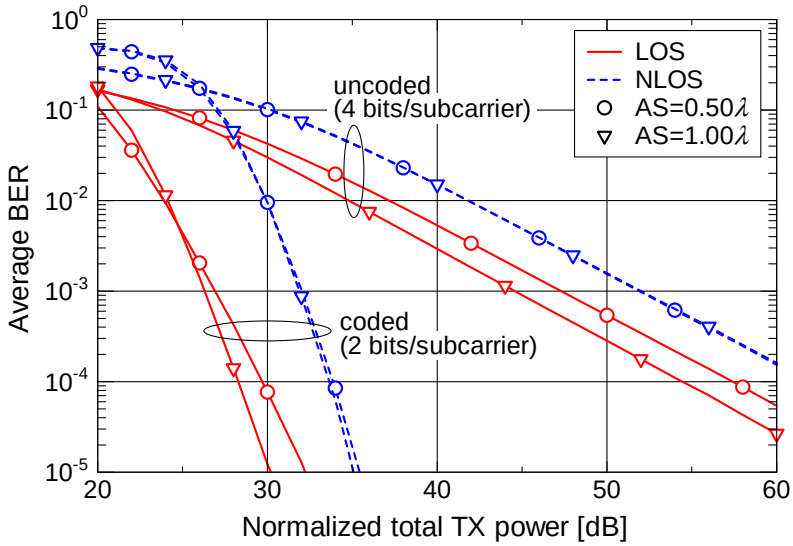

(b) TX-*y*/RX-*y*

Figure 4.27: BER performance of MIMO-OFDM SDM for measured 2×2 MIMO channels.

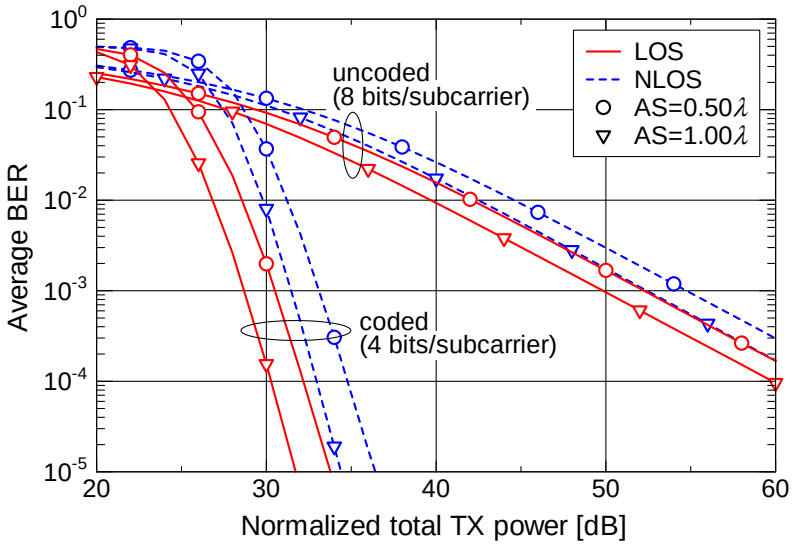

(a) TX-*x*/RX-*x*

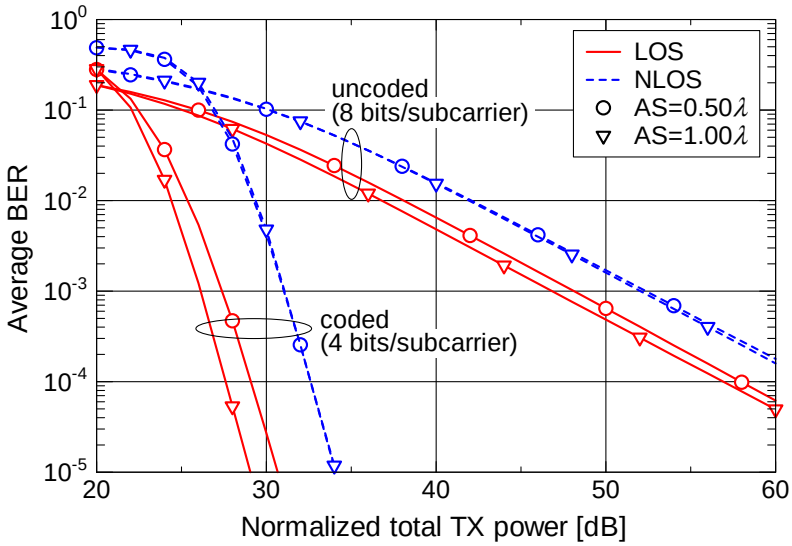

(b) TX-*y*/RX-*y*

Figure 4.28: BER performance of MIMO-OFDM SDM for measured 4 × 4 MIMO channels.

Table 4.4: RX fading correlations (averaged correlations for 4×4 MIMO).

		TX-*x*/RX-*x*		TX-*y*/RX-*y*	
		AS $= 0.50\lambda$	AS $= 1.00\lambda$	AS $= 0.50\lambda$	AS $= 1.00\lambda$
2×2	LOS	0.63	0.54	0.86	0.47
	NLOS	0.31	0.10	0.29	0.04
4×4	LOS	0.41	0.47	0.82	0.32
	NLOS	0.23	0.08	0.21	0.07

4.4.3 Conclusions

By using channel data measured in an indoor environment, the practical performance of MIMO-OFDM SDM has been examined. It has been shown that even in a coded case the LOS scenario still provides better performance than the NLOS one in the measurement site. However, it should be noted that MIMO-OFDM SDM systems in LOS environments may obtain lower space-frequency diversity effects.

Chapter 5

Pseudo Eigenbeam-Space Division Multiplexing (PE-SDM) in Frequency-Selective MIMO Channels

5.1 Introduction

In a frequency-selective MIMO channel, the use of OFDM transmission is effective because it is robust to delay paths [14, 15, 52, 53]. The optimum processing at the transmitter in a MIMO-OFDM system is beamforming based on eigenvectors at each subcarrier to orthogonalize the MIMO channel [54, 55]. Also in MIMO-SC transmission, we can apply eigenbeams to space-frequency domain equalization where the eigenbeam is calculated at each orthogonal frequency point [56]. However, since the computational complexity of SVD or EVD is very high, the total calculation load of SVD or EVD increases in proportion to the number of active frequency points. Hence, it is necessary to reduce the load.

In addition, conventional SVD or EVD has another problem. This procedure includes phase ambiguity itself and is individually executed at each frequency point. Even if it would be possible to remove such phase ambiguity, the order of eigenvalues/eigenvectors may change at some frequency points in a frequency selective channel, and it is still difficult to find such order switching over discrete frequency points. Thus, frequency continuity of the transmit weight is difficult to be maintained. These emphasize frequency selectivity of the effective channel, which is observed at the receiver through both the effects of transmit weight and the MIMO channel. As a result, the impulse response has very large delay spread.

In the case without beamforming, it has been reported that the receiver can accurately estimate frequency-selective MIMO channels by using time windowing in both time- and frequency-domain estimation [57–62]. These schemes are commonly based on the concept

of improving SNR by limiting the impulse response duration and suppressing the noise power outside the window. Unfortunately, it is difficult to employ these schemes to estimate the effective channel because of its large delay spread, as will be shown later. Maintaining frequency continuity of the effective channel is, therefore, one of the important issues in a beamforming system.

Choi and Heath proposed an interpolation-based beamforming scheme with considering phases of weight vectors in a MIMO-OFDM system with limited weight feedback [63]. In the method, the phases of eigenvectors are adjusted to provide good interpolation property at the transmitter side. However, the method does not guarantee maintaining frequency continuity so that utilizing the method as a solution for frequency continuity is currently inapplicable in that form.

To solve the issues raised above, the author proposes the pseudo eigenvector (PEV) technique which can reduce the calculation load and maintain frequency continuity of the effective channel. It will be shown that the pseudo E-SDM (PE-SDM) technique can provide almost the same or better MIMO-OFDM performance compared with the E-SDM when the receiver refines the effective channel estimate with time windowing. Such frequency-domain beamforming can also be applied to SC systems with FDE at the receiver [62]. Thus, in addition to MIMO-OFDM, the author evaluates the throughput performance of PE-SDM in MIMO-SC systems with MMSE-FDE comparing with the E-SDM where a similar concept proposed in [63] is applied to improve frequency continuity. Also, focusing on the calculating process of PEVs, a spatial windowing scheme is proposed for improving the accuracy of effective channel estimates. Furthermore, the author also proposes an estimator of effective channels incorporating both the time and spatial windowing schemes, i.e., space-time windowing.

This chapter is organized as follows. §5.2 defines the MIMO system model under a frequency-selective fading environment and introduces the E-SDM transmission. §5.3 describes the concept and procedure of PEV calculation and presents PEV properties. §5.4 proposes a time windowing scheme improving accuracy of effective channel estimation in the PE-SDM transmission. §5.5 reports the practical performance of the PE-SDM transmission applied to MIMO-OFDM systems. In addition, §5.6 reports the PE-SDM throughput performance in MIMO-SC systems with MMSE-FDE along with a proposal of spatial windowing and space-time windowing in channel estimation and an evaluation of channel estimation errors. Note that these two windowing schemes are discussed separately from the time windowing scheme because they require a specific assumption on the system as will be explained in §5.6.2. The author draws conclusions from these results in §5.7.

5.2 MIMO Broadband System Model and E-SDM

This section clarifies a MIMO broadband wireless system model under a frequency-selective fading environment. Note that in the following a baseband system is discussed. To facilitate the following discussion in the frequency domain, it is assumed that a guard interval (GI) is added to the beginning of each transmitted symbol in multicarrier transmission

such as OFDM or each transmitted block in a SC system. This assumption ensures that the received sequence has periodicity within the FFT window duration and that there is no inter-symbol interference in the multicarrier case or inter-block interference in the SC case. When the transmitter beamforms at each frequency point to spatially multiplex K substreams ($K \leq \min(N_{\mathrm{tx}}, N_{\mathrm{rx}})$), an N_{rx}-dimensional RX signal vector at frequency point f is expressed as

$$\boldsymbol{r}(f) = \boldsymbol{H}_F(f)\boldsymbol{U}(f)\sqrt{\boldsymbol{P}(f)}\boldsymbol{s}(f) + \boldsymbol{n}(f), \tag{5.1}$$

where $\boldsymbol{H}_F(f)$ is an $N_{\mathrm{rx}} \times N_{\mathrm{tx}}$ channel matrix, $\boldsymbol{U}(f)$ is an $N_{\mathrm{tx}} \times K$ TX weight matrix, $\sqrt{\boldsymbol{P}(f)}$ is a K-dimensional diagonal matrix that is a square root of a K-dimensional TX power matrix $\boldsymbol{P}(f) = \mathrm{diag}\,[p_1(f), \ldots, p_K(f)]$, $\boldsymbol{s}(f)$ is a K-dimensional TX signal vector[1], and $\boldsymbol{n}(f)$ is an N_{rx}-dimensional thermal noise vector, which obeys a complex Gaussian process of zero mean and variance of σ^2. Here, we define an $N_{\mathrm{rx}} \times K$ effective channel matrix $\boldsymbol{B}_F(f)$ in the following equation

$$\boldsymbol{B}_F(f) = \boldsymbol{H}_F(f)\boldsymbol{U}(f)\sqrt{\boldsymbol{P}(f)} \tag{5.2}$$

$$= [\boldsymbol{b}_{F,1}(f) \ \cdots \ \boldsymbol{b}_{F,K}(f)]\,. \tag{5.3}$$

That is, the effective channel is composed of the actual channel and TX beams. Substituting (5.2) into (5.1) yields

$$\boldsymbol{r}(f) = \boldsymbol{B}_F(f)\boldsymbol{s}(f) + \boldsymbol{n}(f). \tag{5.4}$$

Optimum beamforming is achieved by employing eigenvectors (hereinafter referred to as true eigenvectors (TEVs)) as TX weight vectors. Under an assumption of $K = \min(N_{\mathrm{tx}}, N_{\mathrm{rx}})$, the SVD of the channel matrix is expressed as

$$\boldsymbol{H}_F(f) = \boldsymbol{V}_e(f)\boldsymbol{\Sigma}(f)\boldsymbol{U}_e^H(f), \tag{5.5}$$

where

$$\boldsymbol{V}_e(f) = [\boldsymbol{v}_{e,1}(f) \ \cdots \ \boldsymbol{v}_{e,K}(f)] \qquad (N_{\mathrm{rx}} \times K) \tag{5.6}$$

$$\boldsymbol{U}_e(f) = [\boldsymbol{u}_{e,1}(f) \ \cdots \ \boldsymbol{u}_{e,K}(f)] \qquad (N_{\mathrm{tx}} \times K) \tag{5.7}$$

$$\boldsymbol{\Sigma}(f) = \mathrm{diag}\left[\sqrt{\lambda_1(f)}, \ldots, \sqrt{\lambda_K(f)}\right]. \tag{5.8}$$

Here, both $\boldsymbol{v}_{e,i}(f)$ and $\boldsymbol{u}_{e,i}(f)$ ($i = 1, \ldots, K$) are TEVs, and $\lambda_1(f), \ldots, \lambda_K(f)$ are eigenvalues in descending order. When we utilize $\boldsymbol{U}_e(f)$ ($= \boldsymbol{H}_F^H(f)\boldsymbol{V}_e(f)\boldsymbol{\Sigma}^{-1}(f)$) as the TX weight matrix $\boldsymbol{U}(f)$, the receiver observes the effective channel as

$$\boldsymbol{B}_{F,e}(f) = \boldsymbol{H}_F(f)\boldsymbol{U}_e(f)\sqrt{\boldsymbol{P}(f)}. \tag{5.9}$$

[1]Note that in this model the power allocated to the substreams $\sqrt{\boldsymbol{P}(f)}$ is separated from the transmitted signal $\boldsymbol{s}(f)$, unlike the case in §2.3.2. Here it is assumed that signal elements $s_1(f), \ldots, s_K(f)$ in the vector $\boldsymbol{s}(f)$ have the same mean power, i.e., $E[s_1(f)] = \cdots = E[s_K(f)] = 1$.

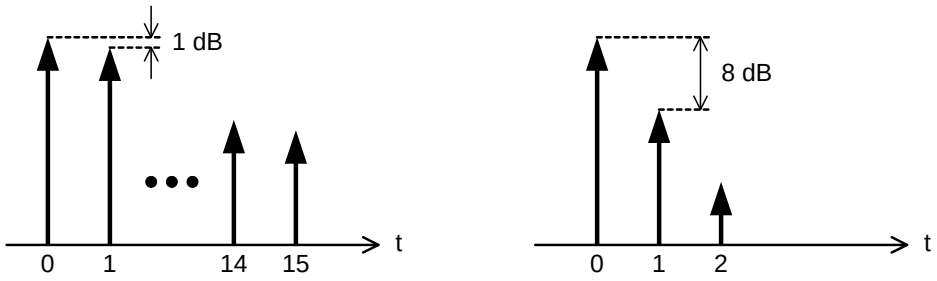

(a) Scenario A (16 paths, $T_d = 15$) (b) Scenario B (3 paths, $T_d = 2$)

Figure 5.1: Two multipath fading scenarios.

In this case, the matrix $\boldsymbol{V}_e(f)$ enables the receiver to separate the spatially multiplexed signals without inter-substream interference as follows

$$\boldsymbol{y}(f) = \boldsymbol{V}_e^H(f)\boldsymbol{r}(f) \tag{5.10}$$

$$= \boldsymbol{\Sigma}(f)\sqrt{\boldsymbol{P}(f)}\boldsymbol{s}(f) + \boldsymbol{V}_e^H(f)\boldsymbol{n}(f). \tag{5.11}$$

Equation (5.11) indicates that the SNR of the ith detected substream is in proportion to $\lambda_i(f)$. This is the E-SDM scheme, which is the optimum transmission also in a frequency-selective MIMO channel.

Obtaining TEVs at each frequency point, however, increases the computational load. Also, in general, TEVs are calculated without consideration of their frequency continuity so that they enlarge the delay spread of the impulse response of the effective channel, as will be demonstrated in §5.3.3. Addressing these issues, the author proposes the PEV scheme in the next section.

In the following sections §5.3–5.5, we consider two multipath scenarios as illustrated in Fig. 5.1, where T_d indicates the maximum time delay of paths. Scenario A is an environment where there are 16 sample-spaced i.i.d. Rayleigh paths ($T_d = 15$) with average 1-dB decaying. Therefore, its frequency selectivity is relatively high. On the other hand, Scenario B has three sample-spaced i.i.d. Rayleigh paths ($T_d = 2$) with average 8-dB decaying so that it results in lower frequency selectivity. In other words, Scenario B is close to a frequency-flat fading environment.

5.3 Pseudo Eigenvector Calculation

5.3.1 Virtual RX Weight Matrix

First, we define an $N_{\text{rx}} \times N_{\text{rx}}$ RX autocorrelation function matrix $\boldsymbol{R}_{\text{rx}}(\tau)$ by

$$\boldsymbol{R}_{\text{rx}}(\tau) = \frac{1}{\sqrt{N_f}} \sum_{t=0}^{N_f-1} \boldsymbol{H}_T(t)\boldsymbol{H}_T^H(t+\tau) \tag{5.12}$$

$$= \frac{1}{\sqrt{N_f}} \sum_{t=0}^{T_d} \boldsymbol{H}_T(t)\boldsymbol{H}_T^H(t+\tau), \tag{5.13}$$

where both t and τ denote time point indices, N_f indicates the FFT size, and $\boldsymbol{H}_T(t)$ represents the channel matrix of the path at time t, which can be obtained by applying the IFFT to $\boldsymbol{H}_F(f)$. The RX autocorrelation function matrix has the property of $\boldsymbol{R}_{\text{rx}}(-\tau) = \boldsymbol{R}_{\text{rx}}^H(\tau)$ and is also in a Fourier transform pair relationship with $\boldsymbol{H}_F(f)\boldsymbol{H}_F^H(f)$. That is, we have

$$\boldsymbol{R}_{\text{rx}}(\tau) = \mathcal{F}^{-1}\left[\boldsymbol{H}_F(f)\boldsymbol{H}_F^H(f)\right], \tag{5.14}$$

where $\mathcal{F}^{-1}[\cdot]$ indicates the IFFT operation. In the function $\boldsymbol{R}_{\text{rx}}(\tau)$, only $\boldsymbol{R}_{\text{rx}}(0)$ is a non-negative Hermitian matrix. The sum of its diagonal elements $\text{tr}[\boldsymbol{R}_{\text{rx}}(0)]$ corresponds to the whole energy of the channel. Note that $\boldsymbol{R}_{\text{rx}}(0)$ is equivalent to the sum or average of $\boldsymbol{H}_F(f)\boldsymbol{H}_F^H(f)$ over all the frequency points as follows

$$\boldsymbol{R}_{\text{rx}}(0) = \frac{1}{\sqrt{N_f}} \sum_{f=0}^{N_f-1} \boldsymbol{H}_F(f)\boldsymbol{H}_F^H(f). \tag{5.15}$$

The EVD of $\boldsymbol{R}_{\text{rx}}(0)$ is expressed as

$$\boldsymbol{R}_{\text{rx}}(0) = \boldsymbol{V}_0 \boldsymbol{\Lambda}_0 \boldsymbol{V}_0^H, \tag{5.16}$$

where $\boldsymbol{\Lambda}_0$ is an N_{rx}-dimensional diagonal matrix composed of descending ordered eigenvalues of $\boldsymbol{R}_{\text{rx}}(0)$, and $\boldsymbol{V}_0$ is an N_{rx}-dimensional unitary matrix. The proposal is based on using $\boldsymbol{V}_0^H$ as a tentative RX weight matrix. The next subsection describes the method to obtain the TX weight matrix from $\boldsymbol{V}_0^H$.

5.3.2 Pseudo Eigenvector Calculation

In order to maintain the frequency continuity of the effective channel, the frequency continuity of the TX weight vectors must be accomplished. Here, the author proposes a PEV for the TX weight. The following describes the concept and the calculation procedure of the vectors.

We redefine $K = \min(N_{\text{tx}}, N_{\text{rx}})$. Also, matrices $\boldsymbol{V}_{0,K}$ and $\boldsymbol{\Lambda}_{0,K}$ are defined as an $N_{\text{rx}} \times K$ matrix composed of the first K column vectors of $\boldsymbol{V}_0$ and a K-dimensional diagonal matrix composed of the first K diagonal elements of $\boldsymbol{\Lambda}_0$, respectively. The matrix $\boldsymbol{V}_{0,K}^H$

can be considered as a frequency-flat RX weight matrix for the mean of $\boldsymbol{H}_F(f)\boldsymbol{H}_F^H(f)$ averaged over all frequencies. If the channel characteristic is frequency-flat, i.e., $\boldsymbol{H}_F(f) = \boldsymbol{H}_F$, $\boldsymbol{V}_{0,K}^H$ and $\boldsymbol{H}_F^H\boldsymbol{V}_{0,K}\sqrt{\boldsymbol{\Lambda}_{0,K}}^{-1}$ will be the optimum RX and TX weight matrices, respectively. Expanding this assumption, we can assume that $\boldsymbol{H}_F^H(f)\boldsymbol{V}_{0,K}\sqrt{\boldsymbol{\Lambda}_{0,K}}^{-1}$ approximates to the ideal TX matrix $\boldsymbol{U}_e(f)$ in the frequency-selective channel. It is clear that $\boldsymbol{H}_F^H(f)\boldsymbol{V}_{0,K}\sqrt{\boldsymbol{\Lambda}_{0,K}}^{-1}$ has frequency continuity. However, unlike $\boldsymbol{U}_e(f)$, the matrix $\boldsymbol{H}_F^H(f)\boldsymbol{V}_{0,K}\sqrt{\boldsymbol{\Lambda}_{0,K}}^{-1}$ is not composed of orthonormal vectors that are required for the TX weight vectors. Therefore, we ignore $\sqrt{\boldsymbol{\Lambda}_{0,K}}^{-1}$ and consider applying orthonormalization to column vectors of $\boldsymbol{H}_F^H(f)\boldsymbol{V}_{0,K}$ to obtain a PEV matrix. Here, the author proposes applying the Gram-Schmidt (GS) orthonormalization as

$$\boldsymbol{U}'_e(f) = \mathcal{GS}\left[\boldsymbol{H}_F^H(f)\boldsymbol{V}_{0,K}\right] \tag{5.17}$$

$$= \left[\boldsymbol{u}'_{e,1}(f)\ \cdots\ \boldsymbol{u}'_{e,K}(f)\right], \tag{5.18}$$

where $\mathcal{GS}[\cdot]$ denotes the GS operation. Details on the GS orthonormalization are described in Appendix B.

Tsunekawa et al. proposed a similar method, which obtains a TX weight matrix by GS processing in a MIMO-OFDM system [82]. For simple hardware implementation, it orthonormalizes column vectors of the channel itself, i.e., $\mathcal{GS}\left[\boldsymbol{H}_F^H(f)\right]$, in descending order of their Euclidean norms. Orthonormalizing in this order is efficient in terms of obtaining vectors that are similar to TEVs. However, such ordering may cause frequency discontinuity of the obtained vectors because the order is not the same at all frequency points. (The effect and frequency discontinuity due to ordering will be discussed in §5.3.6.) Since the author's major purpose is to maintain frequency continuity of TX vectors, in (5.17) we naturally orthonormalize column vectors in the order of column number. The first column vector $\boldsymbol{u}'_{e,1}(f)$ has the best frequency continuity because only normalization is applied. Since subsequent column vectors are affected by both orthogonalization and normalization, their frequency continuity is expected to be less. However, since these processings are applied to the vectors originally having frequency continuity, subsequent column vectors also tend to have frequency continuity.

Consequently, the proposed method enables us to maintain frequency continuity of the vectors and the effective channel with a reduced calculation load. In the following, §5.3.3 and §5.3.4 show its frequency continuity and low numerical complexity, respectively. It should be noted that the orthogonality of received substreams might be lost when the difference between PEVs and TEVs cannot be ignored. That is, $\boldsymbol{U}_e'^H(f)\boldsymbol{H}_F^H(f)\boldsymbol{H}_F(f)\boldsymbol{U}'_e(f)$ is nearly, but not quite, a diagonal matrix. Therefore, since in spatial multiplexing there is inter-substream interference at the receiver, we need to suppress the interference to detect substreams.

Table 5.1: RMS delay spreads of effective channels for a 4 × 4 MIMO case ($N_f = 64$).

		RMS delay spread [samples]	
		PEV	TEV
Scenario A	substream #1	2.97	10.24
	substream #2	3.57	14.43
	substream #3	4.41	17.36
	substream #4	4.45	17.67
	multipath	3.47	
Scenario B	substream #1	0.30	4.33
	substream #2	0.37	7.05
	substream #3	0.48	9.01
	substream #4	0.60	9.61
	multipath	0.43	

5.3.3 Power Delay Profile of Effective Channels

This subsection demonstrates that PEVs can achieve frequency continuity of effective channels. Here, we define an impulse response matrix $\boldsymbol{B}_T(f)$ by

$$\boldsymbol{B}_T(t) = \mathcal{F}^{-1}\left[\boldsymbol{B}_F(f)\right] \tag{5.19}$$

$$= \left[\boldsymbol{b}_{T,1}(t) \ \cdots \ \boldsymbol{b}_{T,K}(t)\right], \tag{5.20}$$

where $\boldsymbol{b}_{T,i}(t)$ is an N_{rx}-dimensional impulse response vector corresponding to the ith substream. Although it is difficult to examine frequency continuity from the frequency-domain characteristics, we can easily see it in the time domain. That is, as the effective channel $\boldsymbol{B}_F(f)$ has better frequency continuity, its delay spread is lower. The delay spread for the ith substream can be examined by calculating $E\left[\|\boldsymbol{b}_{T,i}(t)\|^2\right]$, where $E[\cdot]$ denotes an expectation, and $\|\cdot\|$ denotes the Euclidean norm. Accordingly, we evaluate frequency continuity of effective channels by using their delay spreads.

Figures 5.2 and 5.3 illustrate mean power delay profiles of effective channels in a 4 × 4 MIMO system under the two multipath scenarios. In addition, their root mean square (RMS) delay spreads are listed in Table 5.1. The FFT size was $N_f = 64$, and TX weights with equal power were multiplied at all N_f frequency points. Results were averaged over 100,000 different effective channels. It should be noted that, for TEV cases, the EVD of $\boldsymbol{H}_F^H(f)\boldsymbol{H}_F(f)$ was calculated under a constraint forcing the first element of each TEV to be real.

Unlike actual channels $\boldsymbol{H}_T(t)$, effective channels have responses also in the region of $t < 0$ as shown in Figs. 5.2 and 5.3 because TX beams have their own frequency characteristics, and their impulse responses are not causal. Since TEVs naturally do not have frequency continuity, they obviously cause large delay spread regardless of the multipath scenario and substream. This means that TEVs generally cause frequency discontinuity

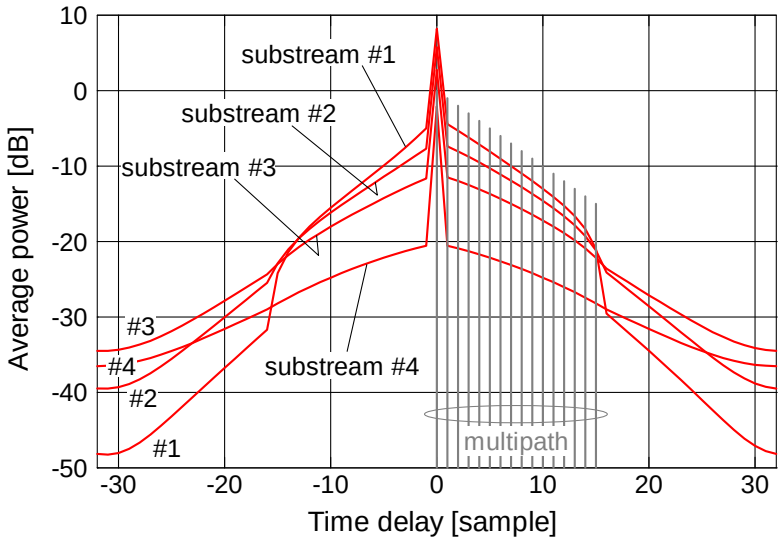

(a) PEV case

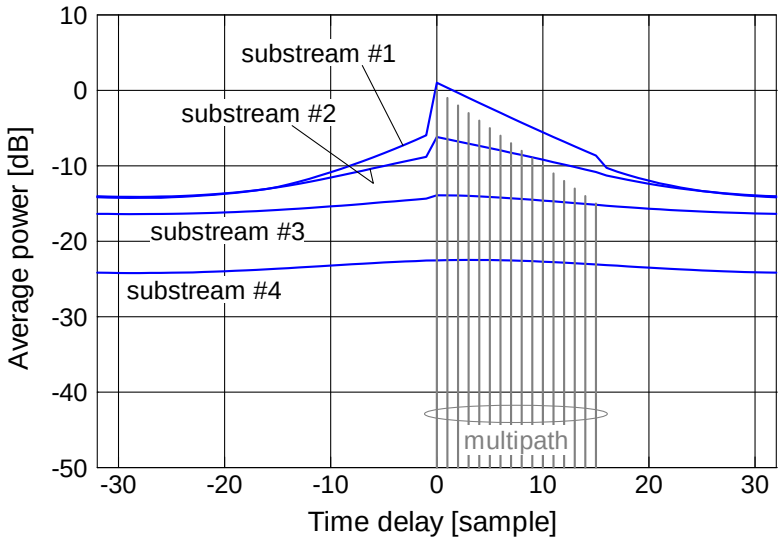

(b) TEV case

Figure 5.2: Mean power delay profiles of effective channels in a 4×4 MIMO case in Scenario A ($N_f = 64$).

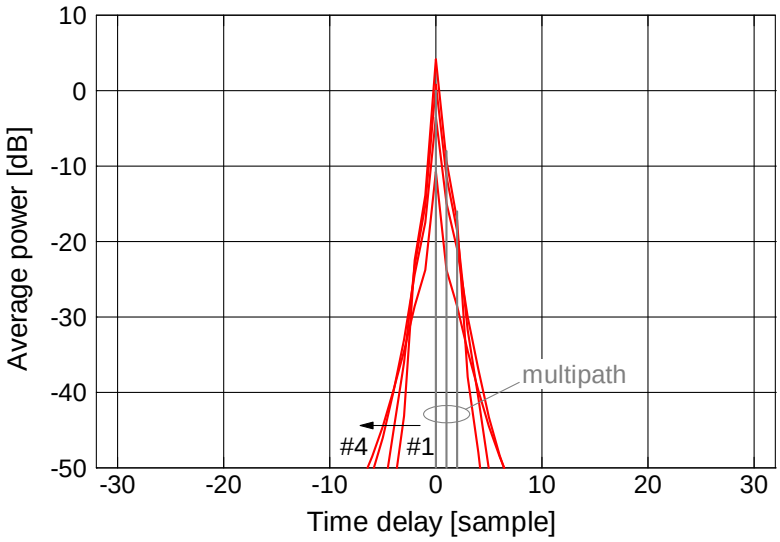

(a) PEV case

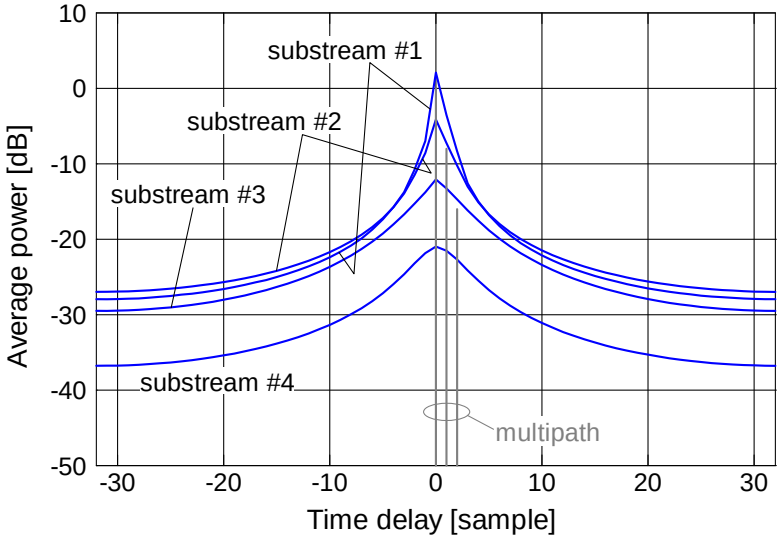

(b) TEV case

Figure 5.3: Mean power delay profiles of effective channels in a 4×4 MIMO case in Scenario B ($N_f = 64$).

of the effective channels. Note that mean power delay profiles for TEV cases would show almost flat characteristics regardless of the scenario and substream if TEVs were calculated without the constraint mentioned above. On the other hand, PEVs concentrate impulse responses in the region of $|t| \leq T_d$ and give high peaks at $t = 0$ regardless of the substream. Also, the responses in the region of $|t| > T_d$ are at a significantly low level, especially for Scenario B. This means that the delay spreads of effective channels are highly reduced by using PEVs. Consequently, we can say that PEVs as TX weights can maintain frequency continuity of effective channels. Thus, time windowing can be utilized to improve accuracy of the effective channel estimation, as will be shown later.

5.3.4 Numerical Complexity

The proposed PEV scheme has lower computational complexity compared with calculation of TEVs. To verify it, this subsection examines their mean and maximum numbers of complex multiplications per frame for 2×2 and 4×4 MIMO cases with the same setup as the previous subsection, as listed in Table 5.2. The complexity in the PEV scheme was examined for the EVD of $\boldsymbol{R}_{\mathrm{rx}}(0)$ and the GS operation of $\boldsymbol{H}_F^H(f)\boldsymbol{V}_{0,K}$, and that in the TEV scheme was examined for the EVD of $\boldsymbol{H}_F^H(f)\boldsymbol{H}_F(f)$ for comparison, where EVD was solved by Jacobi method. Therefore, it should be noted that they do not contain calculation of FFT, matrix multiplication, and the summation in (5.13). For the TEV scheme, to speed up the convergence in EVD, $\boldsymbol{U}_e(f-1)$ obtained at the adjacent frequency point $f-1$ was utilized as an initial unitary matrix for $\boldsymbol{U}_e(f)$. Since Scenario B has lower frequency selectivity, this initial value setting decreases number of iterations in EVD. Although, for the 2×2 MIMO case, both schemes have almost the same complexity, for the 4×4 MIMO case the PEV scheme can reduce it to about 1/11 (Scenario A) – 1/9 (Scenario B) of that in the TEV one when comparing mean numbers of complex multiplications. Even in comparison of maximum numbers which are important factors for evaluating implementability of algorithms, PEVs for the 4×4 MIMO can be computed with about 1/8 complexity of TEV calculation in both scenarios. Independence of complexity on the multipath scenario for the 2×2 MIMO case is because both the GS orthonormalization and a two-dimensional eigenvalue problem can be solved with simple equations of fixed complexity (without iterative calculations).

5.3.5 Pseudo Eigenvalue

Here, let us define a pseudo eigenvalue $\lambda'_i(f)$ of the ith substream at frequency point f by

$$\lambda'_i(f) = \left\| \boldsymbol{H}_F(f)\boldsymbol{u}'_{e,i}(f) \right\|^2 \tag{5.21}$$

$$= \boldsymbol{u}'^H_{e,i}(f)\boldsymbol{H}_F^H(f)\boldsymbol{H}_F(f)\boldsymbol{u}'_{e,i}(f). \tag{5.22}$$

The pseudo eigenvalue $\lambda'_i(f)$ is in proportion to the received SNR of the ith substream in the case of single-beam transmission using $\boldsymbol{u}'_{e,i}(f)$. In the above equation, $\lambda'_i(f)$ becomes the true eigenvalue $\lambda_i(f)$ by replacing $\boldsymbol{u}'_{e,i}(f)$ by the ith TEV $\boldsymbol{u}_{e,i}(f)$.

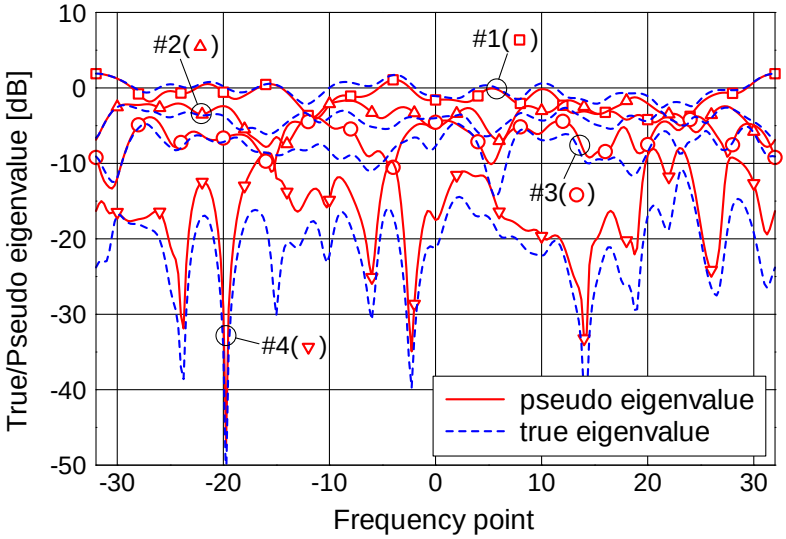

(a) Scenario A

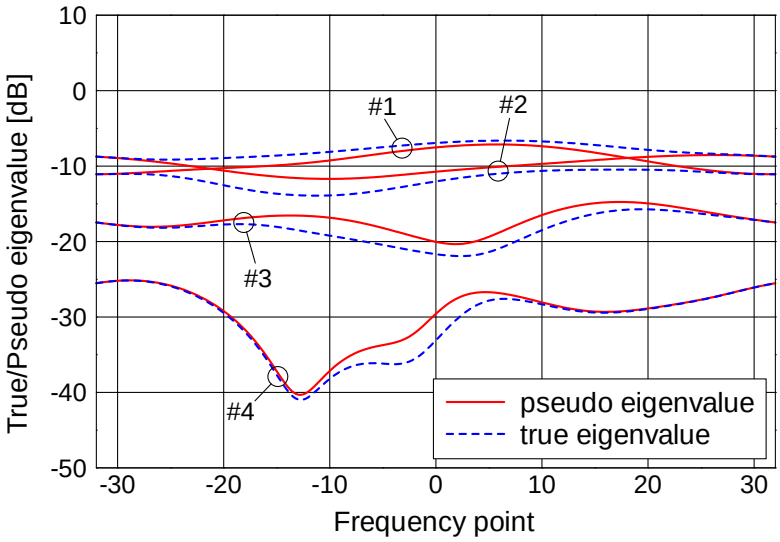

(b) Scenario B

Figure 5.4: Examples of pseudo and true eigenvalues for a 4×4 MIMO case.

Table 5.2: Mean and maximum numbers of complex multiplications per fading state for 2×2 and 4×4 MIMO cases.

		Number of complex multiplications (mean/max)	
		PEV	TEV
2×2	Scenario A	1,074/1,074	1,152/1,152
	Scenario B	1,074/1,074	1,152/1,152
4×4	Scenario A	6,581/11,784	73,674/86,604
	Scenario B	6,453/11,784	59,994/88,338

Figure 5.4 shows examples of true and pseudo eigenvalues for a 4×4 MIMO system under the two multipath scenarios. Since both true and pseudo eigenvalues for Scenario A fluctuate in the frequency domain, we can say that the scenario has high frequency selectivity. On the other hand, for Scenario B its fading appears closer to frequency-flat fading, which is the assumed condition in the PEV calculation as described in §5.3.2. Thus, pseudo eigenvalues for Scenario B are in good agreement with eigenvalues so that PEVs are expected to be similar to TEVs. However, especially for Scenario A, some pseudo eigenvalues do not agree well with corresponding true eigenvalues. It is conjectured that PEVs in such regions mismatch with the channel, and that inter-substream interference may be larger. Note that, especially for Scenario A, while true eigenvalues are in descending order regardless of the frequency point, the order of pseudo eigenvalues can change depending on the frequency selectivity. This is expected to relate to high frequency continuity, i.e., low delay spreads, of effective channels shown in Figs. 5.2 and 5.3.

5.3.6 On Effects of Ordering in GS Processing

As stated in §5.3.2, vector norm-based ordering in GS processing is effective to obtain vectors similar to TEVs. However, since the order changes at some frequency points in a frequency selective fading environment, such ordering may cause frequency discontinuity of the vectors and effective channels. This subsection examines and proves these effects of ordering. For the sake of convenience, hereinafter the PEV scheme using GS operation with norm-based ordering is referred to as PEV with norm-ordered GS.

Figure 5.5 illustrates the example of pseudo eigenvalues of 4×4 MIMO obtained by PEVs with norm-ordered GS in Scenario B, where the multipath channel state is the same as that in Fig. 5.4(b). Compared with the conventional PEV case shown in Fig. 5.4(b), PEVs with norm-ordered GS provide pseudo eigenvalues closer to true eigenvalues. We can say that the ordering is effective to obtain better weight vectors. However, it is seen that frequency discontinuity points occur due to the ordering. Let us discuss the impact of the discontinuity on delay spreads in the following.

Figure 5.6 shows mean power delay profiles of effective channels obtained by PEVs with norm-ordered GS in a 4×4 MIMO system. Here, figures (a) and (b) are comparable

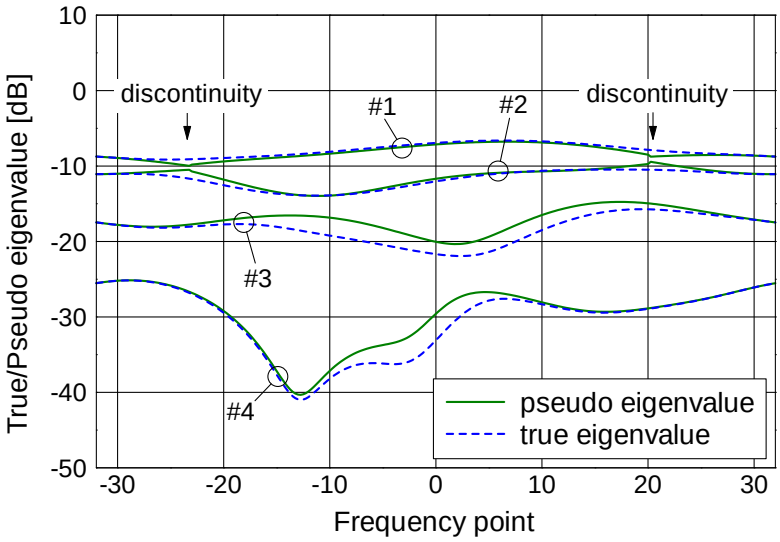

Figure 5.5: Example of pseudo eigenvalues of 4×4 MIMO obtained by PEVs with norm-ordered GS in Scenario B.

to Figs. 5.2 and 5.3 because of the same setups and scenarios, respectively. It is obvious that in both scenarios the ordering causes larger delay spreads compared with the conventional PEV cases shown in Figs. 5.2(a) and 5.3(a). Consequently, while ordering is an effective solution to calculate weight vectors closer to TEVs, it may cause frequency discontinuity and enlarge delay spreads of effective channels. In the study, therefore, such ordering in the PEV calculation is not employed.

5.4 Estimation Scheme of Effective Channel in PE-SDM

The previous section clarified characteristics of the PEVs. This section proposes an effective channel estimation scheme in PE-SDM transmission, in which PEVs are employed as TX weight vectors. Although a beamforming technique in the frequency domain can be applied to SC systems [56] as will be shown later, in this section the author discusses it in a MIMO-OFDM system.

5.4.1 Frequency Domain Estimation of Effective Channel

It is presumed that the data frame has a long preamble to estimate the effective channel at the receiver. The preamble is composed of $N_{\mathrm{LP}} = 2^n$ OFDM symbols, which have a space-time orthogonal Walsh-Hadamard code, and is different in each substream. The number of the training symbols is determined by the maximum number of substreams $K_{\max} = \min(N_{\mathrm{tx}}, N_{\mathrm{rx}})$. When $K_{\max} = 2$, the preamble has $N_{\mathrm{LP}} = 2^1 = 2$ training

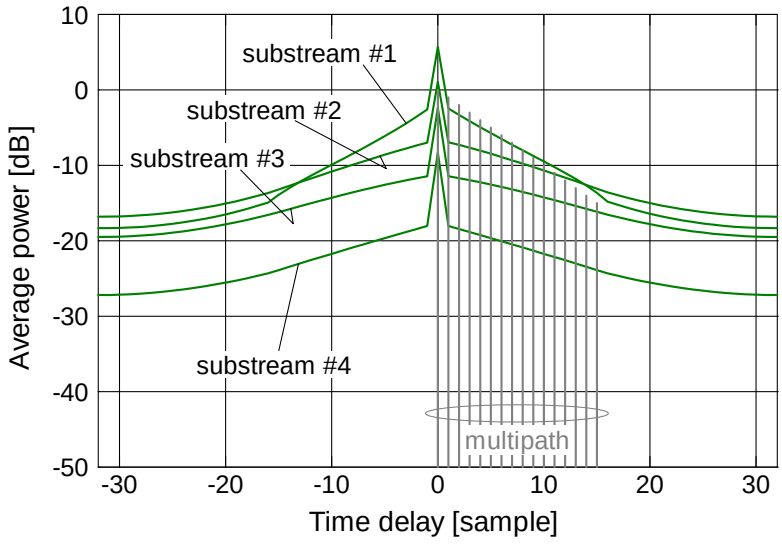

(a) Scenario A

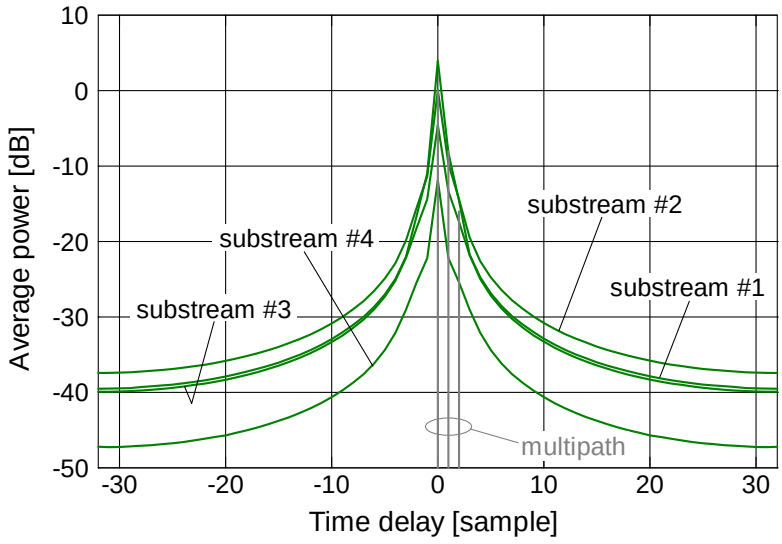

(b) Scenario B

Figure 5.6: Mean power delay profiles of effective channels in a 4×4 MIMO case of PEV with norm-ordered GS.

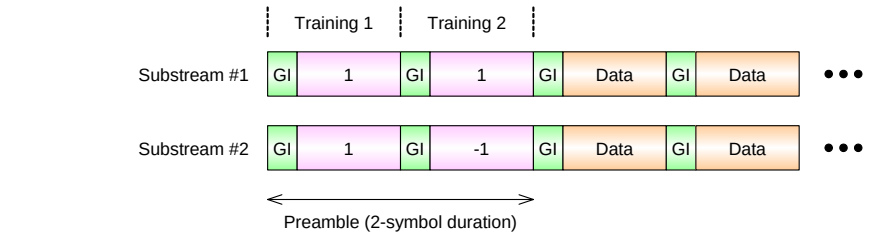

(a) Case of $N_{\mathrm{LP}} = 2$

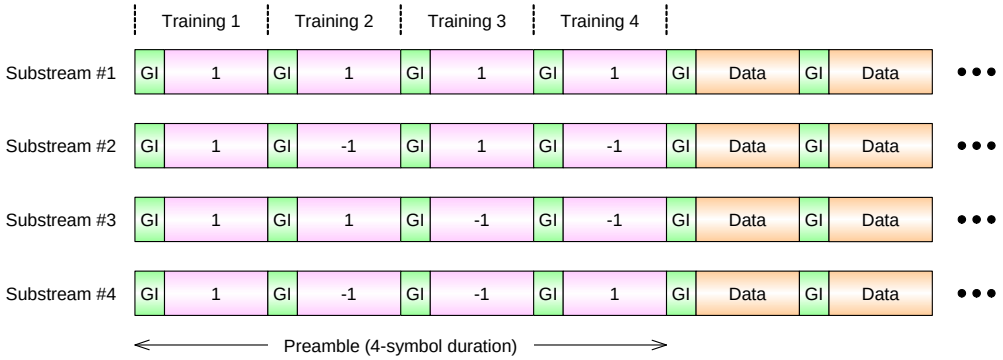

(b) Case of $N_{\mathrm{LP}} = 4$

Figure 5.7: Frame formats.

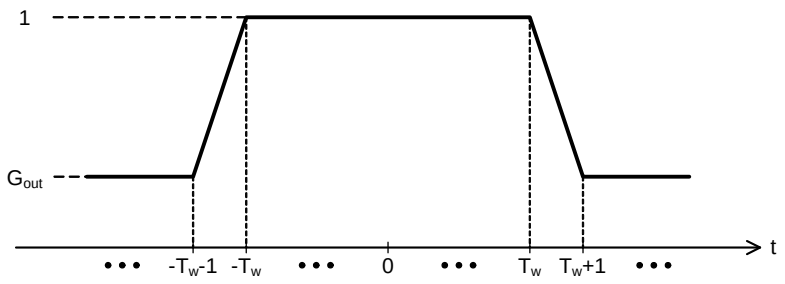

Figure 5.8: Time window function.

symbols as shown in Fig. 5.7(a). Since $K_{\max} = 4$ in a 4×4 MIMO system, the preamble has $N_{\mathrm{LP}} = 2^2 = 4$ training symbols to separate $K_{\max}$ substreams at the receiver as shown in Fig. 5.7(b). The receiver can estimate the effective channel of the desired substream in the frequency domain by linearly combining the N_{LP} symbols after the correspondent code multiplication [55].

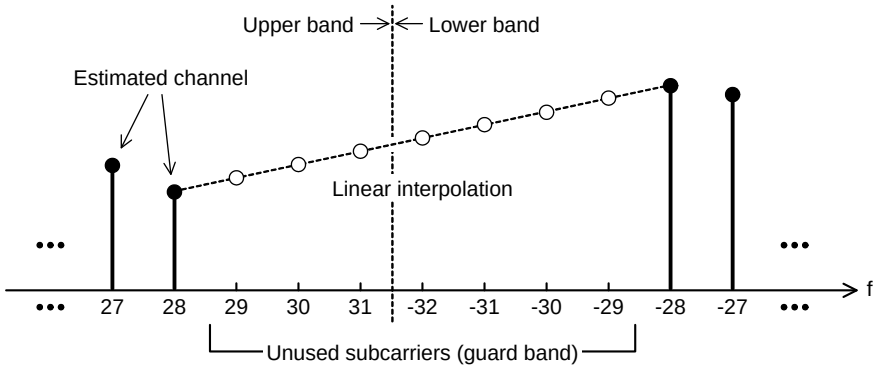

Figure 5.9: Concept of linear interpolation of an estimated channel in the frequency domain ($N_f = 64$).

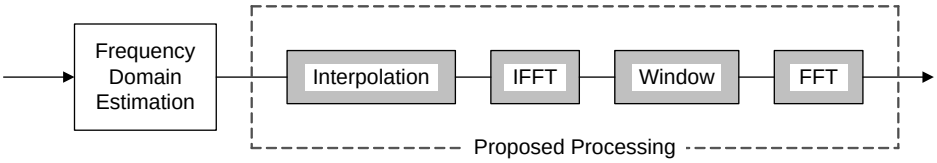

Figure 5.10: Process flow chart of effective channel estimation with time windowing.

5.4.2 Time-Windowing Scheme in PE-SDM

In addition to the above channel estimation method, we can improve the accuracy of the estimated effective channel in PE-SDM by applying the following simple processing. As stated in §5.3.3, the impulse responses of effective channels in PE-SDM are concentrated in the range of $|t| \leq T_d$ and are at a significantly lower level in $|t| > T_d$ (Figs. 5.2 and 5.3). Accordingly, when the effective channel is estimated using the above method, its impulse response in $|t| > T_d$ ought to be dominated by thermal noise. Then the author proposes to reduce thermal noise components included in the effective channel estimates by time windowing. For the sake of simplicity, in the study the author considers applying a simple time window function as illustrated in Fig. 5.8, where T_w is defined as the time window width, and G_{out} denotes the attenuation level outside the window ($G_{\mathrm{out}} \leq 1$). The impulse response, which is obtained by applying the IFFT to the effective channel estimate, is multiplied by the window. When we set $T_w \geq T_d$, we can efficiently capture the impulse response concentrated in $|t| \leq T_d$, and thermal noise components outside the window, i.e., $|t| > T_w$, are reduced. However, when some subcarriers are not used for transmission, such as guard bands, the IFFT distorts the impulse response [59]. To avoid this, values at the unused subcarriers are interpolated before the IFFT. Under the assumption that the effective channel is cyclic in the frequency domain, linear interpolation is simply done by using estimated values of the used subcarriers, which are the closest

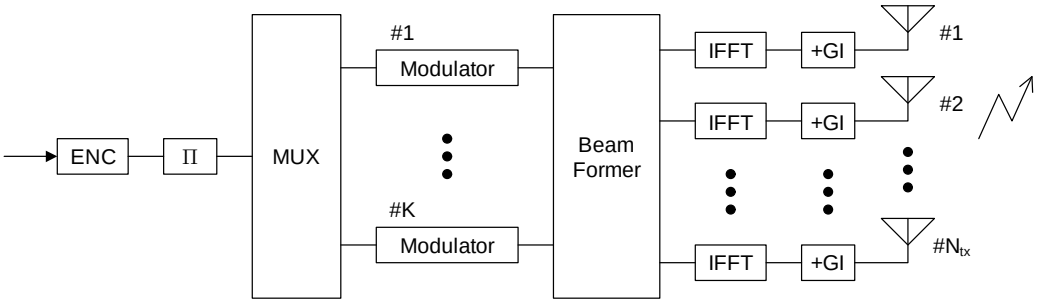

(a) Transmitter structure

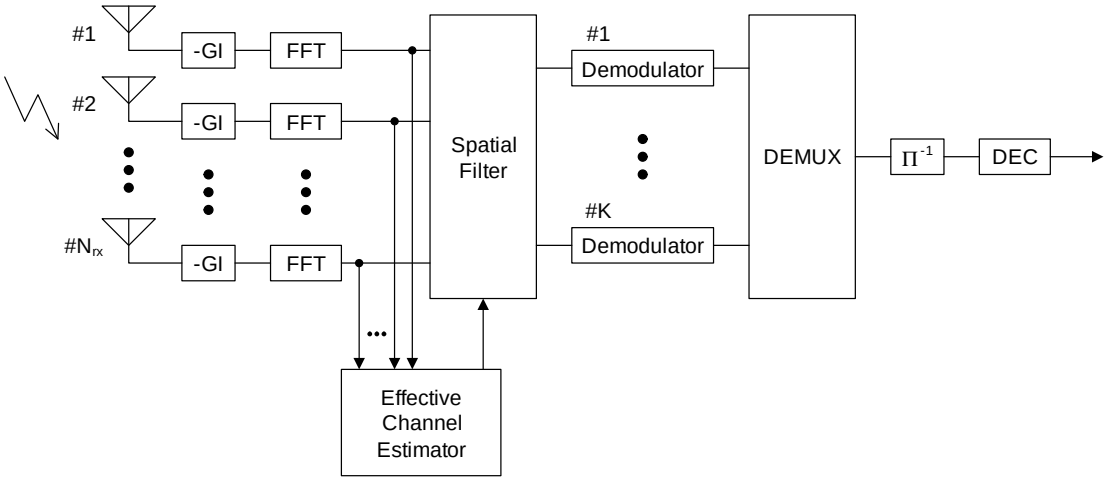

(b) Receiver structure

Figure 5.11: Block diagram.

to unused subcarriers (Fig. 5.9). After time windowing, we obtain the refined effective channel estimate by applying the FFT to the impulse response. A process flow chart of the effective channel estimation with time windowing is illustrated in Fig. 5.10.

5.5 MIMO-OFDM Computer Simulations

To evaluate the proposed pseudo eigenbeam technique and time windowing scheme, this section examines BER performance of PE-SDM comparing with that of E-SDM by computer simulations.

5.5.1 System Structure

Figure 5.11 illustrates both the transmitter and receiver structures. A transmitted data sequence is encoded and randomly interleaved before multiplexing. This process yields an effect of space-frequency diversity in a decoded sequence at the receiver. Then encoded

Table 5.3: MIMO-OFDM simulation parameters.

MIMO systems	2×2 ($N_{\mathrm{LP}} = 2$), 4×4 ($N_{\mathrm{LP}} = 4$)
No. of FFT points	$N_f = 64$
No. of subcarriers	56
GI duration	16 samples
Channel model	Quasi-static i.i.d. Rayleigh fading Scenario A, Scenario B
Substream detection	MMSE spatial filtering
Encoding	BCC (constraint length 3 and rate 1/2) with space-time-frequency random bit-interleaving
Decoding	Soft-decision Viterbi algorithm
No. of data symbols	8
Bit rate	8 coded bits/symbol/subcarrier
Modulation schemes	QPSK, 16QAM, 64QAM, 256QAM
Substream quality	E-SDM: $E\left[\lambda_i(f)\right]/\sigma^2$, PE-SDM: $E\left[\lambda_i'(f)\right]/\sigma^2$
No. of trial frames	100,000

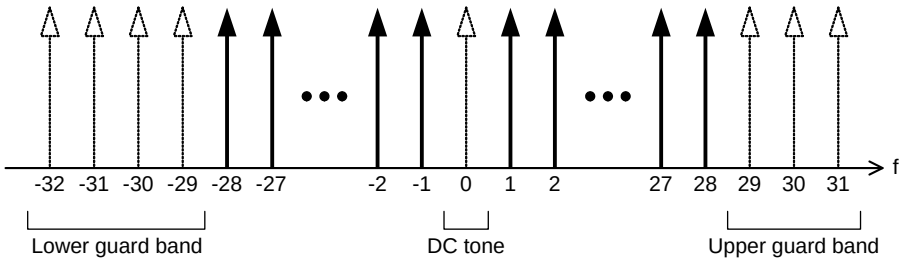

Figure 5.12: Subcarrier arrangement.

bits are mapped to constellations for each substream and beamformed based on power-allocated weight matrices $\boldsymbol{U}(f)\sqrt{\boldsymbol{P}(f)}$ at all subcarriers. According to the IEEE802.11a standard [5, 6], a modulation scheme is common to all the subcarriers in each substream. It is also assumed that TX power allocation is common to all the subcarriers, i.e., $\boldsymbol{P}(f) = \boldsymbol{P}$, to simplify TX processing and not to enlarge the delay spread of the effective channel.

At the receiver, GIs are removed from the received signals, and then the FFT is applied to them. Substreams are detected at each subcarrier by a spatial filter based on the effective channel estimate. The demultiplexed sequence are deinterleaved and decoded, and then we obtain an estimated data sequence.

5.5.2 Simulation Conditions

Table 5.3 lists the MIMO-OFDM simulation parameters. The performance for 2×2 and 4×4 MIMO systems was examined. Referring to the IEEE802.11a standard and contents in the IEEE802.11n standardization [5,6], the FFT size was set to $N_f = 64$, and 56 subcarriers were used for transmission, except for those in guard bands and at the center as illustrated in Fig. 5.12. Each OFDM symbol had 80 samples because of the GI duration of 16 samples.

It was assumed that the transmitter had perfect CSI by feedback through an error-free channel in a frequency division duplex system [55, 63, 83] or by channel estimation at the transmitter in a time division duplex system [32, 84]. On the other hand, it was assumed that only the number of substreams and modulation schemes were known at the receiver except in the "perfect CSI case" where the CSI is also known. In the estimated CSI case, the time window width T_w was set to T_d under the assumption that the receiver could accurately estimate the maximum time delay of paths. The attenuation level $G_{\rm out} = -10$ dB was used because it provided stable improvement of effective channel estimates in various MIMO cases. The MMSE criterion was used for determining spatial filter weights. A $K \times N_{\rm rx}$ MMSE weight matrix $\boldsymbol{W}(f)$ at subcarrier f is given by

$$\boldsymbol{W}(f) = \hat{\boldsymbol{B}}_F^H(f) \left\{ \hat{\boldsymbol{B}}_F(f) \hat{\boldsymbol{B}}_F^H(f) + \sigma^2 \boldsymbol{I}_{N_{\rm rx}} \right\}^{-1} \tag{5.23}$$

$$= \left[\boldsymbol{w}_1(f) \ \cdots \ \boldsymbol{w}_K(f) \right]^T, \tag{5.24}$$

where $\hat{\boldsymbol{B}}_F(f)$ indicates an effective channel estimate, $\boldsymbol{I}_{N_{\rm rx}}$ denotes an $N_{\rm rx}$-dimensional unit matrix. A K-dimensional MMSE output vector is obtained by multiplying $\boldsymbol{r}(f)$ by $\boldsymbol{W}(f)$. A data sequence was coded by a BCC encoder with constraint length of three and coding rate of 1/2. A data frame was composed of eight OFDM symbols. The random bit interleaver size corresponded to the frame size. Soft-decision Viterbi decoding was applied. LLR calculation for the decoding was the same as in §2.5. In order to reflect channel quality depending on the substream and subcarrier, the obtained LLR was multiplied by the corresponding SINR at the MMSE spatial filter output, i.e., $\boldsymbol{w}_i^T(f) \hat{\boldsymbol{b}}_{F,i}(f) / \left\{ 1 - \boldsymbol{w}_i^T(f) \hat{\boldsymbol{b}}_{F,i}(f) \right\}$ (see §2.4.4).

Eight coded bits were assigned per OFDM symbol per subcarrier. The system prepared four modulation schemes: QPSK, 16QAM, 64QAM, and 256QAM. Under these conditions and total TX power constraint, the transmitter optimally determines the modulation scheme and TX power per substream so as to give the minimum BER averaged over utilized substreams after Viterbi decoding[2] [30, 71]. The transmitter employed mean eigenvalue $E\left[\lambda_i(f)\right]$ or mean pseudo eigenvalue $E\left[\lambda_i'(f)\right]$ averaged over all subcarriers in each substream as the substream-quality measure in the decision.

[2]Specifically, it was assumed at the transmitter that the SNR after Viterbi decoding is equivalently increased by $d_{\rm free}$ times that before decoding, where $d_{\rm free}$ denotes the minimum free distance which is inherent to the BCC encoder [71]. See [71] for the details of an analysis on BCC. Note that the BCC used in this simulation has $d_{\rm free} = 5$.

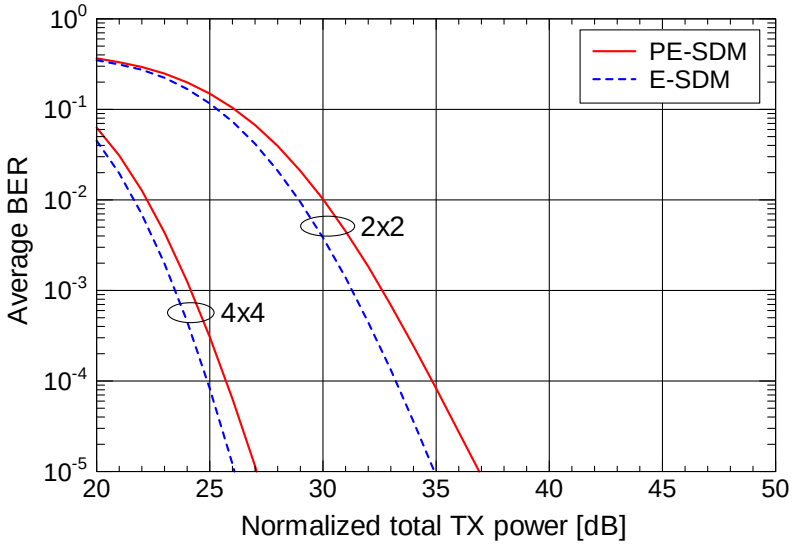

(a) Scenario A

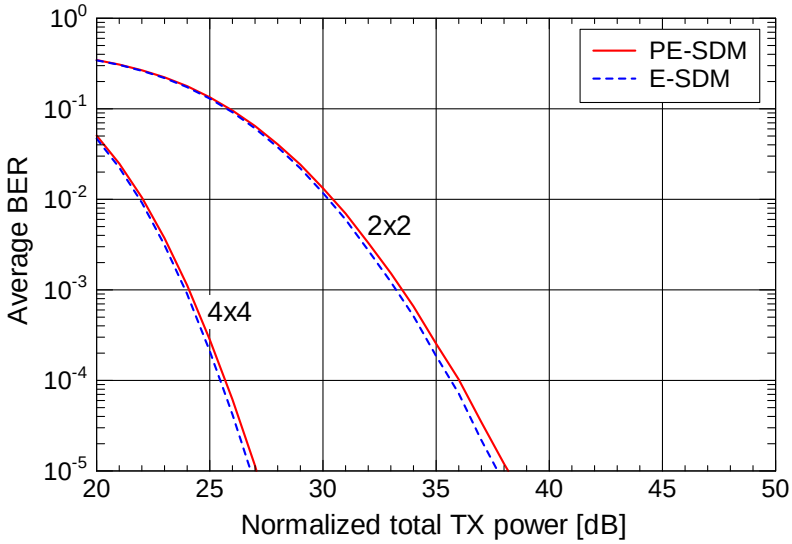

(b) Scenario B

Figure 5.13: Average BER performance for the perfect CSI case.

5.5.3 Simulation Results

Figure 5.13 shows the average BER performance versus normalized total TX power for the case of perfect CSI at the receiver. Here, the normalized total TX power, which is introduced for fair comparison of PE-SDM and E-SDM, denotes the total TX power normalized to the TX power yielding average E_s/N_0 of 0 dB in a case of single-antenna OFDM transmission in the corresponding multipath fading scenario. Thus, note that actual TX power

depends on the total power of multipaths.

It is evident that the performance for the 4×4 MIMO system is significantly improved compared with that for the 2×2 MIMO system regardless of PE-SDM/E-SDM and the scenario. This is yielded by an increase in the MIMO channel capacity. Let us compare the basic performance of PE-SDM with that of E-SDM. In E-SDM, since the transmitter utilizes TEVs of the channel at each subcarrier, the optimum beamforming gives excellent performance in both 2×2 and 4×4 MIMO systems. Compared with E-SDM, the performance for PE-SDM deteriorates due to gain loss, which occurs in reducing inter-substream interference by spatial filtering. At the BER of 10^{-5}, the degradation of PE-SDM for Scenario A is about 2 dB and 1 dB for 2×2 and 4×4 MIMO cases, respectively. However, that for Scenario B is less than 0.5 dB for both MIMO cases. The difference between the scenarios is due to the accuracy of produced PEVs as stated in §5.3.5. The PE-SDM scheme is, hence, more effective in lower delay spread environments.

The BER performance for the estimated CSI case is shown in Fig. 5.14. When the receiver estimates the effective channel only in the frequency domain, both the E-SDM and PE-SDM performances deteriorate by 2–3 dB compared with the perfect CSI case regardless of the number of antennas. However, with time windowing in addition to the frequency-domain estimation, the PE-SDM obtains about 1 dB and 2 dB gain for Scenario A and Scenario B, respectively. This implies that the impulse responses of the effective channels in the PE-SDM are well concentrated within the window and that thermal noise components outside the window are effectively reduced. Because of these benefits, the PE-SDM performance is almost the same as the E-SDM one for Scenario A, and the PE-SDM for Scenario B provides better performance than the E-SDM. The significant gain for Scenario B is because the receiver could narrow the time window width optimally since it was assumed that the receiver could accurately estimate the maximum time delay T_d. It is difficult in practice, however, to achieve such accurate estimation, and the time window width T_w depends on the delay profile of the effective channel, i.e., its frequency continuity. In a practical case where T_w is set more roughly, the effect of the time windowing may decrease. Therefore, setting of T_w and window shape should be examined in the future work. Note that error floors are observed for the E-SDM performance with time windowing regardless of the fading scenario and number of antennas because time windowing caused distortion in the impulse responses of the effective channel estimates as evidenced by Figs. 5.2(b), 5.3(b), and 5.8.

Here, let us discuss additional complexity at the receiver for time windowing, separately from the numerical complexity required at the transmitter for obtaining PEVs/TEVs (see §5.3.4). We compare the complexity with substantial calculation at the receiver composed of conventional frequency-domain channel estimation (FDCE) and MMSE weight generation. Table 5.4 lists the maximum numbers of complex multiplications needed at the receiver for FDCE, MMSE, and time windowing. These numbers were counted under a full-substream transmission case in each MIMO system, i.e., two-substream transmission in 2×2 MIMO and four-substream transmission in 4×4 MIMO. We can see that time windowing costs 48.2% and 35.9% increases in computational complexity in 2×2 and

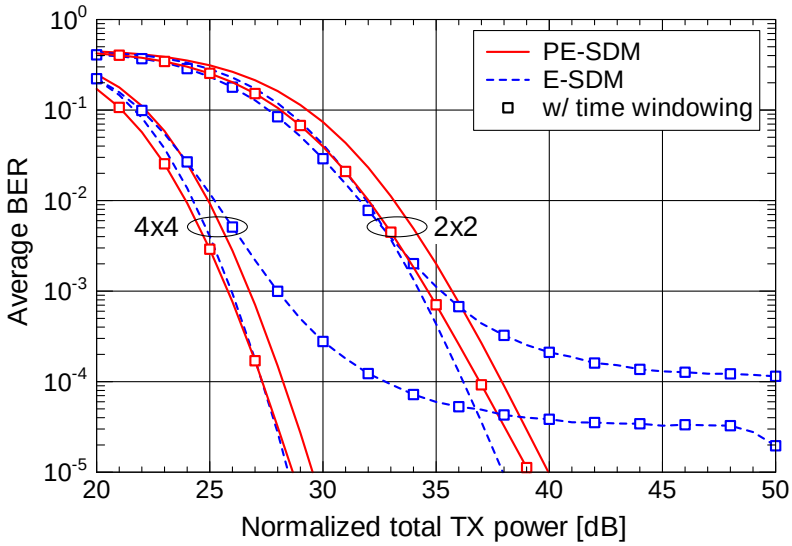

(a) Scenario A

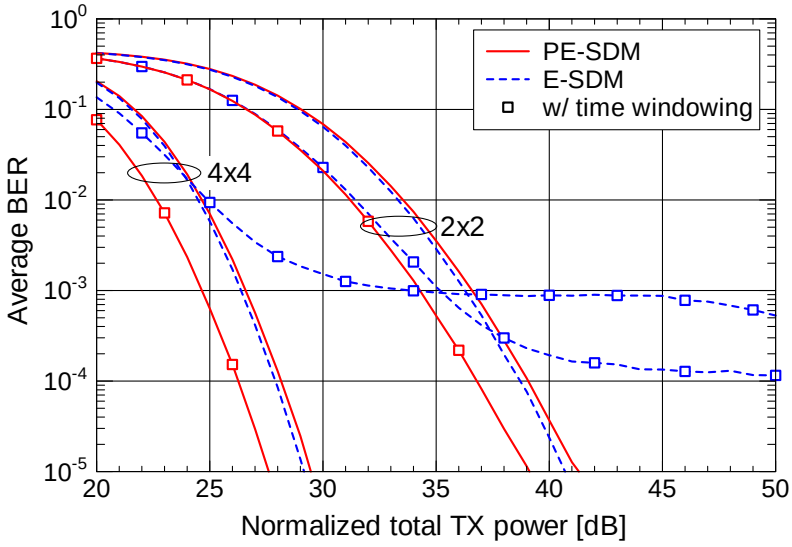

(b) Scenario B

Figure 5.14: Average BER performance for the estimated CSI case.

Table 5.4: Maximum numbers of complex multiplications at the receiver per frame for conventional frequency-domain channel estimation (FDCE), MMSE weight calculation, and time windowing (TW).

	Number of complex multiplications (maximum value)	
	FDCE + MMSE	TW
2×2 MIMO (2 substreams)	1,376 + 1,876 = 3,252	1,566
4×4 MIMO (4 substreams)	6,528 + 10,920 = 17,448	6,264

4×4 MIMO cases, respectively, from the substantial calculation load (FDCE + MMSE). As illustrated in Fig. 5.10, time window processing is composed of interpolation, IFFT, windowing, and FFT, and about 98% cost for time windowing is occupied by FFT and IFFT. Thus, the hardware implementation cost would be negligible if we can reuse the FFT and IFFT circuits for other purposes.

5.6 Numerical Analysis in MIMO-SC Systems

So far, the author has proposed the PEV technique which can reduce the calculation load and maintain frequency continuity of the effective channel. The result showed that the PE-SDM technique can provide almost the same or better MIMO-OFDM performance compared with the E-SDM when the receiver refines the effective channel estimate with time windowing. Such frequency-domain beamforming can also be applied to SC systems with FDE at the receiver [62]. This section evaluates the throughput performance of PE-SDM in a SC system with MMSE-FDE and is compared with E-SDM, in the latter a similar concept proposed in [63] is applied to improve frequency continuity. Also, focusing on the calculating process of PEVs, a spatial windowing scheme is proposed for improving the accuracy of effective channel estimates. In addition, the author also proposes an estimator of effective channels incorporating both the time and spatial windowing schemes, i.e., space-time windowing.

5.6.1 Power Delay Profile of Effective Channels

Figure 5.15 illustrates mean power delay profiles of effective channels for a 4×4 MIMO case. In addition, RMS delay spreads for 2×2, 3×3, and 4×4 MIMO cases are listed in Table 5.5. The FFT size was $N_f = 256$, and TX weights with equal power were multiplied at all N_f frequency points. The multipath scenario was the same as Scenario A in the above sections. That is, $\boldsymbol{H}_T(t)$ was assumed to have 16 sample-spaced paths ($T_d = 15$) with average 1-dB decaying as illustrated by vertical lines in Fig. 5.15. Delay profiles were averaged over 100,000 different channels. As a first step to improve frequency continuity

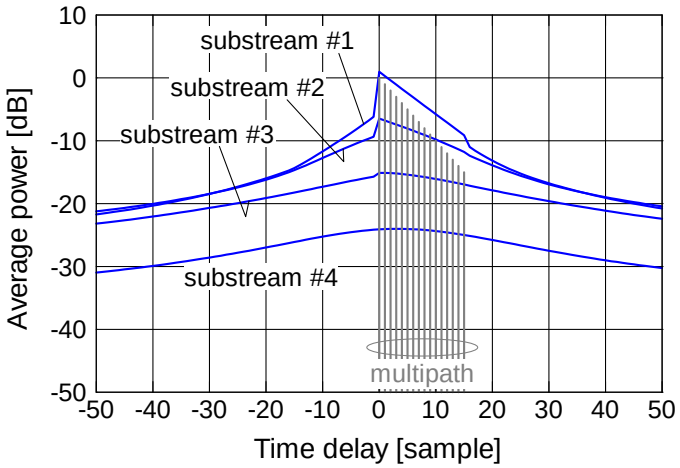

(a) TEV

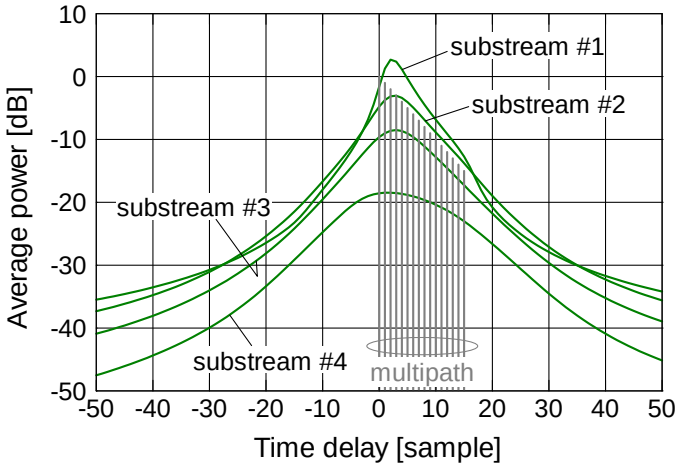

(b) TEV with PC

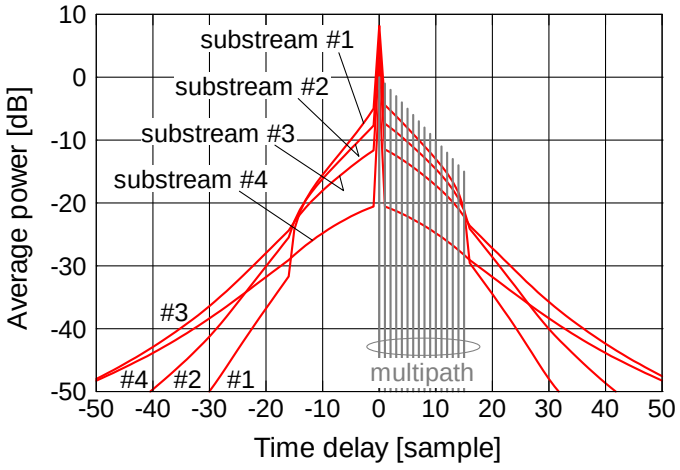

(c) PEV

Figure 5.15: Power delay profiles of effective channels (4×4 MIMO, $N_f = 256$).

Table 5.5: RMS delay spreads of effective channels in samples ($N_f = 256$).

		substream			
		#1	#2	#3	#4
2×2	TEV	18.05	21.82	—	—
	TEV w/ PC	5.40	7.69	—	—
	PEV	3.03	3.44	—	—
3×3	TEV	25.74	38.11	41.94	—
	TEV w/ PC	5.65	7.27	9.24	—
	PEV	2.99	3.84	4.21	—
4×4	TEV	22.99	36.36	47.24	49.33
	TEV w/ PC	5.88	7.57	8.52	10.52
	PEV	2.97	3.58	4.53	4.85
multipath		3.47			

for the TEV case, the EVD of $\boldsymbol{H}_F^H(f)\boldsymbol{H}_F(f)$ was calculated under a constraint forcing the first element of each TEV to be real, as in §5.3.3.

Figure 5.15(a) illustrates delay profiles of effective channels in the TEV case. Like the case in §5.3.3, since TEVs naturally have very limited frequency continuity, delay spread of each substream becomes quite large. Note that mean power delay profiles for the TEV case would be almost flat for all substreams if TEVs were calculated without the constraint mentioned above.

To mitigate the frequency discontinuity in the TEV case, the author introduces the following compensation scheme based on a phase rotation arising from the concept in [63]. We first estimate a phase difference in an average sense between two consecutive ith eigenvectors in the frequency domain by

$$\Delta_i(f) = \frac{\boldsymbol{u}_{e,i}^H(f)\boldsymbol{u}_{e,i}(f-1)}{\left|\boldsymbol{u}_{e,i}^H(f)\boldsymbol{u}_{e,i}(f-1)\right|}. \tag{5.25}$$

Then we reduce the phase difference between $\boldsymbol{u}_{e,i}(f-1)$ and $\boldsymbol{u}_{e,i}(f)$ by multiplying $\boldsymbol{u}_{e,i}(f)$ by $\Delta_i(f)$ since arbitrary phase rotation does not change eigenvector properties of $\boldsymbol{u}_{e,i}(f)$. By applying the procedure from $f = 1$ to $N_f - 1$ successively, we can prevent a fast phase rotation in the frequency domain. Figure 5.15(b) shows results of TEVs after the phase compensation (PC). Although this compensation scheme is not a global optimization to achieve frequency continuity, all substreams have lower delay spreads compared with the TEV case without the PC shown in Fig. 5.15(a). Therefore, in computer simulations in §5.6.4 and §5.6.5 TEVs after the PC are used in order to apply time windowing even for the E-SDM case.

In contrast, we can see that such efforts are unnecessary for PEVs as shown in Fig. 5.15(c). PEVs concentrate impulse responses in the region of $|t| \leq T_d$ and give high peaks at $t = 0$ regardless of the substream. Also, the responses in the region of $|t| > T_d$

are at a significantly low level. This means that the delay spreads of effective channels are highly reduced by using PEVs, as evidenced by Table 5.5. Consequently, we can say that PEVs as TX weights can maintain frequency continuity of effective channels.

5.6.2 Spatial Windowing and Space-Time Windowing

In the following, it is assumed that beamformed training blocks, which are composed of $N_{\mathrm{tr}} = 2^n$ blocks with space-time orthogonal codes, are transmitted prior to actual data blocks to estimate the effective channel in the frequency domain at the receiver [55], i.e., under the same assumption as in §5.4. Then the receiver can obtain the effective channel estimate $\hat{\boldsymbol{B}}_F(f)$.

Here, it is assumed that the receiver shares the unitary matrix $\boldsymbol{V}_0$ based on (5.16) with the transmitter. It is known that a GS operation achieves QR decomposition of a target matrix. Therefore, according to (5.17), an $N_{\mathrm{tx}} \times N_{\mathrm{rx}}$ matrix $\boldsymbol{H}_F^H(f)\boldsymbol{V}_0$ can be decomposed by using $\boldsymbol{U}_e'(f)$ as follows

$$\boldsymbol{H}_F^H(f)\boldsymbol{V}_0 = \boldsymbol{U}_e'(f)\boldsymbol{T}(f), \tag{5.26}$$

where $\boldsymbol{T}(f)$ is a $K \times N_{\mathrm{rx}}$ upper triangular matrix ($K \leq N_{\mathrm{rx}}$). We can rewrite (5.26) as

$$\boldsymbol{T}^H(f) = \boldsymbol{V}_0^H\boldsymbol{H}_F(f)\boldsymbol{U}_e'(f). \tag{5.27}$$

In the PE-SDM, an effective channel matrix is expressed as

$$\boldsymbol{B}_F(f) = \boldsymbol{H}_F(f)\boldsymbol{U}_e'(f)\sqrt{\boldsymbol{P}(f)}. \tag{5.28}$$

When the effective channel $\boldsymbol{B}(f)$ is multiplied by $\boldsymbol{V}_0^H$ on the left, i.e., $\boldsymbol{V}_0^H\boldsymbol{B}_F(f)$, it is transformed to a lower triangular matrix as follows

$$\begin{aligned}
\boldsymbol{V}_0^H\boldsymbol{B}_F(f) &= \boldsymbol{V}_0^H\boldsymbol{H}_F(f)\boldsymbol{U}_e'(f)\sqrt{\boldsymbol{P}(f)} && (5.29)\\
&= \boldsymbol{T}^H(f)\sqrt{\boldsymbol{P}(f)} && (5.30)\\
&= \begin{bmatrix} a_{11} & 0 & \cdots & 0 \\ a_{21} & a_{22} & \ddots & 0 \\ \vdots & \vdots & \ddots & \vdots \\ a_{N_{\mathrm{rx}}1} & a_{N_{\mathrm{rx}}2} & \cdots & a_{N_{\mathrm{rx}}K} \end{bmatrix} && (5.31)\\
&= \begin{bmatrix} \boldsymbol{V}_0^H\boldsymbol{b}_{F,1}(f) & \cdots & \boldsymbol{V}_0^H\boldsymbol{b}_{F,K}(f) \end{bmatrix} && (5.32)
\end{aligned}$$

Thus, the multiplication of $\boldsymbol{V}_0^H$ triangulates the effective channel matrix. For an estimated effective channel $\hat{\boldsymbol{B}}_F(f)$, however, upper triangular elements in $\boldsymbol{V}_0^H\hat{\boldsymbol{B}}_F(f)$ are not zero unlike the above ideal case due to thermal noise. The proposal is to add zero padding to the corresponding elements in $\boldsymbol{V}_0^H\hat{\boldsymbol{B}}_F(f)$ to improve the accuracy of effective channel estimates. This can be thought as spatial windowing. After the zero padding, we obtain

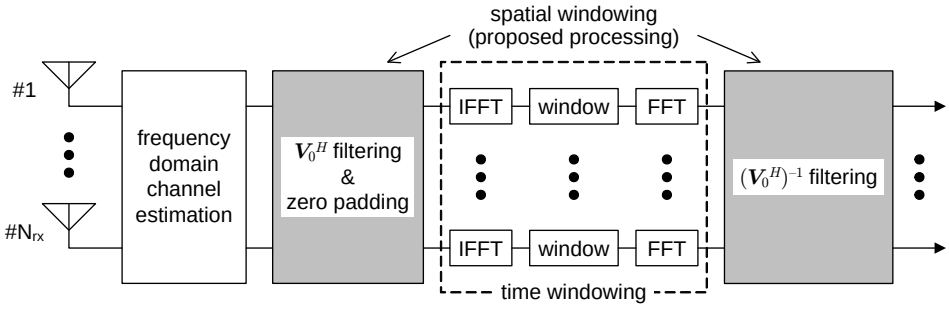

Figure 5.16: Process flow chart of channel estimation with space-time windowing.

a refined estimate $\tilde{\boldsymbol{B}}_F(f)$ by multiplying it by $(\boldsymbol{V}_0^H)^{-1}$ on the left. Since $\boldsymbol{V}_0$ is a unitary matrix, both multiplications of $\boldsymbol{V}_0^H$ and $(\boldsymbol{V}_0^H)^{-1}$ do not cause noise enhancement.

We can formulate the above procedure as follows. A diagonal zero-padding matrix for the ith substream is defined as

$$\boldsymbol{Z}_i = \mathrm{diag}(0, \cdots, 0, \underbrace{1, \cdots, 1}_{i\text{th}\sim N_{\mathrm{rx}}\text{th}}), \tag{5.33}$$

where the first $(i-1)$ diagonal elements in the matrix are 0, and the other diagonal elements are 1. Thus, $\boldsymbol{Z}_1$ for the first substream becomes an N_{rx}-dimensional unit matrix $\boldsymbol{I}_{N_{\mathrm{rx}}}$. Using $\boldsymbol{Z}_i$ and $\boldsymbol{V}_0^H$, spatial windowing for an initial effective channel estimate of the ith substream $\hat{\boldsymbol{b}}_{F,i}(f)$ can be expressed as

$$\tilde{\boldsymbol{b}}_{F,i}(f) = (\boldsymbol{V}_0^H)^{-1}\boldsymbol{Z}_i\boldsymbol{V}_0^H\hat{\boldsymbol{b}}_{F,i}(f). \tag{5.34}$$

Note that spatial windowing for the first substream is meaningless because we have

$$(\boldsymbol{V}_0^H)^{-1}\boldsymbol{Z}_1\boldsymbol{V}_0^H = \boldsymbol{I}_{N_{\mathrm{rx}}}. \tag{5.35}$$

The spatial windowing scheme can be combined with the time windowing scheme, i.e., space-time windowing. Its process flow chart is illustrated in Fig. 5.16. Since $\boldsymbol{V}_0^H$ is a frequency-flat weight matrix, it does not change the frequency characteristics. Thus, the $\boldsymbol{V}_0^H$ (and $(\boldsymbol{V}_0^H)^{-1}$) filtering is applicable independently of time windowing.

Moreover, we can reduce the number of target channel elements that need FFT/IFFT when time windowing is applied after multiplication of $\boldsymbol{V}_0^H$. For example, in a four-substream transmission in a 4×4 MIMO system, all 16 channel elements in $\hat{\boldsymbol{B}}_F(f)$ need FFT/IFFT processing. On the other hand, the number of lower triangular channel elements in $\boldsymbol{V}_0^H\hat{\boldsymbol{B}}_F(f)$ is 10 so that we can reduce the FFT/IFFT complexity in the time windowing part to $10/16 = 62.5\%$ with space-time windowing.

5.6.3 System Structure

Figure 5.17 illustrates both the transmitter and receiver structures. A transmitted data sequence is encoded and randomly bit-interleaved before multiplexing. This process yields

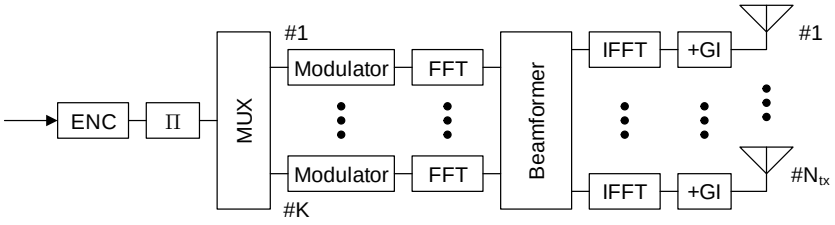

(a) Transmitter structure

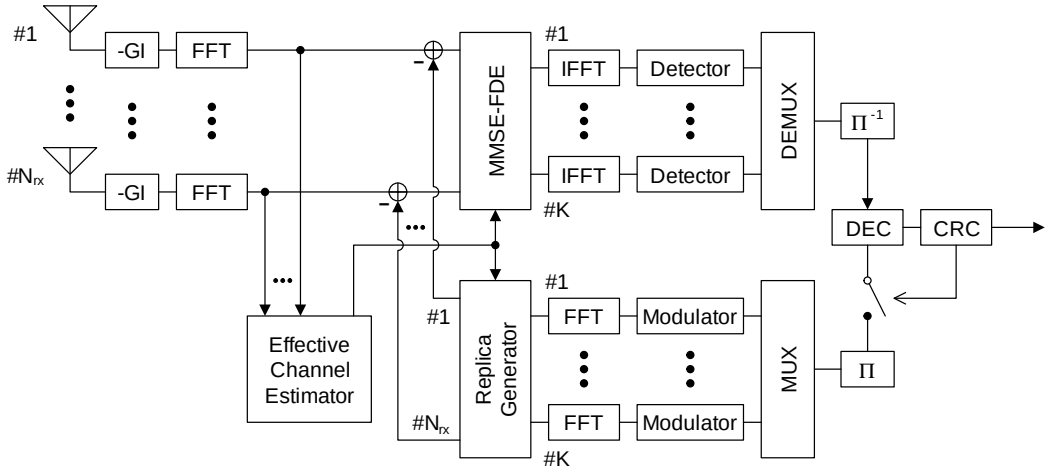

(b) Receiver structure

Figure 5.17: Block diagrams of transmitter and receiver.

an effect of spatial diversity in a decoded sequence at the receiver. Each modulated sequence is beamformed based on power-allocated weight matrices $\boldsymbol{U}(f)\sqrt{\boldsymbol{P}(f)}$ after applying the FFT. In the study, TX power allocation is common to all the frequency points, i.e., $\boldsymbol{P}(f) = \boldsymbol{P}$, to simplify TX control and not to enlarge the delay spread of the effective channel. After the IFFT, a GI is added at beginning of a signal transmitted from each TX antenna.

At the receiver, after GI removal and FFT operation, the received signals are equalized and separated to substreams by the MMSE-FDE based on the effective channel estimate [62, 85, 86]. As in (2.41), a $K \times N_{\mathrm{rx}}$ MMSE weight matrix at frequency point f is given by

$$\boldsymbol{W}(f) = \hat{\boldsymbol{B}}_F^H(f)\left\{\hat{\boldsymbol{B}}_F(f)\hat{\boldsymbol{B}}_F^H(f) + \sigma^2\boldsymbol{I}_{N_{\mathrm{rx}}}\right\}^{-1} \tag{5.36}$$

$$= \begin{bmatrix} \boldsymbol{w}_1^T(f) \\ \vdots \\ \boldsymbol{w}_K^T(f) \end{bmatrix}, \tag{5.37}$$

where $(\cdot)^T$ denotes the transpose. A K-dimensional MMSE output vector is obtained by

Table 5.6: MIMO-SC simulation parameters.

No. of antennas	$N_{\mathrm{tx}} = N_{\mathrm{rx}} = 4$ (4×4 MIMO)
No. of FFT points	$N_f = 256$ (symbols)
GI duration	16 symbols
Channel model	1-dB decaying 16 symbol-spaced paths ($T_d = 15$) Quasi-static i.i.d. Rayleigh fading
Training sequence	8-stage PN sequence (BPSK)
Training blocks	$N_{\mathrm{tr}} = 4$ blocks with 4×4 Walsh-Hadamard code
Time window width	$T_w = 15, 31, 47$
Attenuation level	$G_{\mathrm{out}} = 0$ ($-\infty$ dB)
Equalization	MMSE-FDE
Encoding	BCC (constraint length of 7 and original rate of 1/2)
Decoding	Max-log-MAP
No. of PIC iterations	2 iterations (maximum)
Modulation schemes	QPSK, 16QAM, 64QAM
Coding rate	1/2 (original), 3/4 (punctured)
Substream quality	E-SDM: $E[\lambda_i(f)]/\sigma^2$, PE-SDM: $E[\lambda_i'(f)]/\sigma^2$

multiplying $\boldsymbol{r}(f)$ by $\boldsymbol{W}(f)$ on the left, i.e., $\boldsymbol{W}(f)\boldsymbol{r}(f)$. The demultiplexed sequence is deinterleaved and decoded, and then we obtain an estimated data sequence. In PE-SDM, inter-substream interference may occur at the receiver as stated before. In addition to the MMSE-FDE, the receiver therefore applies a frequency-domain PIC using soft replica symbols [87] when a cyclic redundancy check detects errors in the estimated data sequence.

5.6.4 Simulation Conditions

Table 5.6 lists the simulation parameters. The throughput performance for a 4×4 MIMO system was examined. The FFT size N_f and the GI were set to 256 and 16, respectively. Thus, the transmitted block size became 272 symbols in total.

It was assumed that the transmitter had perfect CSI by feedback through an error-free channel, where channel transition during the feedback interval was negligible [55]. To share $\boldsymbol{V}_0$ between the both sides, $\boldsymbol{V}_0$ calculated at the receiver was also fed back to the transmitter simultaneously. It can be said that the additional feedback amount due to $\boldsymbol{V}_0$ is not serious since feedback information for estimated impulse responses $\hat{\boldsymbol{H}}_T(0), \ldots, \hat{\boldsymbol{H}}_T(T_d)$ is dominant. On the other hand, in data transmission, it was assumed that only the modulation schemes and coding rate were known at the receiver except the "perfect CSI case" where the CSI of effective channels is also known.

To estimate an effective channel for each substream at the receiver, the transmitter sent four training blocks composed of a BPSK-modulated PN sequence prior to data blocks. Here, we had four training sequences orthogonalized by a four-dimensional Walsh-Hadamard

code. The receiver estimated the effective channel in the frequency domain by combining the four blocks after the correspondent Walsh-Hadamard code multiplication. The attenuation level of time windowing was simply set to $G_{\text{out}} = 0$. LLR calculation for decoding was the same as in §2.5. In order to give consideration to channel-quality difference among the substreams, the obtained LLR was multiplied by the estimated SINR at the MMSE-FDE output of the ith substream, which is calculated by

$$\gamma_i = \frac{\dfrac{1}{N_f}\displaystyle\sum_{f=0}^{N_f-1} \boldsymbol{w}_i^T(f)\hat{\boldsymbol{b}}_{F,i}(f)}{1 - \dfrac{1}{N_f}\displaystyle\sum_{f=0}^{N_f-1} \boldsymbol{w}_i^T(f)\hat{\boldsymbol{b}}_{F,i}(f)}. \tag{5.38}$$

The maximum number of iterations in the PIC was two because more iterations did not provide visible improvement on performance.

A data sequence was coded by a BCC encoder with constraint length of seven and original coding rate of 1/2. In addition, coding rate 3/4 was also prepared with puncturing to increase the data rate. See [6] for the details of the puncturing pattern. The system used three modulation schemes: QPSK, 16QAM, and 64QAM. Considering the number of substreams, we had a total of 66 transmission patterns, or modulation and coding schemes (MCS), ranging from 1 to 18 bits per SDM-symbol as listed in Tables 5.7 and 5.8. For each pattern, the transmitter determined the optimum TX power allocation so as to give the minimum BER averaged over utilized substreams after Viterbi decoding, as in §5.5.2[3]. Note that, while the original BCC with constraint length of seven and rate 1/2 has $d_{\text{free}} = 10$, the punctured BCC with rate 3/4 has $d_{\text{free}} = 5$ [6, 71]. The transmitter employed mean eigenvalue $E\left[\lambda_i(f)\right]$ or mean pseudo eigenvalue $E\left[\lambda_i'(f)\right]$ averaged over all frequency points as the substream-quality measure.

[3] Actually, TX power allocation was determined so as to give the same BERs in all the utilized substreams because the Lagrange multiplier method giving the minimum BER has a tendency to give the same BER in each substream.

Table 5.7: MCS for a 4 × 4 MIMO system part 1 (1–7 bits per SDM-symbol).

index	modulation schemes				coding rate	bits/symbol
	substream #1	substream #2	substream #3	substream #4		
#1	QPSK	—	—	—	1/2	1
#2	QPSK	—	—	—	3/4	1.5
#3	16QAM	—	—	—	1/2	2
#4	QPSK	QPSK	—	—	1/2	2
#5	64QAM	—	—	—	1/2	3
#6	16QAM	QPSK	—	—	1/2	3
#7	QPSK	QPSK	QPSK	—	1/2	3
#8	16QAM	—	—	—	3/4	3
#9	QPSK	QPSK	—	—	3/4	3
#10	16QAM	16QAM	—	—	1/2	4
#11	64QAM	QPSK	—	—	1/2	4
#12	16QAM	QPSK	QPSK	—	1/2	4
#13	QPSK	QPSK	QPSK	QPSK	1/2	4
#14	64QAM	—	—	—	3/4	4.5
#15	16QAM	QPSK	—	—	3/4	4.5
#16	QPSK	QPSK	QPSK	—	3/4	4.5
#17	64QAM	16QAM	—	—	1/2	5
#18	64QAM	QPSK	QPSK	—	1/2	5
#19	16QAM	16QAM	QPSK	—	1/2	5
#20	16QAM	QPSK	QPSK	QPSK	1/2	5
#21	64QAM	64QAM	—	—	1/2	6
#22	64QAM	16QAM	QPSK	—	1/2	6
#23	16QAM	16QAM	16QAM	—	1/2	6
#24	64QAM	QPSK	QPSK	QPSK	1/2	6
#25	16QAM	16QAM	QPSK	QPSK	1/2	6
#26	16QAM	16QAM	—	—	3/4	6
#27	64QAM	QPSK	—	—	3/4	6
#28	16QAM	QPSK	QPSK	—	3/4	6
#29	QPSK	QPSK	QPSK	QPSK	3/4	6
#30	64QAM	64QAM	QPSK	—	1/2	7
#31	64QAM	16QAM	16QAM	—	1/2	7
#32	64QAM	16QAM	QPSK	QPSK	1/2	7
#33	16QAM	16QAM	16QAM	QPSK	1/2	7

Table 5.8: MCS for a 4 × 4 MIMO system part 2 (7.5–18 bits per SDM-symbol).

index	modulation schemes				coding rate	bits/symbol
	substream #1	substream #2	substream #3	substream #4		
#34	64QAM	16QAM	—	—	3/4	7.5
#35	64QAM	QPSK	QPSK	—	3/4	7.5
#36	16QAM	16QAM	QPSK	—	3/4	7.5
#37	16QAM	QPSK	QPSK	QPSK	3/4	7.5
#38	64QAM	64QAM	16QAM	—	1/2	8
#39	64QAM	64QAM	QPSK	QPSK	1/2	8
#40	64QAM	16QAM	16QAM	QPSK	1/2	8
#41	16QAM	16QAM	16QAM	16QAM	1/2	8
#42	64QAM	64QAM	64QAM	—	1/2	9
#43	64QAM	64QAM	16QAM	QPSK	1/2	9
#44	64QAM	16QAM	16QAM	16QAM	1/2	9
#45	64QAM	64QAM	—	—	3/4	9
#46	64QAM	16QAM	QPSK	—	3/4	9
#47	16QAM	16QAM	16QAM	—	3/4	9
#48	64QAM	QPSK	QPSK	QPSK	3/4	9
#49	16QAM	16QAM	QPSK	QPSK	3/4	9
#50	64QAM	64QAM	16QAM	16QAM	1/2	10
#51	64QAM	64QAM	QPSK	—	3/4	10.5
#52	64QAM	16QAM	16QAM	—	3/4	10.5
#53	64QAM	16QAM	QPSK	QPSK	3/4	10.5
#54	16QAM	16QAM	16QAM	QPSK	3/4	10.5
#55	64QAM	64QAM	64QAM	16QAM	1/2	11
#56	64QAM	64QAM	64QAM	64QAM	1/2	12
#57	64QAM	64QAM	16QAM	—	3/4	12
#58	64QAM	64QAM	QPSK	QPSK	3/4	12
#59	64QAM	16QAM	16QAM	QPSK	3/4	12
#60	16QAM	16QAM	16QAM	16QAM	3/4	12
#61	64QAM	64QAM	64QAM	—	3/4	13.5
#62	64QAM	64QAM	16QAM	QPSK	3/4	13.5
#63	64QAM	16QAM	16QAM	16QAM	3/4	13.5
#64	64QAM	64QAM	16QAM	16QAM	3/4	15
#65	64QAM	64QAM	64QAM	16QAM	3/4	16.5
#66	64QAM	64QAM	64QAM	64QAM	3/4	18

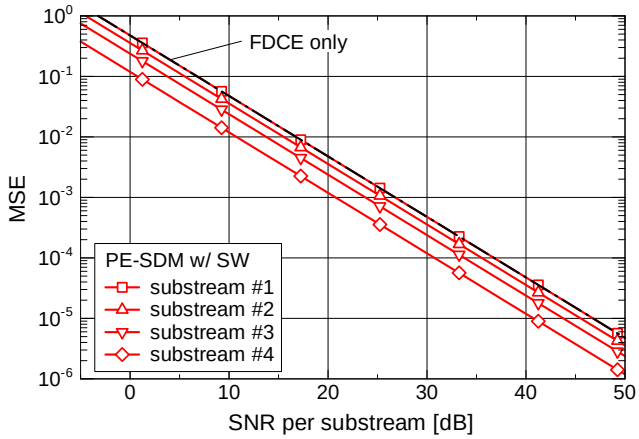

Figure 5.18: MSE performance in the PE-SDM case with spatial windowing.

5.6.5 Analysis of Channel Estimation Error

Before presenting the throughput performance, we evaluate channel estimation error with various windowing schemes in this subsection. Mean square error (MSE) of effective channel estimates for the ith substream is defined as

$$e_i = E\left[\left\|\hat{\boldsymbol{b}}_{F,i}(f) - \boldsymbol{b}_{F,i}(f)\right\|^2\right]. \tag{5.39}$$

This subsection examines MSE performance in the 4×4 MIMO system under a four-substream transmission constraint.

Figure 5.18 shows MSE performance versus SNR per substream in the PE-SDM case with spatial windowing. Here, "SW" denotes spatial windowing, and "FDCE only" denotes a result of FDCE without any windowing schemes. Note that spatial windowing was not applied to the first substream as mentioned in §5.6.2. We can see that with spatial windowing, MSE decreases as the substream index increases, and that channel estimates of the fourth substream are significantly refined. This is because the most zero-padded substream is the fourth substream as seen from (5.34). Therefore, we can expect that effect of spatial windowing appears as more substreams are utilized.

Figure 5.19 demonstrates effects of time windowing and space-time windowing on the MSE in the PE-SDM case. In addition, Fig. 5.20 shows MSE performance in the E-SDM case with time windowing. Here, "TW" and "STW" denote time windowing and space-time windowing, respectively.

In most time windowing cases of the PE-SDM, MSE floors can be seen in the high SNR region, whereas channel estimation accuracy is improved in the low SNR region. Those MSE floors become worse in the E-SDM case. These phenomena can be explained by delay profiles of effective channels illustrated in Figs. 5.15(b) and (c). Unlike actual multipath channels, effective channels have large delay spreads beyond time window width T_w, especially in the E-SDM case shown in Fig. 5.15(b). Also, the delay spread becomes larger

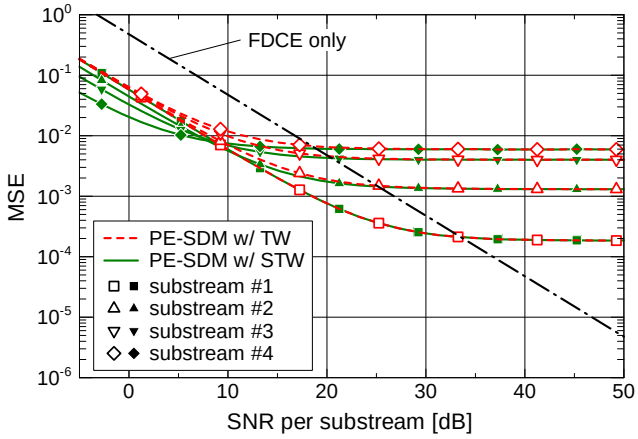

(a) $T_w = 15$

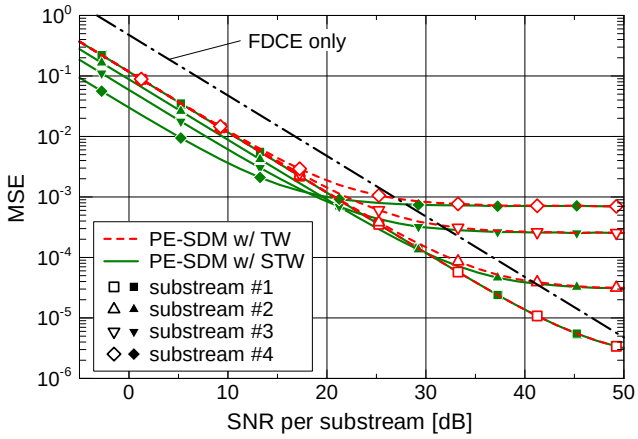

(b) $T_w = 31$

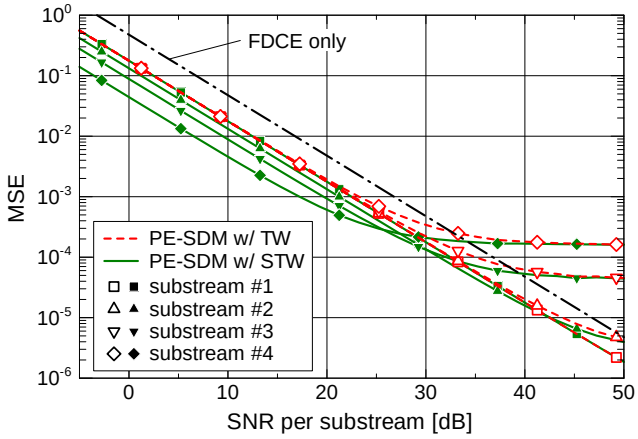

(c) $T_w = 47$

Figure 5.19: MSE performance in the PE-SDM case with time windowing and space-time windowing.

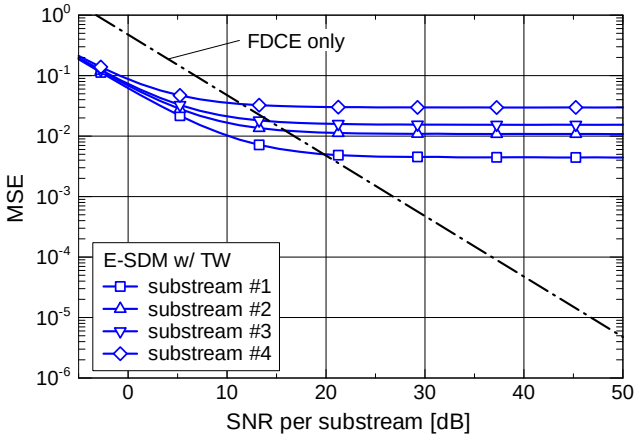

(a) $T_w = 15$

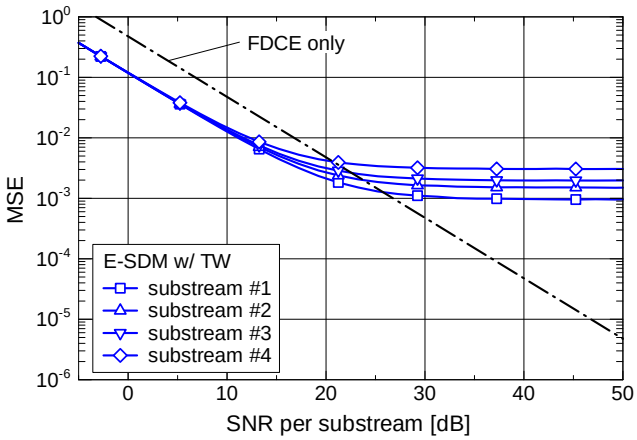

(b) $T_w = 31$

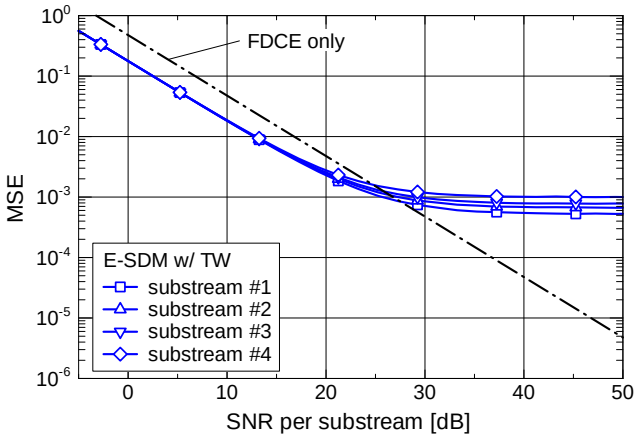

(c) $T_w = 47$

Figure 5.20: MSE performance in the E-SDM case with time windowing.

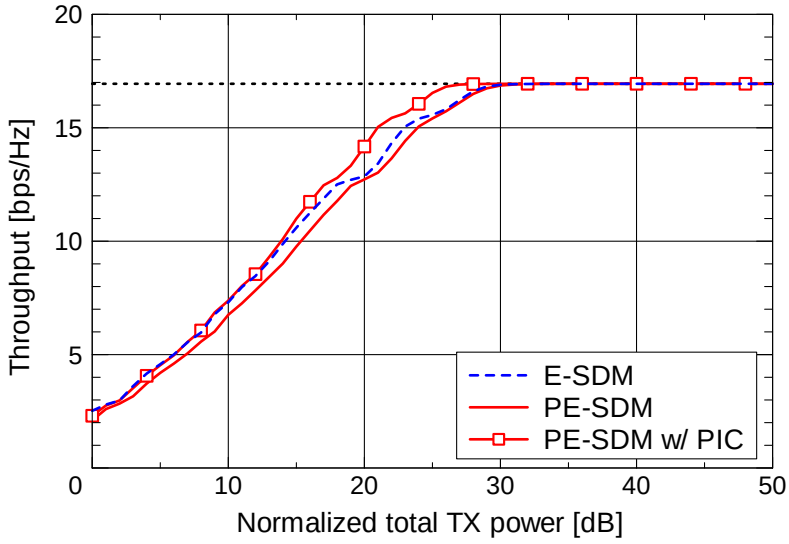

Figure 5.21: Throughput performance for the perfect CSI case.

as the substream index increases. Therefore, suppressing the channel impulse responses outside the time window simply causes a distortion in the effective channel estimation.

MSE floors in the PE-SDM case are, however, at lower levels compared with those in the E-SDM case. In the case of $T_w = 31$, while all the substreams in the E-SDM case show MSE floors, MSE of the first substream in the PE-SDM case linearly decreases as SNR increases. This is a benefit of frequency continuity of effective channels yielded by PEVs. Moreover, we can refine channel estimates by combining time windowing with spatial windowing, i.e., by space-time windowing, as shown in Fig. 5.19.

5.6.6 Throughput Performance

Figure 5.21 shows the throughput performance versus normalized total TX power for the case of perfect CSI at the receiver. Here, the normalized total TX power, which is introduced for fair comparison of PE-SDM and E-SDM, denotes the total TX power normalized to the TX power yielding average SNR of 0 dB in a case of single-antenna transmission under the same multipath environment. Note that the normalized total TX power is a different measure from SNR per substream used in Figs. 5.18, 5.19, and 5.20. The dotted horizontal line denotes the maximum throughput of 16.94 bps/Hz which is achieved when a transmission of 64QAM $\times$ 4 substreams with coding rate 3/4 succeeds ($6 \times 4 \times (3/4) \times (256/272) = 16.94$ bps/Hz).

Let us compare the basic performance of PE-SDM with that of E-SDM. In E-SDM, since the transmitter utilizes TEVs at each frequency point, the optimum beamforming gives excellent performance. Compared with E-SDM, the performance for PE-SDM deteriorates due to gain loss, which occurs in reducing inter-substream interference by the

Table 5.9: Maximum numbers of complex multiplications at the receiver per block for FDCE, MMSE, and three windowing schemes in the 4×4 MIMO case.

	Maximum number of complex multiplications
FDCE + MMSE	30,720 + 48,641 = 79,361
TW	32,768
SW	12,288
STW (TW + SW)	20,480 + 12,288 = 32,768

MMSE-FDE. At the throughput of 10 bps/Hz, the degradation of PE-SDM is about 1 dB.

By applying the PIC, however, we can compensate for the degradation and obtain better performance than E-SDM in the high TX power region over 10 dB. Achievement of higher throughput is yielded by use of more substreams so that the benefit of the PIC appears more clearly in this region. Meanwhile, it should be said that a part of the numerical complexity of TEV calculation is somewhat shifted into the PIC. However, the maximum additional computational load of the PIC with two iterations is only 26,113 complex multiplications in these cases. As in the later discussion, considering the calculation complexity required at the receiver, we can say that employment of the PIC is quite reasonable.

Next, the author examines the effect of time windowing on the performance in the estimated CSI case in Fig. 5.22. Here, the PIC is not used. Recalling Figs. 5.8 and 5.15, it is expected for PE-SDM that effective channel estimates can be improved as the time window width T_w becomes narrower up to T_d. As shown in the low SNR region in Fig. 5.19(a), although the narrowest case of $T_w = T_d = 15$ provides performance improvement in a low TX power region less than 20 dB, the throughput saturates before reaching the maximum one of 16.94 bps/Hz due to channel distortion caused by the window. As a result, the case of $T_w = 31$ provides stable improvement in the PE-SDM performance over a wide SNR range, where obtained gains at the throughput of 10 bps/Hz and 15 bps/Hz are 2.5 dB and 3 dB, respectively. (The optimum T_w and window shape should be examined in the future work because they depend on the multipath scenario.) Note that all the E-SDM cases with time windowing could not achieve the maximum throughput due to channel distortion shown in Fig. 5.20. It is confirmed that E-SDM in the case of $T_w = 63$ can achieve the maximum throughput whereas no improvement gain is obtained at the throughput of 15 bps/Hz.

Figure 5.23 shows the PE-SDM performance with time windowing, spatial windowing, and space-time windowing, where the time window width was set to $T_w = 31$. In comparison to the case of FDCE without any windowing schemes, spatial windowing provides 1 dB and 1.5 dB gains at the throughput of 10 bps/Hz and 15 bps/Hz, respectively. Moreover, space-time windowing yields higher gains of 2.8 dB and 3.8 dB at those throughput levels, respectively.

Here, let us discuss additional complexity at the receiver for the windowing schemes, separately from the numerical complexity required at the transmitter for

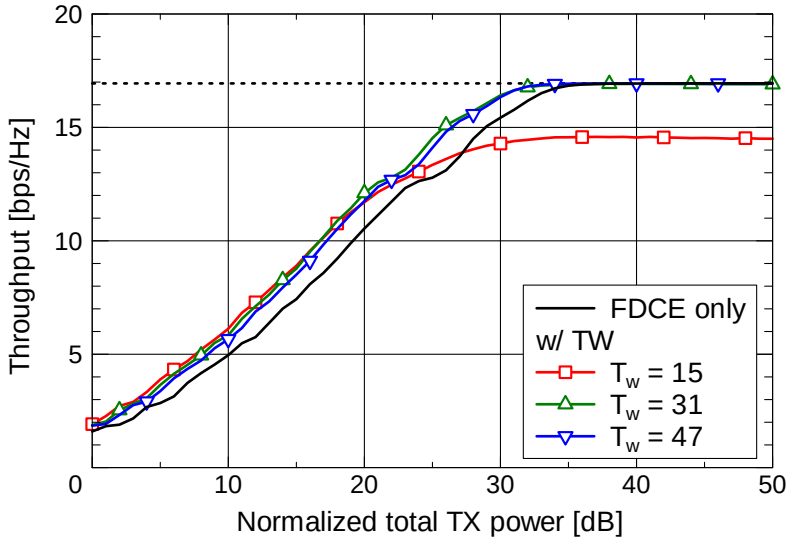

(a) PE-SDM

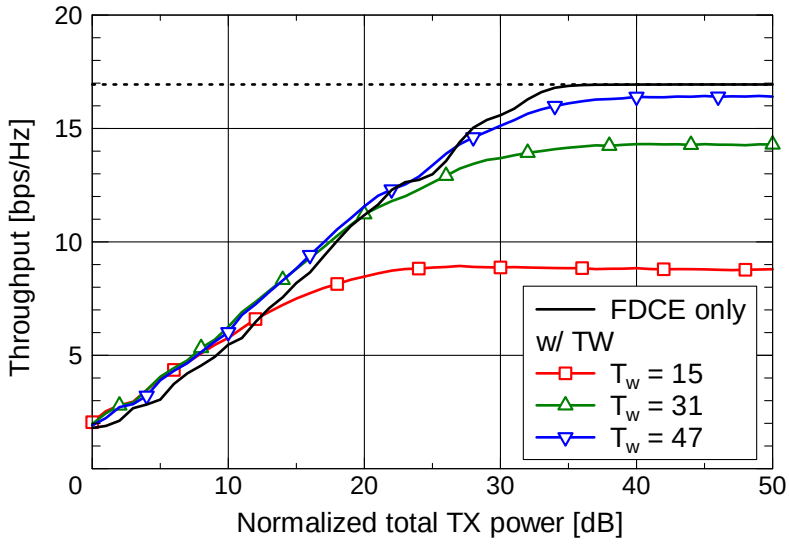

(b) E-SDM

Figure 5.22: Effect of time windowing on throughput performance.

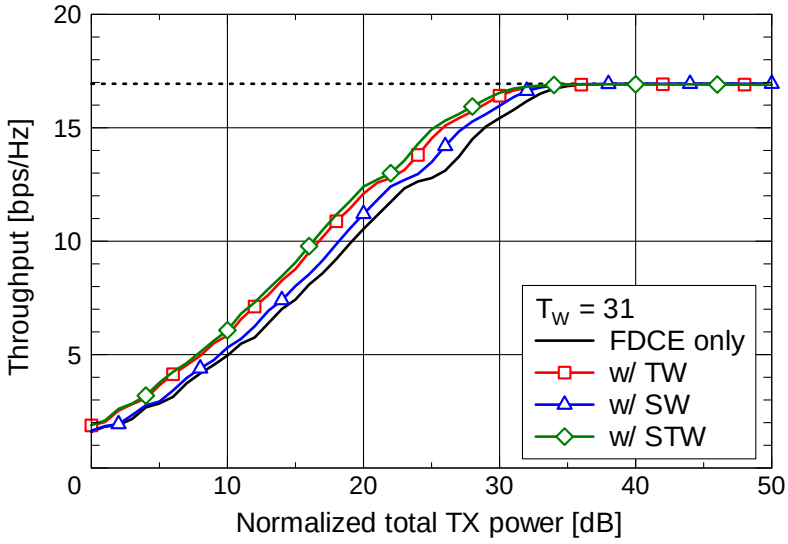

Figure 5.23: Effects of spatial windowing and space-time windowing on throughput performance.

obtaining PEVs/TEVs. Table 5.9 lists the maximum numbers of complex multiplications required at the 4×4 MIMO receiver for three windowing schemes: time windowing, spatial windowing, and space-time windowing. As a reference, the complexity of mandatory calculations (FDCE and MMSE weight generation) at the receiver is also listed at the top of Table 5.9. These numbers were counted under a four-substream transmission case. We can see that time windowing costs 41.3% increase in computational complexity from the substantial calculation load (FDCE + MMSE). As illustrated in Fig. 5.16, time window processing is composed of IFFT, windowing, and FFT, and about 98% cost for time windowing is occupied by FFT and IFFT (as mentioned in §5.5.3). Thus, the hardware implementation cost would be negligible if we can reuse the FFT and IFFT circuits for other purposes.

On the other hand, spatial windowing costs only a 15.5% increase. In addition, since space-time windowing can reduce the number of target channel elements which require FFT/IFFT as stated in §5.6.2, the total calculation load becomes less than the sum of time and spatial windowing. Actually, it is identical to that of the time windowing in this case. Considering the improvement gain mentioned above, space-time windowing can be said to be an effective solution.

Figure 5.24 shows the throughput performance with/without the PIC and space-time windowing in the estimated CSI case. Although the PIC can be applied to E-SDM in the estimated CSI case, the author does not consider it because the PIC did not provide visible improvement. In space-time windowing, the time window width was set to $T_w = 31$. For PE-SDM only with space-time windowing, a 3–4 dB gain is obtained compared with the case without space-time windowing, and a 1.5–3 dB gain is obtained compared with the

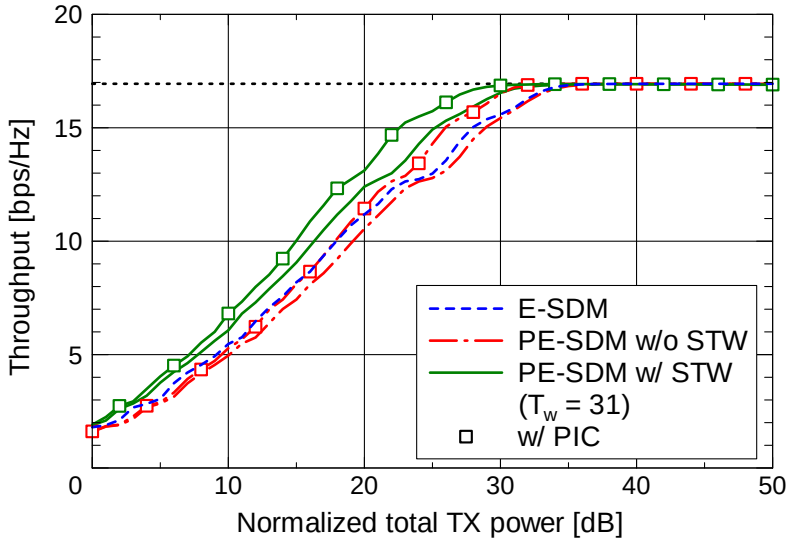

Figure 5.24: Throughput performance for the estimated CSI case.

E-SDM case in the high throughput region over 10 bps/Hz. Consequently, with space-time windowing, the performance difference between the perfect and estimated CSI cases is only 1 dB and 1.5 dB at the throughput of 10 bps/Hz and 15 bps/Hz, respectively. Both with the PIC and with space-time windowing, the PE-SDM obtains gains of 3 dB and 5.5 dB over the E-SDM at those throughput levels, respectively.

5.7 Conclusions

The author has proposed pseudo eigenvectors for frequency-selective MIMO channels. They can be calculated with less complexity than that of conventional EVD or SVD, and they can maintain frequency continuity of the effective channel observed at the receiver. Although the subchannel orthogonality in PE-SDM is lost due to the disagreement between the pseudo and true eigenvectors, the author confirmed that there was less performance degradation in a less frequency-selective fading environment, and it is possible to compensate for the degradation by the channel estimation improvement arising from the frequency-continuity property. Thus, when the receiver incorporates a channel estimator exploiting the property such as time windowing, PE-SDM can provide almost the same or even better performance compared with E-SDM.

Moreover, the author has also proposed spatial windowing and space-time windowing schemes exploiting pseudo eigenvector properties in order to improve the accuracy of estimation of effective channels. Although these two windowing schemes require a share of the matrix $\boldsymbol{V}_0$ between the transmitter and receiver, a channel estimator incorporating space-time windowing can refine channel estimates more than time windowing only. In

contrast, time windowing is currently inapplicable to E-SDM due to larger delay spread even though phase ambiguity of eigenvectors can be reduced in some degree by introducing the phase compensation scheme. Consequently, it has been shown that PE-SDM provides better throughput performance compared with E-SDM because of benefit arising from the space-time windowing.

Chapter 6

PE-SDM Performance Evaluation Using Measured Channel Data

In Chapter 5, the author clarified the availability of proposed PE-SDM in broadband systems based on typical channel models, which are assumed to be i.i.d. Rayleigh fading. Actual communication environments, however, might be LOS environments. Frequency selectivity in LOS environments tends to be lower due to a direct wave component, i.e., a high level component as described in §4.4. That is, we might have more frequency-flat channels in LOS environments. In the procedure of PEV calculation derived in §5.3.2, it is tentatively assumed that the channel is frequency-flat. Therefore, it is considered that LOS conditions are relatively closer to the assumption, so we can expect to obtain better PEVs in LOS environments. This chapter presents PE-SDM performance in actual environments by using the measured indoor LOS and NLOS channel data. Note that, as well as in §4.4, in the following the cases of AS $= 0.50\lambda$ and 1.00λ are examined to simplify the discussion.

6.1 System Structure

To evaluate PE-SDM performance in actual environments, here MIMO-OFDM systems are employed. Figure 6.1 illustrates the transmitter and receiver structures. The transmitter is the same as that in §5.5. A transmitted data sequence is encoded and randomly interleaved before multiplexing. This process yields an effect of space-frequency diversity in a decoded sequence at the receiver. Then encoded bits are mapped to constellations for each substream and beamformed based on power-allocated weight matrices $\boldsymbol{U}(f)\sqrt{\boldsymbol{P}(f)}$ at all subcarriers. According to the IEEE802.11a standard [5, 6], a modulation scheme is common to all the subcarriers in each substream. It is also assumed that TX power allocation is common to all the subcarriers, i.e., $\boldsymbol{P}(f) = \boldsymbol{P}$, to simplify TX processing and not to enlarge the delay spread of the effective channel.

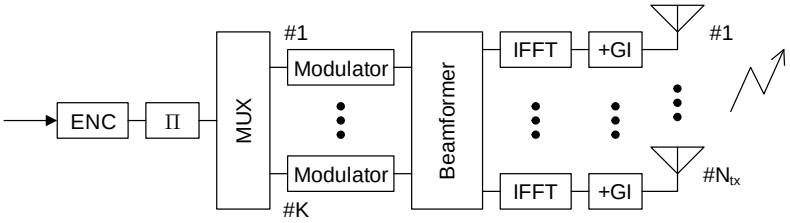

(a) Transmitter structure

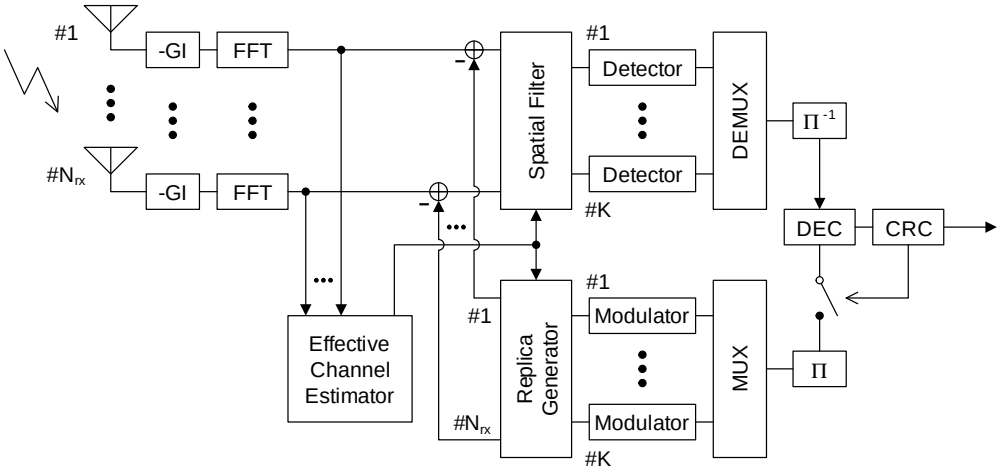

(b) Receiver structure

Figure 6.1: Block diagram of a MIMO-OFDM beamforming system.

At the receiver, GIs are removed from the received signals, and then the FFT is applied to them. Substreams are detected at each subcarrier by a MMSE spatial filter based on the effective channel estimate. The demultiplexed sequence is deinterleaved and decoded, and then we obtain an estimated data sequence. In PE-SDM, inter-substream interference may occur at the receiver. In addition to the MMSE spatial filtering, the receiver therefore applies a frequency-domain PIC-MMSE using soft replica symbols [87] when a cyclic redundancy check detects errors in the estimated data sequence.

Figure 6.2 illustrates the process flow chart of PE-SDM channel estimation in a MIMO-OFDM system. As in §5.4.1, it is presumed that the data frame has a long preamble with appropriate length (two OFDM symbols for 2×2 MIMO cases and four OFDM symbols for 4×4 MIMO cases) to separate and estimate effective channels for the utilized substreams at the receiver. Unlike the case of SC systems in §5.6, generally in OFDM systems we have unloaded subcarriers such as a DC tone or guard bands (see Fig. 5.12). When some subcarriers are not used for transmission, applying the IFFT to frequency-domain channel estimates distorts their impulse responses as stated in §5.4.2. To compensate estimates at those subcarriers, the effective channel estimator in this chapter therefore incorporates the same linear interpolator as shown in Fig. 5.9 for each channel element before the subse-

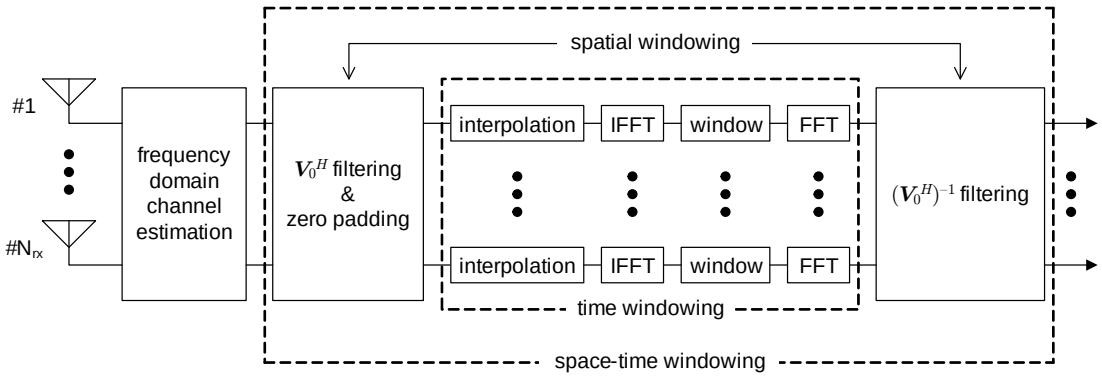

Figure 6.2: Process flow chart of PE-SDM channel estimation in a MIMO-OFDM system with inactive subcarriers.

quent time-windowing processing, i.e., IFFT, time windowing, and FFT.

6.2 Simulation Conditions

Table 6.1 lists the MIMO-OFDM simulation parameters. Referring to the IEEE802.11a standard and contents in the IEEE802.11n standardization [5, 6], the FFT size was set to $N_f = 64$, and 56 subcarriers were used for transmission, except for those in guard bands and at the center as illustrated in Fig. 5.12. Each OFDM symbol had 80 samples (4 μs) because of the GI duration of 16 samples.

It was assumed that the transmitter had perfect CSI by feedback through an error-free channel in a FDD system [55,63,83]. On the other hand, it was assumed that only the number of substreams and modulation schemes were known at the receiver except the "perfect CSI case" where the CSI is also known. To share $\boldsymbol{V}_0$ between the both sides, $\boldsymbol{V}_0$ calculated at the receiver was also fed back to the transmitter simultaneously. It can be said that the additional feedback amount due to $\boldsymbol{V}_0$ is not serious since feedback information for estimated impulse responses $\hat{\boldsymbol{H}}_T(0), \ldots, \hat{\boldsymbol{H}}_T(T_d)$ is dominant. In the estimated CSI case, the time window width T_w was set to the GI length, i.e., 16-sample duration. The attenuation level $G_{\text{out}} = 0$ ($-\infty$ dB) was used for the sake of simplicity. For comparison, performance of the conventional SDM was also examined. Since channel impulse responses in the SDM case are within the GI interval, time windowing for SDM was applied to channel estimates as illustrated in Fig. 6.3.

The MMSE criterion was used for determining the spatial filter weights. A data sequence was coded by a BCC encoder with constraint length of seven and coding rate of 1/2. A data frame was composed of eight OFDM symbols. The random bit interleaver size corresponded to the frame size. Soft-decision Viterbi decoding was applied.

In addition to the rate 1/2, coding rate 3/4 was also prepared with puncturing to increase the data rate [6]. In this case, the system used three modulation schemes: QPSK, 16QAM,

Table 6.1: MIMO-OFDM simulation parameters.

MIMO systems	2×2 ($N_{\mathrm{LP}} = 2$), 4×4 ($N_{\mathrm{LP}} = 4$)
Array orientation	TX-*x*/RX-*x*, TX-*y*/RX-*y*
AS	0.50λ, 1.00λ
Total channel sets	$7 \times 7 \times 1{,}473 = 72{,}177$
Bandwidth	20 MHz
FFT size	64 points (312.5 kHz interval)
No. of active subcarriers	56 (Fig. 5.12)
GI length	16 samples (800 ns)
OFDM symbol length	80 samples (4 μs)
Frame size	8 OFDM symbols
No. of FFT points	$N_f = 64$
No. of subcarriers	56
GI duration	16 samples
Substream detection	MMSE spatial filtering
Encoding	BCC (constraint length 7 and rate 1/2) with space-time-frequency random bit-interleaving
Decoding	Soft-decision Viterbi algorithm
Substream quality	E-SDM: $E\left[\lambda_i(f)\right]/\sigma^2$, PE-SDM: $E\left[\lambda_i'(f)\right]/\sigma^2$
Time window width T_w	16 samples (GI length)
Attenuation level in time windowing G_{out}	0 ($-\infty$ dB)

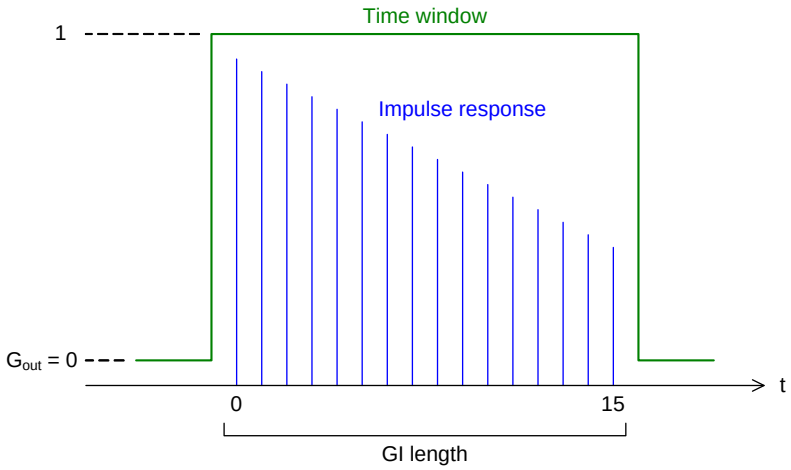

Figure 6.3: Time window function for the conventional SDM.

and 64QAM. Considering the number of substreams, we had a total of 66 transmission patterns as listed in Tables 5.7 and 5.8, where, note that, rates marked in bits/symbol in these tables become bits/symbol/subcarrier in the MIMO-OFDM systems. Also, since the number of substreams in 2×2 MIMO-OFDM cases is up to two substreams, corresponding transmission patterns in these tables (#1–#6, #8–#11, #14, #15, #17, #21, #26, #27, #34, and #45) were used, and the maximum achievable rate was 9 bits/symbol/subcarrier. TX power allocation at the transmitter was the same as in §5.6.4. Note that, in the conventional SDM, transmission pattern indices #4, #9, #10, #21, #26, and #45 were used for 2×2 MIMO-OFDM SDM, and #13, #29, #41, #56, #60, and #66 were used for 4×4 MIMO-OFDM SDM because of equal resource allocation.

6.3 Throughput Performance of MIMO-OFDM PE-SDM in Actual Indoor Environments

Figures 6.4–6.7 show throughput performances of PE-SDM, E-SDM, and SDM for the perfect CSI cases. Here the throughput was calculated as follows; each transmission pattern is first tried, and the packet having the maximum rate is found among successful packets without any errors after RX processing. Considering the OFDM symbol length, the achievable throughput in the fading state was calculated by

$$\text{Throughput} = \frac{N_b \times N_c}{T_s}, \tag{6.1}$$

where N_b and N_c denote the achievable number of information bits/symbol/subcarrier and the number of active subcarriers, respectively, and T_s indicates the OFDM symbol length (4 μs). Thus, the maximum throughput was $(9 \times 56)/(4.0 \times 10^{-6}) = 126$ Mbps and $(18 \times 56)/(4.0 \times 10^{-6}) = 252$ Mbps for 2×2 and 4×4 MIMO cases, respectively. Note that the above throughput calculation does not consider the insertion loss due to the long preamble. The mean throughput was obtained by averaging achievable throughputs for all 72,177 fading states. Also, the maximum number of PIC iterations was set to two and five for PE-SDM and SDM, respectively, because further iterations did not yield visible improvement on the performance. Hence, we can say that computational complexity of E-SDM and SDM is dominant at the transmitter and receiver because of TX weight calculation and PIC processing, respectively, and that of PE-SDM is distributed over the transmitter and receiver.

In the 2×2 MIMO cases, the three transmission schemes PE-SDM, E-SDM, and SDM provide almost the same performance except the case of AS $= 0.50\lambda$ in the LOS scenario. In the 4×4 MIMO cases, however, beamforming schemes PE-SDM and E-SDM clearly outperform SDM especially in the LOS scenario. The improvement is because of beamforming and fading correlations. As stated in Chapter 4, the presence of a LOS component yields high fading correlations as seen in Figs. 4.3–4.5. In particular in the case of AS $= 0.50\lambda$, the LOS gain variation due to mutual coupling enlarges correlations

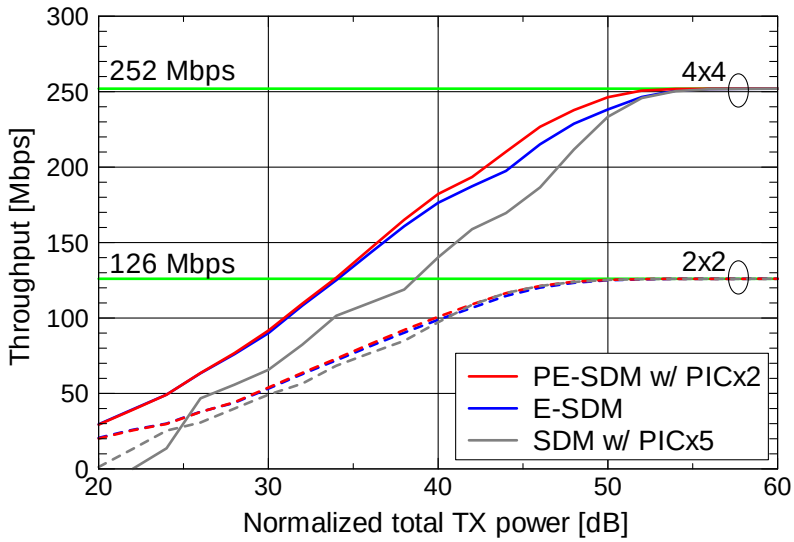

(a) AS $= 0.50\lambda$

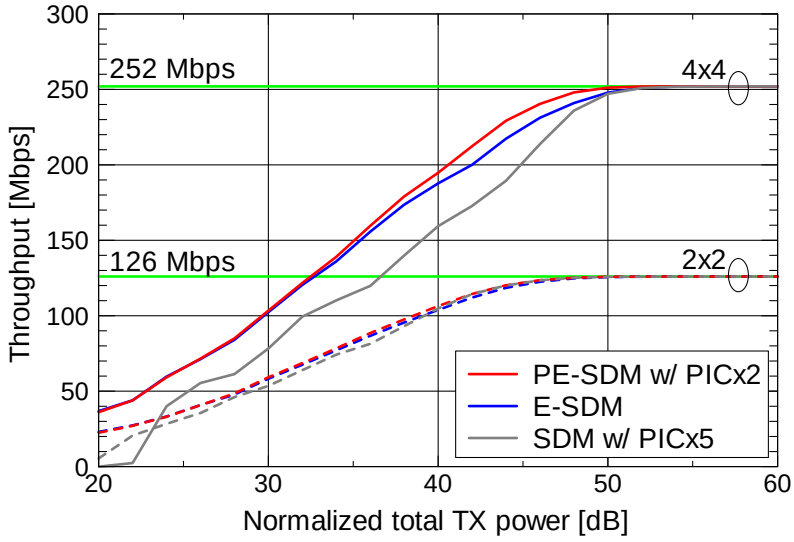

(b) AS $= 1.00\lambda$

Figure 6.4: Throughput performance in the case of TX-*x*/RX-*x* array orientation in the LOS scenario (perfect CSI).

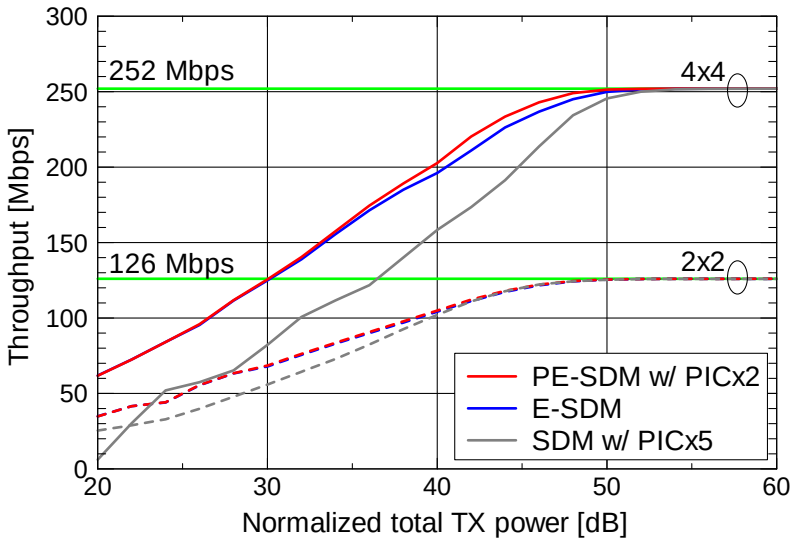

(a) AS $= 0.50\lambda$

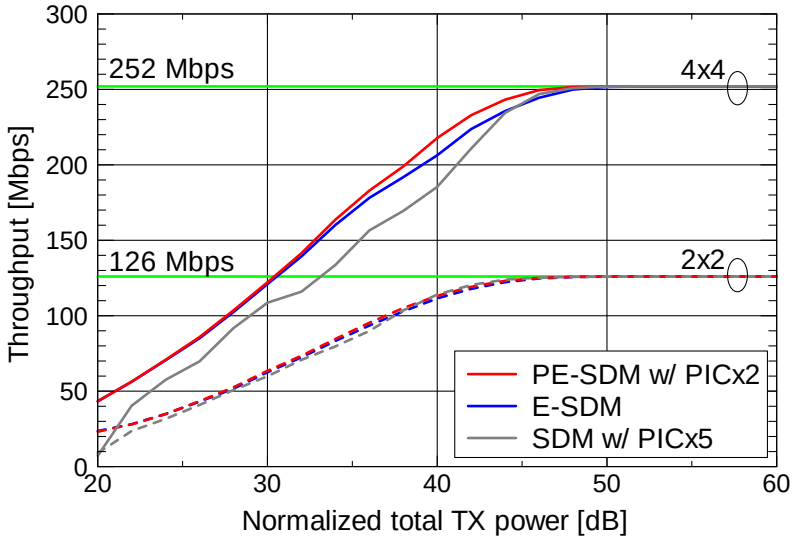

(b) AS $= 1.00\lambda$

Figure 6.5: Throughput performance in the case of TX-*y*/RX-*y* array orientation in the LOS scenario (perfect CSI).

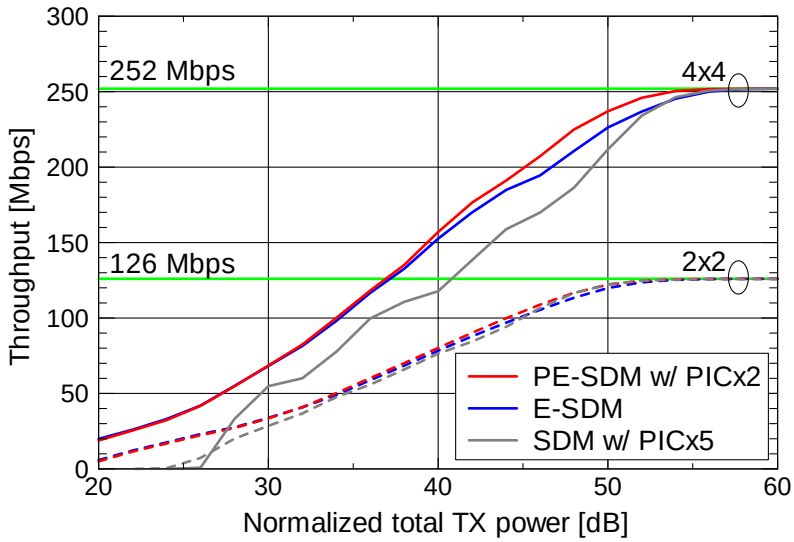

(a) AS $= 0.50\lambda$

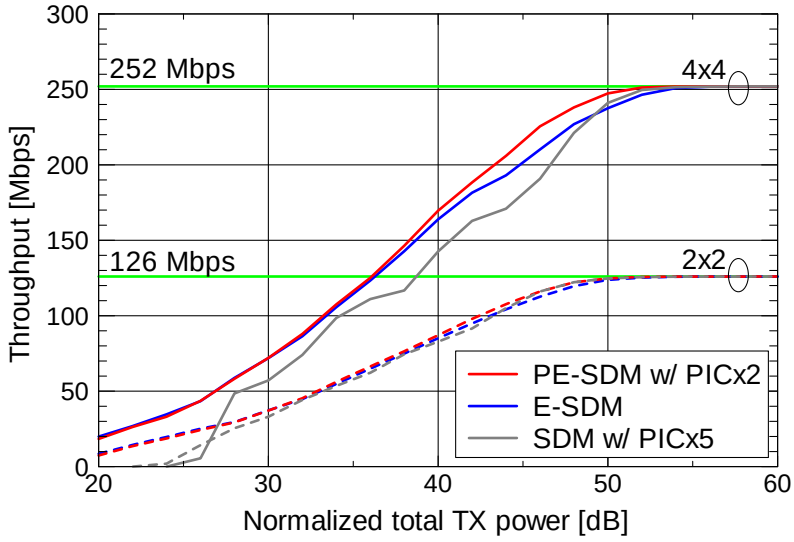

(b) AS $= 1.00\lambda$

Figure 6.6: Throughput performance in the case of TX-*x*/RX-*x* array orientation in the NLOS scenario (perfect CSI).

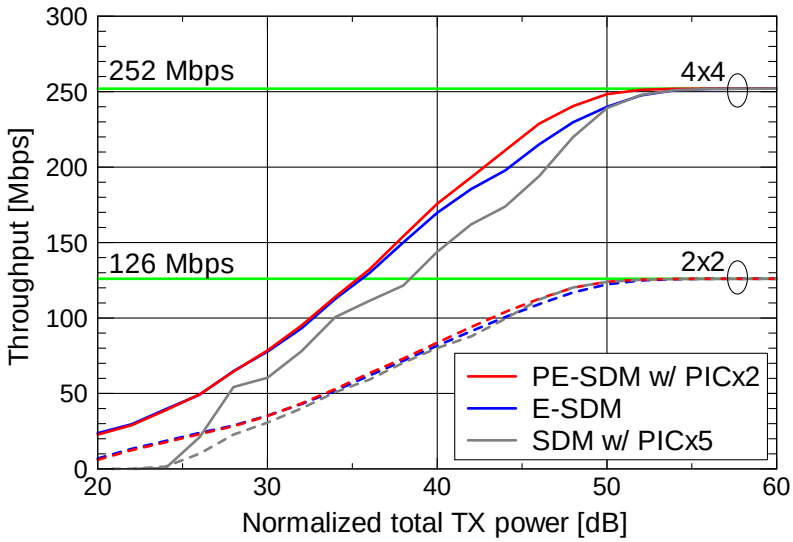

(a) AS $= 0.50\lambda$

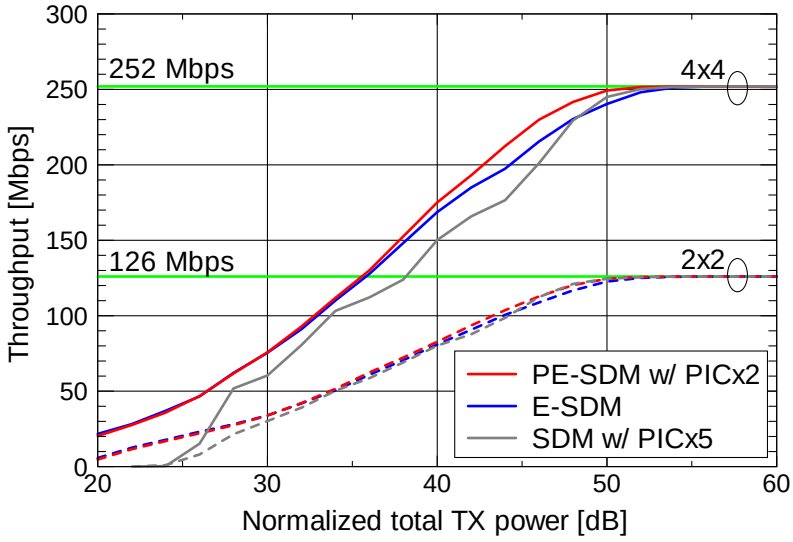

(b) AS $= 1.00\lambda$

Figure 6.7: Throughput performance in the case of TX-*y*/RX-*y* array orientation in the NLOS scenario (perfect CSI).

so that channels become undesirable for SDM. On the other hand, the issue of correlated channels can be resolved by beamforming and substream control. Not only in E-SDM but also in PE-SDM in which generally there is inter-substream interference at the receiver, we can obtain stable performance by limiting the number of substreams and adapting resource allocation.

When comparing PE-SDM with E-SDM for the 4×4 MIMO cases, we can see that PE-SDM outperforms E-SDM in the high throughput region over 150 Mbps. However, the difference between them appears less in the LOS scenario. As stated in §4.4, LOS environments generally have less frequency-selective channels due to a LOS component. The component has larger amplitudes so that it is highly considered in calculation of $\boldsymbol{R}_{\mathrm{rx}}(0)$ and $\boldsymbol{V}_0$ in (5.15) and (5.16), respectively. As well, PEV calculation tentatively assumes that the channel is frequency-flat as explained in §5.3.2. As a result, these factors are considered to yield near-optimal beamforming in PE-SDM.

Figures 6.8–6.11 demonstrate throughput performances for the estimated CSI cases, i.e., more practical cases, where the channel estimator in PE-SDM incorporated the space-time windowing. In SDM, both cases of channel estimators with/without the time windowing explained in the previous section were examined. We notice that performances of SDM with time windowing cannot reach the maximum throughput for both 2×2 and 4×4 MIMO cases. The reason for the saturation can be explained by using Fig. 6.12 which shows an example of time-domain channel distortion in SDM under the case of Scenario A, i.e., the 1-dB decaying 16-path model. When we have unloaded subcarriers such as guard bands, time-domain channel estimates obtained by the IFFT are distorted without compensation for the subcarriers as shown by "w/o interpolation." While the distortion can be mitigated by introducing linear interpolation to compensate for the blind channels as shown by "w/ interpolation," we still have residual distortion outside the time window especially in the range of $-10 < t < 0$. It is considered that it may cause the saturation in SDM throughput performances. Although the issue can be resolved by introducing other channel estimation schemes proposed in [59] or [88], in the case the receiver would require large additional memory space to store the channel estimation matrix and also would require a large number of complex multiplications.

As proved in §5.6, PE-SDM with space-time windowing provides remarkable performance improvement even for the measured channels. The validity of space-time windowing depends on the channel property as discussed in Chapter 5; that is, time windowing is more applicable in fading environments with lower delay spread where we can expect more frequency continuity of the effective channels, and the effect of spatial windowing appears more when utilizing more substreams, i.e., when channels are less correlated. Therefore, it is considered that the LOS scenario is more suitable for time windowing, and the NLOS scenario is a more appropriate condition to apply spatial windowing. We can say that the proposed space-time windowing scheme is based on a complementary property across delay spread and fading correlation issues.

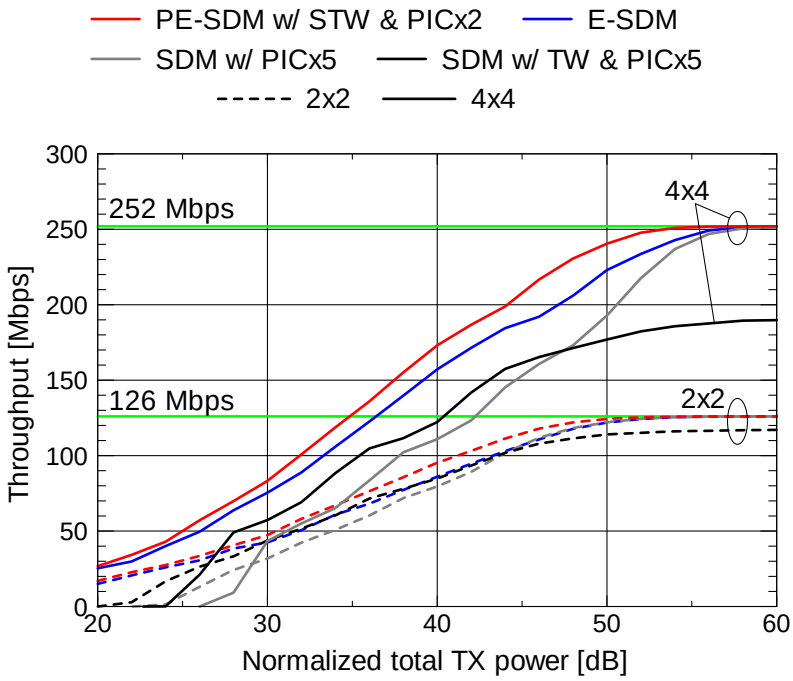

(a) AS $= 0.50\lambda$

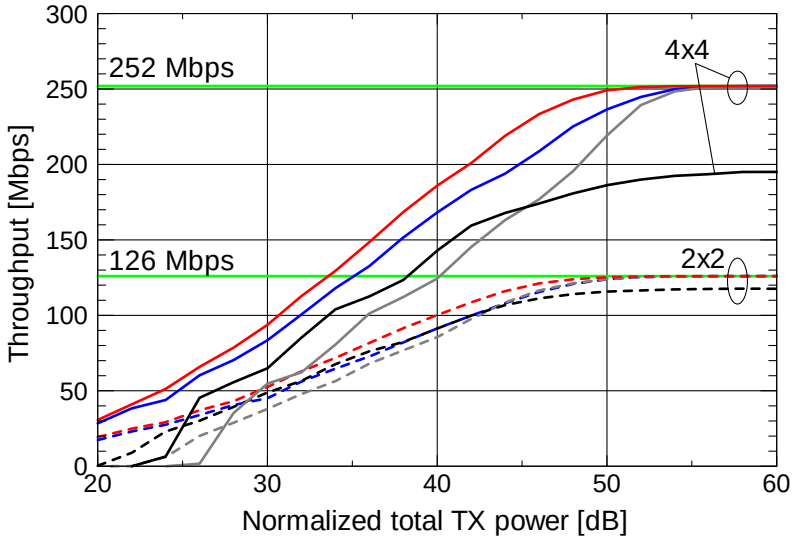

(b) AS $= 1.00\lambda$

Figure 6.8: Throughput performance in the case of TX-*x*/RX-*x* array orientation in the LOS scenario (estimated CSI).

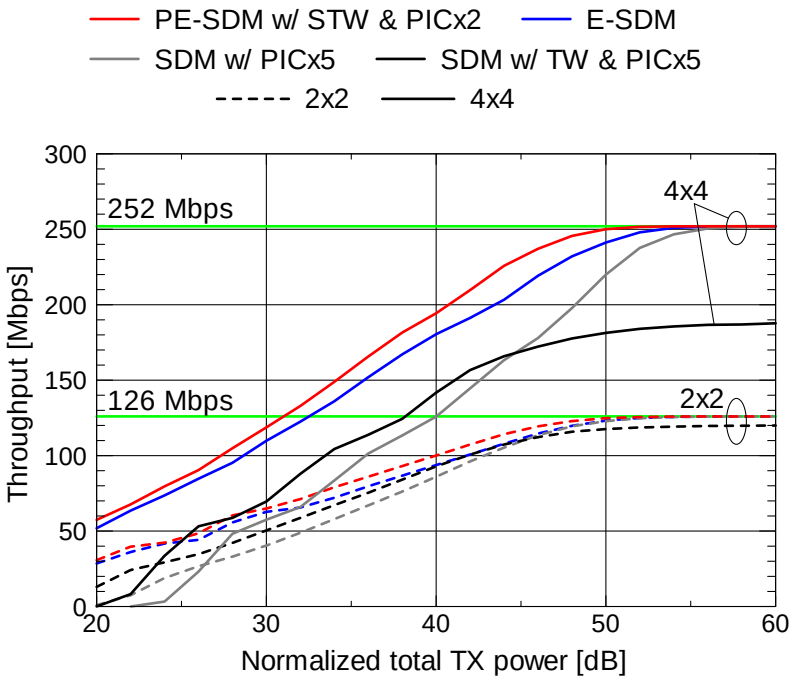

(a) AS = 0.50λ

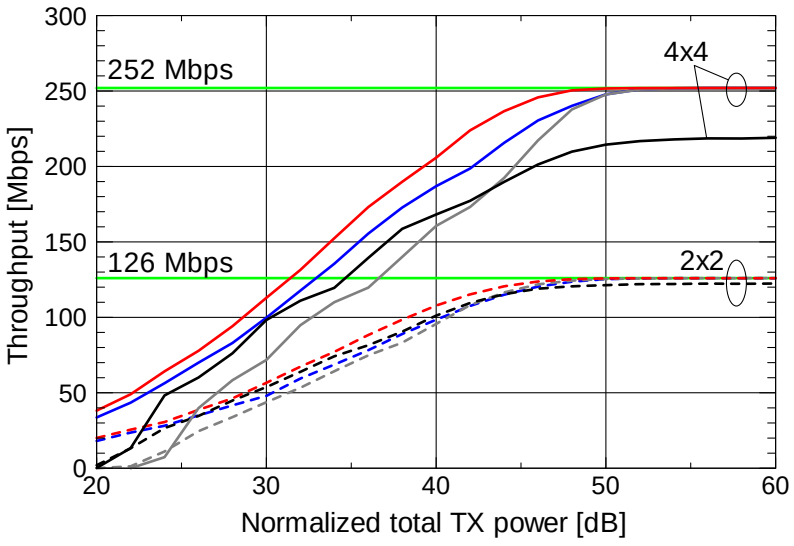

(b) AS = 1.00λ

Figure 6.9: Throughput performance in the case of TX-*y*/RX-*y* array orientation in the LOS scenario (estimated CSI).

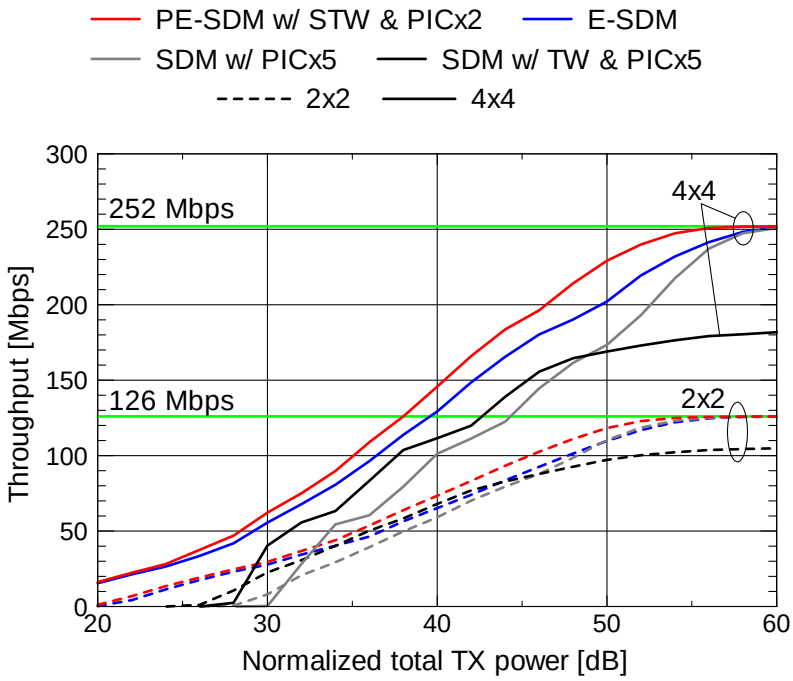

(a) AS $= 0.50\lambda$

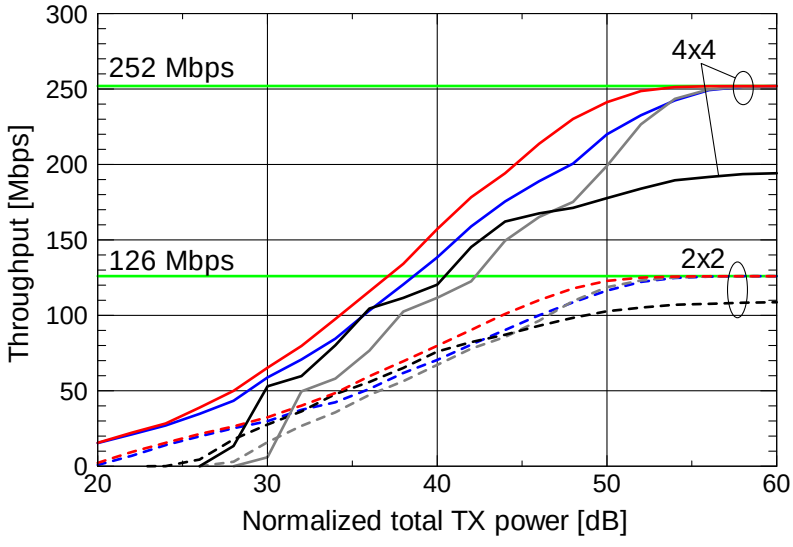

(b) AS $= 1.00\lambda$

Figure 6.10: Throughput performance in the case of TX-*x*/RX-*x* array orientation in the NLOS scenario (estimated CSI).

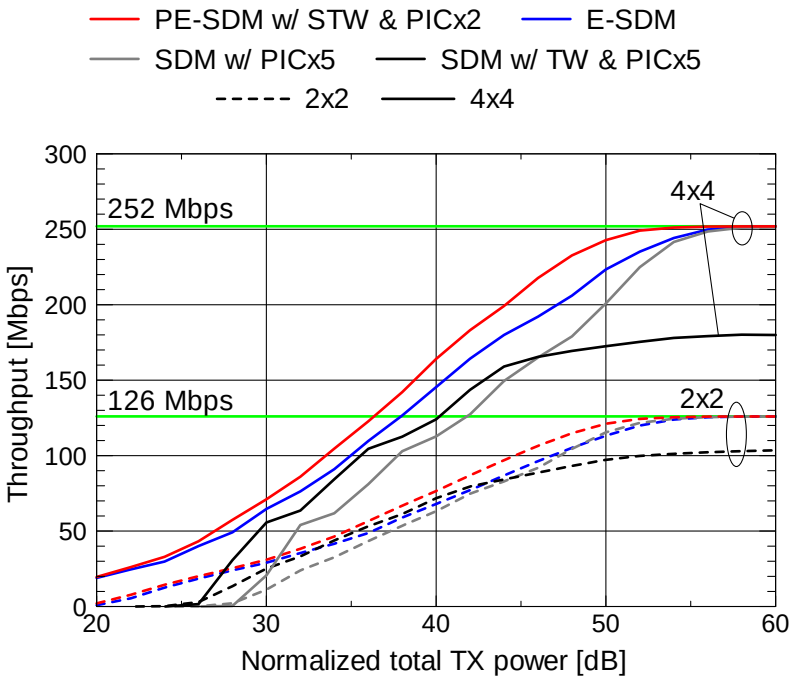

(a) AS $= 0.50\lambda$

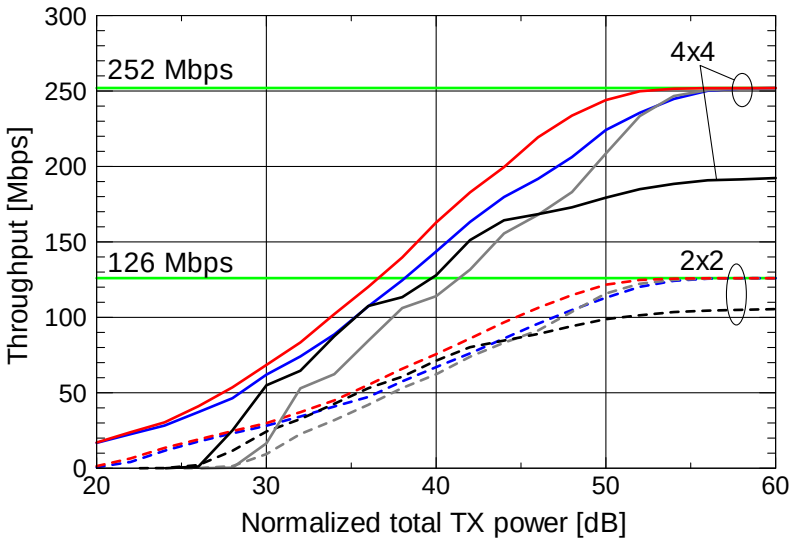

(b) AS $= 1.00\lambda$

Figure 6.11: Throughput performance in the case of TX-y/RX-y array orientation in the NLOS scenario (estimated CSI).

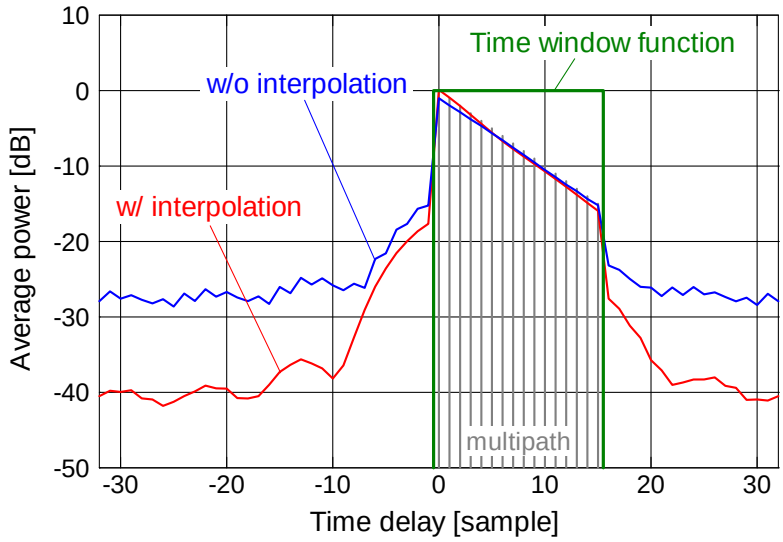

Figure 6.12: Example of time-domain channel distortion caused by time windowing (Scenario A).

6.4 Conclusions

The author has evaluated throughput performance of PE-SDM in actual fading environments by using measured data. PE-SDM and E-SDM results showed that beamforming schemes with adaptive resource allocation provide better performance compared with the conventional SDM. Even in actual environments, PE-SDM outperforms E-SDM even despite of the low computational complexity at the transmitter, so that we can say that it has more implementability. Also, of course communication systems cannot choose actual propagation environments, but the proposed space-time windowing scheme enables us to improve PE-SDM communication quality irrespective of the environment.

Chapter 7

Conclusions and Future Work

In this dissertation the author has considered MIMO spatial multiplexing as one of the promising ways to meet the growing demand of higher-speed wireless communications. Both experimental and implementational approaches toward spatial multiplexing have been taken. The former is a performance evaluation of spatial multiplexing through an indoor channel measurement campaign, and the latter is a proposal of a practical and near-optimal beamforming scheme named PE-SDM for broadband MIMO wireless systems. The author finally integrated these two approaches of the work into an experimental evaluation of PE-SDM transmission to explore the availability and implementability of PE-SDM in actual fading environments.

7.1 Summary

After giving the background and motivation of the dissertation in Chapter 1, an overview of MIMO spatial multiplexing was presented in Chapter 2. In addition, for simulating i.i.d. time-varying MIMO channels using multiple Jakes rings, the author proposed simple and effective conditions for the arrangement of scattering points to achieve stable fading properties. The results showed that the proposed arrangement provides higher statistical stability in generating time-varying i.i.d. channels.

Chapter 3 outlined the conducted 5.2 GHz-band MIMO indoor channel measurement campaign and described characteristics of the measured LOS and NLOS scenarios including example measurements, TOA/DOA estimation, and Nakagami-Rice K-factor estimation. It was proved that the measurement site was a multipath-rich environment, and that the K-factor in the LOS scenario was relatively small (1.6 dB $\leq K \leq$ 2.0 dB). On the other hand, the author found that the NLOS scenario provided Rayleigh fading.

Chapter 4 clarified the basic performance of SDM and E-SDM in actual fading environments using the measured channels along with analysis of channel and antenna char-

acteristics including azimuthal antenna patterns, fading correlations, channel distributions, and eigenvalue distributions. It is well known that an LOS environment does not have independent fading because an LOS component causes high fading correlation. From the measurement results, the author verified this fact and also found that the LOS scenario is not an i.i.d. fading environment when each channel element is observed by antennas including mutual coupling effects. However, MIMO SDM in the LOS scenario provides higher capacities and lower bit error rates than in the NLOS scenario under the same transmit power constraint. Hence, the utility of MIMO SDM in an LOS environment has been proved. Meanwhile, the antenna gain in an array with narrow antenna spacing deteriorates due to mutual coupling effects. The decrease in gain will cause performance degradation in MIMO systems equipped with numerous antennas. Under the LOS scenario, the performance of MIMO SDM depends on the array configuration, i.e., the array orientation and antenna spacing. Also, it was found that the LOS scenario gives better E-SDM performance than the NLOS one does due to higher received power, i.e., presence of a direct wave. Although channel capacities did not indicate clear benefits of E-SDM, we obtained excellent BER performance by employing E-SDM compared with conventional SDM. It was also found that the maximum channel capacity criterion, i.e, water-filling theorem, and the minimum BER criterion have different tendencies in resource allocation. Moreover, in the LOS scenario the BER performance of E-SDM is more dependent on the MIMO configuration than SDM. In addition to these studies, the behavior of coded MIMO-OFDM SDM in the same scenarios was examined as a practical case of spatial multiplexing. It was shown that even in a coded case the LOS scenario still provides better performance than the NLOS one in the measurement site. However, it was also proved that MIMO-OFDM SDM systems in LOS environments may obtain lower space-frequency diversity effects.

For frequency-selective fading MIMO channels in broadband systems, Chapter 5 proposed a pseudo eigenvector scheme for the purposes of reducing computational complexity in transmit weight calculation and maintaining frequency continuity of effective channels observed at the receiver. Also, the practical performance of the pseudo E-SDM (PE-SDM) transmission in MIMO-OFDM systems is evaluated. The simulation results showed that PE-SDM provides almost the same or better performance compared with E-SDM when the receiver employs a time-windowing-based channel estimation available in the low delay spread cases. Then, the author evaluated throughput performance of PE-SDM in a MIMO single-carrier system with MMSE-FDE and compared it with one of the E-SDM systems considering frequency continuity. In addition, focusing on the calculating process of pseudo eigenvectors, the author also proposed spatial windowing and space-time windowing schemes improving the accuracy of effective channel estimates. The simulation results showed that PE-SDM provides almost the same or better throughput performance with less complexity even in single-carrier transmission in comparison to E-SDM, and that the PE-SDM performance difference between perfect CSI and estimated CSI cases is only 1 dB and 1.5 dB at throughput levels of 10 bps/Hz and 15 bps/Hz, respectively, when the receiver refines channel estimates using the space-time windowing.

Chapter 6 showed an integrated work that explored the practical utility of PE-SDM based on the measured channel data. Through a performance evaluation assuming IEEE802.11n, it was clarified that even in actual environments PE-SDM outperforms E-SDM in despite of low computational complexity at the transmitter. Also, the author confirmed that the proposed space-time windowing scheme is effective irrespective of the channel property. As a result, in the estimated CSI case, it was proved in the 4×4 MIMO-OFDM system that PE-SDM can achieve the throughput of 200 Mbps with lower transmit power by at least 5 dB compared with the conventional SDM in the measurement site.

Summarizing, the main contributions in this dissertation are as follows.

- Despite higher fading correlations and non i.i.d. channel characteristics, the performance of MIMO SDM in the LOS scenario is better than that in the NLOS one. However, the performance in the measured LOS scenario largely depends on the array configuration.
- The BER of E-SDM outperforms that of SDM not only in i.i.d. channels but also in measured channels, and E-SDM gives better performance in the LOS scenario. Also, the performance of E-SDM in the LOS scenario is more dependent on the array configuration than that of the conventional SDM.
- With the proposed pseudo eigenvector scheme, we can maintain frequency continuity of the effective channel with low computational complexity in frequency-selective fading. PE-SDM, in which pseudo eigenvectors are used as transmit weights, provides almost the same or better performance compared with E-SDM when the receiver exploits specific properties of pseudo eigenvectors in channel estimation.

7.2 Future Work

Although the author has investigated the availability of spatial multiplexing for future wireless communications, there are several issues left that should be considered for future work.

In Chapter 4, the performance of SDM and E-SDM in a measurement site was examined. The author also conducted a 2×2 MIMO measurement campaign in another indoor environment [79,80]. These measurement campaigns yielded almost the same conclusions. However, measurement setups in these two environments were not practical but artificial, e.g., a large metal partition for the NLOS conditions and symmetric placement of TX and RX tables. Therefore, to confirm the tendencies shown in the chapter, we should carry out more practical measurement campaigns assuming actual wireless systems such as WLANs for future work.

Considering the work on PE-SDM, the calculation of pseudo eigenvectors gives the priority of frequency continuity to the first substream as stated in §5.3.2 and seen from Tables 5.1 & 5.5, Figs. 5.2, 5.3, 5.15, and 5.19. Thus, further work to maintain frequency continuity of the second and subsequent substreams would be an important issue. Adaptation of time windowing including window shape, window width, and attenuation level

should be considered as well. Also, a global solution to achieve frequency continuity of eigenvectors is our ultimate goal[1], and individual assignment of transmit power over entire frequency points under the frequency continuity constraint would be a challenging theme. The author thinks that it is necessary to investigate implementability of PE-SDM not only by computer simulations but also by using actual processing devices.

Through all the work in the dissertation, the author has assumed that the channel is quasi-static when transmitting a block. However, generally actual mobile communications can be conducted in time-variant fading environments. It has been reported that the performance of beamforming schemes deteriorates when the channel is time-varying [32, 84, 90, 91]. To assess the mobility of PE-SDM, therefore, we should analyze its performance over time-variant channels. The author also expects that PE-SDM will be expanded to multiuser MIMO systems [92–101] in future wireless systems.

[1]The EVD scheme investigated in [89] may provide us with a clue to consider the global solution.

References

[1] Japan Ministry of Internal Affairs and Communications, *Press Release on May 23, 2007 (in Japanese)*. [Online]. Available: http://www.soumu.go.jp/s-news/2007/070523_3.html

[2] W.C. Jakes, Jr., *Microwave Mobile Communications*. New York: Wiley, 1974.

[3] Special issue, Wireless personal communications, *IEEE Commun. Mag.*, Jan. 1995.

[4] M. Kuramoto and K. Kinoshita, "The dawn of mobile communication systems: From car phones to handheld phones," *J. IEICE (Japanese Edition)*, vol. 89, no. 8, pp. 740–745, Aug. 2006.

[5] IEEE802.11, *The Working Group Setting the Standards for Wireless LANs*. [Online]. Available: http://www.ieee802.org/11/

[6] J. Terry and J. Heiskala, *OFDM Wireless LANs: A Theoretical and Practical Guide*. Indianapolis: SAMS, 2002.

[7] G.J. Foschini and M.J. Gans, "On limits of wireless communications in a fading environment when using multiple antennas," *Wirel. Pers. Commun.*, vol. 6, pp. 311–335, March 1998.

[8] I.E. Telatar, "Capacity of multi-antenna Gaussian channels," *Euro. Trans. Telecommun.*, vol. 1, no. 6, pp. 585–595, Nov./Dec. 1999.

[9] D. Gesbert, M. Shafi, D.S. Shiu, P. Smith, and A. Naguib, "From theory to practice: An overview of MIMO space-time coded wireless systems," *IEEE J. Sel. Areas Commun.*, vol. 21, no. 2, pp. 281–302, April 2003.

[10] A. Paulraj, R. Nabar, and D. Gore, *Introduction of space-time wireless communications*. Cambridge University Press, 2003.

[11] A.J. Paulraj, D.A. Gore, R.U. Nabar, and H. Bölcskei, "An overview of MIMO communications—A key to gigabit wireless," *Proc. IEEE*, vol. 92, no. 2, pp. 198–218, Feb. 2004.

[12] M. Jankiraman, *Space-time codes and MIMO systems*. Artech House, 2004.

[13] E. Biglieri, R. Calderbank, A. Constantinides, A. Goldsmith, A. Paulraj, and H.V. Poor, *MIMO Wireless Communications*. New York: Cambridge University Press, 2007.

[14] S. Nanda, R. Walton, J. Ketchum, M. Wallace, and S. Howard, "A high-performance MIMO OFDM wireless LAN," *IEEE Commun. Mag.*, vol. 43, no. 2, pp. 101–109, Feb. 2005.

[15] A. Ghosh, D.R. Wolter, J.G. Andrews, and R. Chen, "Broadband wireless access with WiMax/802.16: Current performance benchmarks and future potential," *IEEE Commun. Mag.*, vol. 43, no. 2, pp. 129–136, Feb. 2005.

[16] C.E. Shannon, "A mathematical theory of communication," *The Bell System Technical Journal*, vol. 27, pp. 379–423, 623–656, July, Oct. 1948.

[17] I. Telatar, "Capacity of multi-antenna Gaussian channels," *Tech. Rep. #BL0112170-950615-07TM, AT&T Bell Laboratories*, 1995.

[18] G.J. Foschini, "Layered space-time architecture for wireless communication in a fading environment when using multi-element antennas," *Bell Labs Tech. J.*, vol. 6, no. 2, pp. 41–59, 1996.

[19] G.D. Golden, G.J. Foschini, R.A. Valenzuela, and P.W. Wolniansky, "Detection algorithm and initial laboratory results using V-BLAST space-time communication architecture," *Electron. Lett.*, vol. 35, no. 1, pp. 14–16, Jan. 1999.

[20] P.W. Wolniansky, G.J. Foschini, G.D. Golden, and R.A. Valenzuela, "V-BLAST: An architecture for realizing very high data rates over the rich-scattering wireless channel," *Proc. ISSSE-98*, Sept. 1998.

[21] M.J. Gans, N. Amitay, Y.S. (Albert) Yeh, T.C. Damen H. Xu, R.A. Valenzuela, T. Sizer, R. Storz, D. Taylor, W.M. MacDonald, C. Tran, and A. Adamiecki, "Outdoor BLAST measurement system at 2.44 GHz: Calibration and initial results," *IEEE J. Sel. Areas Commun.*, vol. 20, no. 3, pp. 570–583, April 2002.

[22] S.M. Alamouti, "A simple transmit diversity technique for wireless communications," *IEEE J. Sel. Areas Commun.*, vol. 16, no. 8, pp. 1451–1458, Oct. 1998.

[23] V. Tarokh, N. Seshadri, and A.R. Calderbank, "Space-time codes for high data rate wireless communication: Performance criterion and code construction," *IEEE Trans. Inf. Theory*, vol. 44, no. 2, pp. 744–765, March 1998.

[24] V. Tarokh, H. Jafarkhani, and A.R. Calderbank, "Space-time block codes from orthogonal designs," *IEEE Trans. Inf. Theory*, vol. 45, no. 5, pp. 1456–1467, July 1999.

[25] G.J. Foschini, G.D. Golden, R.A. Valenzuela, and P.W. Wolniansky, "Simplified processing for high spectral efficiency wireless communication employing multi-element arrays," *IEEE J. Sel. Areas Commun.*, vol. 17, no. 11, pp. 1841–1852, Nov. 1999.

[26] G.J. Foschini, D. Chizhik, M.J. Gans, C. Papadias, and R.A. Valenzuela, "Analysis and performance of some basic space-time architectures," *IEEE J. Sel. Areas Commun.*, vol. 21, no. 3, pp. 303–320, April 2003.

[27] K. Ban, M. Katayama, T. Yamazato, and A. Ogawa, "Joint optimization of transmitter/receiver with multiple transmit/receive antennas in band-limited channels," *IEICE Trans. Commun.*, vol. E83-B, pp. 1697–1704, Aug. 2000.

[28] H. Sampath, P. Stoica, and A. Paulraj, "Generalized linear precoder and decoder design for MIMO channels using the weighted MMSE criterion," *IEEE Trans. Commun.*, vol. 49, no. 12, pp. 2198–2206, Dec. 2001.

[29] A. Scaglione, P. Stoica, S. Barbossa, G.B. Giannakis, and H. Sampath, "Optimal designs for space-time linear precoders and decoders," *IEEE Trans. Signal Process.*, vol. 50, no. 5, pp. 1051–1064, May 2002.

[30] K. Miyashita, T. Nishimura, T. Ohgane, Y. Ogawa, Y. Takatori, and K. Cho, "High data-rate transmission with eigenbeam-space division multiplexing (E-SDM) in a MIMO channel," *Proc. IEEE VTC2002-Fall*, vol. 3, pp. 1302–1306, Sept. 2002.

[31] Y. Karasawa, "MIMO propagation channel modeling," *IEICE Trans. Commun.*, vol. E88-B, no. 5, pp. 1829–1842, May 2005.

[32] G. Lebrun, J. Gao, and M. Faulkner, "MIMO transmission over a time-varying channel using SVD," *IEEE Trans. Wireless Commun.*, vol. 4, no. 2, pp. 757–764, March 2005.

[33] L. Dai, S-D. Zhou, H-R. Zhuang, and Y. Yao, "Closed-loop MIMO architecture based on water-filling," *Electon. Lett.*, vol. 38, no. 25, pp. 1718–1720, Dec. 2002.

[34] M.A. Jensen and J.W. Wallace, "A review of antennas and propagation for MIMO wireless communications," *IEEE Trans. Antennas & Propagat.*, vol. 52, no. 11, pp. 2810–2824, Nov. 2004.

[35] D-S. Shiu, G.J. Foschini, M.J. Gans, and J.M. Kahn, "Fading correlation and its effect on the capacity of multielement antenna systems," *IEEE Trans. Commun.*, vol. 48, no. 3, pp. 502–513, March 2000.

[36] I.J. Gupta and A.A. Ksienski, "Effect of mutual coupling on the performance of adaptive arrays," *IEEE Trans. Antennas & Propagat.*, vol. AP-31, no. 5, pp. 785–791, Sept. 1983.

[37] H. Iura, H. Yamada, Y. Ogawa, and Y. Yamaguchi, "Optimal antenna matching and mutual coupling effect of antenna array in MIMO receiver," *IEICE Trans. Commun.*, vol. E90-B, no. 4, pp. 960–967, April 2007.

[38] H. Steyskal and J.S. Herd, "Mutual coupling compensation in small array antennas," *IEEE Trans. Antennas & Propagat.*, vol. 38, no. 12, pp. 1971–1975, Dec. 1990.

[39] P.N. Fletcher, M. Dean, and A.R. Nix, "Mutual coupling in multi-element array antennas and its influence on MIMO channel capacity," *Electron. Lett.*, vol. 39, no. 4, pp. 342–344, Feb. 2003.

[40] P. Uthansakul, M. Uthansakul, and M.E. Bialkowski, "Improving MIMO system capacity by compensating mutual coupling in transmitting/receiving array antennas," *Proc. IEEE AP-S Intl. Symp. 2004*, vol. 2, pp. 1724–1727, June 2004.

[41] J.W. Wallace and M.A. Jensen, "Mutual coupling in MIMO wireless systems: A rigorous network theory analysis," *IEEE Trans. Wireless Commun.*, vol. 3, no. 4, pp. 1317–1325, July 2004.

[42] A.F. Molisch, M. Steinbauer, M. Toeltsch, E. Bonek, and R.S. Thomä, "Capacity of MIMO systems based on measured wireless channels," *IEEE J. Sel. Areas Commun.*, vol. 20, no. 3, pp. 561–569, April 2002.

[43] T. Mitsui, M. Otani, C.H.Y. Eugene, K. Sakaguchi, and K. Araki, "Indoor MIMO channel measurements for evaluation of effectiveness of array antenna configurations," *Proc. IEEE VTC2003-Fall*, vol. 1, pp. 84–88, Oct. 2003.

[44] P. Kyritsi, D.C. Cox, R.A. Valenzuela, and P.W. Wolniansky, "Correlation analysis based on MIMO channel measurements in an indoor environment," *IEEE J. Sel. Areas Commun.*, vol. 21, no. 5, pp. 713–720, June 2003.

[45] K. Yu, M. Bengtsson, B. Ottersten, D. McNamara, P. Karlsson, and M. Beach, "Modeling of wide-band MIMO radio channels based on NLoS indoor measurements," *IEEE Trans. Veh. Technol.*, vol. 53, no. 3, pp. 655–665, May 2004.

[46] C. Waldschmidt and W. Wiesbeck, "Compact wide-band multimode antennas for MIMO and diversity," *IEEE Trans. Antennas & Propagat.*, vol. 52, no. 8, pp. 1963–1969, Aug. 2004.

[47] D.P. McNamara, M.A. Beach, P.N. Fletcher, and P. Karlsson, "Capacity variation of indoor multiple-input multiple-output channels," *Electron. Lett.*, vol. 36, no. 24, pp. 2037–2038, Nov. 2000.

[48] T. Svantesson and J. Wallace, "On signal strength and multipath richness in multi-input multi-output systems," *Proc. IEEE ICC'03*, vol. 4, pp. 2683–2687, May 2003.

[49] J.P. Kermoal, L. Schumacher, K.I. Pedersen, P.E. Mogensen, and F. Frederiksen, "A stochastic MIMO radio channel model with experimental validation," *IEEE J. Sel. Areas Commun.*, vol. 20, no. 6, pp. 1211–1226, Aug. 2002.

[50] H. Özcelik, M. Herdin, H. Hofstetter, and E. Bonek, "Capacity of different MIMO systems based on indoor measurements at 5.2GHz," *Proc. EPMCC 2003*, pp. 463–466, April 2003.

[51] W. Weichselberger, M. Herdin, H. Özcelik, and E. Bonek, "A stochastic MIMO channel model with joint correlation of both link ends," *IEEE Trans. Wireless Commun.*, vol. 5, no. 1, pp. 90–100, Jan. 2006.

[52] H. Sampath, S. Talwar, J. Tellado, V. Erceg, and A. Paularj, "A fourth-generation MIMO-OFDM broadband wireless system: Design, performance, and field trial results," *IEEE Commun. Mag.*, vol. 40, no. 9, pp. 143–149, Sept. 2002.

[53] G.G. Raleigh and V.K. Jones, "Multivariate modulation and coding for wireless communication," *IEEE J. Sel. Areas Commun.*, vol. 17, no. 5, pp. 851–866, May 1999.

[54] L.H. Doan, S.H. Ting, K. Sakaguchi, and K. Araki, "Hierarchical subgroup power and modulation coding adaptation—A new frequency-space link adaptation scheme in MIMO-OFDM eigenmode adaptive transmission system," *Proc. IEEE VTC2005-Spring*, vol. 2, pp. 668–672, May/June 2005.

[55] Y. Ohwatari, B.H. Phu, Y. Ogawa, T. Nishimura, and T. Ohgane, "Reduction of the amount of channel state information feedback in MIMO-OFDM eigenbeam-space division multiplexing systems," *Proc. IEEE VTC2006-Fall*, Sept. 2006.

[56] K. Ozaki, A. Nakajima, and F. Adachi, "Frequency-domain eigenbeam-SDM and equalization for high speed data transmissions," *Proc. IEEE VTC2006-Fall*, Sept. 2006.

[57] Y. Li, N. Seshadri, and S. Ariyavisitakul, "Channel estimation for ofdm system with transmitter diversity in mobile wireless channels," *IEEE J. Sel. Areas Commun.*, vol. 17, no. 3, pp. 461–471, March 1999.

[58] Y. Li, "Simplified channel estimation for OFDM systems with multiple transmit antennas," *IEEE Trans. Wireless Commun.*, vol. 1, no. 1, pp. 67–75, Jan. 2002.

[59] Y. Ogawa, K. Nishio, T. Nishimura, and T. Ohgane, "Channel estimation and signal detection for space division multiplexing in a MIMO-OFDM system," *IEICE Trans. Commun.*, vol. E88-B, no. 1, pp. 10–18, Jan. 2005.

[60] A. Chini, Y. Wu, M. El-Tanany, and S. Mahmoud, "Filtered decision feedback channel estimation for OFDM-based DTV terrestrial broadcasting system," *IEEE Trans. Broadcasting*, vol. 44, no. 1, pp. 2–11, March 1998.

[61] T. Fukuhara, H. Yuan, Y. Takeuchi, and H. Kobayashi, "A novel channel estimation method for OFDM transmission technique under fast time-variant fading channel," *Proc. IEEE VTC2003-Spring*, vol. 4, pp. 2343–2347, April 2003.

[62] K. Ishihara, K. Takeda, and F. Adachi, "Pilot-assisted decision feedback channel estimation for STTD OFDM mobile radio," *IEICE Trans. Commun.*, vol. E88-B, no. 2, pp. 561–567, Feb. 2005.

[63] J. Choi and R.W. Heath, Jr., "Interpolation based transmit beamforming for MIMO-OFDM with limited feedback," *IEEE Trans. Signal Process.*, vol. 53, no. 11, pp. 4125–4135, Nov. 2005.

[64] P. Dent, G.E. Bottomley, and T. Croft, "Jakes fading model revisited," *Electron. Lett.*, vol. 29, no. 13, pp. 1162–1163, June 1993.

[65] T. Ohgane, T. Nishimura, and Y. Ogawa, "Applications of space division multiplexing and those performance in a MIMO channel," *IEICE Trans. Commun.*, vol. E88-B, no. 5, pp. 1843–1851, May 2005.

[66] E. Viterbo and J. Boutros, "A universal lattice code decoder for fading channels," *IEEE Trans. Inf. Theory*, vol. 45, no. 5, pp. 1639–1642, July 1999.

[67] M.O. Damen, K. Abed-Meraim, and J.C. Belfiore, "A generalized sphere decoder for asymmetrical space-time communication architecture," *Electron. Lett.*, vol. 36, no. 2, pp. 166–167, Jan. 2000.

[68] M.O. Damen, K. Abed-Meraim, and S. Burykh, "Iterative QR detection for BLAST," *Wireless Personal Commun.*, vol. 19, pp. 179–191, 2001.

[69] K.J. Kim, J. Yue, R.A. Iltis, and J.D. Gibson, "A QRD-M/Kalman filter-based detection and channel estimation algorithm for MIMO-OFDM systems," *IEEE Trans. Wireless Commun.*, vol. 4, no. 2, pp. 710–721, March 2005.

[70] H. Kawai, K. Higuchi, N. Maeda, M. Sawahashi, T. Ito, Y. Kakura, A. Ushirokawa, and H. Seki, "Likelihood function for QRM-MLD suitable for soft-decision turbo decoding and its performance for OFCDM MIMO multiplexing in multipath fading channel," *IEICE Trans. Commun.*, vol. E88-B, no. 1, pp. 47–57, Jan. 2005.

[71] J.G. Proakis, *Digital Communications, fourth ed*. New York: McGraw-Hill, 2000.

[72] H. Matsuoka, S. Sampei, N. Morinaga, and Y. Kamio, "Adaptive modulation system with punctured convolutional code for high quality personal communication systems," *IEICE Trans. Commun.*, vol. E79-B, no. 3, pp. 328–334, March 1996.

[73] C. Berrou, A. Glavieux, and P. Thitimajshima, "Near Shannon-limit error-correcting coding: Turbo codes," *Proc. IEEE ICC'93*, pp. 1064–1070, May 1993.

[74] R.G. Gallager, *Low-Density Parity-Check Codes*. M.I.T. Press, Cambridge, 1963.

[75] S. Chung, G.D. Forney, T.J. Richardson, and R. Urbanke, "On the design of low-density parity-check codes within 0.0045 dB of the Shannon limit," *IEEE Commun. Lett.*, vol. 5, pp. 58–60, Feb. 2001.

[76] Y. Ogawa, N. Hamaguchi, K. Ohshima, and K. Itoh, "High-resolution analysis of indoor multipath propagation structure," *IEICE Trans. Commun.*, vol. E78-B, no. 11, pp. 1450–1457, Nov. 1995.

[77] Y. Ogawa, H. Nishimoto, T. Nishimura, and T. Ohgane, "Performance of MIMO spatial multiplexing in indoor line-of-sight environments," *Proc. IEEE VTC2005-Fall*, vol. 4, pp. 2398–2402, Sept. 2005.

[78] J-S. Jiang and M.A. Ingram, "Spherical-wave model for short-range MIMO," *IEEE Trans. Commun.*, vol. 53, no. 9, pp. 1534–1541, Sept. 2005.

[79] H. Nishimoto, Y. Ogawa, T. Nishimura, and T. Ohgane, "Performance of MIMO-SDM in indoor line-of-sight environments based on 5.2GHz measurements," *Proc. ISAP2004*, vol. 2A4-4, pp. 345–348, Aug. 2004.

[80] ——, "Availability of MIMO spatial multiplexing in line-of-sight channels," *Proc. IEEE APWCS2005*, pp. 40–44, Aug. 2005.

[81] S. Kaiser, "Spatial transmit diversity techniques for broadband OFDM systems," *Proc. IEEE GLOBECOM 2000*, vol. 3, pp. 1824–1828, Nov. 2000.

[82] K. Tsunekawa, K. Nishimori, R. Kudo, Y. Takatori, and N. Tachikawa, "Beamforming and antenna design techniques for realizing wideband MIMO-OFDM system," *Proc. IEEE AP-S Intl. Symp. 2005*, vol. 2A, pp. 329–332, July 2005.

[83] Q. Li and X.E. Lin, "Compact feedback for MIMO-OFDM systems over frequency selective channels," *Proc. IEEE VTC2005-Spring*, vol. 1, pp. 187–191, May/June 2005.

[84] B.H. Phu, Y. Ogawa, T. Ohgane, and T. Nishimura, "Channel extrapolation techniques for E-SDM systems in time-varying fading environments," *IEICE Trans. Commun.*, vol. E89-B, no. 11, pp. 3083–3092, Nov. 2006.

[85] D. Falconer, S.L. Ariyavisitakul, A. Benyamin-Seeyar, and B. Eidson, "Frequency domain equalization for single-carrier broadband wireless systems," *IEEE Commun. Mag.*, vol. 40, no. 4, pp. 58–66, April 2002.

[86] M.V. Clark, "Adaptive frequency-domain equalization and diversity combining for broadband wireless communications," *IEEE J. Sel. Areas Commun.*, vol. 16, no. 8, pp. 1385–1395, Oct. 1998.

[87] A. Nakajima and F. Adachi, "Iterative joint PIC and 2D MMSE-FDE for turbo-coded HARQ with SC-MIMO multiplexing," *Proc. IEEE VTC2006-Spring*, pp. 2503–2507, May 2006.

[88] H. Schmidt, V. Kühn, K.-D. Kammeyer, R. Rückriem, and S. Fechtel, "Channel tracking in wireless OFDM systems," *Proc. SCI 2001*, July 2001.

[89] J.G. McWhirter, P.D. Baxter, T. Cooper, S. Redif, and J. Foster, "An EVD algorithm for para-Hermitian polynomial matrices," *IEEE Trans. Signal Process.*, vol. 55, no. 5, pp. 2158–2169, May 2007.

[90] S. Ting, K. Sakaguchi, and K. Araki, "Performance analysis of MIMO eigenmode transmission system under realistic channel and system conditions," *IEICE Trans. Commun.*, vol. E87-B, no. 8, pp. 2222–2232, Aug. 2004.

[91] T. Nishimura, T. Tsutsumi, T. Ohgane, and Y. Ogawa, "Compensation of channel information error using first order extrapolation in eigenbeam space division multiplexing (E-SDM)," *Proc. 2005 IEEE/ACES Intl. Conf. Wireless Communications and Applied Computational Electromagnetics*, pp. 44–47, April 2005.

[92] M. Rim, "Multi-user downlink beamforming with multiple transmit and receive antennas," *Electron. Lett.*, vol. 38, no. 25, pp. 1725–1726, Dec. 2002.

[93] K-K. Wong, R.D. Murch, and K.B. Letaief, "Performance enhancement of multiuser MIMO wireless communication systems," *IEEE Trans. Commun.*, vol. 50, no. 12, pp. 1960–1970, Dec. 2002.

[94] J. Chung, C-S. Hwang, K. Kim, and Y.K. Kim, "A random beamforming technique in MIMO systems exploiting multiuser diversity," *IEEE J. Sel. Areas Commun.*, vol. 21, no. 5, pp. 848–855, June 2003.

[95] L-U. Choi and R.D. Murch, "A transmit preprocessing technique for multiuser MIMO systems using a decomposition approach," *IEEE Trans. Wireless Commun.*, vol. 3, no. 1, pp. 20–24, Jan. 2004.

[96] Q.H. Spencer, A.L. Swindlehurst, and M. Haardt, "Zero-forcing methods for downlink spatial multiplexing in multiuser MIMO channels," *IEEE Trans. Signal Process.*, vol. 52, no. 2, pp. 461–471, Feb. 2004.

[97] M.H.M Costa, "Writing on dirty paper," *IEEE Trans. Inf. Theory*, vol. IT-29, no. 3, pp. 439–441, May 1983.

[98] C.B. Peel, "On 'Dirty Paper Coding'," *IEEE Signal Process. Mag.*, pp. 112–113, May 2003.

[99] G. Caire and S. Shamai (Shitz), "On the achievable throughput of a multiantenna Gaussian broadcast channel," *IEEE Trans. Inf. Theory*, vol. 49, no. 7, pp. 1691–1706, July 2003.

[100] W. Yu and J.M. Cioffi, "Sum capacity of Gaussian vector broadcast channels," *IEEE Trans. Inf. Theory*, vol. 50, no. 9, pp. 1875–1892, Sept. 2004.

[101] W. Yu, D.P. Varodayan, and J.M. Cioffi, "Trellis and convolutional precoding for transmitter-based interference presubtraction," *IEEE Trans. Commun.*, vol. 53, no. 7, pp. 1220–1230, July 2005.

Appendix A

Scattering Coefficients for the Measured Antenna Arrays

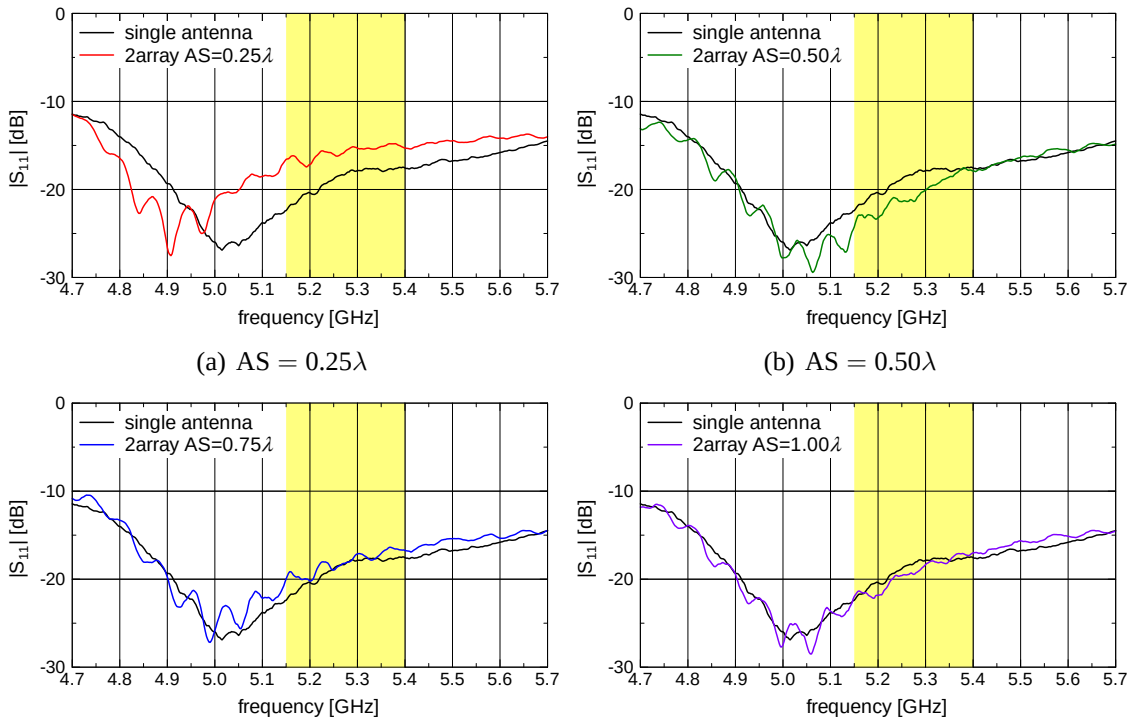

(a) AS $= 0.25\lambda$

(b) AS $= 0.50\lambda$

(c) AS $= 0.75\lambda$

(d) AS $= 1.00\lambda$

Figure A.1: $|S_{11}|$ performance (return loss) for each two-element array with mutual coupling.

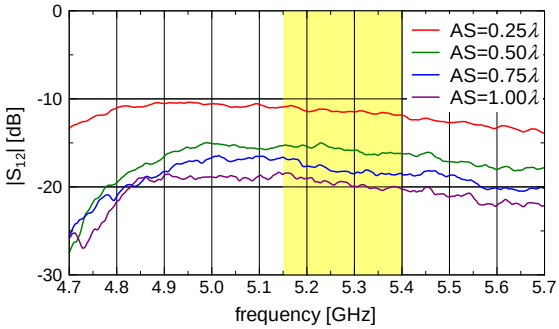

Figure A.2: $|S_{12}|$ performance for two-element arrays with mutual coupling (calibration by the data that had been obtained when the cables to the antenna ports were directly connected).

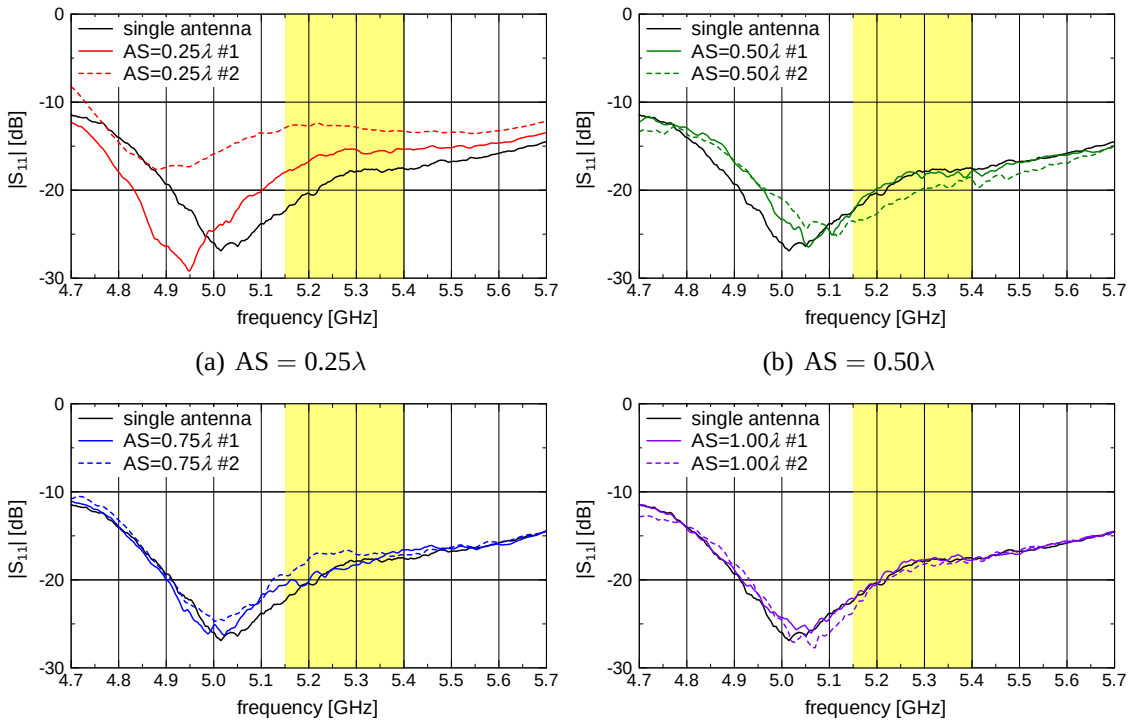

(a) AS $= 0.25\lambda$ (b) AS $= 0.50\lambda$

(c) AS $= 0.75\lambda$ (d) AS $= 1.00\lambda$

Figure A.3: $|S_{11}|$ performance (return loss) for each four-element ULA with mutual coupling, extracting antennas #1 and #2.

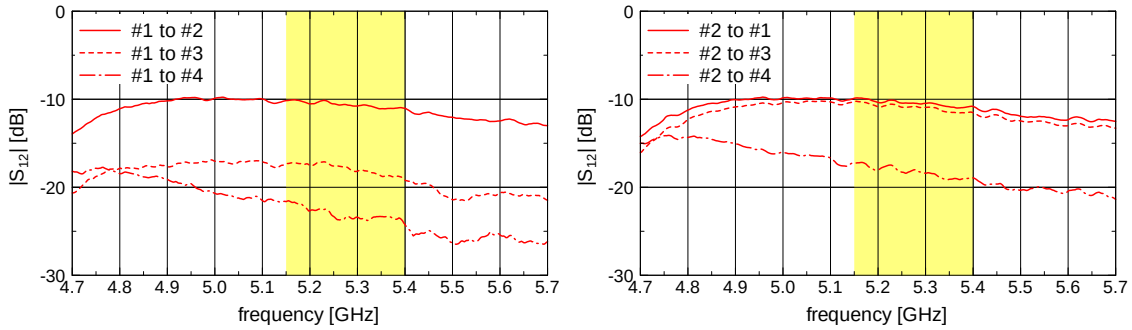

(a) from #1

(b) from #2

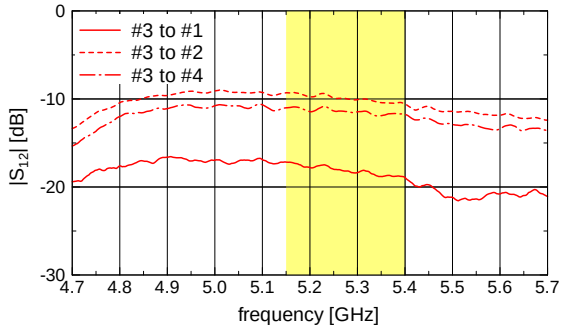

(c) from #3

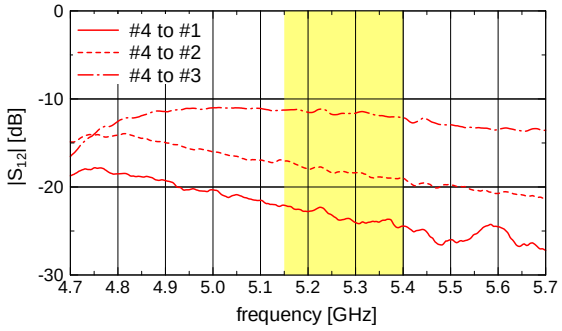

(d) from #4

Figure A.4: $|S_{12}|$ performance for four-element ULAs with mutual coupling in the AS $=$ 0.25λ case (calibration by the data that had been obtained when the cables to the antenna ports were directly connected).

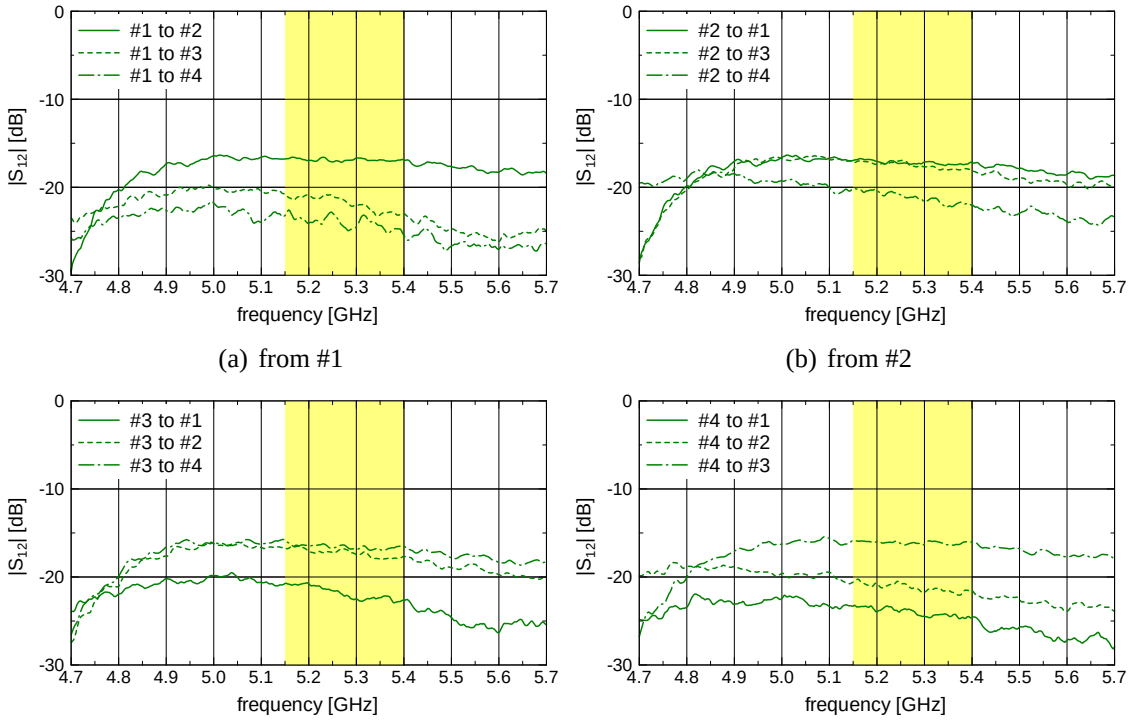

(a) from #1

(b) from #2

(c) from #3

(d) from #4

Figure A.5: $|S_{12}|$ performance for four-element ULAs with mutual coupling in the AS $=$ 0.50λ case (calibration by the data that had been obtained when the cables to the antenna ports were directly connected).

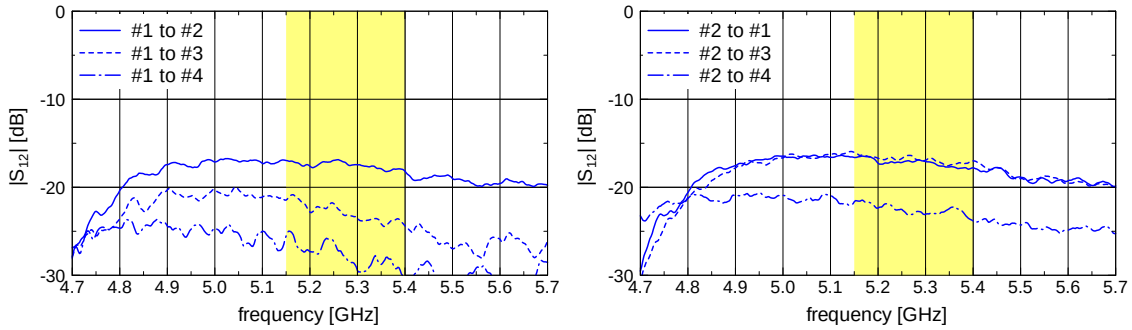

(a) from #1 (b) from #2

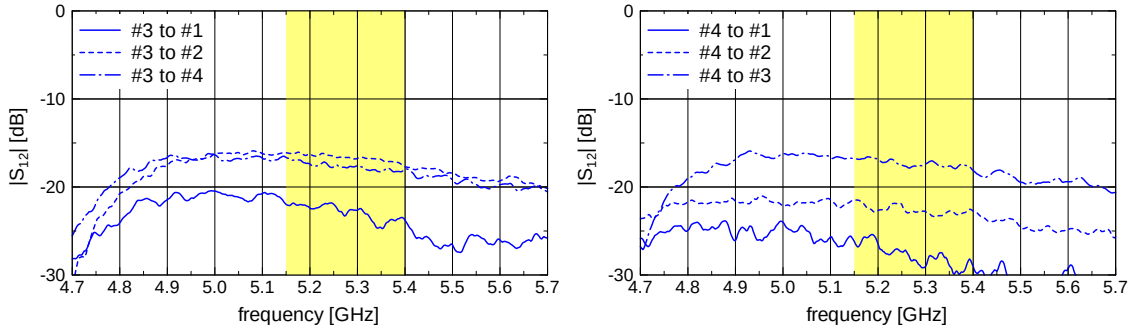

(c) from #3 (d) from #4

Figure A.6: $|S_{12}|$ performance for four-element ULAs with mutual coupling in the AS $=$ 0.75λ case (calibration by the data that had been obtained when the cables to the antenna ports were directly connected).

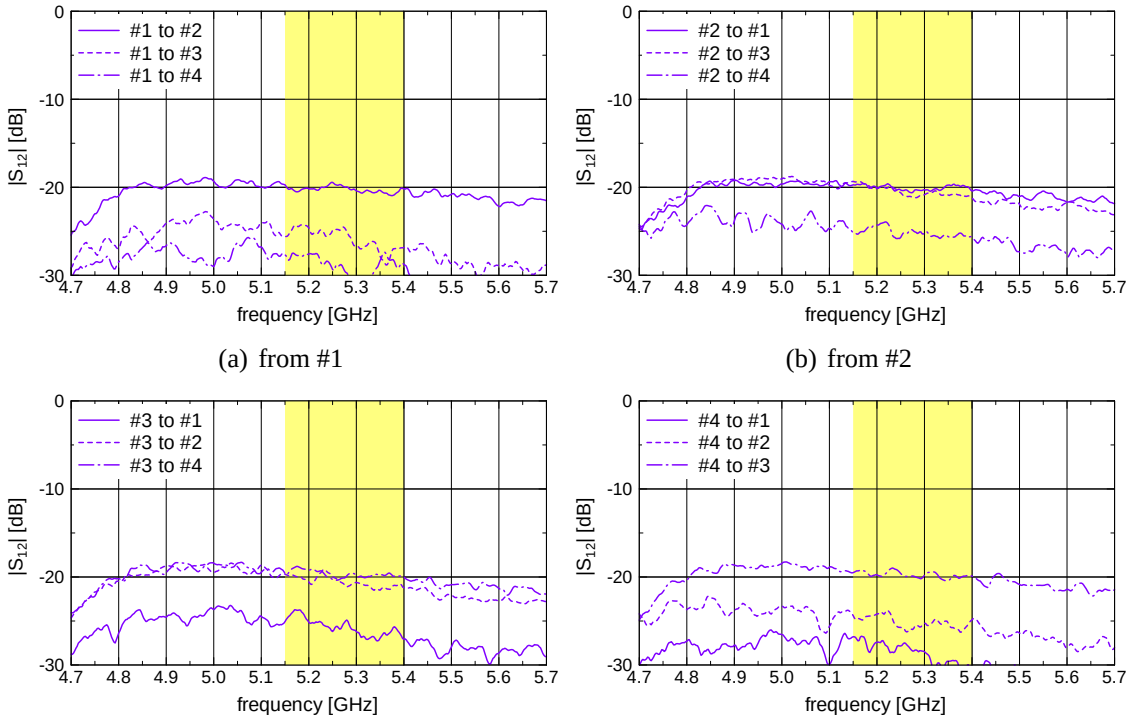

(a) from #1

(b) from #2

(c) from #3

(d) from #4

Figure A.7: $|S_{12}|$ performance for four-element ULAs with mutual coupling in the AS $=$ 1.00λ case (calibration by the data that had been obtained when the cables to the antenna ports were directly connected).

Appendix B

Gram-Schmidt Orthonormalization

In the following GS orthonormalization is briefly explained.

Consider that there are M linearly independent vectors $\boldsymbol{a}_1, \ldots, \boldsymbol{a}_M$ of which dimensions are N ($N \geq M$), and that we convert them into an orthonormal system. Note that none of the vectors are a zero vector, i.e., $\boldsymbol{a}_i \neq \boldsymbol{0}$ for $i = 1, \ldots, M$. First, one of the vectors $\boldsymbol{a}_1$ is normalized, and the normalized vector is defined as $\boldsymbol{e}_1$:

$$\boldsymbol{e}_1 = \frac{\boldsymbol{a}_1}{\|\boldsymbol{a}_1\|}. \tag{B.1}$$

Next, another vector $\boldsymbol{a}_2$ is orthogonalized to $\boldsymbol{e}_1$. A nonorthogonal component included in $\boldsymbol{a}_2$ is given by

$$\left(\boldsymbol{e}_1^H \boldsymbol{a}_2\right) \boldsymbol{e}_1. \tag{B.2}$$

By subtracting the above component from $\boldsymbol{a}_2$, we obtain an orthogonalized vector $\boldsymbol{a}_2'$ as

$$\boldsymbol{a}_2' = \boldsymbol{a}_2 - \left(\boldsymbol{e}_1^H \boldsymbol{a}_2\right) \boldsymbol{e}_1. \tag{B.3}$$

Orthogonal relation between $\boldsymbol{a}_1$ and $\boldsymbol{a}_2'$ is verified as follows:

$$\begin{aligned}
\boldsymbol{a}_1^H \boldsymbol{a}_2' &= \boldsymbol{a}_1^H \left\{\boldsymbol{a}_2 - \left(\boldsymbol{e}_1^H \boldsymbol{a}_2\right) \boldsymbol{e}_1\right\} && \text{(B.4)}\\
&= \boldsymbol{a}_1^H \boldsymbol{a}_2 - \boldsymbol{a}_1^H \left(\boldsymbol{e}_1^H \boldsymbol{a}_2\right) \boldsymbol{e}_1 && \text{(B.5)}\\
&= \boldsymbol{a}_1^H \boldsymbol{a}_2 - \left(\boldsymbol{e}_1^H \boldsymbol{a}_2\right) \boldsymbol{a}_1^H \boldsymbol{e}_1 && \text{(B.6)}\\
&= \boldsymbol{a}_1^H \boldsymbol{a}_2 - \frac{\boldsymbol{a}_1^H}{\|\boldsymbol{a}_1\|} \boldsymbol{a}_2 \frac{\|\boldsymbol{a}_1\|^2}{\|\boldsymbol{a}_1\|} && \text{(B.7)}\\
&= \boldsymbol{a}_1^H \boldsymbol{a}_2 - \boldsymbol{a}_1^H \boldsymbol{a}_2 && \text{(B.8)}\\
&= 0. && \text{(B.9)}
\end{aligned}$$

Table B.1: Algorithm of GS orthonormalization.

for $i = 1, \ldots, M$
  for $j = 1, \ldots, i-1$
    $\boldsymbol{a}_i \leftarrow \boldsymbol{a}_i - \left(\boldsymbol{e}_j^H \boldsymbol{a}_i\right) \boldsymbol{e}_j$
  next j
  $\boldsymbol{e}_i \leftarrow \dfrac{\boldsymbol{a}_i}{\|\boldsymbol{a}_i\|}$
next i

Then, a vector orthonormalized to $\boldsymbol{e}_1$ (or $\boldsymbol{a}_1$) is obtained by

$$\boldsymbol{e}_2 = \frac{\boldsymbol{a}_2'}{\|\boldsymbol{a}_2'\|}. \tag{B.10}$$

When applying the above calculation to the subsequent vectors $\boldsymbol{a}_3, \ldots, \boldsymbol{a}_M$, we obtain M orthonormal vectors $\boldsymbol{e}_1, \ldots, \boldsymbol{e}_M$. This procedure is GS orthonormalization and summarized in Table B.1. For example, orthonormalization to the third vector $\boldsymbol{a}_3$ is expressed as follows:

$$\boldsymbol{a}_3' = \boldsymbol{a}_3 - \left(\boldsymbol{e}_1^H \boldsymbol{a}_3\right) \boldsymbol{e}_1 \tag{B.11}$$

$$\boldsymbol{a}_3'' = \boldsymbol{a}_3' - \left(\boldsymbol{e}_2^H \boldsymbol{a}_3'\right) \boldsymbol{e}_2 \tag{B.12}$$

$$\boldsymbol{e}_3 = \frac{\boldsymbol{a}_3''}{\|\boldsymbol{a}_3''\|}. \tag{B.13}$$

Here, let us define an $N \times M$ matrix $\boldsymbol{A}$ composed of $\boldsymbol{a}_1, \ldots, \boldsymbol{a}_M$, i.e., $\boldsymbol{A} = [\boldsymbol{a}_1 \ \cdots \ \boldsymbol{a}_M]$. And, an orthonormal matrix $\boldsymbol{U} = [\boldsymbol{e}_1 \ \cdots \ \boldsymbol{e}_M]$ is also defined. In this dissertation, the author expresses the above procedure by using a GS operator $\mathcal{GS}[\cdot]$ as follows:

$$\boldsymbol{U} = \mathcal{GS}[\boldsymbol{A}]. \tag{B.14}$$

Norm-ordered GS orthonormalization (see §5.3.6) is achieved by selecting the maximum-norm vector among orthogonalized vectors in each stage. For example, norm-ordered GS orthonormalization in the second stage is expressed as follows:

$$\boldsymbol{a}_2' = \boldsymbol{a}_2 - \left(\boldsymbol{e}_1^H \boldsymbol{a}_2\right) \boldsymbol{e}_1 \tag{B.15}$$

$$\vdots \tag{B.16}$$

$$\boldsymbol{a}_M' = \boldsymbol{a}_M - \left(\boldsymbol{e}_1^H \boldsymbol{a}_M\right) \boldsymbol{e}_1 \tag{B.17}$$

$$m_2 = \arg \max_{m;\, 2 \le m \le M} \|\boldsymbol{a}_m'\| \tag{B.18}$$

$$\boldsymbol{e}_2 = \frac{\boldsymbol{a}_{m_2}'}{\|\boldsymbol{a}_{m_2}'\|}, \tag{B.19}$$

Table B.2: Algorithm of norm-ordered GS orthonormalization.

for $i = 1, \ldots, M$
  for $j = i, \ldots, M$
    $\boldsymbol{b}_j \leftarrow \boldsymbol{a}_j$
    for $k = 1, \ldots, i-1$
      $\boldsymbol{b}_j \leftarrow \boldsymbol{b}_j - \left(\boldsymbol{e}_k^H \boldsymbol{b}_j\right) \boldsymbol{e}_k$
    next k
  next j
  $m_i = \arg \underset{m;\, i \le m \le M}{\max} \|\boldsymbol{b}_m\|$
  $\boldsymbol{e}_i \leftarrow \dfrac{\boldsymbol{b}_{m_i}}{\|\boldsymbol{b}_{m_i}\|}$
  for $j = 1, \ldots, m_i - 1$
    $\boldsymbol{a}_{m_i - j + 1} \leftarrow \boldsymbol{a}_{m_i - j}$
  next j
next i

where it is assumed that $\boldsymbol{a}_1$ is the maximum-norm vector in the first stage. The algorithm is listed in Table B.2.

As stated in §5.6.2, GS orthonormalization achieves QR decomposition of a target matrix. A matrix $\boldsymbol{Q} = \boldsymbol{U}$ suitable for SIC-QRD (see §2.4.4) is obtained by selecting the minimum-norm vector in each stage instead of the maximum-norm vector. For example, in the second stage, the following evaluation is used instead of (B.18)

$$m_2 = \arg \min_{m;\, 2 \le m \le M} \|\boldsymbol{a}'_m\|. \tag{B.20}$$

Appendix C

Amplitude Correction for MMSE Outputs

The MMSE algorithm has been introduced in §2.4.2, and SINR of its output has also been discussed in §2.4.4. The algorithm provides good performance while it is a linear detection scheme. However, it involves an issue on amplitudes of output signals. In the following, the author would like to clarify the issue and to introduce a countermeasure, which has been taken in this dissertation.

Let us assume a MIMO SDM system which has N antennas at both ends, i.e., $N_{\mathrm{tx}} = N_{\mathrm{rx}} = N$. Also, it is assumed that a given MIMO channel is an N-dimensional unit matrix, i.e., $\boldsymbol{H} = \boldsymbol{I}_N$. That is, in this assumption, the channel nature is already orthogonal so that there is no inter-substream interference at the receiver. According to the derivation in §2.4.2, an MMSE weight matrix is calculated as

$$\boldsymbol{W}_{\mathrm{mmse}} = \boldsymbol{H}^H \left(\boldsymbol{H}\boldsymbol{H}^H + \frac{\sigma^2}{N}\boldsymbol{I}_N \right)^{-1} \tag{C.1}$$

$$= \boldsymbol{I}_N \left(\boldsymbol{I}_N\boldsymbol{I}_N + \frac{\sigma^2}{N}\boldsymbol{I}_N \right)^{-1} \tag{C.2}$$

$$= \frac{1}{1 + \dfrac{\sigma^2}{N}}\boldsymbol{I}_N. \tag{C.3}$$

We can notice that the above coefficient is less than 1. When multiplying the received signal vector by the calculated weight matrix, an MMSE output signal vector is expressed

as

$$\boldsymbol{W}_{\text{mmse}}\,\boldsymbol{r}(t) = \boldsymbol{W}_{\text{mmse}}\left\{\boldsymbol{H}\boldsymbol{s}(t) + \boldsymbol{n}(t)\right\} \tag{C.4}$$

$$= \frac{1}{1+\dfrac{\sigma^2}{N}}\boldsymbol{I}_N\boldsymbol{I}_N\boldsymbol{s}(t) + \frac{1}{1+\dfrac{\sigma^2}{N}}\boldsymbol{I}_N\boldsymbol{n}(t) \tag{C.5}$$

$$= \frac{1}{1+\dfrac{\sigma^2}{N}}\boldsymbol{s}(t) + \frac{1}{1+\dfrac{\sigma^2}{N}}\boldsymbol{n}(t). \tag{C.6}$$

Unlike the ZF case in (2.21), it is clear from the above equation that we do not have an output signal vector with correct amplitudes, especially when thermal noise power σ^2 is relatively high, i.e., low SNR. The amplitude error does not have a serious impact on PSK-modulated signals, where detection is independent of their amplitudes. However, when we employ a modulation scheme having information on its amplitude, such as 16QAM or 64QAM, the accuracy of symbol detection may be deteriorated by the error. Also, even in a PSK modulation, LLR calculation in a coding case may be affected because a Euclidean distance between the output symbol and replica symbol is dependent on the error. Therefore, we should compensate for the error for more accurate signal detection.

Here, the $N_{\text{rx}} \times N_{\text{tx}}$ MIMO channel $\boldsymbol{H}$ is redefined as a general i.i.d. channel, unlike the above case. When multiplying the received signal vector $\boldsymbol{r}(t)$ by the kth MMSE weight vector $\boldsymbol{w}_{\text{mmse},k}$, the output symbol is expressed as

$$\hat{s}_k(t) = \boldsymbol{w}_{\text{mmse},k}^T\boldsymbol{r}(t) \tag{C.7}$$

$$= \boldsymbol{w}_{\text{mmse},k}^T\boldsymbol{H}\boldsymbol{s}(t) + \boldsymbol{w}_{\text{mmse},k}^T\boldsymbol{n}(t) \tag{C.8}$$

$$= \boldsymbol{w}_{\text{mmse},k}^T\boldsymbol{h}_k s_k(t) + \sum_{i=1,i\neq k}^{N_{\text{tx}}} \boldsymbol{w}_{\text{mmse},k}^T\boldsymbol{h}_i s_i(t) + \boldsymbol{w}_{\text{mmse},k}^T\boldsymbol{n}(t). \tag{C.9}$$

In the above equation, the first and second terms denote the desired signal and residual inter-substream interference signal components, respectively. An amplitude coefficient of the desired signal component, which corresponds to $\dfrac{1}{1+(\sigma^2/N)}$ in (C.6), is defined as

$$c_{\text{amp},k} = \boldsymbol{w}_{\text{mmse},k}^T\boldsymbol{h}_k < 1, \tag{C.10}$$

which corresponds to the kth diagonal element in the matrix $\boldsymbol{W}_{\text{mmse}}\boldsymbol{H}$. We can obtain the desired signal component with correct amplitude by multiplying the output signal by an inverse of $c_{\text{amp},k}$:

$$\frac{1}{c_{\text{amp},k}}\hat{s}_k(t) = s_k(t) + \frac{1}{c_{\text{amp},k}}\sum_{i=1,i\neq k}^{N_{\text{tx}}} \boldsymbol{w}_{\text{mmse},k}^T\boldsymbol{h}_i s_i(t) + \frac{1}{c_{\text{amp},k}}\boldsymbol{w}_{\text{mmse},k}^T\boldsymbol{n}(t). \tag{C.11}$$

This is the amplitude correction for MMSE output signals. By applying the multiplication of $1/c_{\text{amp},k}$ to the MMSE weight vector in advance, we can compensate for the error without

post processing. Expanding to all the N_{tx} signals, an amplitude-corrected MMSE weight matrix is given by

$$\boldsymbol{W}'_{\mathrm{mmse}} = \boldsymbol{C}_{\mathrm{amp}}^{-1} \boldsymbol{W}_{\mathrm{mmse}}, \tag{C.12}$$

where

$$\boldsymbol{C}_{\mathrm{amp}} = \mathrm{diag}\left(c_{\mathrm{amp},1}, c_{\mathrm{amp},2}, \ldots, c_{\mathrm{amp},N_{\mathrm{tx}}}\right). \tag{C.13}$$

We should consider the same issue also in a broadband SC system with MMSE-FDE. However, in the system, the demultiplexing (equalization) and detection domains are the frequency and time domains, respectively. Amplitude correction in each frequency point does not make sense in terms of obtaining frequency diversity gain because it may cause noise enhancement depending on the channel, i.e., the frequency point. Therefore, we should take a global approach toward the issue. The author considers that multiplication of a constant value to the FDE output does not change its SNR or SINR. In the SC system with MMSE-FDE, therefore, the author estimates an amplitude coefficient in the same average sense as the output SINR in (5.38) as follows:

$$c_{\mathrm{amp},k} = \frac{1}{N_f} \sum_{f=0}^{N_f-1} \boldsymbol{w}_{\mathrm{mmse},k}^{T}(f) \boldsymbol{h}_k(f). \tag{C.14}$$

This can be regarded as a scaled direct current (DC) component, i.e., a component at $t = 0$, of the IFFT output of an equivalent channel $\boldsymbol{w}_{\mathrm{mmse},k}^{T}(f)\boldsymbol{h}_k(f)$ because the above equation is also expressed as

$$c_{\mathrm{amp},k}(t=0) = \frac{1}{N_f} \sum_{f=0}^{N_f-1} \boldsymbol{w}_{\mathrm{mmse},k}^{T}(f) \boldsymbol{h}_k(f)\, e^{j2\pi f \cdot 0}. \tag{C.15}$$

The DC component of the equivalent channel is considered as a desired channel component in FDE. Therefore, we can compensate for an amplitude error included in the kth MMSE-FDE output signals by dividing them by $c_{\mathrm{amp},k}$.

Figure C.1 demonstrates the effect of the amplitude correction mentioned above on the BER performance. Figure C.1(a) shows average BER performance of MIMO SDM with MMSE spatial filtering, where simulation conditions are the same as in the COS case shown in §2.5.2 and Fig. 2.16 except modulation schemes. While we cannot see the effect of the correction in the QPSK case, a visible improvement is obtained in the QAM cases, especially in the 16QAM case. In the 64QAM case, however, the improvement seems less than the 16QAM case. The 64QAM modulation has more closely-arrayed signal points than 16QAM. So, the accuracy of signal detection may not sufficiently benefit from the correction. Although there are differences in improvement, we can say that the amplitude correction scheme is still effective. Figure C.1(b) also shows the performance in a SISO-SC system with MMSE-FDE, where the FFT size was 256, i.e., the block size was 256 symbols, and the multipath channel had 16 symbol-spaced paths which corresponded to the CP length. Also, BCC with constraint length of three and coding rate 1/2 was applied, and then a coded sequence was randomly bit-interleaved. Even in the system, we can see almost the same tendency as in the MIMO SDM case mentioned above.

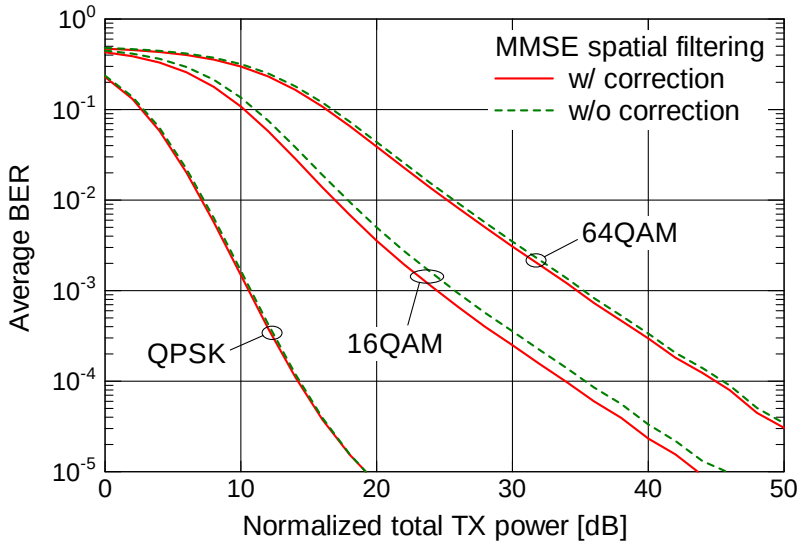

(a) 4×4 MIMO in the COS case

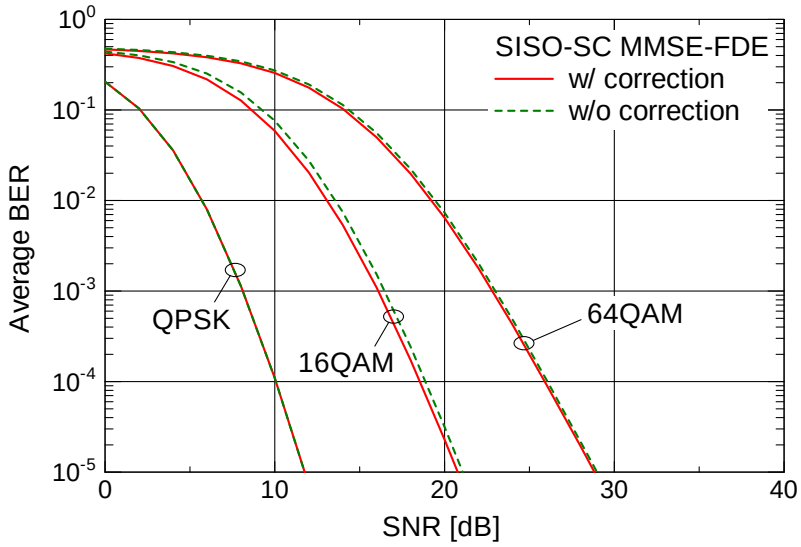

(b) SISO-SC with MMSE-FDE

Figure C.1: Effect of amplitude correction on average BER performance.

Acknowledgement

I would like to express my sincere appreciation to Professor Yasutaka Ogawa, Graduate School of Information Science and Technology, Hokkaido University, for the continuing guidance and encouragement during my research. With his insightful comments, I could enrich my view of research along with creating the work in the dissertation.

I am also grateful to Professor Yoshikazu Miyanaga, Professor Toshio Nojima, and Professor Masanori Koshiba, Graduate School of Information Science and Technology, Hokkaido University, for helpful suggestions and observations.

It would not be possible to generate the work in the dissertation without Associate Professor Takeo Ohgane, Graduate School of Information Science and Technology, Hokkaido University. I would like to express my sincere appreciation to him for his invaluable comments and help. I deeply acknowledge the generous support for the work, especially my experiment, from Assistant Professor Toshihiko Nishimura, Graduate School of Information Science and Technology, Hokkaido University.

The Japan Society for the Promotion of Science (JSPS) has been supporting me with a Research Fellowship for Young Scientists for the past three years. I could not have dedicated myself to the work without the support. I would like to, therefore, express my deep gratitude to JSPS.

I wish to thank Dr. Bui Huu Phu, Dr. Julian Leonard Webber, and the other members in the Intelligent Communications Laboratory, Graduate School of Information Science and Technology, Hokkaido University, for their helpful suggestions and observations, and, of course, precious memories of my life in the laboratory with them. In particular, special thanks go to Dr. Webber again for his kind and elaborate English check.

Last, I would like to thank my whole family, especially my parents, for their unconditional love and support.

Hiroshi Nishimoto

Sapporo, December 2007

List of Publications and Awards

Journals

[1] Hiroshi Nishimoto, Yasutaka Ogawa, Toshihiko Nishimura, and Takeo Ohgane, "Performance Evaluation of 2 $\times$ 2 MIMO Space Division Multiplexing Based on Indoor Propagation Measurement," IEICE Trans. Commun. (Japanese Edition), vol.J87-B, no.9, pp.1442–1453, Sept. 2004.

[2] Hiroshi Nishimoto, Yasutaka Ogawa, Toshihiko Nishimura, and Takeo Ohgane, "MIMO E-SDM Transmission Performance in an Actual Indoor Environment," IEICE Trans. Commun., vol.E90-B, no.6, pp.1474–1486, June 2007.

[3] Hiroshi Nishimoto, Yasutaka Ogawa, Toshihiko Nishimura, and Takeo Ohgane, "Measurement-Based Performance Evaluation of MIMO Spatial Multiplexing in a Multipath-Rich Indoor Environment," IEEE Trans. Antennas and Propagation, vol.55, no.12, accepted for publication.

[4] Hiroshi Nishimoto, Toshihiko Nishimura, Takeo Ohgane, and Yasutaka Ogawa, "Pseudo Eigenbeam-Space Division Multiplexing (PE-SDM) in Frequency-Selective MIMO Channels," IEICE Trans. Commun., vol.E90-B, no.11, pp.3197–3207, Nov. 2007.

[5] Hiroshi Nishimoto, Toshihiko Nishimura, Takeo Ohgane, and Yasutaka Ogawa, "Arrangement of Scattering Points in Jakes' Model for i.i.d. Time-Varying MIMO Fading," IEICE Trans. Commun., vol.E90-B, no.11, pp.3311–3314, Nov. 2007.

International Conference

[1] Hiroshi Nishimoto, Yasutaka Ogawa, Toshihiko Nishimura, and Takeo Ohgane, "Performance of MIMO-SDM in Indoor Line-of-Sight Environments Based on 5.2GHz Measurements," 2004 International Symposium on Antennas and Propagation (ISAP2004), 2A4-4, pp.345–348, Sendai, Japan, Aug. 2004.

[2] Yasutaka Ogawa, Hiroshi Nishimoto, Toshihiko Nishimura, and Takeo Ohgane, "Performance of MIMO Space Division Multiplexing in Indoor Environments," 2005

RCIQE International Seminar for 21st Century COE Program, Sapporo, Japan., Feb. 2005.

[3] Yasutaka Ogawa, Hiroshi Nishimoto, Toshihiko Nishimura, and Takeo Ohgane, "Performance of 2 × 2 MIMO Spatial Multiplexing in Indoor Environments," 2005 IEEE/ACES International Conference on Wireless Communications and Applied Computational Electromagnetics, pp.486–489, Honolulu, U.S.A., April 2005.

[4] Hiroshi Nishimoto, Yasutaka Ogawa, Toshihiko Nishimura, and Takeo Ohgane, "Availability of MIMO Spatial Multiplexing in Line-of-Sight Channels," IEEE VTS Asia Pacific Wireless Communications Symposium (APWCS 2005), pp.40–44, Sapporo, Japan, Aug. 2005.

[5] Yasutaka Ogawa, Hiroshi Nishimoto, Toshihiko Nishimura, and Takeo Ohgane, "Performance of MIMO Spatial Multiplexing in Indoor Line-of-Sight Environments," 2005 IEEE Vehicular Technology Conference (VTC2005-Fall), vol.4, pp.2398–2402, Dallas, U.S.A., Sept. 2005.

[6] Yusuke Ohwatari, Hiroshi Nishimoto, Phu Huu Bui, Yasutaka Ogawa, Toshihiko Nishimura, and Takeo Ohgane, "Indoor Propagation Property and Its Application to MIMO-OFDM Systems," PIERS2006, p.528, Tokyo, Japan., Aug. 2006.

[7] Hiroshi Nishimoto, Toshihiko Nishimura, Takeo Ohgane, and Yasutaka Ogawa, "Pseudo Eigenbeam Transmission Technique in Frequency Selective MIMO Channels," 2007 IEEE Vehicular Technology Conference (VTC2007-Spring), 2F-3, pp.2068–2072, Dublin, Ireland, April 2007.

[8] Keiichi Kambara, Hiroshi Nishimoto, Toshihiko Nishimura, Yasutaka Ogawa, and Takeo Ohgane, "Subblock Processing for MMSE-FDE Under Fast Fading Environments," 2007 IEEE Vehicular Technology Conference (VTC2007-Spring), 2P-11, pp.2190–2194, Dublin, Ireland, April 2007.

[9] Phu Huu Bui, Toshihiko Nishimura, Hiroshi Nishimoto, Yasutaka Ogawa, and Takeo Ohgane, "Robust Performance of MIMO E-SDM Systems in Actual Time-Varying Indoor Fading Environments," 2007 IEEE Vehicular Technology Conference (VTC2007-Spring), 11F-2, pp.1460–1464, Dublin, Ireland, April 2007.

[10] Hiroshi Nishimoto, Toshihiko Nishimura, Yasutaka Ogawa, and Takeo Ohgane, "Practical Performance of Coded MIMO-OFDM Spatial Multiplexing in an Actual Indoor Environment," 2007 IEEE Antennas and Propagation Society International Symposium (IEEE AP-S 2007), IF315.5, pp.3876–3879, Honolulu, Hawaii, June 2007.

[11] Phu Huu Bui, Hiroshi Nishimoto, Toshihiko Nishimura, Yasutaka Ogawa, and Takeo Ohgane, "Doppler Spectrum and Performance of E-SDM Systems in Indoor Time-Varying MIMO Channels," 2007 IEEE Antennas and Propagation Society Interna-

tional Symposium (IEEE AP-S 2007), 140.6, pp.1361–1364, Honolulu, U.S.A., June 2007.

[12] Phu Huu Bui, Toshihiko Nishimura, Hiroshi Nishimoto, Yasutaka Ogawa, and Takeo Ohgane, "On the Performance of MIMO E-SDM Systems with Channel Prediction in Indoor Time-Varying Fading Environments," 2007 IEEE Antennas and Propagation Society International Symposium (IEEE AP-S 2007), 106.3, pp.209–212, Honolulu, U.S.A., June 2007.

[13] Hiroshi Nishimoto, Toshihiko Nishimura, Takeo Ohgane, and Yasutaka Ogawa, "On Arrangement of Scattering Points in Jakes' Model for Generating i.i.d. Time-Varying MIMO Channels," 2007 International Symposium on Antennas and Propagation (ISAP2007), POS1-49, pp.1051–1054, Niigata, Japan, Aug. 2007.

[14] Phu Huu Bui, Hiroshi Nishimoto, Toshihiko Nishimura, Takeo Ohgane, and Yasutaka Ogawa, "Effects of Mutual Coupling and Doppler Spectrum on the Performance of 2×2 MIMO E-SDM Systems," 2007 International Symposium on Antennas and Propagation (ISAP2007), POS2-13, pp.1150–1153, Niigata, Japan, Aug. 2007.

[15] Phu Huu Bui, Hiroshi Nishimoto, Toshihiko Nishimura, Takeo Ohgane, and Yasutaka Ogawa, "Impact of Channel Prediction on the Performance of MIMO E-SDM Systems in Actual Dynamic Channels," 2007 International Symposium on Antennas and Propagation (ISAP2007), 4C1-2, pp.1310–1313, Niigata, Japan, Aug. 2007.

[16] Hiroshi Nishimoto, Toshihiko Nishimura, Takeo Ohgane, and Yasutaka Ogawa, "High Throughput Performance of PE-SDM in MIMO Single-Carrier Systems with MMSE-FDE," IEEE International Symposium on Personal, Indoor and Mobile Radio Communications (PIMRC2007), Session 92, 616, Athens, Greece, Sept. 2007.

[17] Hiroshi Nishimoto, Toshihiko Nishimura, Takeo Ohgane, and Yasutaka Ogawa, "Channel Estimation with Space-Time Windowing in MIMO PE-SDM Transmission," 2007 IEEE Vehicular Technology Conference (VTC2007-Fall), pp.541–545, Baltimore, U.S.A., Sept./Oct. 2007.

[18] Phu Huu Bui, Toshihiko Nishimura, Hiroshi Nishimoto, Takeo Ohgane, and Yasutaka Ogawa, "Robust MIMO-OFDM E-SDM Systems With Low Complexity in Time-Varying Indoor Fading Environments," 2007 IEEE Vehicular Technology Conference (VTC2007-Fall), pp.1322–1326, Baltimore, U.S.A., Sept./Oct. 2007.

[19] Yasutaka Ogawa, Huu Phu Bui, Hiroshi Nishimoto, Toshihiko Nishimura, and Takeo Ohgane, "Performance Considerations on MIMO Spatial Multiplexing from the Viewpoint of Antennas and Propagation," 2nd European Conference on Antennas and Propagation (EuCAP 2007), Th2.3.6, Edinburgh, UK, Nov. 2007.

Domestic Conference

[1] Hiroshi Nishimoto, Yasutaka Ogawa, Toshihiko Nishimura, and Takeo Ohgane, "Performance Evaluation of MIMO Space Division Multiplexing in Actual Channels," Technical Report of IEICE Radio Communication Systems, RCS2003-210, pp.139–144, Kanazawa, Nov. 2003 (in Japanese).

[2] Hiroshi Nishimoto, Yasutaka Ogawa, Toshihiko Nishimura, and Takeo Ohgane, "Performance Analysis of MIMO-SDM Based on 5.2GHz Band Measurements in Indoor Environments," Technical Report of IEICE Antennas and Propagation, A·P2004-70, pp.25–30, Sapporo, July 2004 (in Japanese).

[3] Hiroshi Nishimoto, Yasutaka Ogawa, Toshihiko Nishimura, and Takeo Ohgane, "Performance Evaluation of MIMO-SDM Considering Mutual Coupling Based on Indoor Measurements," Technical Report of IEICE Antennas and Propagation, A·P2004-162, pp.53–58, Tokyo, Oct. 2004 (in Japanese).

[4] Hiroshi Nishimoto, Yasutaka Ogawa, Toshihiko Nishimura, and Takeo Ohgane, "Performance Comparison of MIMO-SDM Depending on Array Configurations Based on Indoor Measurements," Technical Report of IEICE Antennas and Propagation, A·P2004-300, pp.123–128, Yokosuka, March 2005 (in Japanese).

[5] Hiroshi Nishimoto, Toshihiko Nishimura, Yasutaka Ogawa, and Takeo Ohgane, "Performance Evaluation of MIMO-SDM Using a Tripole Antenna Based on Indoor Channel Measurements," Technical Report of IEICE Radio Communication Systems, RCS2005-39, pp.71–76, Nagoya, June 2005 (in Japanese).

[6] Hiroshi Nishimoto, Yasutaka Ogawa, Toshihiko Nishimura, and Takeo Ohgane, "Performance Evaluation of MIMO E-SDM Based on Indoor Measurement," Technical Report of IEICE Antennas and Propagation, A·P2005-106, pp.127–132, Akita, Oct. 2005 (in Japanese).

[7] Takahiro Ishida, Hiroshi Nishimoto, Toshihiko Nishimura, Takeo Ohgane, and Yasutaka Ogawa, "A Study on Eigenbeam-Space Division Multiplexing with MMSE-FDE," Technical Report of IEICE Radio Communication Systems, RCS2006-10, pp.55–60, Osaka, April 2006 (in Japanese).

[8] Hiroshi Nishimoto, Toshihiko Nishimura, Takeo Ohgane, and Yasutaka Ogawa, "Pseudo Eigenbeam-Space Division Multiplexing in Frequency Selective Fading Environments," Technical Report of IEICE Radio Communication Systems, RCS2006-56, pp.125–130, Nagoya, June 2006 (in Japanese).

[9] Yusuke Ohwatari, Hiroshi Nishimoto, Toshihiko Nishimura, Takeo Ohgane, and Yasutaka Ogawa, "A Study on Reduction of the Amount of CSI Feedback with Time-domain Channel in MIMO-OFDM Eigenbeam-Space Division Multiplexing

Systems," Technical Report of IEICE Radio Communication Systems, RCS2006-64, pp.31–36, Sapporo, July 2006 (in Japanese).

[10] Hiroshi Nishimoto, Toshihiko Nishimura, Takeo Ohgane, and Yasutaka Ogawa, "Pseudo Eigenbeam SDM with MMSE-FDE for Single Carrier Transmission," Technical Report of IEICE Radio Communication Systems, RCS2006-69, pp.61–66, Sapporo, July 2006 (in Japanese).

[11] Hiroshi Nishimoto, Toshihiko Nishimura, Takeo Ohgane, and Yasutaka Ogawa, "Performance Evaluation of MIMO-OFDM Pseudo Eigenbeam Space Division Multiplexing," Technical Report of IEICE Radio Communication Systems, RCS2006-105, pp.1–6, Sendai, Aug./Sept. 2006 (in Japanese).

[12] Takahiro Ishida, Hiroshi Nishimoto, Toshihiko Nishimura, Takeo Ohgane, and Yasutaka Ogawa, "Performance of Frequency-Flat E-SDM (FFE-SDM) Single Carrier Transmission with MMSE-FDE Incorporating an Interference Canceller," Technical Report of IEICE Radio Communication Systems, RCS2006-106, pp.7–12, Sendai, Aug./Sept. 2006 (in Japanese).

[13] Keiichi Kambara, Hiroshi Nishimoto, Toshihiko Nishimura, Yasutaka Ogawa, and Takeo Ohgane, "A Received Block Division Technique for MMSE-FDE under Fast Fading Environments," Technical Report of IEICE Radio Communication Systems, RCS2006-149, pp.95–100, Takamatsu, Oct. 2006 (in Japanese).

[14] Phu Huu Bui, Toshihiko Nishimura, Hiroshi Nishimoto, Yasutaka Ogawa, and Takeo Ohgane, "Effects of Channel Prediction on MIMO E-SDM System Performance in Actual Time-Varying Fading Environments," Technical Report of IEICE Software Radio, SR2006-55, pp.97–104, Sapporo, Nov./Dec. 2006.

[15] Keiichi Kambara, Hiroshi Nishimoto, Toshihiko Nishimura, Yasutaka Ogawa, and Takeo Ohgane, "Improvement of a Received Block Division Technique for MMSE-FDE under Fast Fading Environments," Technical Report of IEICE Radio Communication Systems, RCS2006-217, pp.7–12, Okinawa, Jan. 2007 (in Japanese).

[16] Hiroshi Nishimoto, Toshihiko Nishimura, Takeo Ohgane, and Yasutaka Ogawa, "A Study on Improvement of Channel Estimation Accuracy in Pseudo Eigenbeam Space Division Multiplexing," Technical Report of IEICE Radio Communication Systems, RCS2006-228, pp.67–72, Okinawa, Jan. 2007 (in Japanese).

[17] Keiichi Kambara, Hiroshi Nishimoto, Toshihiko Nishimura, Yasutaka Ogawa, and Takeo Ohgane, "A Received Block Division Technique with SC/MMSE Turbo Equalization under Fast Fading Environments," Technical Report of IEICE Radio Communication Systems, Ohita, Dec. 2007 (in Japanese), to be presented.

[18] Hiroshi Nishimoto, Toshihiko Nishimura, Yasutaka Ogawa, and Takeo Ohgane, "Performance Evaluation of MIMO Space Division Multiplexing in Line-Of-Sight (LOS)

Channels," Proceedings of the 2003 IEICE Society Conference, B-1-236, p.236, Niigata, Sept. 2003 (in Japanese).

[19] Hiroshi Nishimoto, Yasutaka Ogawa, Toshihiko Nishimura, and Takeo Ohgane, "Effects on MIMO Space Division Multiplexing in Indoor LOS Environments," Proceedings of the 2004 IEICE General Conference, SB-1-5, pp.S33–S34, Tokyo, March 2004 (in Japanese).

[20] Hiroshi Nishimoto, Yasutaka Ogawa, Toshihiko Nishimura, and Takeo Ohgane, "Performance Comparison of MIMO Spatial Multiplexing on Various Array Configurations in Actual Propagation Environments," Proceedings of the 2005 IEICE General Conference, B-1-244, p.244, Osaka, March 2005 (in Japanese).

[21] Toshihiko Nishimura, Hiroshi Nishimoto, Yasutaka Ogawa, and Takeo Ohgane, Evaluation of 3×3 MIMO-SDM Using a Tripole Antenna Based on Indoor Propagation Measurment," Proceedings of the 2005 IEICE General Conference, B-1-241, p.241, Osaka, March 2005 (in Japanese).

[22] Hiroshi Nishimoto, Yasutaka Ogawa, Toshihiko Nishimura, and Takeo Ohgane, "Performance Evaluation of MIMO Eigen-beam Space Division Multiplexing in Actual Environments," Proceedings of the 2005 IEICE Society Conference, BS-1-4, pp.S7–S8, Sapporo, Sept. 2005 (in Japanese).

[23] Hiroshi Nishimoto, Toshihiko Nishimura, Takeo Ohgane, and Yasutaka Ogawa, "Performance of MIMO-OFDM Pseudo Eigenbeam Transmission in an Indoor Propagation Environment," Proceedings of the 2006 IEICE Society Conference, B-1-217, p.217, Kanazawa, Sept. 2006 (in Japanese).

[24] Takahiro Ishida, Hiroshi Nishimoto, Toshihiko Nishimura, Takeo Ohgane, and Yasutaka Ogawa, "Performance of E-SDM Single Carrier Transmission with MMSE-FDE and a Parallel Interference Canceller," Proceedings of the 2006 IEICE Society Conference, B-5-9, p.368, Kanazawa, Sept. 2006 (in Japanese).

[25] Hiroshi Nishimoto, Toshihiko Nishimura, Takeo Ohgane, and Yasutaka Ogawa, "An Effective Channel Estimation Scheme Using Space-Time Windowing in Pseudo Eigenbeam Transmission," Proceedings of the 2007 IEICE General Conference, B-5-25, p.439, Nagoya, March 2007 (in Japanese).

[26] Keiichi Kambara, Hiroshi Nishimoto, Toshihiko Nishimura, Takeo Ohgane, and Yasutaka Ogawa, "A Study on Channel Interpolation for Subblock Processing Using MMSE-FDE under Fast Fading Environments," Proceedings of the 2007 IEICE General Conference, B-5-109, p.523, Nagoya, March 2007 (in Japanese).

[27] Shohei Kato, Hiroshi Nishimoto, Toshihiko Nishimura, Takeo Ohgane, and Yasutaka Ogawa, "Downlink Weights for Multiuser MIMO Systems Using the Gram-Schmidt

Orthogonalization," Proceedings of the 2007 IEICE Society Conference, B-1-202, p.202, Tottori, Sept. 2007 (in Japanese).

Patents

[1] Seigo Nakao, Yasutaka Ogawa, Takeo Ohgane, Toshihiko Nishimura, and Hiroshi Nishimoto, "A Method for Deriving Weight Vectors to Be Used at the Time of Transmitting Signals from a Plurality of Antennas, and Transmitting Apparatus and Communication System Utilizing Said Method," JP Patent Pending, Application Number 2006-151200, May 31, 2006.

[2] Seigo Nakao, Yasutaka Ogawa, Takeo Ohgane, Toshihiko Nishimura, and Hiroshi Nishimoto, "A Method for Deriving Weight Vectors to Be Used at the Time of Transmitting Signals from a Plurality of Antennas, and Transmitting Apparatus and Communication System Utilizing Said Method," US Patent Pending, Application Number 11/806, 488, May 31, 2007.

Awards

[1] 2006 Young Researchers' Award, IEICE, 2007.

[2] Student Paper Award, IEEE Vehicular Technology Society, Japan Chapter, 2007.

[3] 2006 RCS Active Research Award, IEICE, Technical Committee on Radio Communication Systems, 2007.